AD-A149 983 DEVELOPMENT AND APPLICATION OF LOW ENERGY X-RAY AND ELECTRON PHYSICS(U) HAWAII UNIV HONOLULU DEPT OF PHYSICS AND ASTRONOMY B L HENKE 06 DEC 84 1/3

UNCLASSIFIED AFOSR-TR-84-1270 AFOSR-84-0001 F/G 14/5 NL

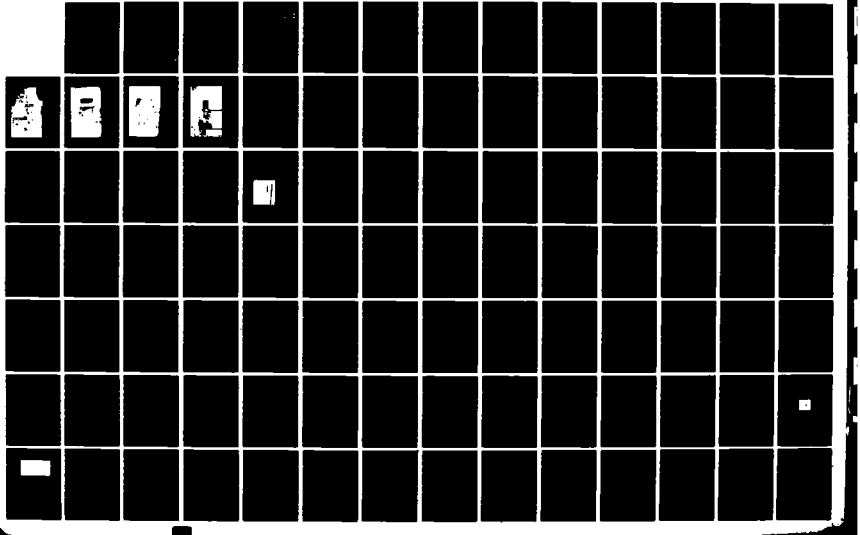

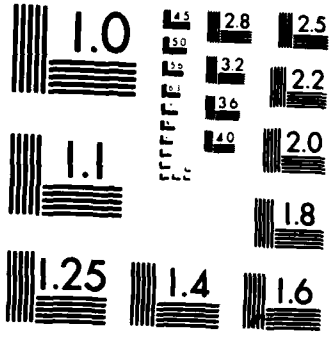

AFOSR-TR- 84-1270

DEVELOPMENT AND APPLICATION OF LOW ENERGY X-RAY AND ELECTRON PHYSICS

FINAL
~~Annual~~ Scientific Report
for the period

01 October 1983 through 30 September 1984

AFOSR Grant 84-0001

BURTON L. HENKE
Principal Investigator

Department of Physics and Astronomy
University of Hawaii
Honolulu, Hawaii 96822

Prepared for the

Air Force Office of Scientific Research
Directorate of Physics
Building 410, Bolling Air Force Base
Washington, D. C. 20332

December 1984

UNCLASSIFIED

SECURITY CLASSIFICATION OF THIS PAGE

REPORT DOCUMENTATION PAGE

1a. REPORT SECURITY CLASSIFICATION: Unclassified	1b. RESTRICTIVE MARKINGS
2a. SECURITY CLASSIFICATION AUTHORITY	3. DISTRIBUTION/AVAILABILITY OF REPORT: Approved for public release; Distribution unlimited.
2b. DECLASSIFICATION/DOWNGRADING SCHEDULE	
4. PERFORMING ORGANIZATION REPORT NUMBER(S)	5. MONITORING ORGANIZATION REPORT NUMBER(S): AFOSR-TR- 84-1220
6a. NAME OF PERFORMING ORGANIZATION: University of Hawaii; 6b. OFFICE SYMBOL (If applicable)	7a. NAME OF MONITORING ORGANIZATION: AFOSR/NP
6c. ADDRESS (City, State and ZIP Code): Department of Physics & Astronomy, 2505 Correa Road, Watanabe 210, Honolulu, Hawaii 96822	7b. ADDRESS (City, State and ZIP Code): Building 410, Bolling AFB, Washington, D.C. 20332-6448
8a. NAME OF FUNDING/SPONSORING ORGANIZATION: AFOSR; 8b. OFFICE SYMBOL (If applicable)	9. PROCUREMENT INSTRUMENT IDENTIFICATION NUMBER: AFOSR Grant 84-0001
8c. ADDRESS (City, State and ZIP Code): Building 410, Bolling AFB, Wasington, D. C. 20332-6448	10. SOURCE OF FUNDING NOS.

PROGRAM ELEMENT NO.	PROJECT NO.	TASK NO.	WORK UNIT NO.
61102F	2301	A8	

11. TITLE (Include Security Classification): DEVELOPMENT AND APPLICATION OF LOW ENERGY X-RAY & ELECTRON PHYSICS

12. PERSONAL AUTHOR(S): Burton L. Henke

13a. TYPE OF REPORT	13b. TIME COVERED	14. DATE OF REPORT (Yr., Mo., Day)	15. PAGE COUNT
~~Annual~~ FINAL	FROM 10-01-83 TO 09-30-84	12-06-84	218

16. SUPPLEMENTARY NOTATION

17. COSATI CODES			18. SUBJECT TERMS (Continue on reverse if necessary and identify by block number)
FIELD	GROUP	SUB. GR.	

19. ABSTRACT (Continue on reverse if necessary and identify by block number) A new spectrograph system has been developed and calibrated in this AFOSR-supported laboratory for the absolute spectrometry of high intensity pulsed x-ray sources (fusion energy and x-ray laser development) in the 100-10,000 eV region. This spectral region is analyzed with fixed elliptically curved crystals and molecular or metal multilayers of 2d-values in the 3-160 A range. Twin channels are utilized for simultaneous time-integrated photographic recording and for time-resolved x-ray streak camera recording. Absolute calibrations of the elliptical analyzers, of the photographic film, and of the gold and CsI transmission photocathodes have been made using monoenergetic, CW laboratory x-ray sources. The overall transmission characteristics of the spectrograph have also been determined. The instrument has been designed for mounting through a pneumatically-controlled high-vacuum valve onto a four-inch port of a one-meter diameter source chamber and includes an appendage, high-vacuum, sputter/ion pre-pumping station. The initial testing and application of this new spectrographic system has been on the University of Rochester's LLE 24-laser-beam OMEGA facility.

20. DISTRIBUTION/AVAILABILITY OF ABSTRACT	21. ABSTRACT SECURITY CLASSIFICATION
UNCLASSIFIED/UNLIMITED ☒ SAME AS RPT. ☒ DTIC USERS ☐	Unclassified

22a. NAME OF RESPONSIBLE INDIVIDUAL	22b. TELEPHONE NUMBER (Include Area Code)	22c. OFFICE SYMBOL
ROBERT J. BARKER	(202) 767-5011	NP

DD FORM 1473, 83 APR EDITION OF 1 JAN 73 IS OBSOLETE.

UNCLASSIFIED

SECURITY CLASSIFICATION OF THIS PAGE

ANNUAL SCIENTIFIC REPORT

AFOSR GRANT 84-0001

DEVELOPMENT AND APPLICATION OF LOW ENERGY X-RAY AND ELECTRON PHYSICS

(01 October 1983 through 30 September 1984)

The work of this AFOSR program for the past year has been concentrated upon the completion of a spectrographic system development, specially designed for the absolute spectrometry of pulsed, high temperature plasma x-ray sources. The principal immediate applications of this new system are for fusion energy and for the development of x-ray lasers.

The basic approach, first initiated on this AFOSR program, has been to use elliptically curved crystal/multilayer analyzers in a two-channel system, one time-resolving and the other time-integrating. A new, specially designed x-ray streak camera has been developed here. Its absolute calibration is obtained through time-integrated spectrometry by the second channel using photographic detection. Accurate, absolute x-ray response models have been developed for appropriate photographic films, expressed as analytical functions suitable for microcomputer conversion of spectral photographic density directly to photons/stearadian-pulse for a given transition (spectral line) of a pulsed x-ray source.

Presented in this report are works that have been recently submitted for publication and entitled:

These works have also been presented by this Principal Investigator as seminars at the National Laboratories, Sandia/Kirtland, Albuquerque, Los Alamos, Livermore and Brookhaven, and at the University of Rochester, N.Y. State University at Stony Brook and the University of California-Berkeley. A listing of these seminars given in 1983/84 is included below (p. 214).

The testing, evaluation and first applications of this new spectrographic system has been carried out this year using the OMEGA 24-laser beam source facility at the University of Rochester. The

results have been described as excellent and the spectrograph is now being used routinely for every shot with this facility on fusion energy and x-ray laser research at this Laboratory for Laser Energetics.

During this project year we have one of our research associates, Dr. Paul Jaanimagi, carrying out the initial testing and applications of the new spectrographic system at the OMEGA facility in Rochester. Here at the University of Hawaii we also have had the important assistance of another research associate, Dr. Narayana Balakrishnan, on the development of the elliptically curved multilayer analyzers that are being applied on the new system for the low-energy x-ray diagnostics of the Rochester experiment. We have been able to obtain Department of Energy supplemental contracts for the participation of these two post-doctoral assistants through the National Laser Users Facilities (NLUF) and through the National Laboratories at Los Alamos and Livermore.

Finally we present in this report a listing of recent publications of this AFOSR program on Low-Energy X-Ray Physics and Technology along with a listing of several reports now in preparation (p. 215).

A Two-Channel, Elliptical Analyzer Spectrograph for Absolute, Time-Resolving/Time-Integrating Spectrometry of Pulsed X-Ray Sources in the 100-10,000 eV Region

B. L. Henke and P. A. Jaanimagi*
Department of Physics and Astronomy
University of Hawaii
Honolulu, Hawaii 96822

ABSTRACT

A new spectrograph system has been developed and calibrated in this laboratory for the absolute spectrometry of high intensity pulsed x-ray sources in the 100-10,000 eV region. This spectral region is analyzed with fixed elliptically curved crystals and molecular or metal multilayers of 2d-values in the 3-160 A range. Twin channels are utilized for simultaneous time-integrated photographic recording and for time-resolved x-ray streak camera recording. Absolute calibrations of the elliptical analyzers, of the photographic film, and of the gold and CsI transmission photocahodes have been made using monoenergetic, CW laboratory x-ray sources. The overall transmission characteristics of the

spectrograph have also been determined. The instrument has been designed for mounting through a pneumatically-controlled high-vacuum valve onto a four-inch port of a one-meter diameter source chamber and includes an appendage, high-vacuum, sputter/ion pre-pumping station. The initial dynamic testing and application of this new spectrographic system has been on the University of Rochester's LLE 24-laser-beam OMEGA facility.

---

*Current address: University of Rochester, Laboratory for Laser Energetics, 250 East River Road, Rochester, New York 14623.

I. INTRODUCTION

There is a considerable need at this time for absolute time-resolved/time-integrated spectrometry of high intensity, pulsed x-ray sources in the 100-10,000 eV photon energy region. Typically these sources are the high temperature plasmas as involved, for example, in fusion energy research, and in materials excited by the large synchrotron radiation facilities. The spatial extents of the sources to be measured (or imaged) usually subtend a relatively small angle at the spectrograph. The pulse structure to be analyzed requires time resolution in usually the picosecond to microsecond range. We describe here an instrument that can accomplish this type of spectrometry which has been constructed and CW-source calibrated in this laboratory and is now being applied to the diagnostics of laser-produced plasmas with the OMEGA facility at the Laboratory for Laser Energetics, University of Rochester.

In preparation for this type of x-ray spectrograph development we have recently completed some basic studies in low-energy x-ray spectroscopy as reported in Refs. 1-9.

In Ref. 1 we discuss the geometrical and physical x-ray optics for fixed, Bragg reflecting analyzers for pulsed source spectrometry. This study led to the choice of elliptically curved, fixed Bragg crystals or multilayers for the analyzing element

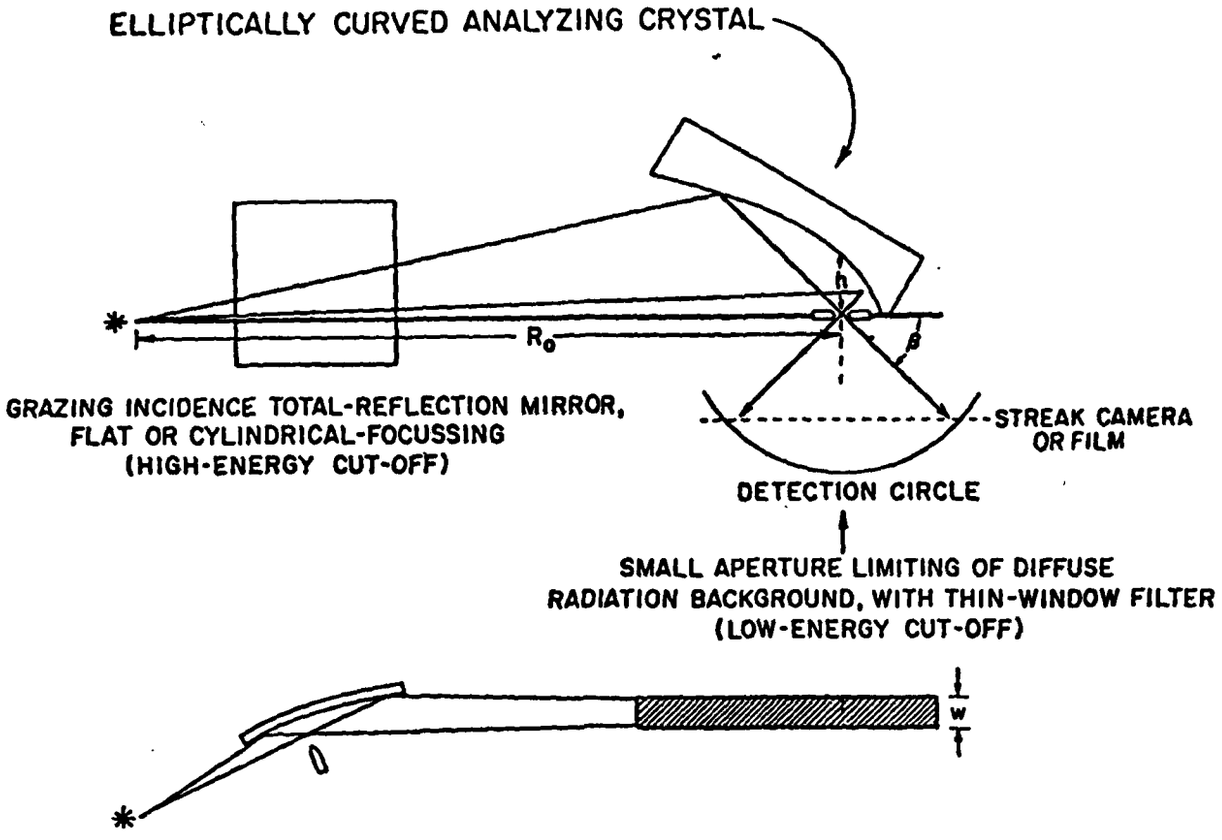

Figure 1. The basic optical geometry of elliptical analyzer spectroscopy.

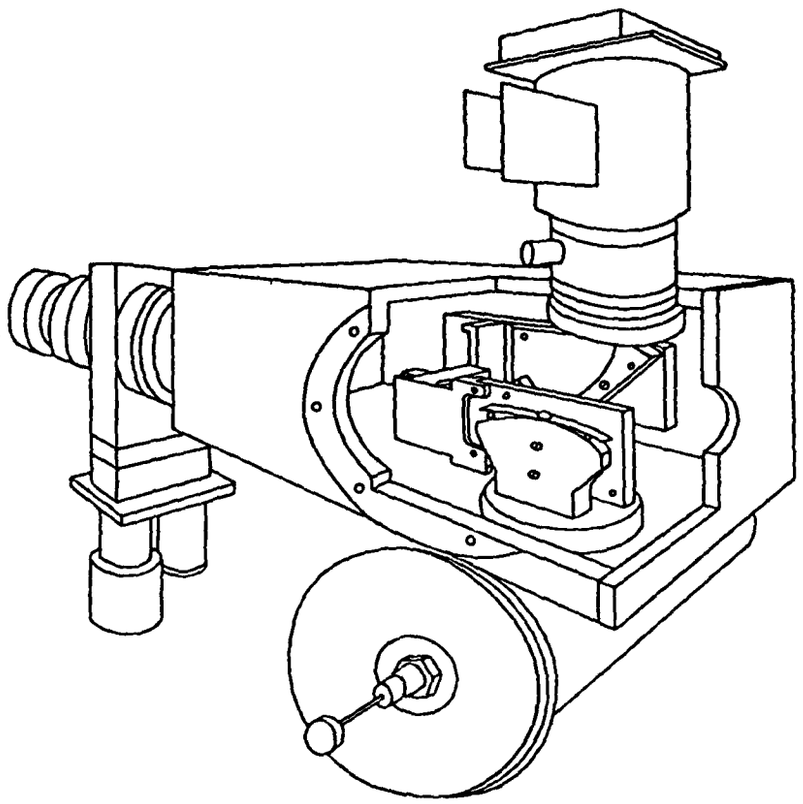

Figure 2. Cut-away drawing illustrating the mounting of the two elliptical analyzer channels in the SPEAXS system.

Fig. 1). Some of the advantages of this type of dispersive geometry may be summarized as follows:

(a) With the source at one focal point for the given elliptical geometry, all reflected radiation passes through the second focal point where an effective scatter aperture may be located and is the geometric center for a normal-incidence detection circle along which photographic or electronic position-sensitive detection may be effectively applied.

(b) Small band-pass and/or low-energy cut-off filter foils may be mounted across this scatter aperture. High-energy cut-off mirror monochromators may lbe easily introduced between the elliptical analyzer and the source (as shown in Fig. 1).

(c) As described in Ref. 1, spectroscopy with spatial resolution for linear or two-dimensional source distributions may be accomplished by using slits or curved focussing mirror monochromators with the elliptical analyzers.

(d) This elliptical geometry yields a relatively simple analytical spectrometer transmission function for absolute photometric analysis along the detection circle (as discussed in Ref. 1).

In the design of the present instrument it was considered important to be able to measure simultaneously the spectrum of a subnanosecond source with time integration and with time-resolution in the 10 picosecond range. To accomplish this, two identical elliptical analyzer channels were utilized, one to a photographic film camera and the other to a specially designed, large entrance

slit x-ray streak camera. This Streak camera /Photographic camera Elliptical Analyzer X-ray Spectrograph will be referred to as the SPEAXS system.

Presented here in Sec. II is a description of the basic design features of this SPEAXS system along with those for the alignment procedure for application to the "point" laser-produced sources. In Sec. III we describe the response of the crystal/multilayer analyzers that we have chosen for the 100-10,000 eV region and that of associated low- and high-energy cut-off characteristics of practical filters and mirror monochromators. In Sec. IV we describe the photographic and streak camera detection that is applied with this SPEAXS system. And finally in Sec. V we present some initial measurements on the OMEGA source facility and discuss the combining of calibration results for the generation of an overall transmission function for the SPEAXS system as applied for absolute spectrometry.

II. DESIGN AND CONSTRUCTION OF THE SPEAXS SYSTEM

A drawing of the SPEAXS system is shown in Fig. 2. It has been designed to bolt onto a four-inch-port on the one-meter diameter spherical target chamber of the OMEGA. The source-to-scatter aperture distance (between focal points of the elliptical analyzer) is 120 centimeters. The stainless steel block housing is attached to the chamber through a pneumatically-controlled four-inch vacuum valve and the system is prepumped to 10^{-6} Torr with a Vacion pump backed initially through a molecular seive trap to a mechanical

pump. The twin elliptical analyzer/mirror monochromator stations are mounted through a rear port and are adjustable through two side access ports. A photo of the assembled spectrograph is shown in Fig. 3 with the streak camera mounted above and the photographic camera below the housing.

In order to allow a precise optical alignment of the elliptical analyzers, these along with their associated mirror monochromators are mounted on blocks that are attached to structures which permit small rotations about two axes, one along the center line of the scatter aperture slit and the other perpendicular to the aperture plane and through its center (see Figs. 4 and 5). To achieve optical alignment with a small "point" target, a high precision alignment telescope is precision-fit to each elliptical analyzer block, in turn, with its optical axis of the telescope along the central ray to the source focal point of the ray-system that illuminates the elliptical analyzer. The telescope-and-analyzer block is then rotated to bring the image of an ambient-lighted point target to the middle of the telescope reticule as illustrated Fig. 6. After this alignment, the rotating crystal block mountings are clamped into fixed positions.

When a mirror monochromator is attached to the elliptical analyzer block, with the desired angle of reflection fixed, the optical image that is centered within the alignment telescope field is formed directly by reflected rays presented by the monochromator mirror. (Optically reflecting test analyzers and mirrors are used in this alignment procedure.)

By placing a point source of visible light at the source position (or alternatively, an image of a point source with a ray system that proceeds to illuminate the total elliptical analyzer surface) the optical perfection of the mirror/analyzer system may be evaluated. With proper optical alignment, a sharp line image appears along the center line of the scatter aperture. A "knife edge" test on the uniformity of the optical reflection from the elliptically curved surface may be demonstrated by the uniformity of the illumination along the detection circle.

Finally, the geometrical and smoothness integrity of the crystal/multilayer analyzer surface and absence of crystal defects may be evaluated by testing for waviness and variation of photographic density of photographically recorded x-ray spectral lines on a film placed along the detection circle.

III. CRYSTAL/MULTILAYER ANALYZERS, MIRROR MONOCHROMATORS AND FILTERS

Thin sections of crystals (0.5" x 4.0" and of .005"-.020" thickness) are cemented to standardized, elliptically curved substrates which are machined by a computer-controlled mill. The construction of the elliptical analyzers is described in detail in Ref. 1. The large 2d analyzers are deposited as molecular multilayers (lead salts of straight-chain fatty acids) and directly upon the curved substrates that have been clad with thin glass sections and as described in Refs. 1 and 2. In Table 1 we present a listing of crystals/multilayers that have been chosen for the present

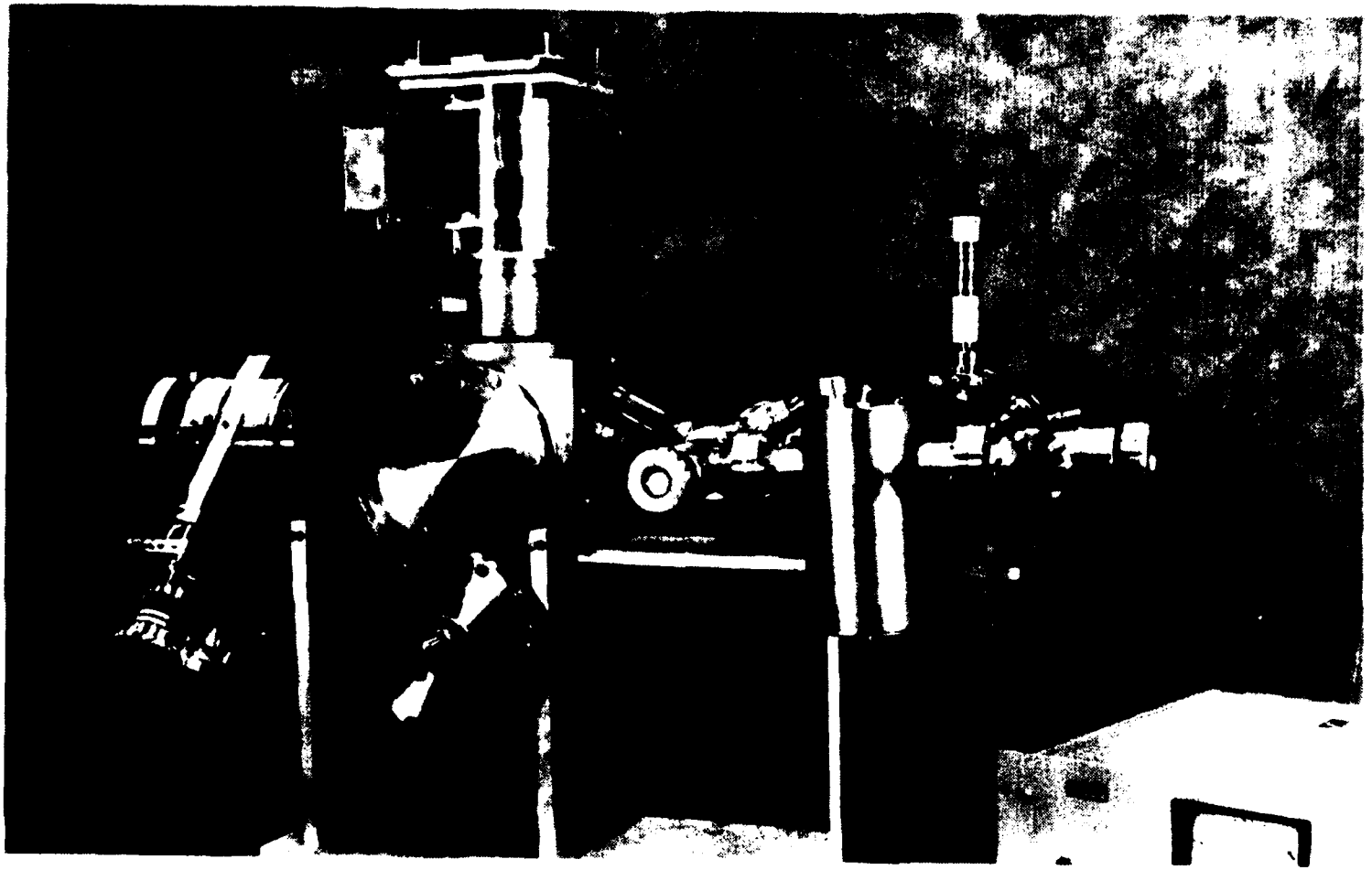

Figure 3. The SPEAXS system with the x-ray streak camera in the up- and the photographic camera in the down-position. Also shown here is a pneumatically controlled four-inch vacuum valve through which the system is bolted onto a one-meter diameter target chamber, and with a VacIon/-molecular sieve appendage prepumping system.

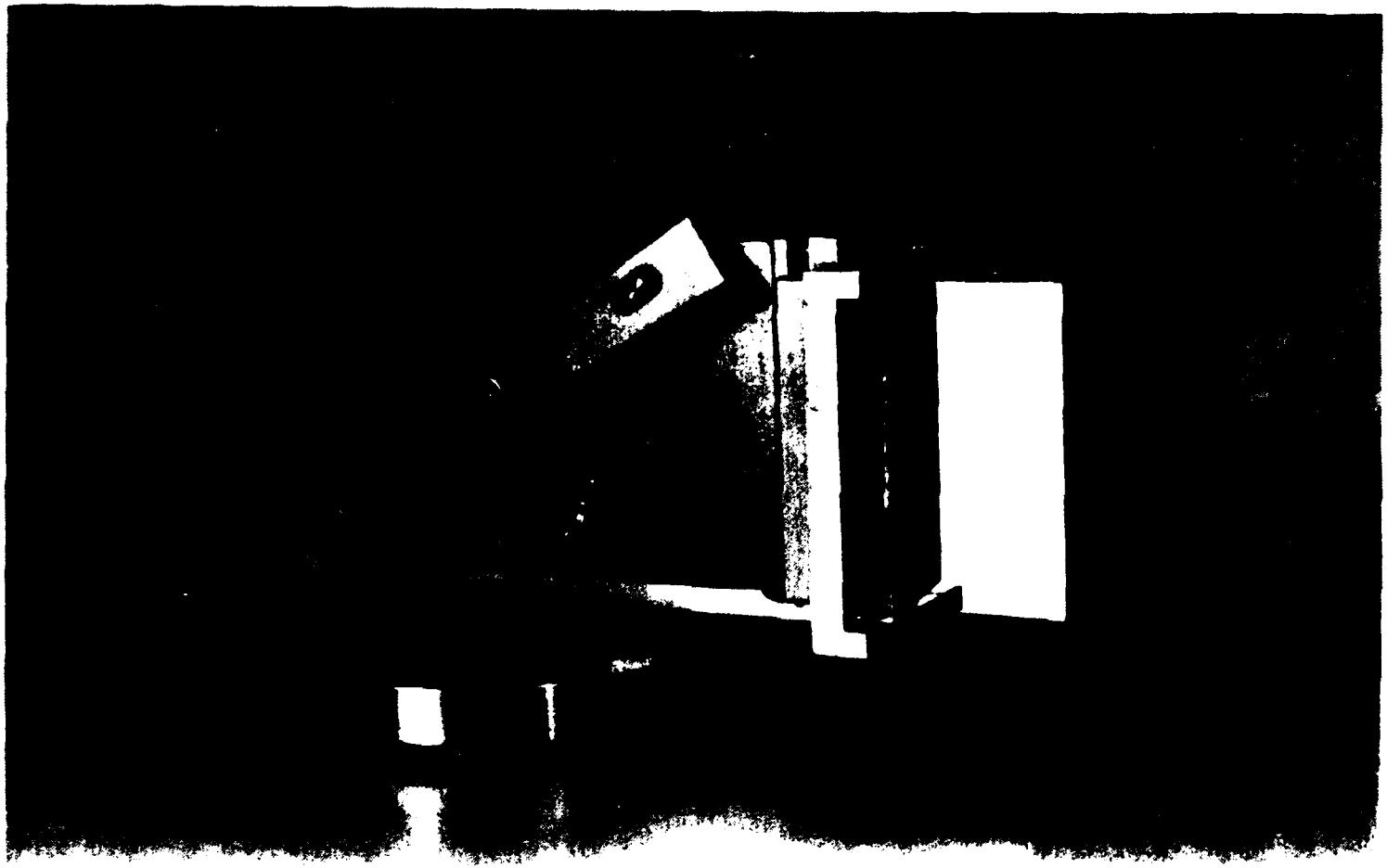

Figure 4. Showing the elliptical analyzer substrate and mirror monochromator attached to the mounting block on the rotating table. The scatter aperture plate is mounted on the bottom of the circular table.

Figure 5. Back view of rotating table as shown in Fig. 4. Shown here is the rotational adjustment of the mounting block orientation about an axis perpendicular to that of the rotating table axis and in the plane of the scatter aperture plate.

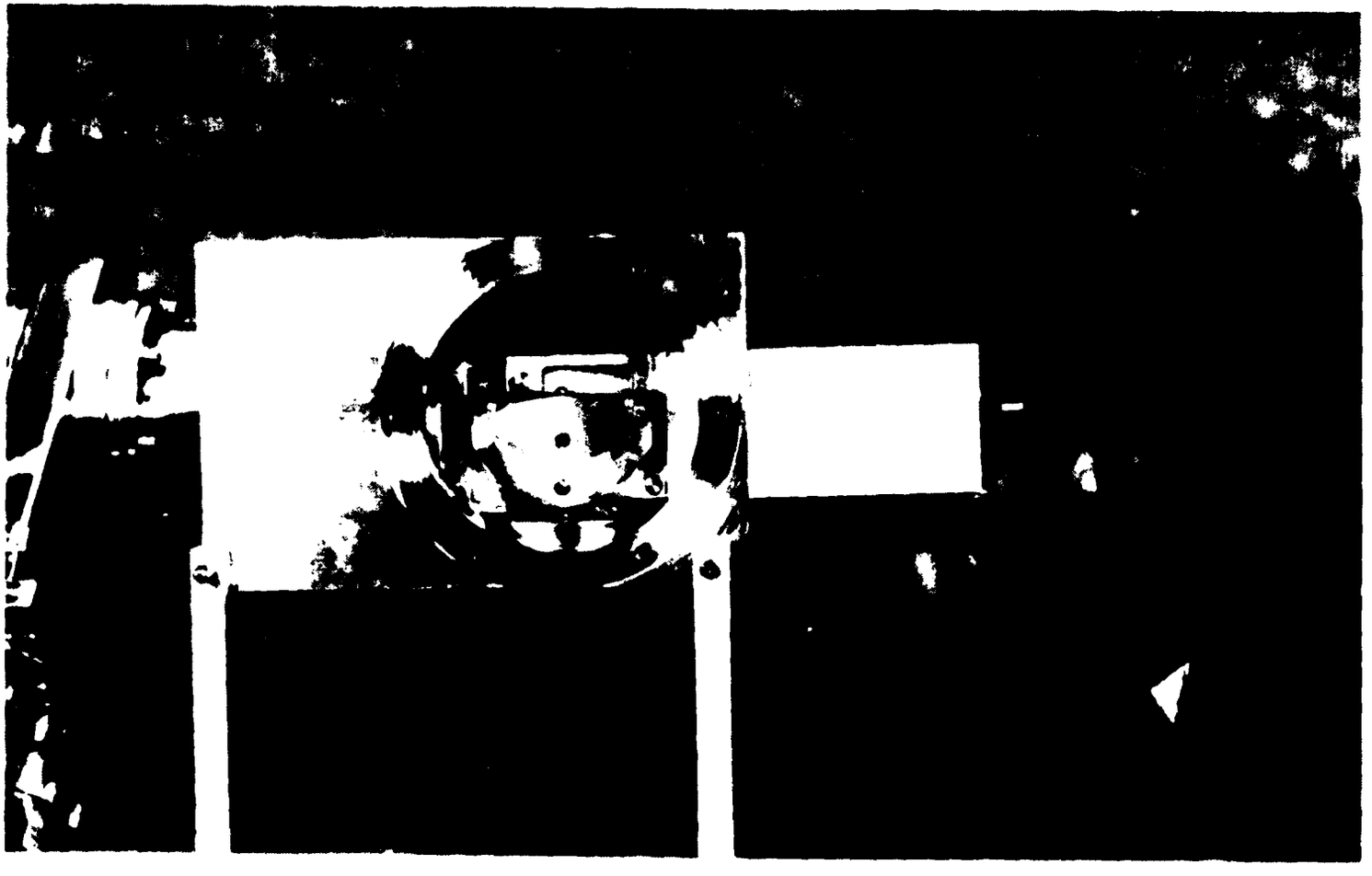

Figure 6. Depicting the alignment procedure. A precision alignment telescope is fastened to each mounting block in turn, rotated about the two axes until the image of the small target is on the center of the reticule. The mounting block is then fixed in this position by tightening mounting bolts accessible through the side ports.

TABLE 1 - Crystal/multilayers for elliptical analyzers having integrated reflectivities as plotted in Fig. 7

No.	Crystal Name	Indices (hkl)	2d	Diffraction Order	E(eV) limits 22.5° - (θ)-67.5°	R (45°) (millirad.)
1	Lif	(200)	4.03	1	8046 - 3333	0.0433
2	Mica	(002)	19.84	3	4900 - 2029	0.0286
3	PET	(002)	8.74	1	3707 - 1535	0.0907
4	Gypsum	(020)	15.19	1	2134 - 884	0.0711
5	Mica	(002)	19.84	1	1633 - 676	0.0136
6	RAP	(1010)	26.12	1	1240 - 514	0.0848
7	KAP	(1010)	26.63	1	1217 - 504	0.0488
8	*Laurate		70.00	1	463 - 192	0.4878
9	Stearate		100.00	1	324 - 134	0.8262
10	Lignocerate		130.00	1	249 - 103	0.9373
11	Melissate		160.00	1	203 - 84	0.8974

*Molecular multilayers of lead salts of straight-chain fatty acids.
**For Bragg angle, θ, equal to 45°.

SPEAXS system and which are currently under evaluation in this laboratory for spectrometry in the 100-10,000 eV region. Given here are the 2d values, photon energy limits for Bragg angles of 22.5 to 67.5 degrees and the calculated integrated reflectivity, R, (Darwin-Prins) at 45° Bragg angle. Our methods for the calculation and experimental measurement of the integrated reflectivities are discussed in Refs. 1, 3 and 4. In Fig. 7, we present the integrated reflectivities for the analyzers listed in Table 1 plotted for the appropriate photon energy segments through the entire 100-10,000 eV region in order to illustrate the "coverage" by this set of analyzers.

In Ref. 3 we have presented detailed reflectivity vs angle of grazing incidence and photon energy curves and tables for the mirror monochromator systems that are currently used in low-energy x-ray spectrometry. Two of these mirror monochromators have been applied in this SPEAXS system to effectively suppress the second and higher order diffracted background radiations. These are with a 30-milliradian reflection from Al and with a 67.5 milliradian reflection from Al_2O_3 having high-energy cut-off characteristics at about 1000 eV and 500 eV, respectively. The reflectivity vs photon energy curves for these mirror monochromators are presented in Fig. 8.

The low-energy background radiation that may be superimposed upon the higher energy measured spectra can be excessive, first, because the sources of interest often have a relatively large component of low-energy x-rays and euv, and, second, because these

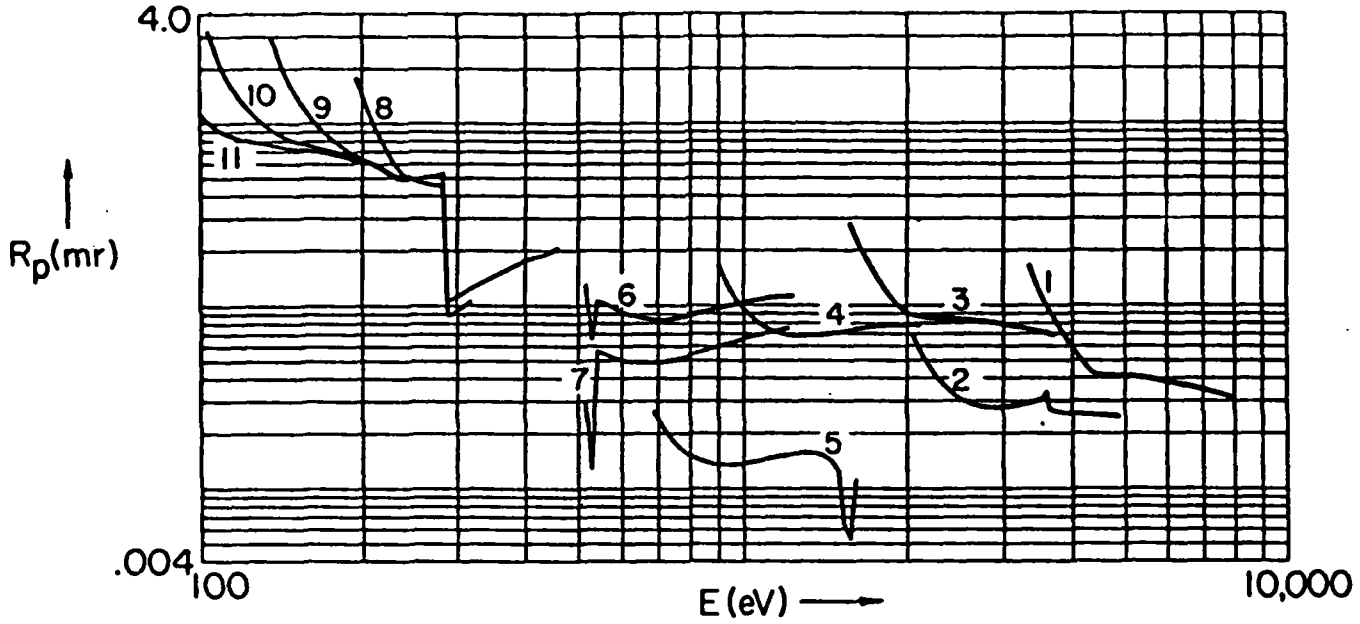

Figure 7. Integrated reflectivity, R(milliradians) vs Photon Energy, E(eV) for eleven crystal/multilayers that may be applied to cover the 100-10,000 eV region as elliptical analyzers. The R-plots have been calculated using the Darwin-Prins model. (See Appendix C for detailed plots.)

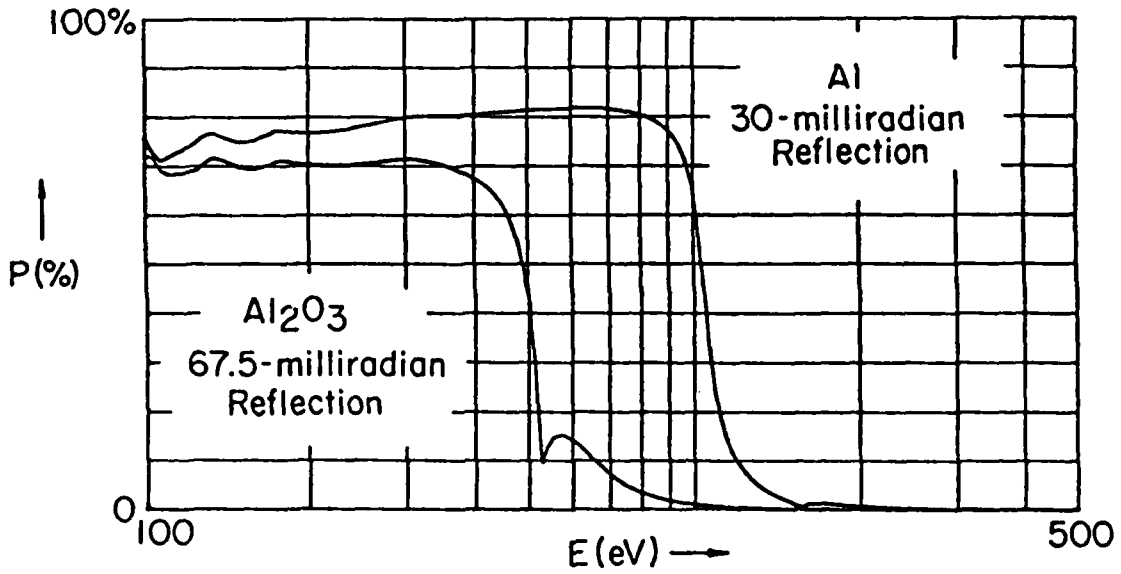

Figure 8. Percent reflectivity, P(%) vs Photon Energy, E(eV), illustrating high-energy cut-off characteristics of a 67.5-milliradian reflection from an Al_2O_3 mirror and of a 30-milliradian reflection from an Al mirror. These monochromators effectively reduce the high-energy background above 500 eV and 1000 eV respectively.

longer wavelength radiations can strongly scatter and specularly reflect from the analyzer surface and effectively compete with the Bragg reflected spectral intensities. To suppress this low-energy background, a relatively thick filter with a strong transmission band for the particular spectral region being measured can often be effective (usually placed at the small scatter aperture). In Table 2 are listed some practical filter materials along with their mass thickness, m (=1/2μ) for which their transmission will be about 60 percent at a photon energy just below a given strong absorption edge (the high-energy limit of the particular transmission band). In Figs. 9 and 10 are plotted the transmission bands in the 100-10,000 eV region of interest here.

IV. PHOTOGRAPHIC AND STREAK CAMERA DETECTION

Particularly in the fusion energy research, time-resolved x-ray diagnostics of high temperature plamas is essential. For the application of the present SPEAXS system on the diagnostics of laser-produced plasmas (with subnanosecond pulses) the required time resolution in the 10 picosecond range has been achieved with a specially designed x-ray streak camera. In order to obtain an absolute calibration of the time-resolved streak spectrum, a simultaneous absolute time-integrated intensity value on the same spectrum is obtained by photographic recording with a parallel, identical elliptical analyzer channel.

In the present instrument an entrance aperture slit to each channel is applied which establishes a spectral line length at the detection circle of 3 millimeters. The one-millimeter width of the 40-millimeter streak camera slit (positioned along a chord of the detection circle) is aligned along the middle of this 3-millimeter wide zone. Correspondingly, a photographic film placed on the detection circle measures spectra within this 3-millimeter wide band, and a subsequent microdensitometer measurement may be with an effective one-millimeter slit length scan averaged through the middle of the exposed 3 mm zone.

A 35-millimeter photographic film is mounted upon a semi-circular film holder of a radius equal to 8.4 cm which may be advanced into this detection circle by means of a sliding/rotating vacuum feedthrough rod permitting four exposures of the 3-millimeter spectral bands to be obtained on each 35 mm film strip. After making these exposures, the film holder cassette may be drawn back against the circular access plate that is sealed by an O-ring to the side of the camera cassette may be as shown in Fig. 3. In this closed position, a light baffle is then rotated into place over the cassette entrance slit and the side plate may then be removed along with the film holder within a light-tight enclosure which can be carried to a darkroom for processing.

The photographic camera and the streak camera can be set to have comparable sensitivities in the x-ray region as established by the choice of the photographic film and of the transmission photocathode material and thickness at the streak camera's entrance

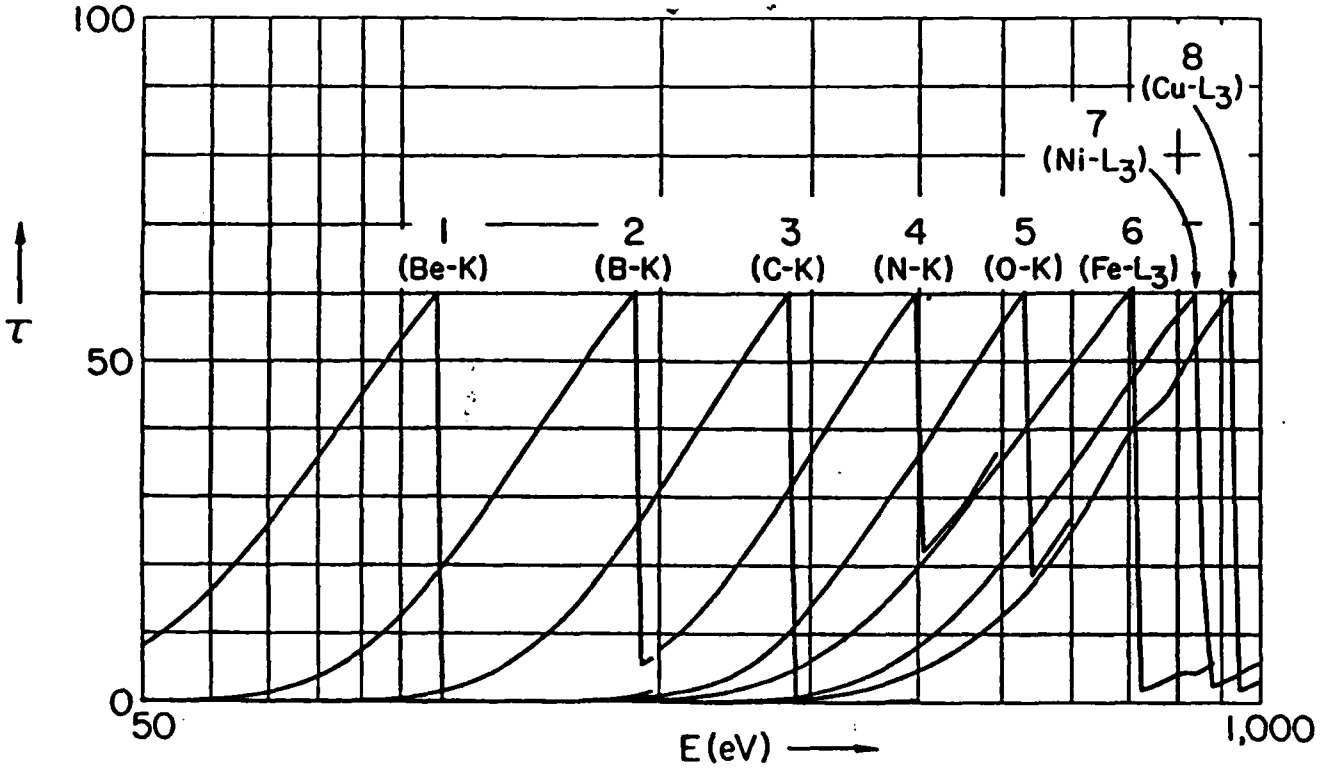

Figure 9. Transmission bands of selected filters listed in Table 2 for the 100-1000 eV region. (See Appendix B for detailed transmission curves which indicate the effectiveness of the low-energy cut-off characteristics.)

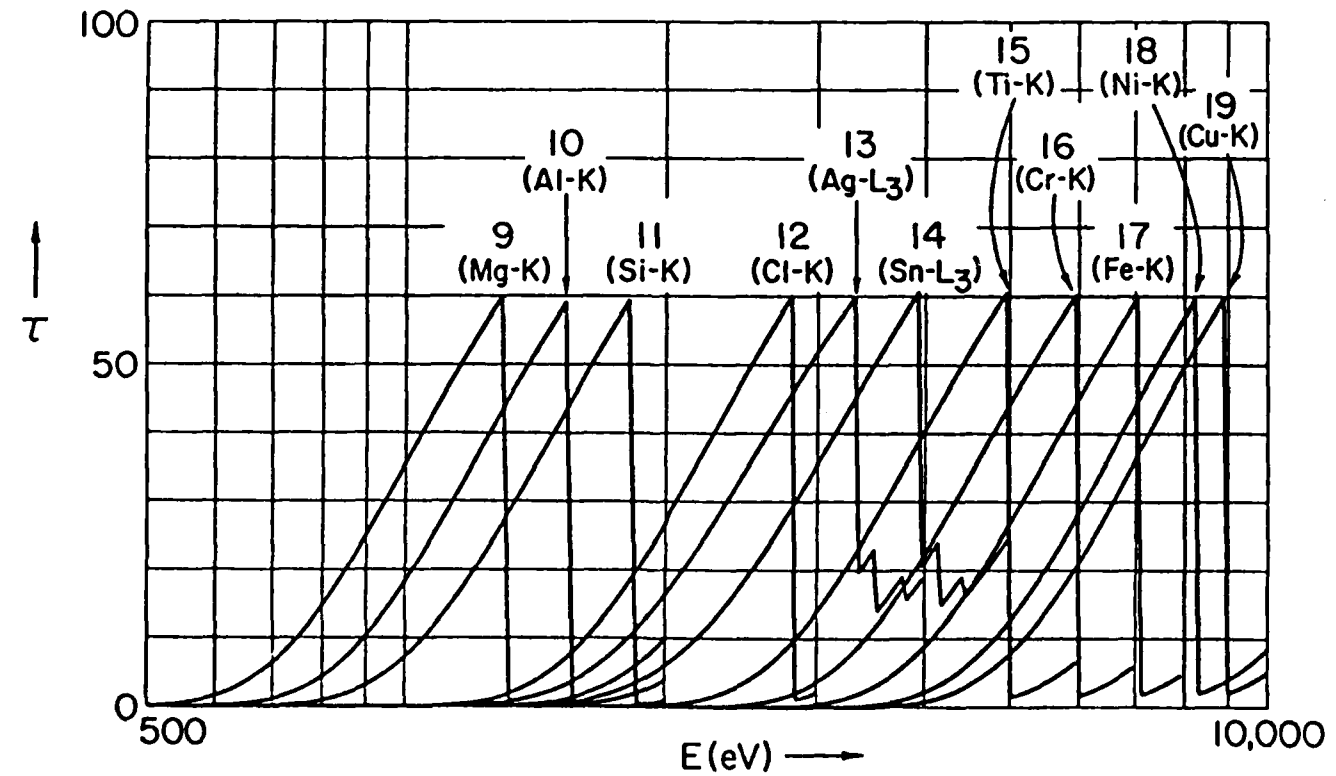

Figure 10. Transmission bands for selected filters listed in Table 2 for the 500-10,000 eV region.

TABLE 2. Mass thickness for filters with transmission band characteristics illustrated in Figs. 9 and 10.

No.	Filter	Edge (eV)	1/2μ (μg/cm²)
1	Beryllium Be	Be-K (111)	81
2	Boron Nitride BN	B-K (188)	68
3	Carbon C	C-K (284)	226
	Polypropylene $(CH_2{=}CHCH_3)_x$	C-K (284)	256
	Formvar $C_5H_7O_2$	C-K (284)	156
	Mylar $C_{10}H_8O_4$	C-K (284)	152
	Kimfol $C_{16}H_{14}O_3$	C-K (284)	181
4	Boron Nitride BN	N-K (400)	66
5	Aluminum Oxide Al_2O_3	O-K (532)	126
	Silicon Dioxide SiO_2	O-K (532)	116
	Polyformaldehyde $(CH_2O)_x$	O-K (532)	92
6	Iron Fe	Fe-L_3(707)	234
7	Nickel Ni	Ni-L_3(854)	279
8	Copper Cu	Cu-L_3(933)	318
9	Magnesium Mg	Mg-K (1303)	1139
10	Aluminum Al	Al-K (1560)	1427
11	Silicon Si	Si-K (1840)	1680
12	Saran $(CH_2{=}CCl_2)_x$	Cl-K (2820)	3151
13	Silver Ag	Ag-L_3(3351)	1296
14	Tin Sn	Sn-L_3(3929)	1669
15	Titanium Ti	Ti-K (4964)	6010
16	Chromium Cr	Cr-K (5989)	7924
17	Iron Fe	Fe-K (7111)	9804
18	Nickel Ni	Ni-K (8331)	11820
19	Copper Cu	Cu-K (8980)	13699

slit. Further adjustment of the sensitivitiy of the two channels is obtained by introducing matched filters of desired absorption thickness at the two scatter aperture as described earlier. Finally, to bring the exposure within the dynamic range of the photographic detection, the four exposures of the film strip may be with four thicknesses of additional filter material that are mounted as a wedge at the entrance slit of the translating film cassette.

After a standardized film processing, the properly exposed photographically recorded spectral line (or continuum) may be microdensitometered to yield a profile in photographic density, D. In Ref. 5 we have described an accurate method for analytically transforming this profile in photographic density, D, to a profile in absolute intensity at the detection circle, I(photons/micrometer^2) using a semi-empirical photographic response function which relates the exposing intensity, I, to the measured density, D', for a given photon energy, E. This function may be combined with the transmission characteristics of the elliptical analyzer channel via a microcomputer to yield an absolute source intensity plot (e.g., photons/stearadian) vs photon energy, E, directly from the microdensitometer data as will be outlined in Sec. V.

Three practical photographic film types have been characterized in detail for absolute spectrometry in the 100-10,000 eV region with the SPEAXS system (see Ref. 5). Their sensitivities vs photon energy, E, are compared in Fig. 11.

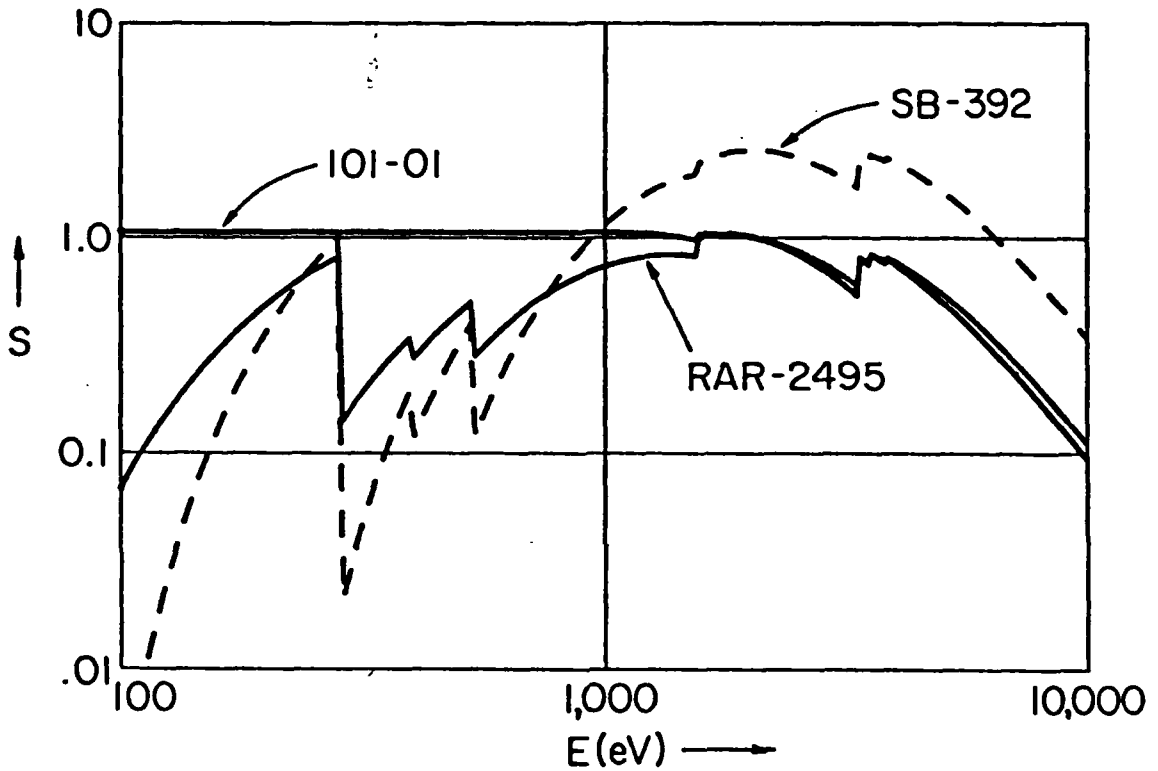

Figure 11. Comparison of the sensitivities in the 100-10,000 eV region of three photographic film types suitable for absolute spectrometry with the SPEAXS system, Kodak's 101, RAR-2495 and SB-392 mm films. (See Ref. 6 for a description of their characterization.) Sensitivity is defined here as the reciprocal of the exposure, $I(\text{photons}/\mu m^2)^{-1}$ that is required to establish a density, D = 0.5.

The spectral range is covered with the x-ray streak camera by positioning the entrance slit along one of three chords on a detection circle (accomplished with straight-through and a tilted mounting flange). The central axis of the camera passes through the focal point at the scatter aperture center and may be mounted so as alternatively to make the angles, -20°, 0 and +20° with the normal to the aperture plane. The minimum distance of the photocathode to the scatter aperture is 24 mm. Because of the large angular dispersion of Bragg reflecting analyzers and because of the mechanical and electrical problems associated with very close coupling of the entrance slit of the streak camera and the analyzer, it becomes of considerable advantage in crystal spectroscopy to employ streak cameras having relatively long entrance slits. For the SPEAXS system an x-ray streak camera has been specially developed that has an entrance slit of 1 by 40 millimeters with more than 300 spatially resolved elements along this slit. And it has the required 10 picosecond resolution. This was accomplished by a systematic series of experimental modifications of the basic structure of the RCA 73435 image tube as suggested by an associated series of measurements and precisely computed electron ray traces following each modification. This tube development is described in detail in the companion work of Ref. 6.

The transmission photocathodes that are used with this streak camera on the SPEAXS system are cesium iodide and gold for relatively high and low sensitivity applications respectively. We have measured the absolute quantum efficiency for these photocathodes (secondary electrons emitted per incident photon) as described in Ref. 7 and examples of the yield vs photon energy

curves for 1000 A CsI films and for 200 A gold films are presented in Figs. 12 and 13.

V. INITIAL RESULTS AND PROCEDURES FOR ABSOLUTE SPECTROMETRY

The initial dynamic tests of the SPEAXS system have been on microballoon targets irradiated by a six-beam ultraviolet laser pulse (λ = 351 nm) using the University of Rochester's Laboratory for Laser Energetics OMEGA facility. In Figs. 14 and 15 are shown examples of photographically recorded spectra using a 12.7 μm Be foil across the scatter aperture and with the LiF and PET analyzing crystals respectively. Exposures were on Kodak's RAR 2495 (35 mm) film. The microdensitometry was with a 30x400 μm slit and with a multi-scan integration of the optical density through the central one millimeter region of the exposed three millimeter band (as also measured by the streak camera's one-millimeter slit).

The spectrum of Fig. 14 was generated by a 600 ps pulse of 200 joules absorbed energy upon a bare glass microballoon of 200 μm diameter. The spectral lines measured here, using the LiF analyzer, are for highly ionized species of calcium (an impurity in the glass).

The spectrum of Fig. 15 was generated by a 600 ps pulse of 200 joules absorbed energy upon a 200 μm diameter glass microballoon that was coated with one μm of aluminum. The spectral lines measured here using the PET analyzer, are for highly ionized species of aluminum and silicon.

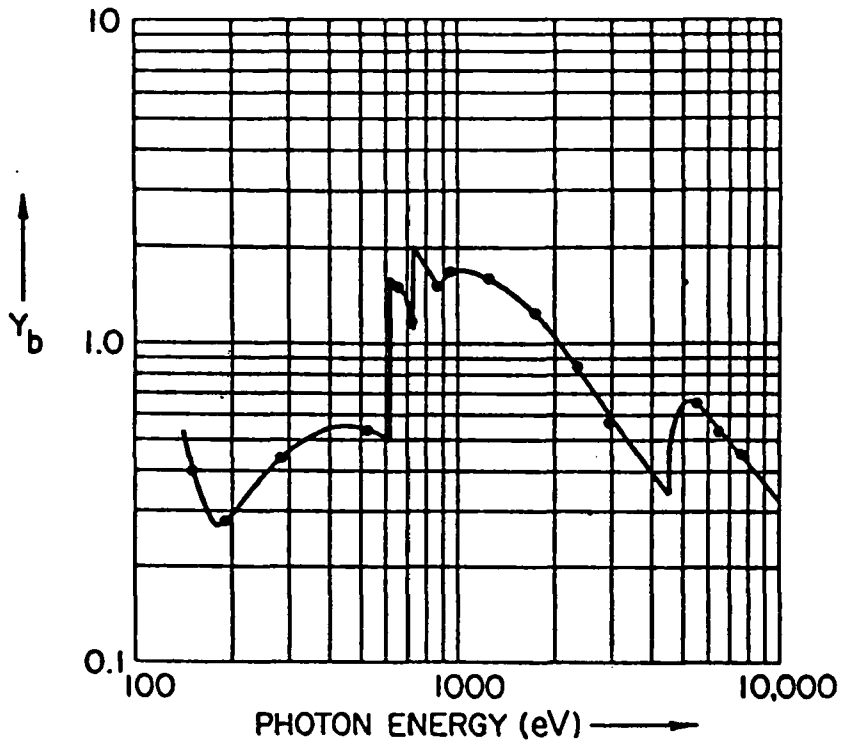

Figure 12. The quantum yield, Y_b (secondary electrons emitted per incident photon) vs photon energy, E (eV) of a 1000 A cesium iodide transmission photocathode (evaporated under high vacuum (see Ref. 8)).

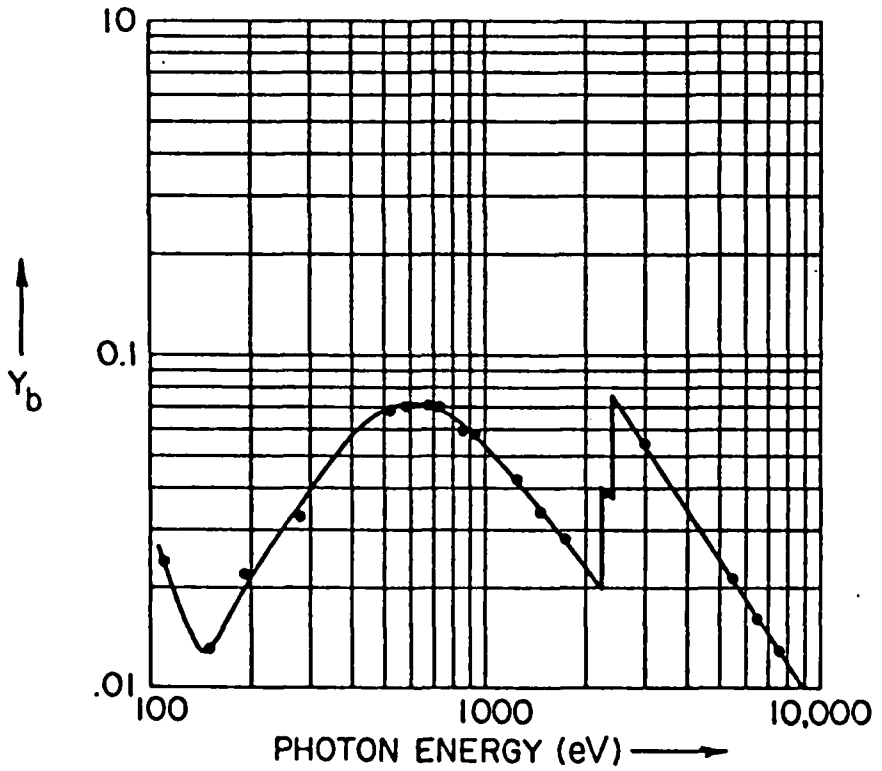

Figure 13. Quantum yield, Y_b (secondary electrons per incident photon) for a 200 A gold transmission photocathode (see Ref. 8).

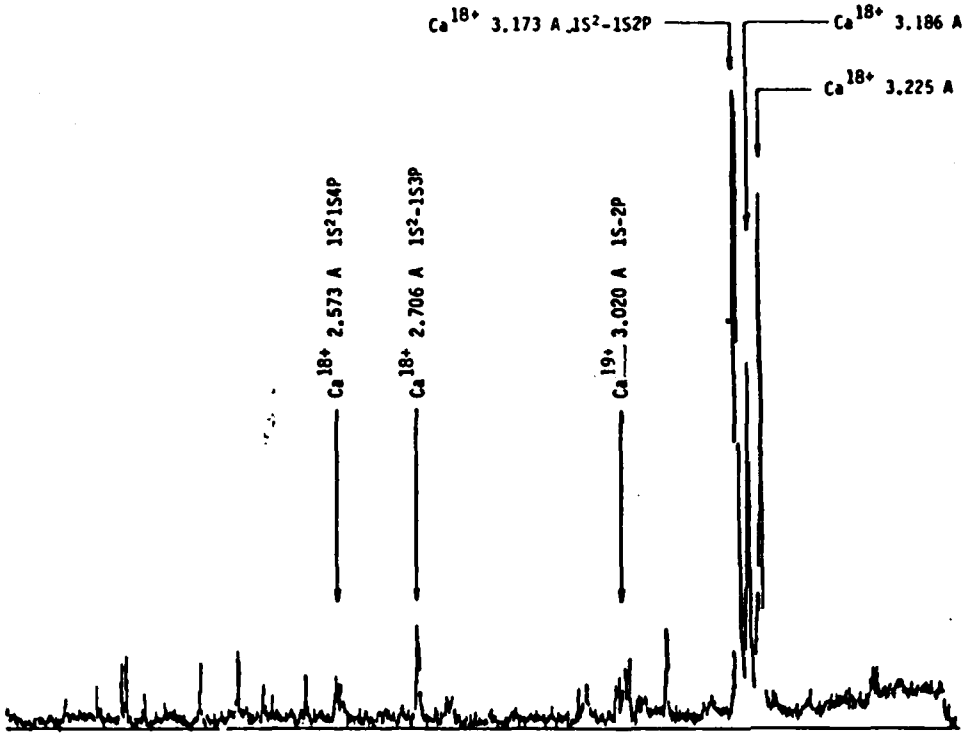

Figure 14. Example of photographically recorded spectrum with the SPEAXS system using the LiF crystal elliptical analyzer. Measuring transitions for Ca^{18+} excited by a 600 ps/200 j pulse of 351 nm blue light of the OMEGA facility upon a 200 μm diameter bare glass microballoon (with densities not corrected for background).

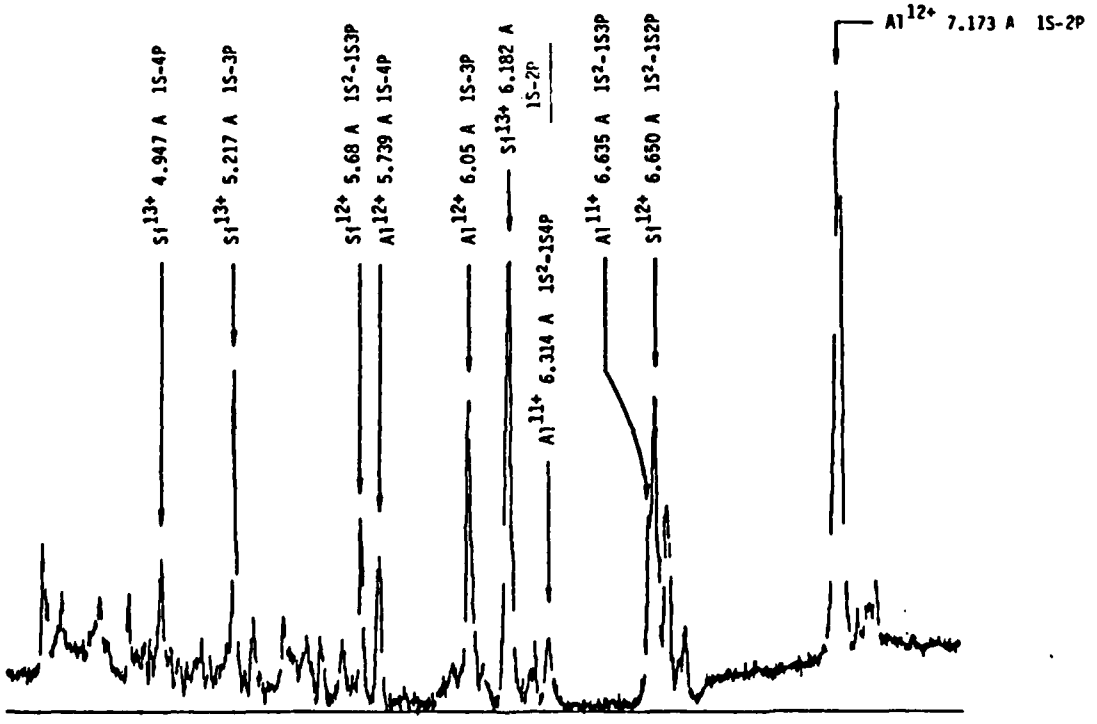

Figure 15. Example of a photographically recorded spectrum with the SPEAXS system using the PET elliptical analyzer. Measuring transitions for the ionized species, Al^{11+}, Al^{12+}, Si^{12+} and Si^{13+} from a 200 μm diameter glass microballoon coated with one μm of Al and excited by a 600 ps/200 j pulse of 351 nm blue light of the OMEGA facility. Exposure on Kodak's RAR-2495 film (film densities not corrected for background).

The intensities along the three millimeter length of the spectral lines as measured with the LiF analyzers were uniform. The measured intensities, however, symmetrically drop off in the first and third millimeter segments along the spectral line for the PET analyzer (and also for the RAP analyzers that have been applied for these initial tests). We believe that this non-uniformity has resulted from a slight curvature of the crystal surface in its short dimension. We hope to improve the flatness of the crystal on the elliptical substrates by varying the mounting adhesives and procedures from those as originally described in Ref. 1.

Presented in Fig. 16 is an example of the initial tests of the x-ray streak camera (a Poloroid photograph of the image intensifier ouput for a spectrum from a bare glass microballoon using a PET analyzing crystal and a CsI transmission photocathode). The wedge shape of the streak lines is the result of some electrical deflection-plate and anode coupling. These effects will be eliminated in a new streak tube now under construction (see Ref. 6). Having elliptically curved analyzers and streak camera optics of improved quality, we may then proceed to measure accurate absolute photon energies and intensities of spectral lines and of continuum distributions.

The absolute photon energy, E(eV), and wavelength, λ(A), may be determined from the measured angular position, β, (see Fig. 1) along the detection circle for the elliptical analyzer by the following relation (from Eq. (6), Ref. 1):

$$\lambda(A) = \frac{2d}{m}\sin\left[\tan^{-1}\left(\frac{1-\epsilon\cos\beta}{\epsilon\sin\beta}\right)\right] = \frac{12,398}{E(eV)}$$

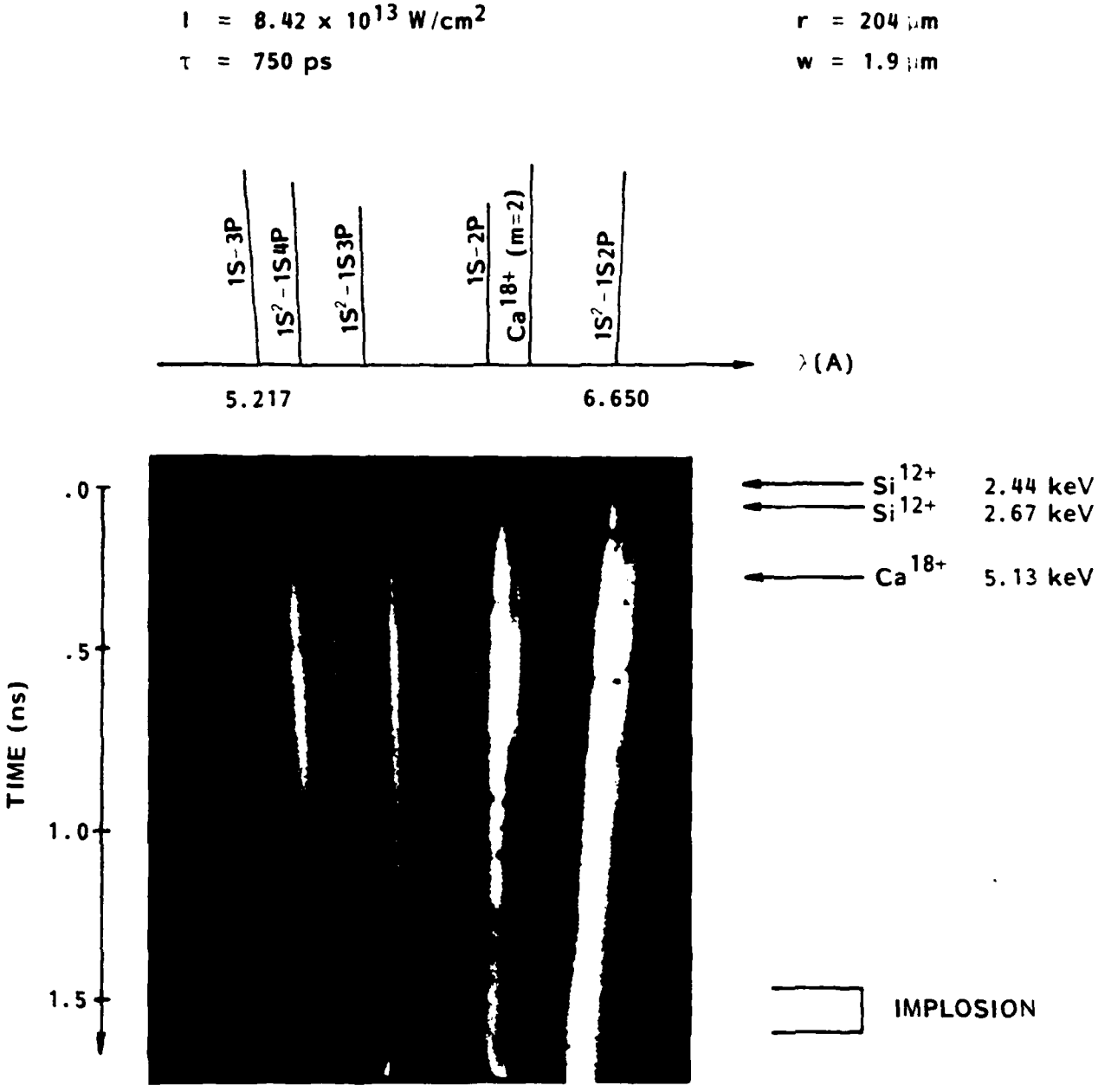

Figure 16. A photograph of the x-ray streak camera output for a spectrum presented to a CsI transmission photocathode by a PET elliptical analyzer. The spectrum was laser-produced from a bare glass microballoon.

Here m is the diffraction order and d is the effective atomic plane spacing of the analyzer (corrected for refraction) and expressed in angstroms. The eccentricity parameter, ε, for the ellipticity of the analyzer has been given in Ref. 1 (Eq. (5)) by the relation:

$$\varepsilon = \sqrt{1+(h/R_0)^2}-h/R_0$$

in which R_0 is the distance between the focal points (between the source and the center of the scatter aperture) and h is the size parameter that measures the distance from the second focal point at the scatter aperture to the elliptical analyzer surface along the ray for β = 90 degrees. (The elliptical geometry of the analyzer is completely characterized by the parameters, R_0 and h which are equal to 120 cm and 5.08 cm respectively for the present SPEAXS system.)

The absolute source brightness for a characteristic line emission at photon energy, E, may be determined as i_0 (photons-emitted-per-pulse/stearadian) by the following relation (see Ref. 1, Eq. (14)):

$$i_0 = \frac{NL}{FMRW(d\chi/d\theta)}$$

where N is the total number of photons measured at the detection circle of radius, r, within a spectral line of length w. L is the constant total-pathlength for all rays from the source point, off the analyzer, through the scatter aperture and then to the detection circle, and given by

$$L = \sqrt{R_0^2+h^2}+h+r$$

F is the filter transmission factor at photon energy, E; M is the monochromator mirror reflectivity factor at photon energy, E; R is

analyzer at photon energy, E; $(dX/d\theta)$ is the ratio of the differential angle in the plane of reflection of the rays that originate at the source to the corresponding differential Bragg angle, $d\theta$, of their reflection from the analyzer. N, for a given spectral line, may be determined by numerically integrating over the spectral line intensity distribution, I(photons/μm^2) vs E as derived from the measured photographic density, D, vs line position, β, using the photographic film response functions described in Ref. 5 (via a microcomputer connected to the microdensitometer).

The filter transmission, F, mirror reflectivity, M, and analyzer integrated reflectivity, R, may be derived by calculations based upon the atomic photoionization cross sections and the complex atomic scattering factors. This procedure has been outlined in Ref. 3. We have presented recently in Ref. 4 the atomic photoionization and scattering factor tables for 94 elements which have been generated by fitting theoretical photoionization vs E curves to the best available experimental data for the 30-10,000 eV region and applying the quantum dispersion theory, with these data to generate the corresponding atomic scattering factors. Also presented in Ref. 4 are the detailed calculations for mirror reflectivities and for crystal/multilayer integrated reflectivities, M and R, for materials that are important in currently applied x-ray diagnostics.

Presented in Appendix A are practical examples of filter transmission curves for the 100-10,000 eV region that have transmission bands which were described in Figs. 9 and 10.

We have found (see Ref. 8) that our theoretically calculated mirror reflectivity curves generally predict well the experimentally measured data only for mirror surface that have been obtained with "state of the art" smoothness. For the mirrors used in the SPEAXS system our calibration procedure is to normalize the theoretically calculated curves to reflectivity curves that we have measured experimentally (for effective averaging of the experimental data).

In Appendix B we present plots for the first and second diffraction orders for the integrated reflectivity, R, for the eleven crystal/multilayer analyzers that have been shown in Fig. 7 for the 100-10,000 eV region. Again, our calibration procedure for the crystal/multilayer analyzers involves fitting the averaging theoretical R vs E curves to directly measured integrated reflectivity data. We have found, as discussed in Ref. 9, that our closest fits with the experimental data are usually with the theoretical curves calculated with the Darwin-Prins model (as applied here for the R-curves shown in Fig. 7 and in Appendix B). Typical R(exp)/R(Darwin-Prins) normalizing ratios that have been determined for the elliptical analyzers calibrated for the present SPEAXS system are given in Table III.

We present in Appendix C a detailed table for the photographic specular density, D, vs. the exposure I (photons/μm^2) and the photon energy, E(eV) in the 100-10,000 eV region for normal incidence upon Kodak's RAR 2495 film. This film has been found to be particularly useful in the general application of the SPEAXS

TABLE 3. Comparison of Experimental and Theoretical Integrated Reflectivity Values - (A Modified Darwin-Prins Model has been applied for the theoretical calculations.)

Analyzer	No. layers	2d	Photon Energy	R_x(mr)	R_p(mr)	R_x/R_p x100
LiF		4.03	4510.8	0.035	0.042	83
Mica - 3rd order		19.84	2293.2	0.027	0.039	70
PET		8.74	2293.2	0.121	0.085	142
Gypsum		15.19	2622.4	0.055	0.055	99
Mica - 1st order		19.84	929.7	0.020	0.013	147
RAP		26.12	676.8	0.088	0.085	104
KAP		26.63	676.8	0.052	0.049	106
Laurate	125	70.00	676.8	0.324	0.382	85
Myristate	200	80.00	192.6	0.940	0.990	95
Stearate	135	100.00	676.8	0.327	0.342	96
Behenate	150	120.00	277.0	0.425	0.532	80
Lignocerate	115	130.00	192.0	0.547	0.617	89
Melissate	100	160.00	277.0	0.359	0.522	69

system. It, along with other film types have been characterized as described in our recent works cited in Ref. 5.

We have outlined above our procedures for determining the number of photons-emitted-per-pulse/stearadian, i_0 , from a "point" source for a particular atomic transition (characteristic line). In Ref. 1 we have also presented a similar procedure for the determination of the Photons-emitted-per-pulse/stearadian-eV, S_0, for a continuum distribution (see Ref. 1, Eq. (15)). And finally, we have described in Ref. 1 a procedure for the determination of the line shape parameters from the experimental spectral line distribution (a spectral line distribution of area under the line equal to the total number of photons, i_0, emitted-per-pulse/stearadian for the given transition and as defined above.) For this line shape analysis, a fold of Gaussian and Lorentzian Shape functions (the Voigt function) was assumed for a sufficiently accurate fit of the experimental line profile. (See Ref. 1, Sec. IV.)

ACKNOWLEDGMENTS

The authors gratefully acknowledge the invaluable assistance of the staff and students on this program, Priscilla Piano, Murray Tester, Ron Tackaberry, Cyril Lance, Siu Lung Kwock, Jeremy Uejio and Gerald Young.

This project is part of an overall program on Low-Energy X-Ray Physics and Technology supported by the Air Force Office of Scientific Research Grant No. 84-0001 and supplementally by the Department of Energy under Contract Nos. DE-AS08-83DP40181 (LANL/LLNL) and DE-AS08-82DP40175 (NLUF).

REFERENCES

1. B. L. Henke, H. T. Yamada and T. J. Tanaka, Rev. Sci. Instrum. 54, 1311 (1983).

2. B. L. Henke, N. S. Balakrishnan and A. R. Bird, "Multilayer Analyzers for Low-Energy X-Ray Spectroscopy (100-500 eV): Part II. Construction and Characterization," in preparation.

3. B. L. Henke, AIP Conference Proceedings No. 75 on Low-Energy X-Ray Diagnostics, Monterey, California (American Institute of Physics, New York, 1981), p. 85, D. T. Attwood and B. L. Henke, Editors.

4. B. L. Henke, P. Lee, T. J. Tanaka, R. L. Shimabukuro and B. K. Fujikawa, Atomic Data and Nuclear Data Tables 27, No. 1 (1982).

5. B. L. Henke, S. L. Kwok, J. Y. Uejio, H. T. Yamada and G. C. Young, J. Opt. Soc. America B (December 1984); B. L. Henke, F. G. Fujiwara, M. A. Tester, C. H. Dittmore and M. A. Palmer, J. Opt. Soc. America B (December 1984).

6. P. A. Jaanimagi and B. L. Henke, "Large Aperture Picosecond X-Ray Streak Camera," to be published.

7. B. L. Henke, J. P. Knauer and K. Premaratne, J. Appl. Phys. 52, 1509 (1981).

8. B. L. Henke, F. G. Fujiwara, R. E. Tackaberry and D. Kania, "Reflectivity Characteristics of Low-Energy Mirror Monochromators," in preparation.

9. B. L. Henke, H. T. Yamada, G. C. Young, S. L. Kwock and J. Y. Uejio, "Multilayer Analyzers for Low-Energy X-Ray Spectroscopy (100-500 eV): Part I. Mathematical Models," in preparation.

APPENDIX A

Transmission band and low-energy cut-off characteristics of selected filters. (For the 100-10,000 eV region having filter thicknesses which yield transmission band peak values of about 60%. The corresponding mass thicknesses, $\rho\chi(\mu g/cm^2)$, are listed in Table 2.)

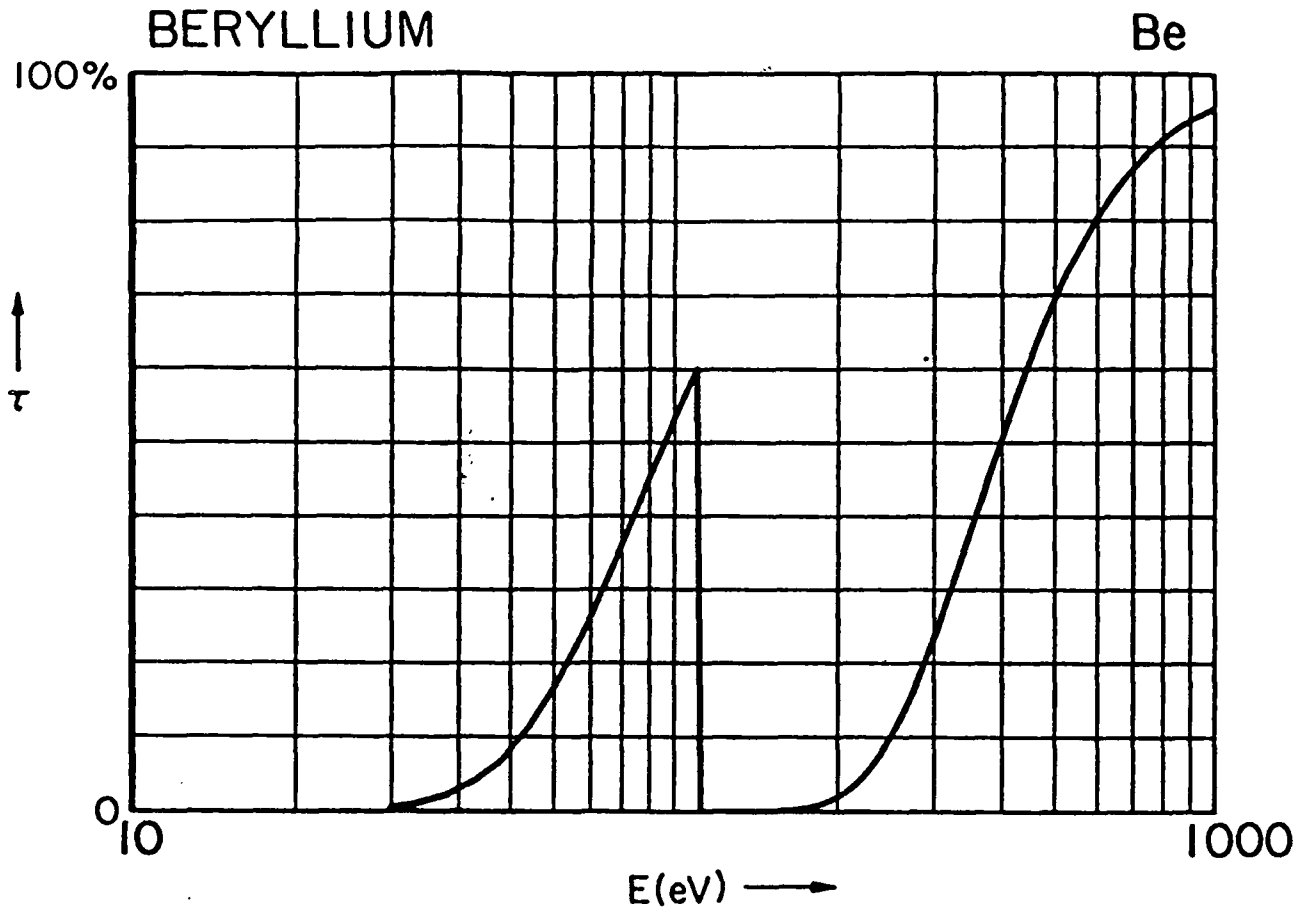
BERYLLIUM
Be
100%
τ
0
10
1000
E(eV)

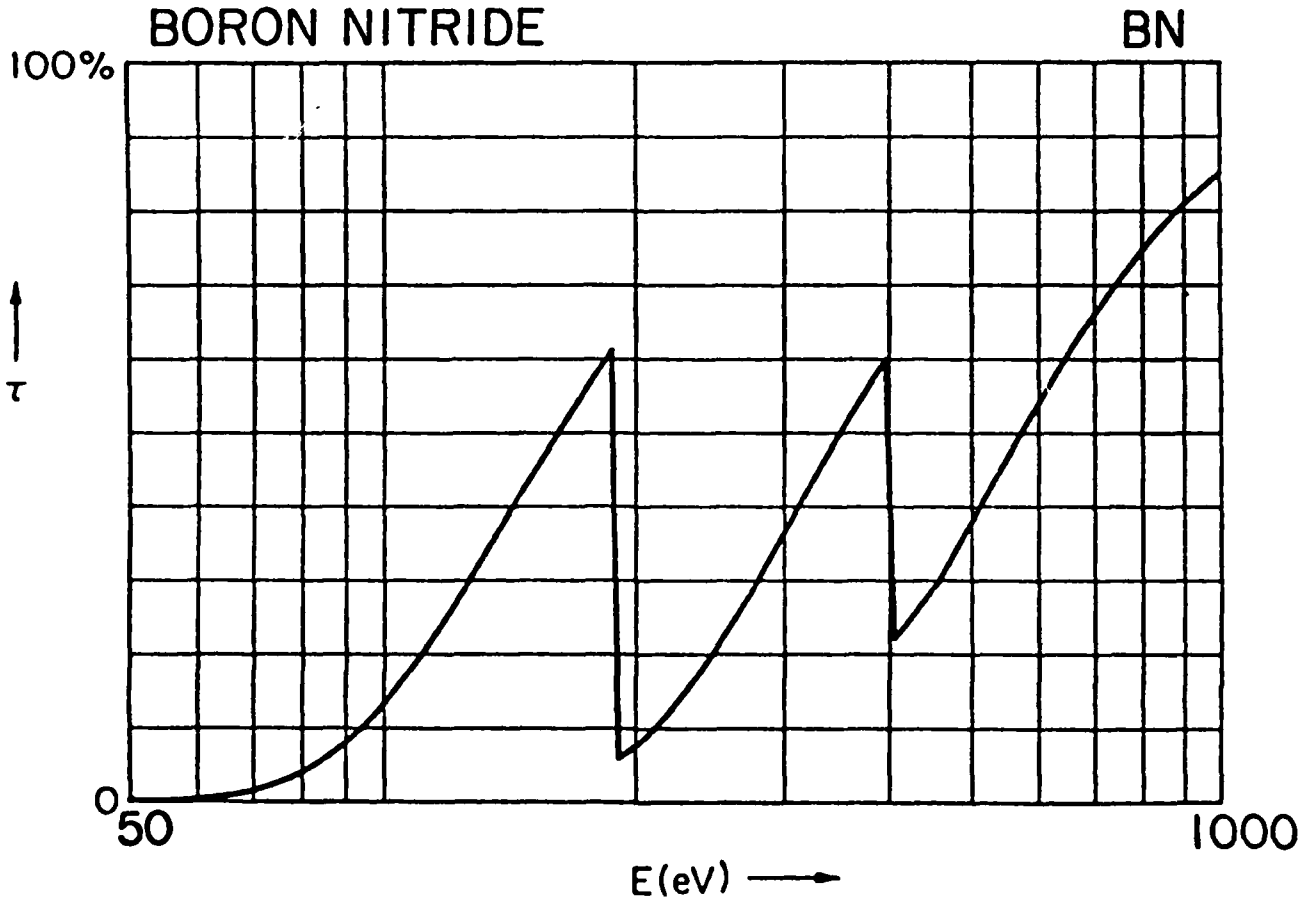
BORON NITRIDE
BN
100%
τ
0
50
1000
E(eV)

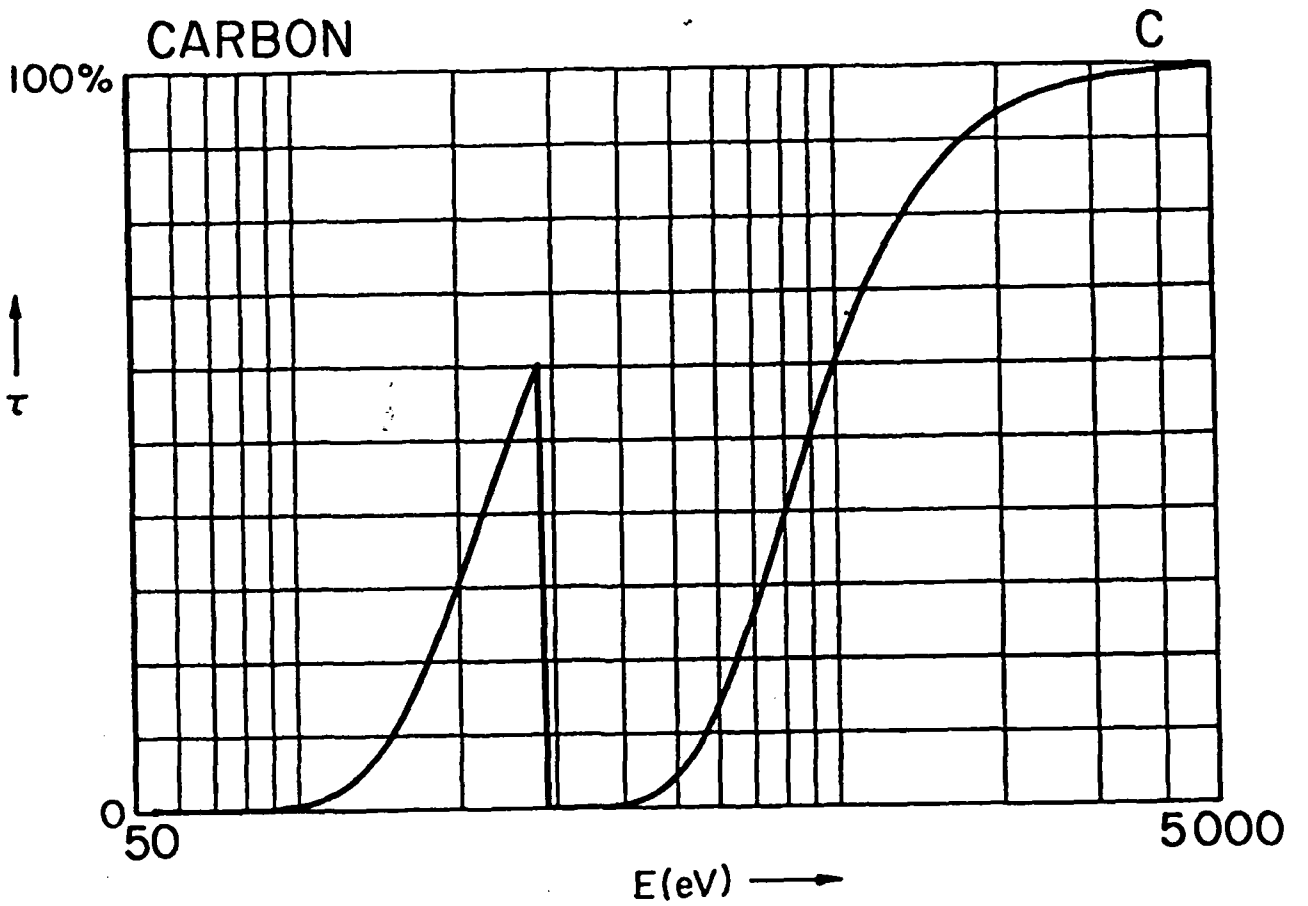
CARBON
C
100%
τ
0
50
5000
E(eV)

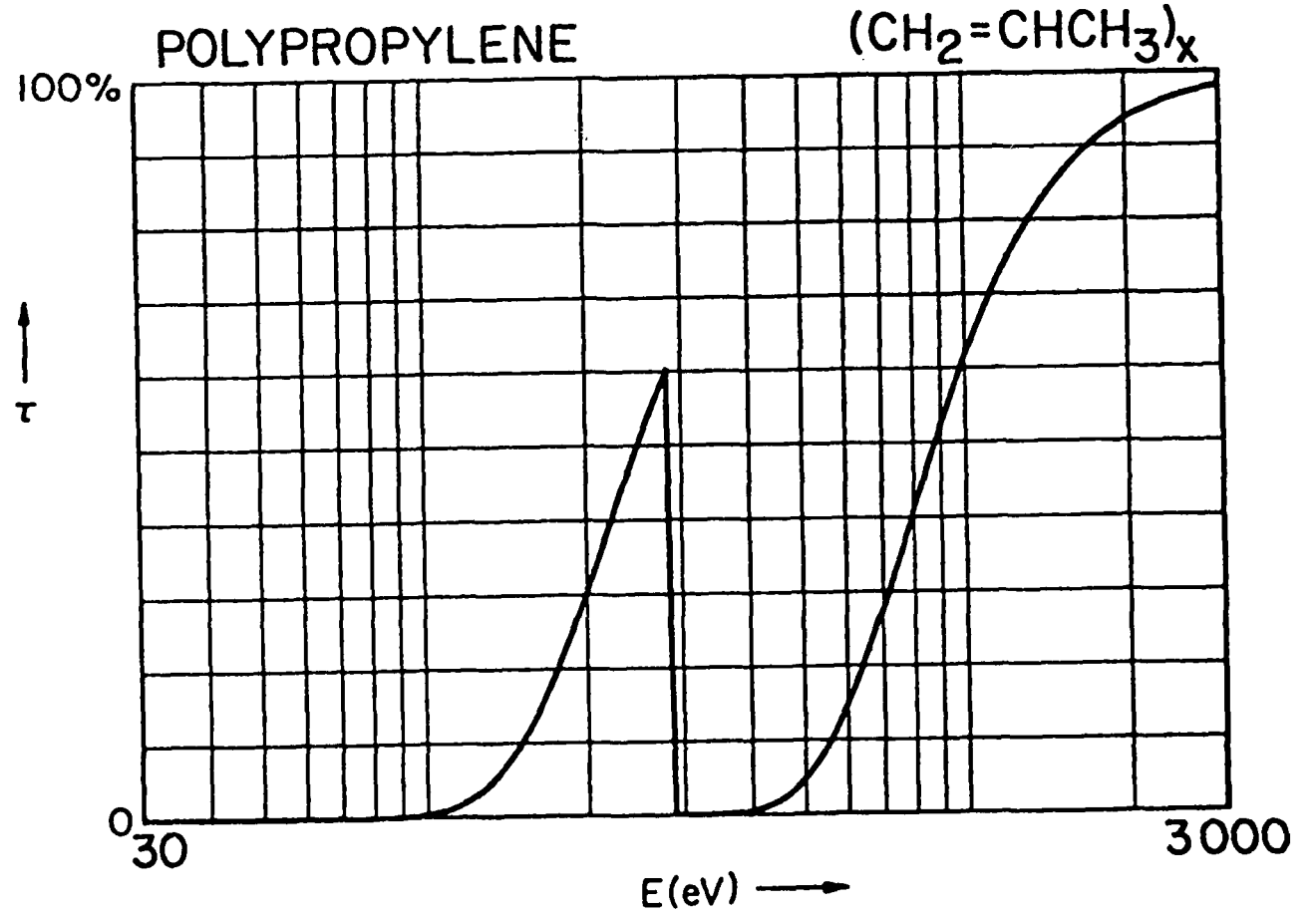
POLYPROPYLENE
(CH2=CHCH3)x
100%
τ
0
30
3000
E(eV)

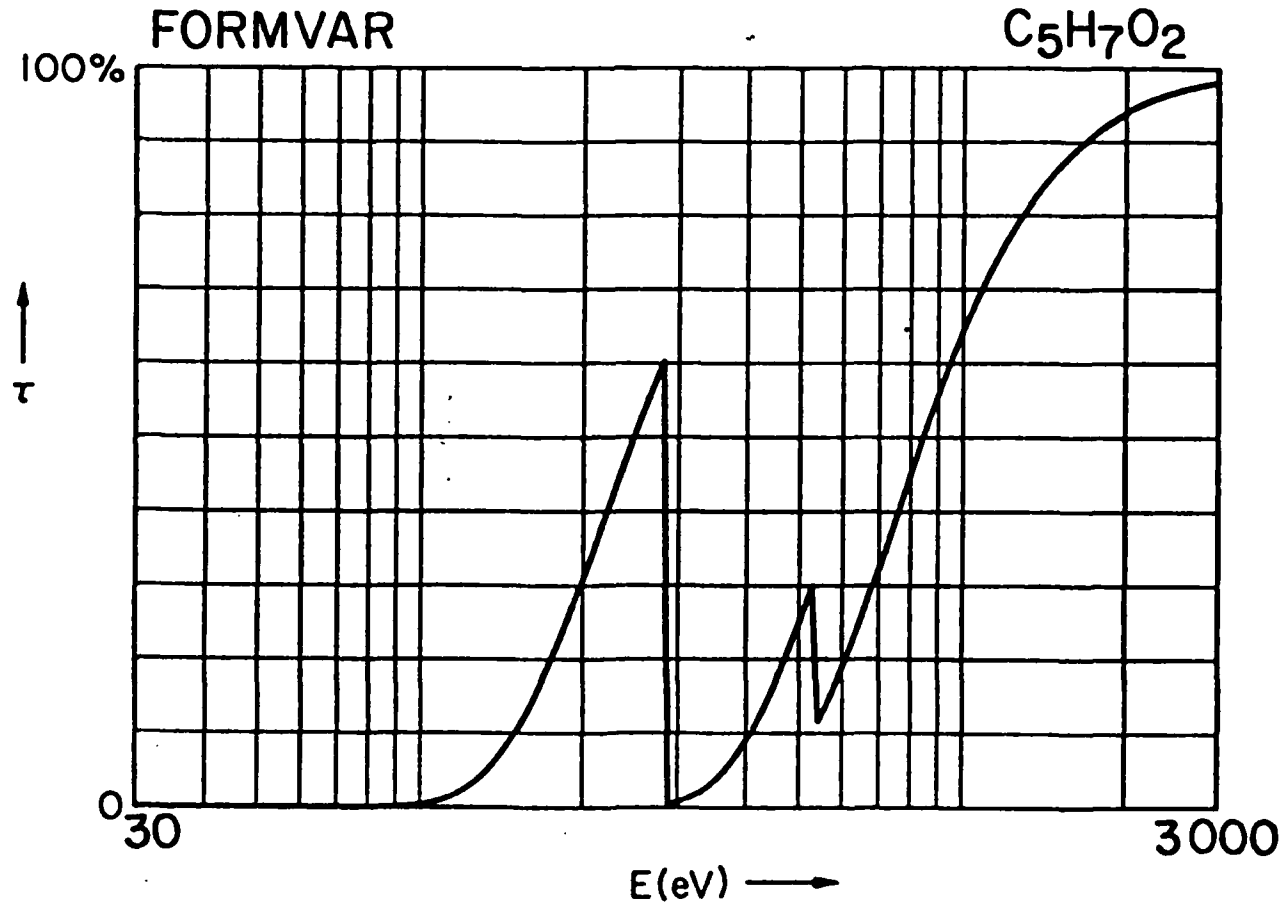
FORMVAR
$C_5H_7O_2$
100%
τ
0
30
3000
E(eV) ⟶

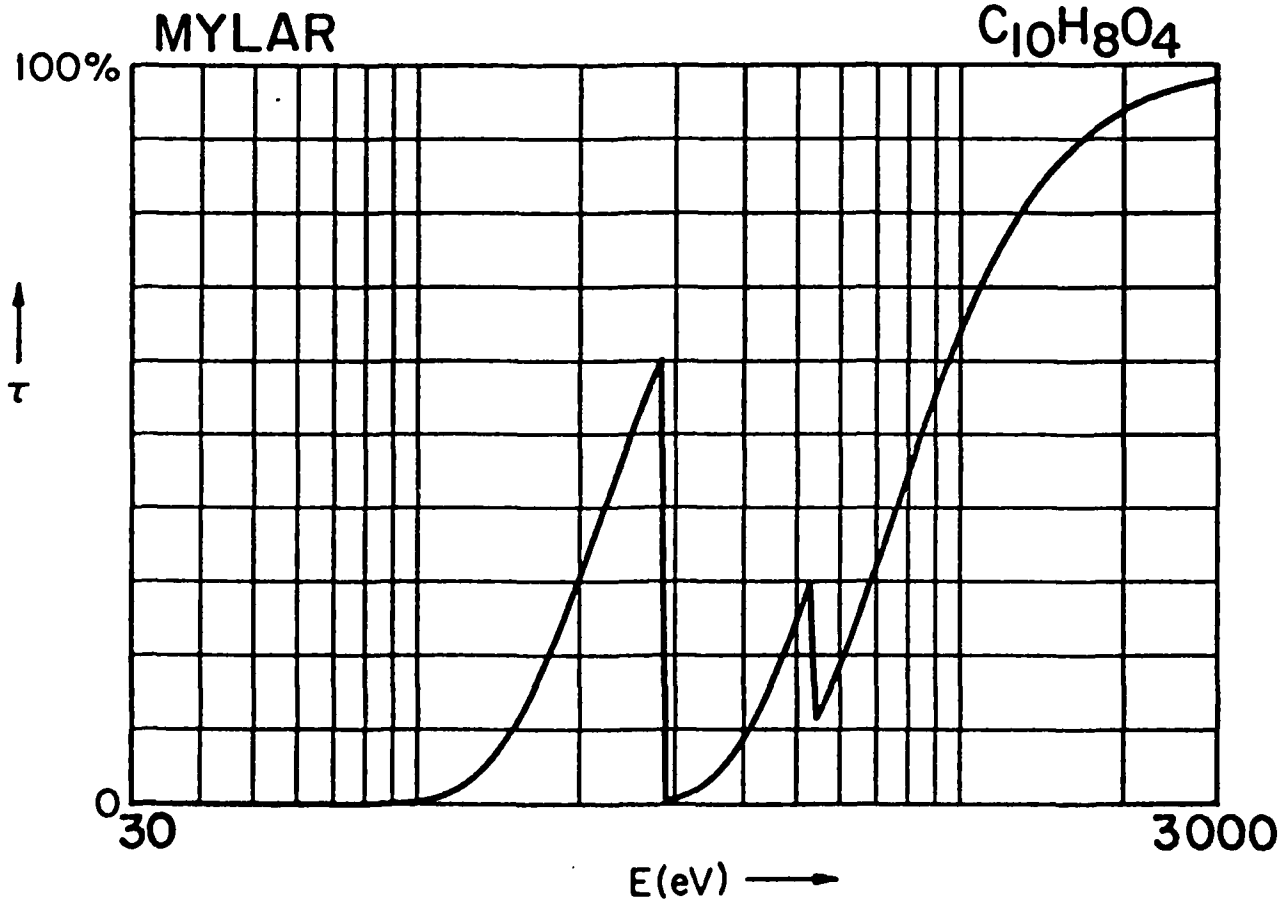
MYLAR
$C_{10}H_8O_4$
100%
τ
0
30
3000
E(eV) ⟶

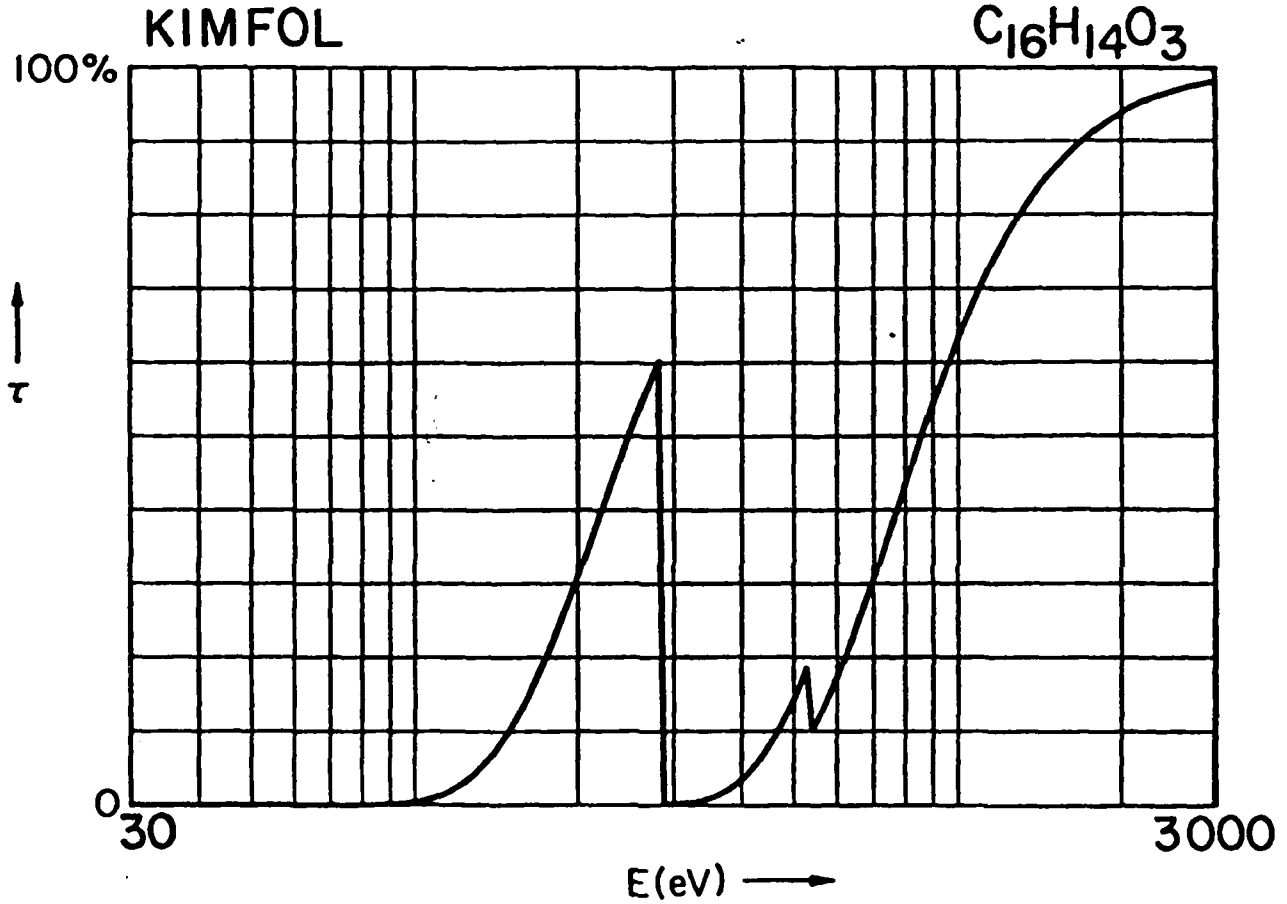
KIMFOL
$C_{16}H_{14}O_3$
100%
τ
0
30
3000
E(eV) ⟶

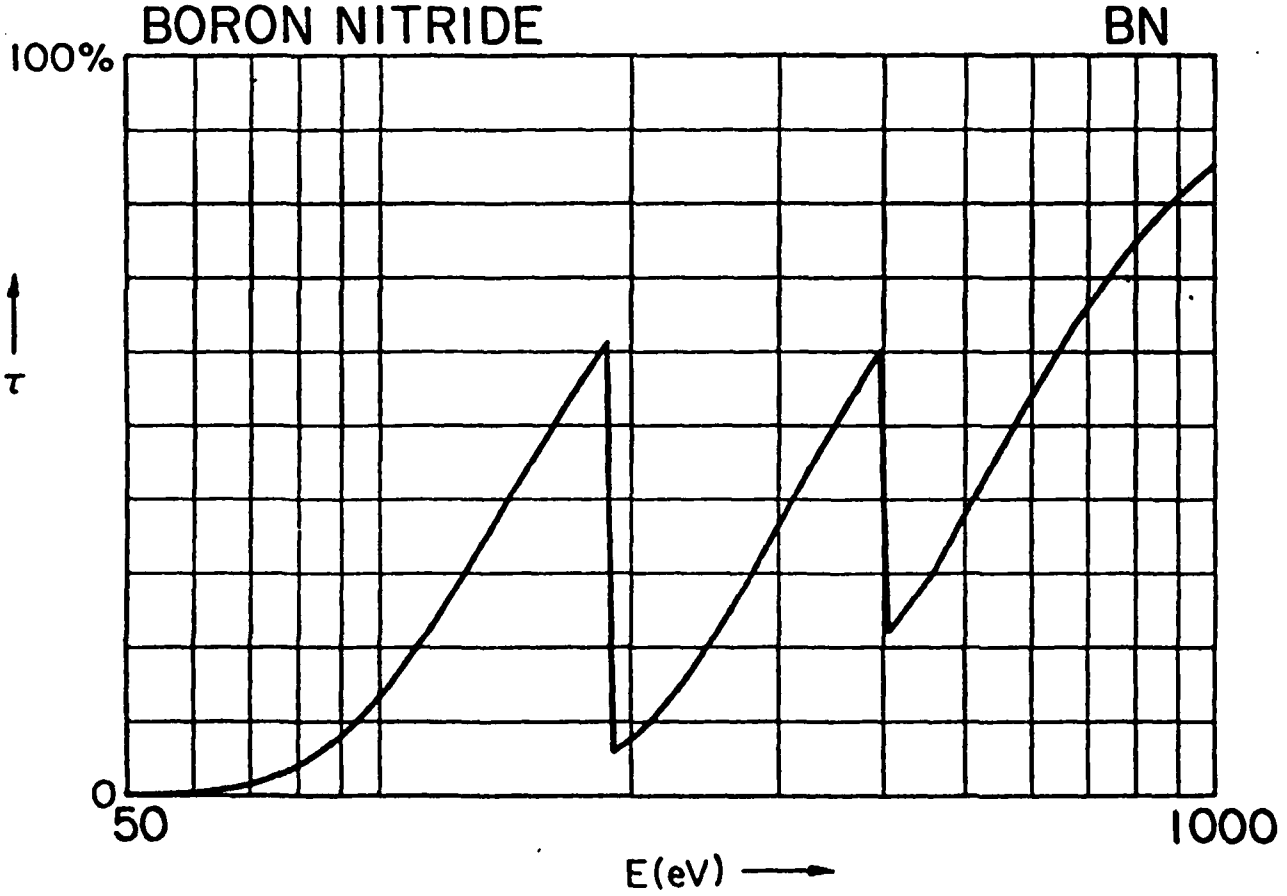
BORON NITRIDE
BN
100%
τ
0
50
1000
E(eV) ⟶

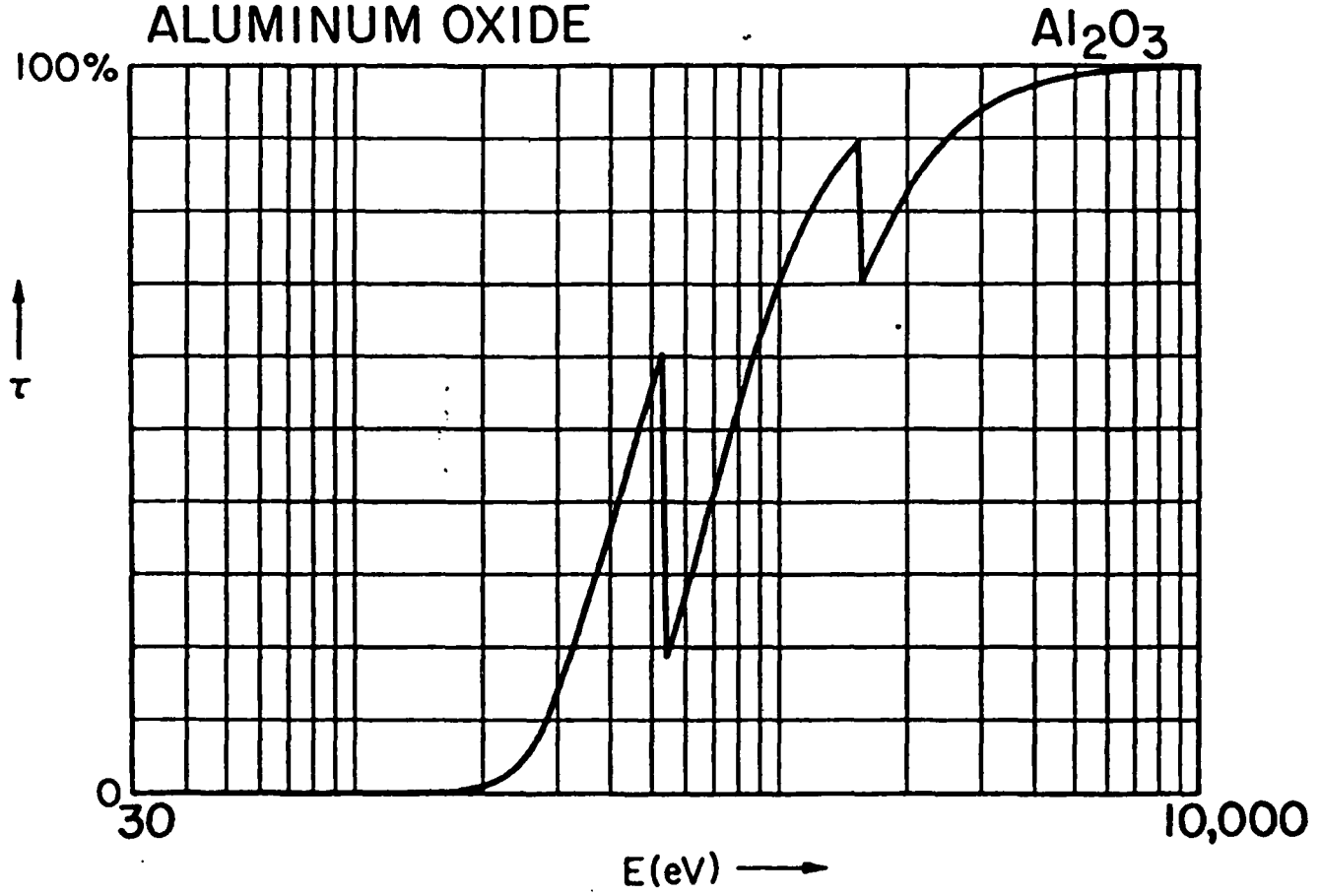
ALUMINUM OXIDE
Al_2O_3
100%
τ
0
30
10,000
E(eV)

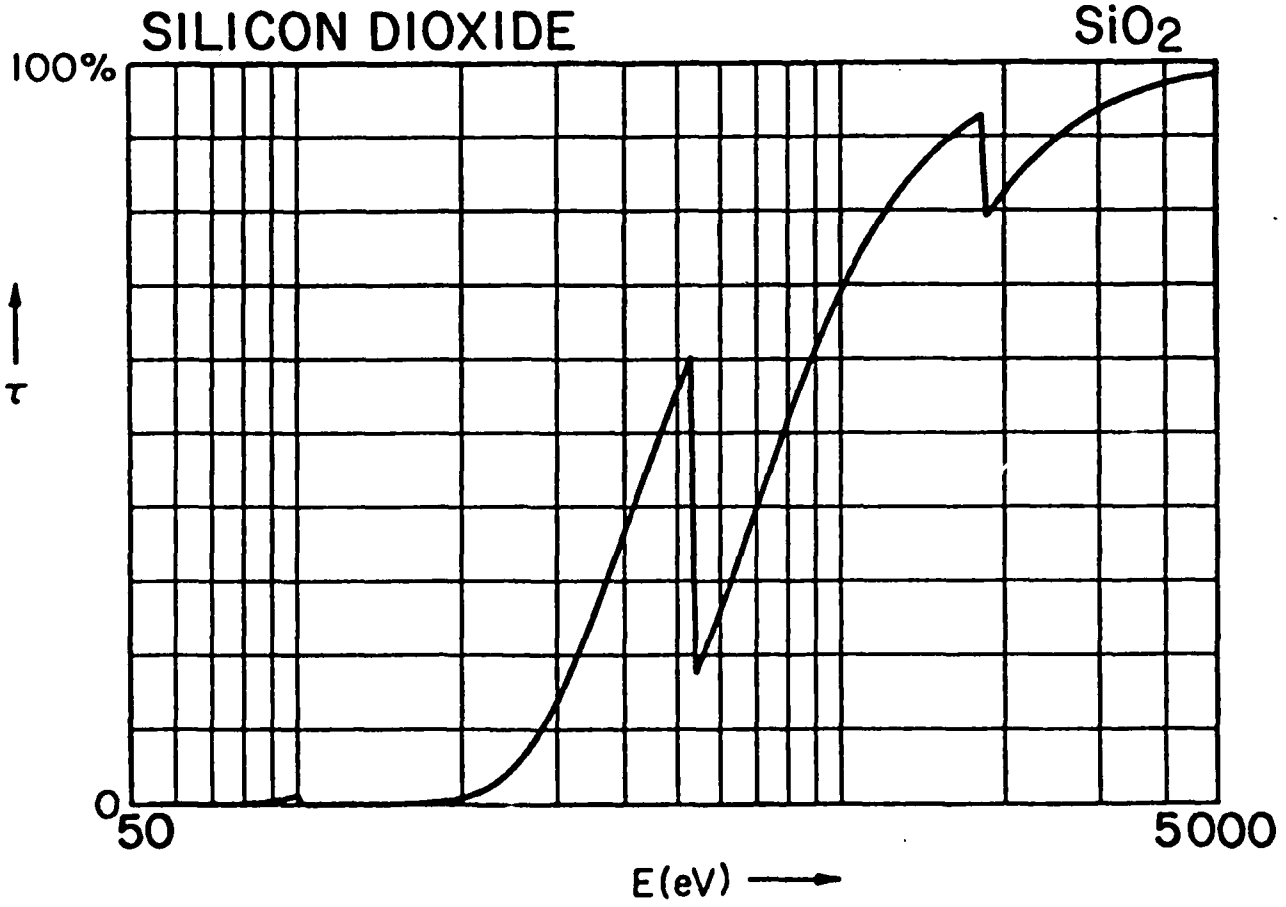
SILICON DIOXIDE
SiO_2
100%
τ
0
50
5000
E(eV)

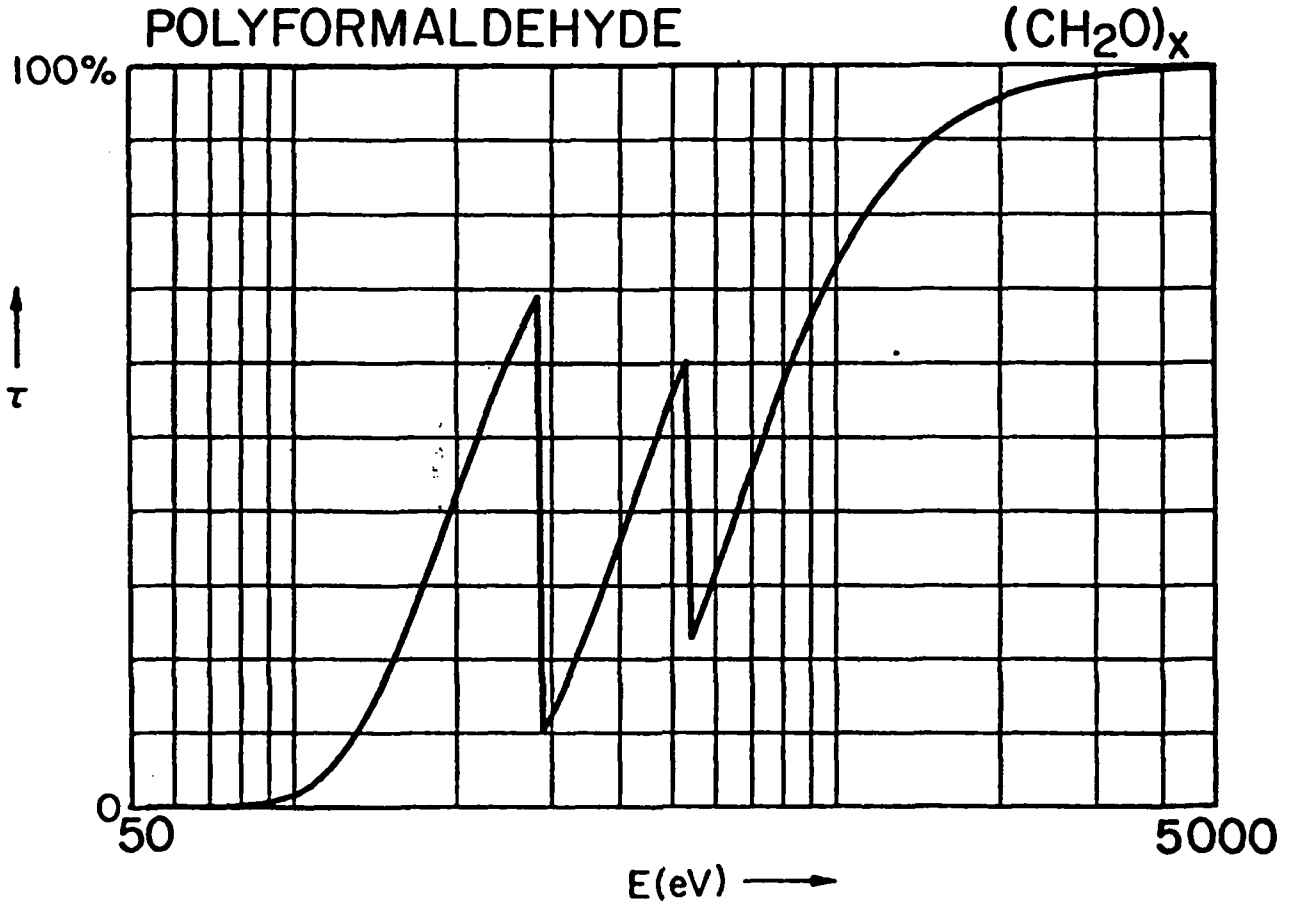
POLYFORMALDEHYDE
$(CH_2O)_x$
100%
τ
0
50
5000
E(eV) ⟶

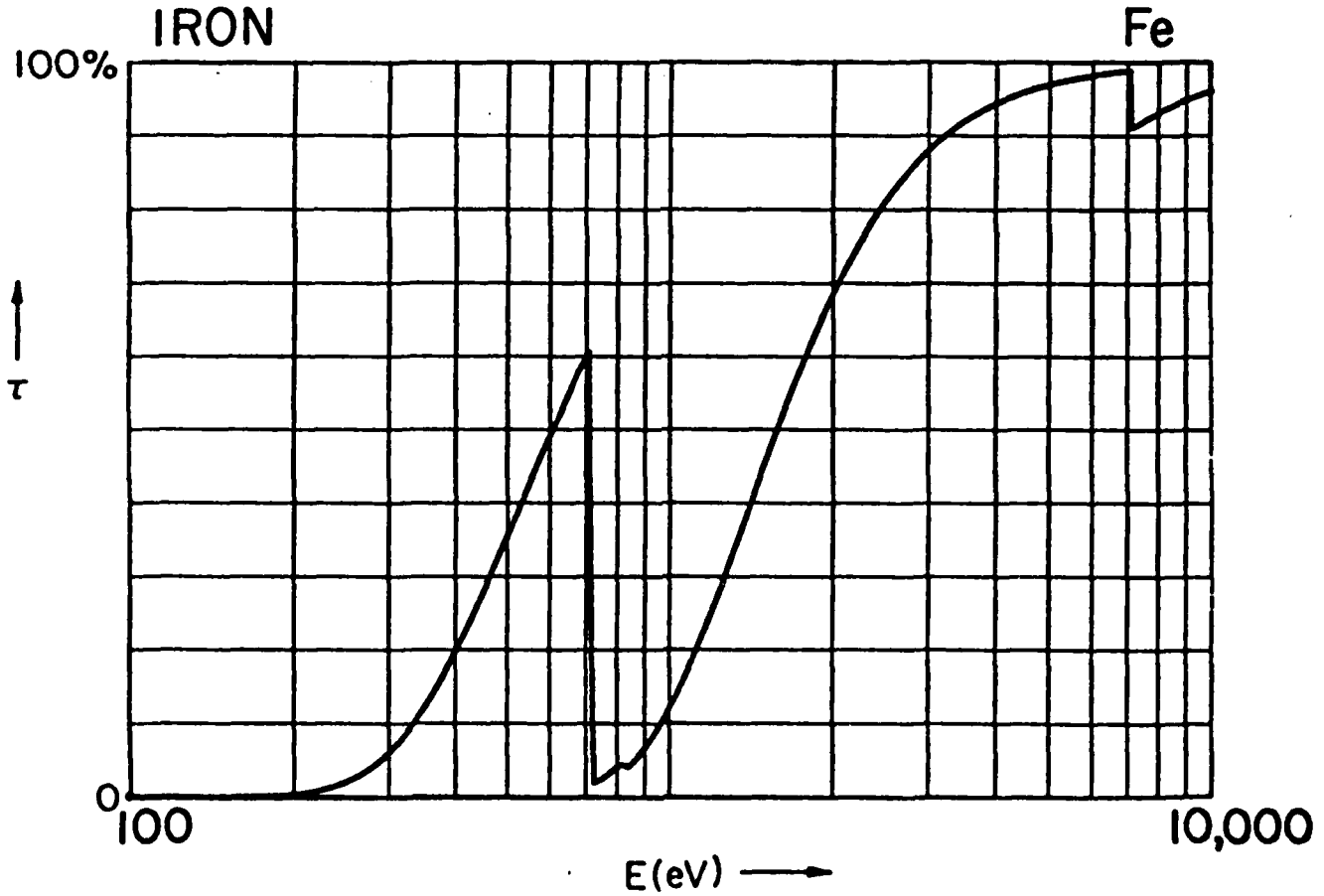
IRON
Fe
100%
τ
0
100
10,000
E(eV) ⟶

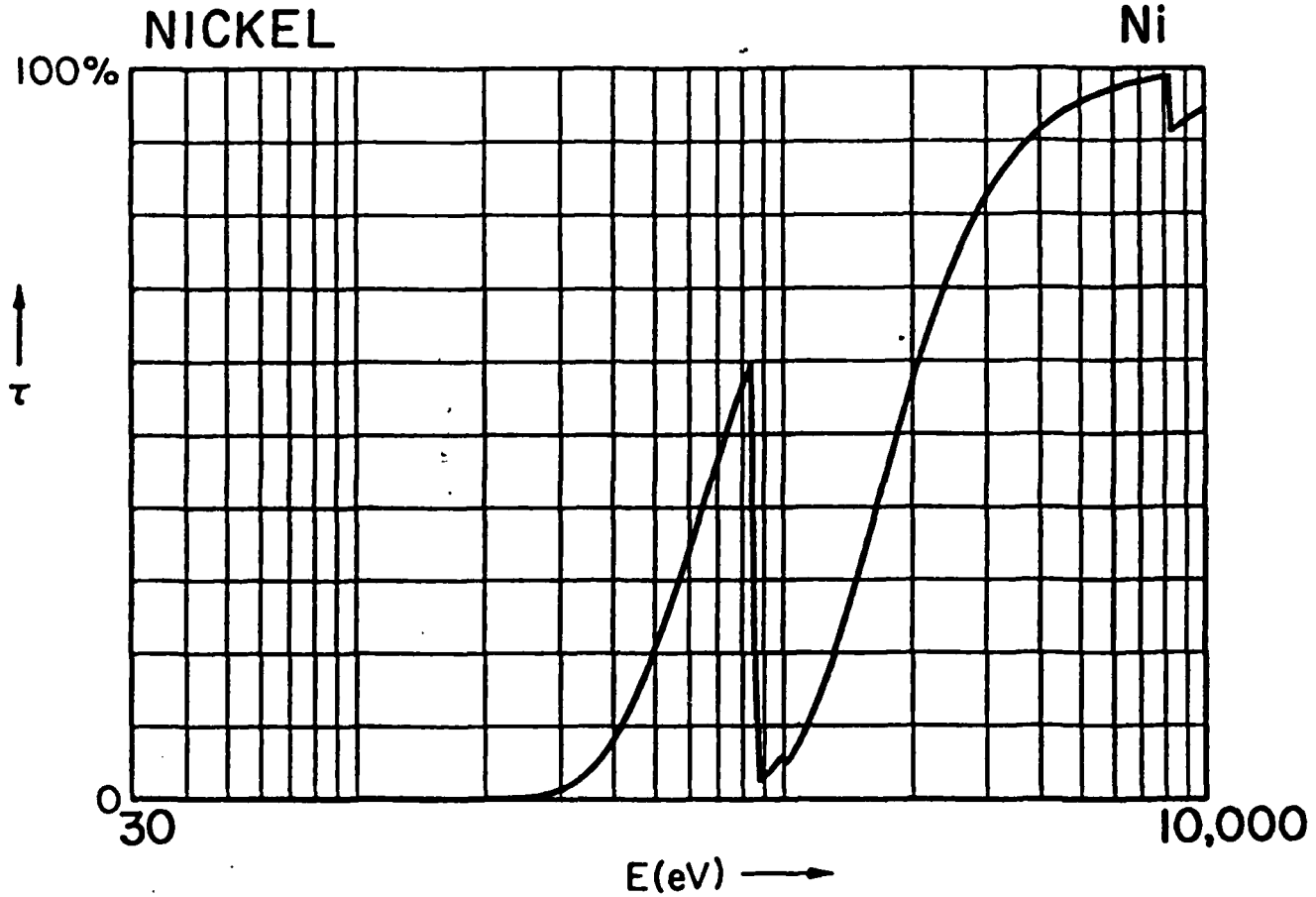
NICKEL
Ni
100%
τ
0
30
10,000
E(eV) ⟶

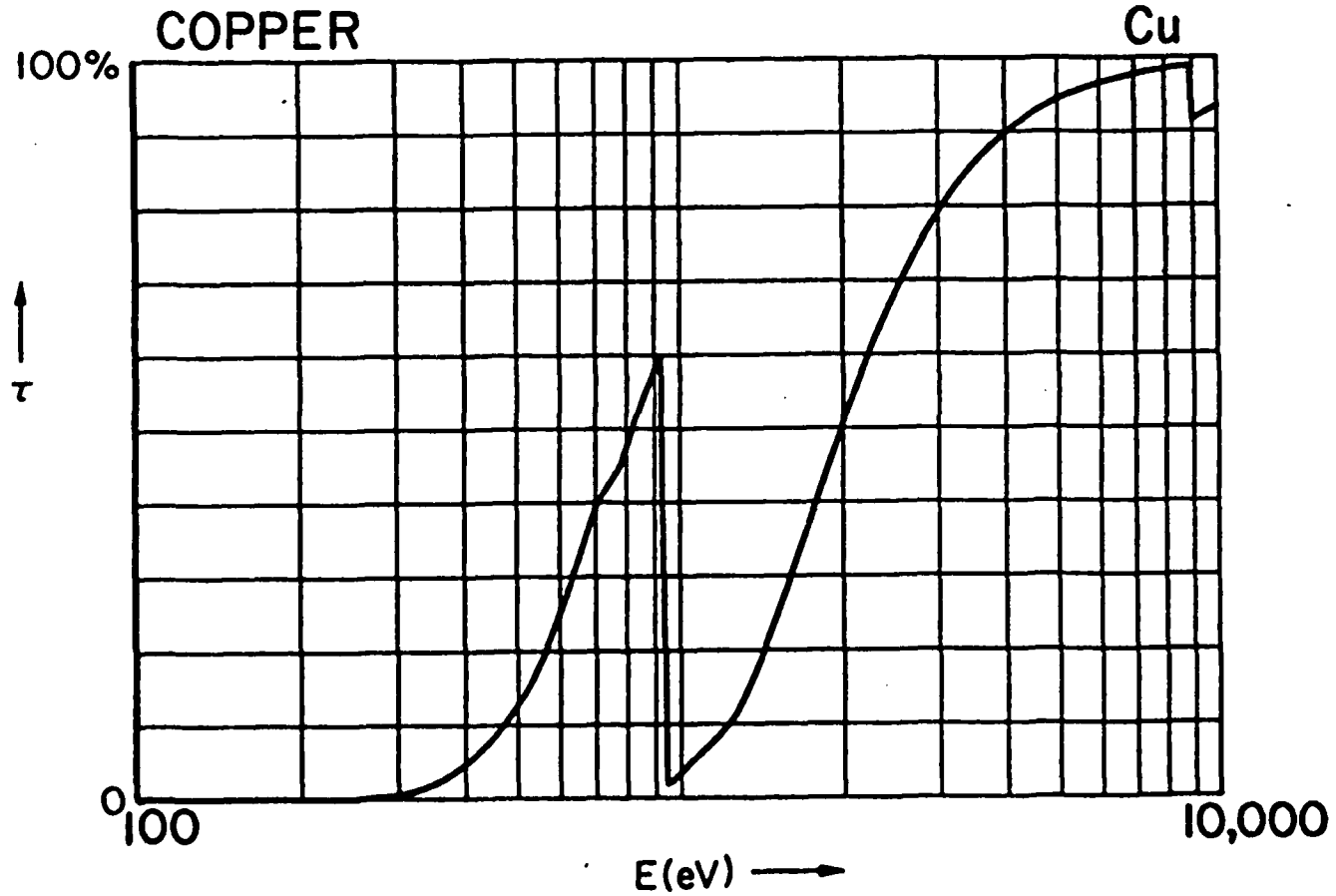
COPPER
Cu
100%
τ
0
100
10,000
E(eV) ⟶

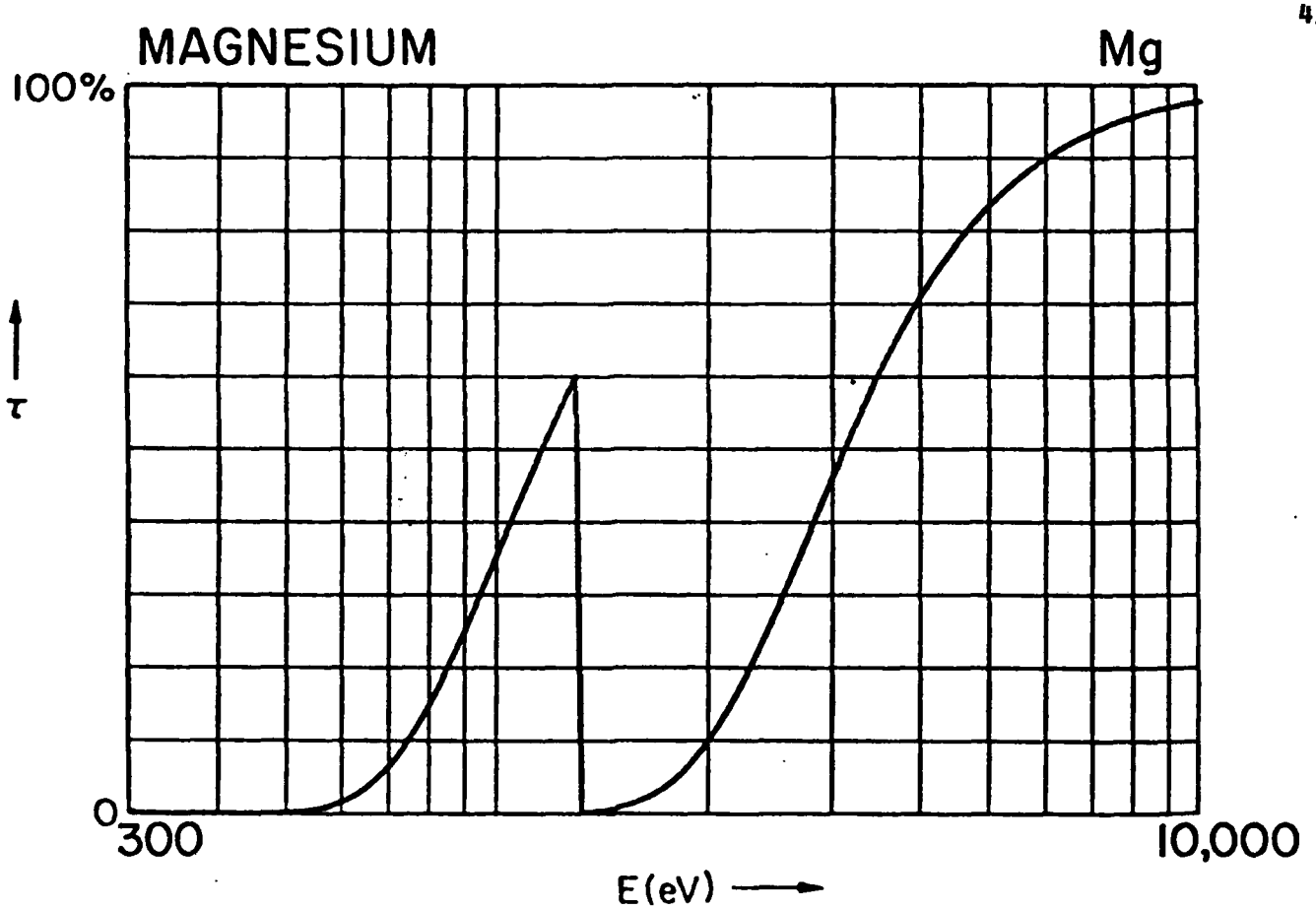
MAGNESIUM
Mg
100%
τ
0
300
10,000
E(eV)

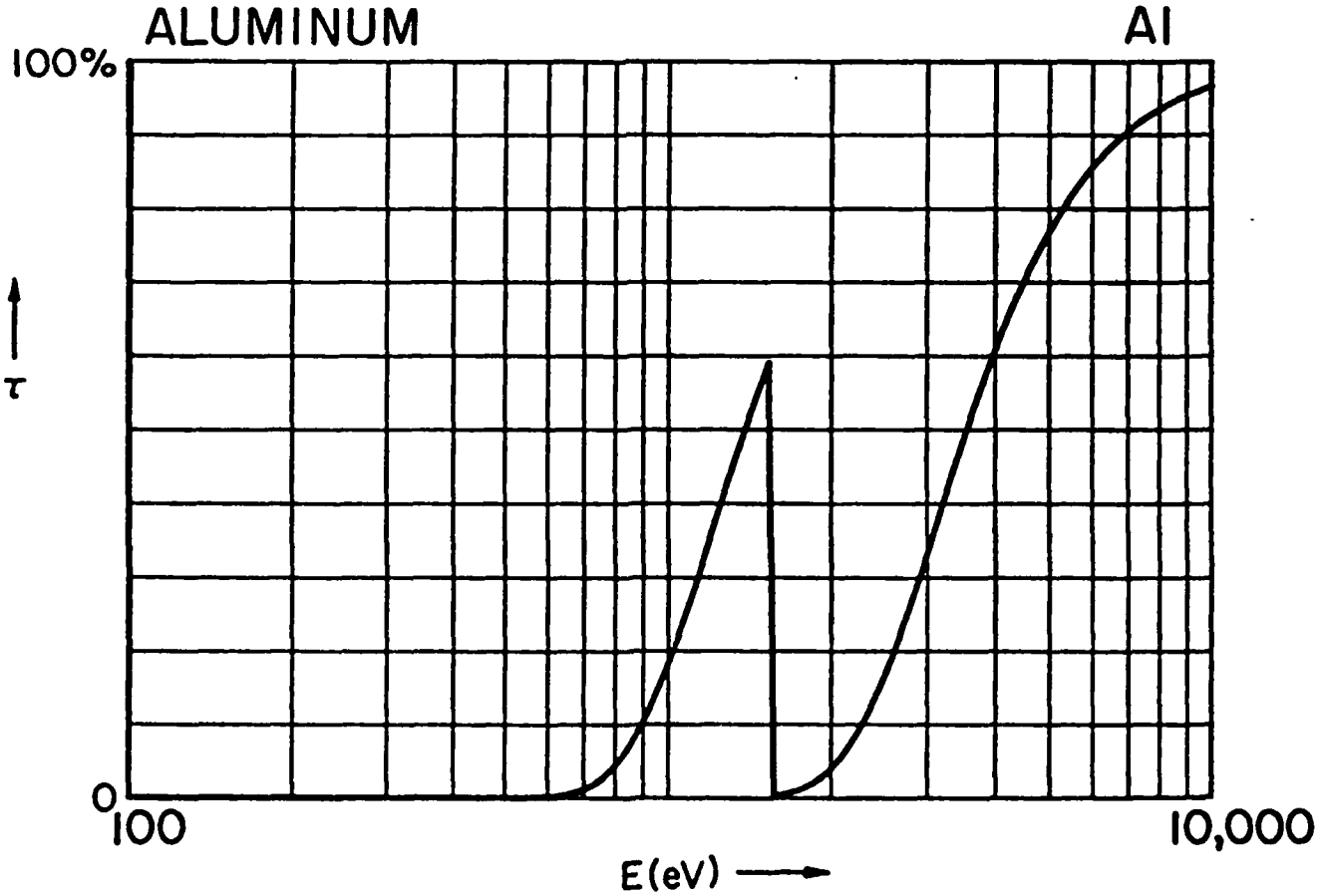
ALUMINUM
Al
100%
τ
0
100
10,000
E(eV)

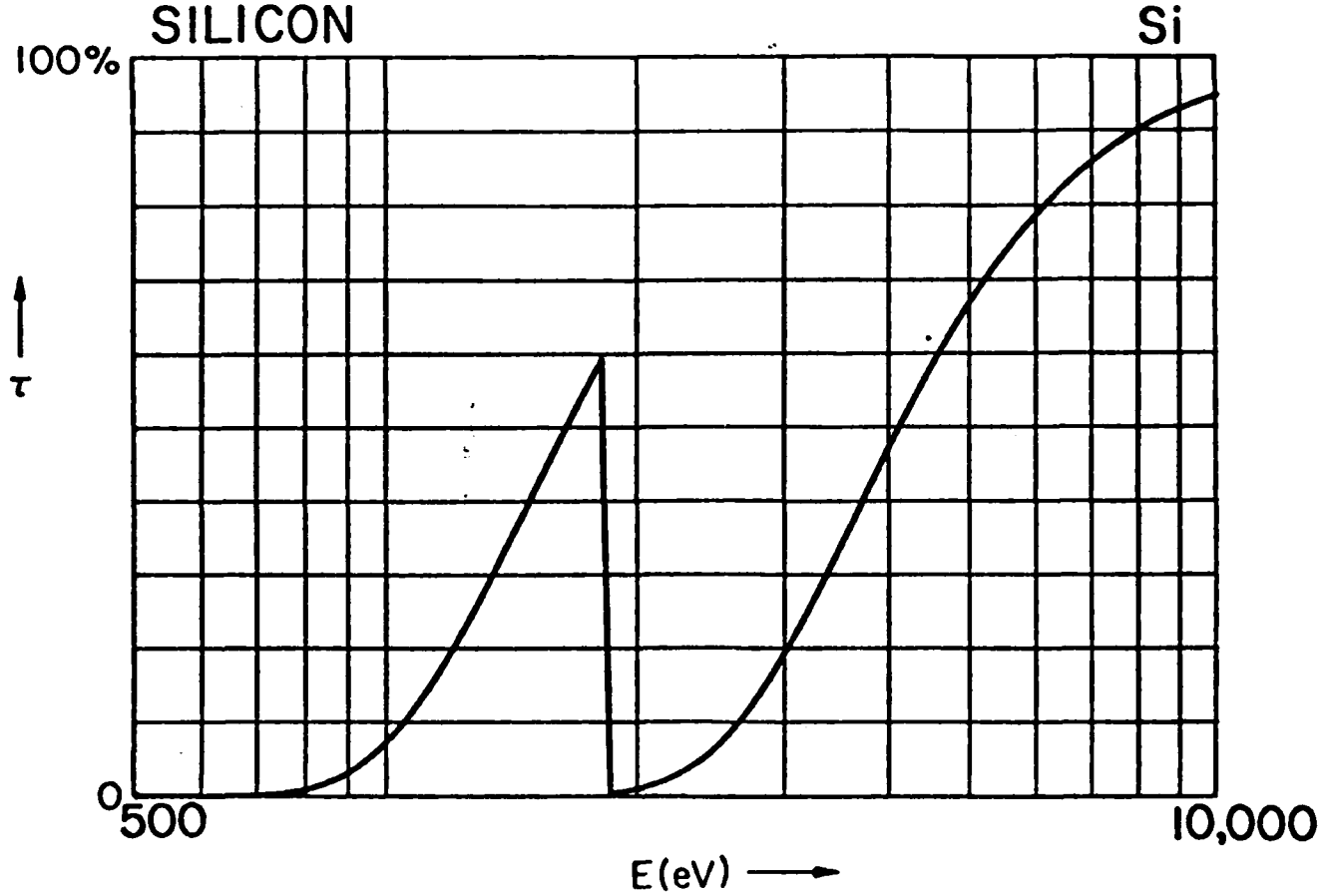
SILICON
Si
100%
τ
0
500
10,000
E(eV)

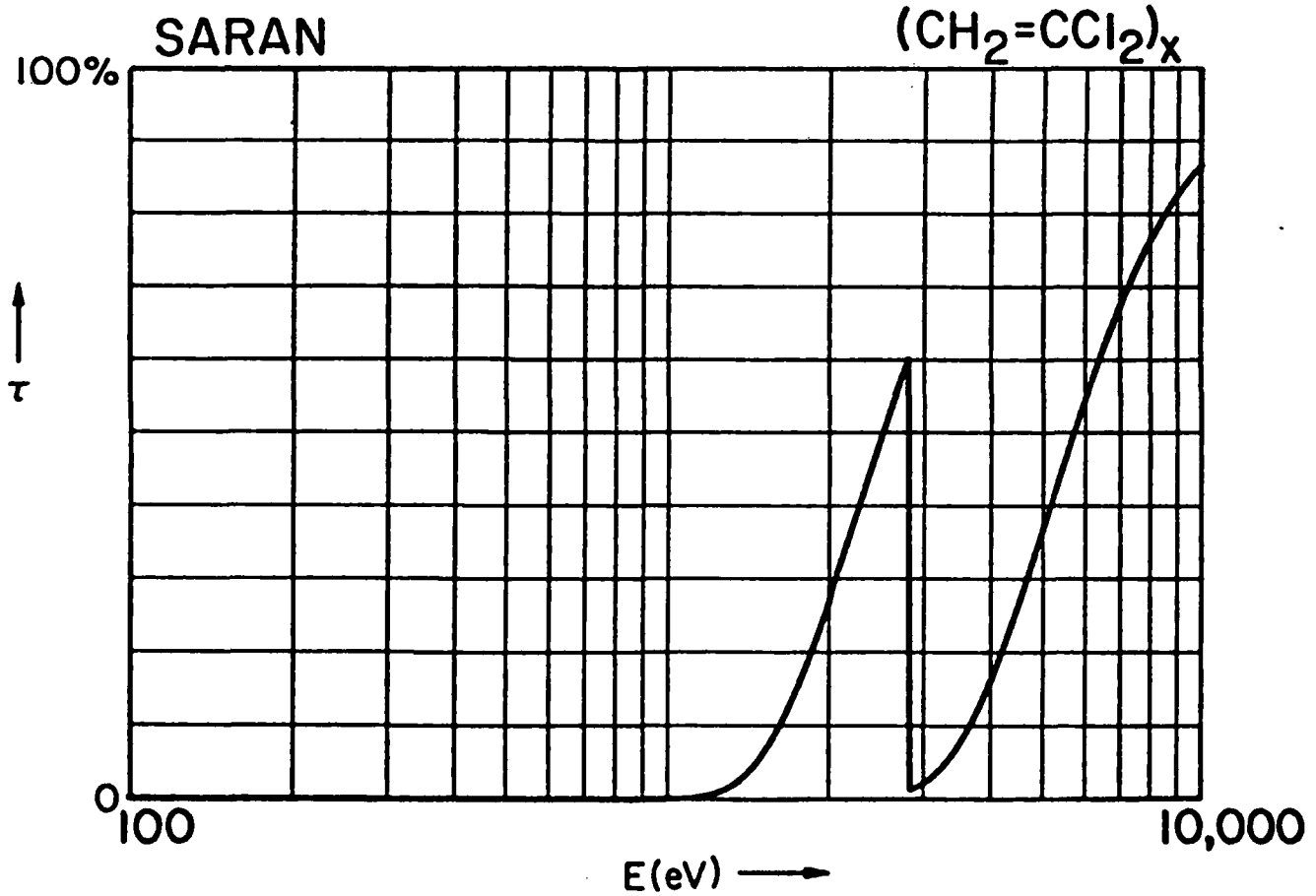
SARAN
(CH2=CCl2)x
100%
τ
0
100
10,000
E(eV)

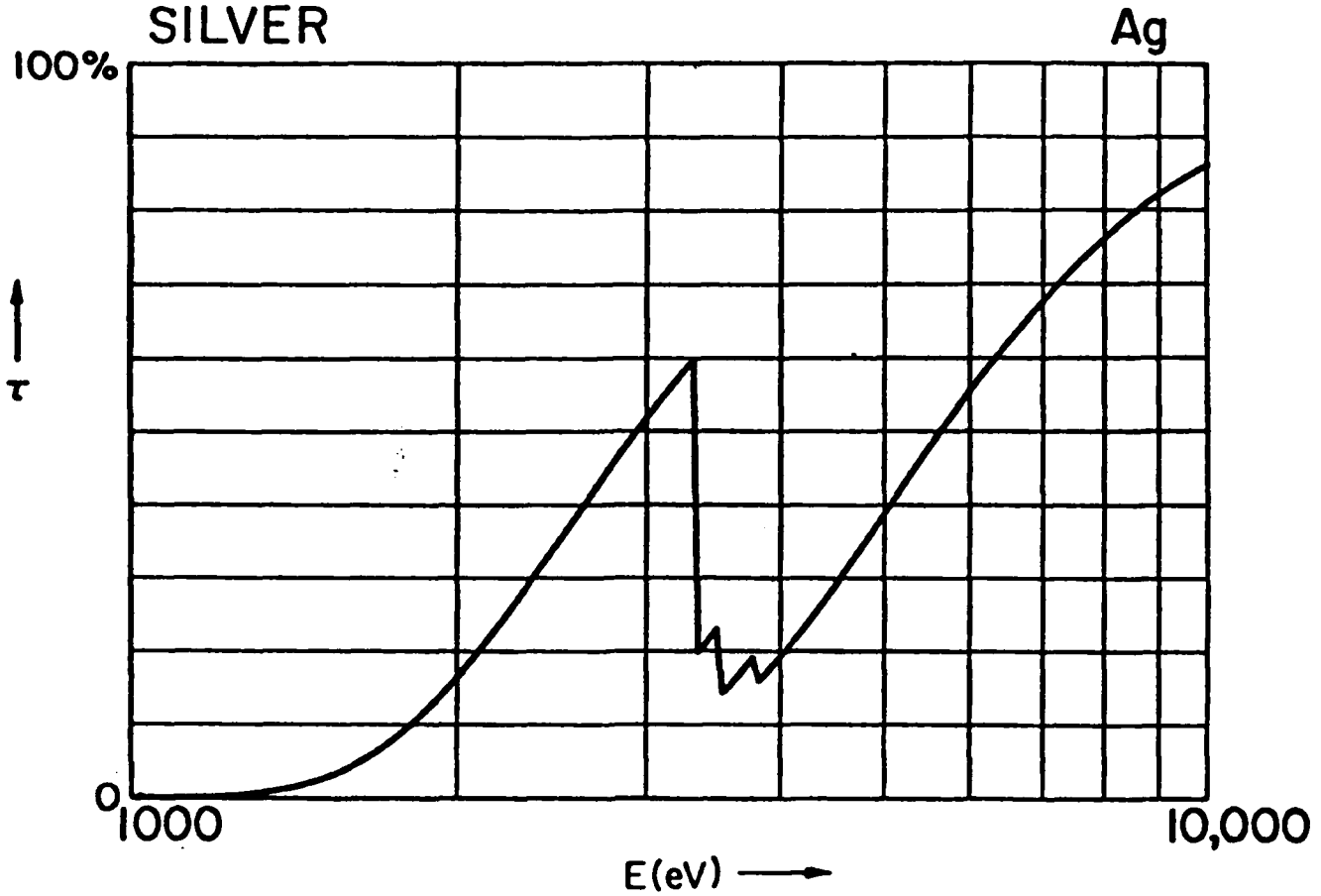
SILVER
Ag
100%
τ
0
1000
10,000
E(eV)

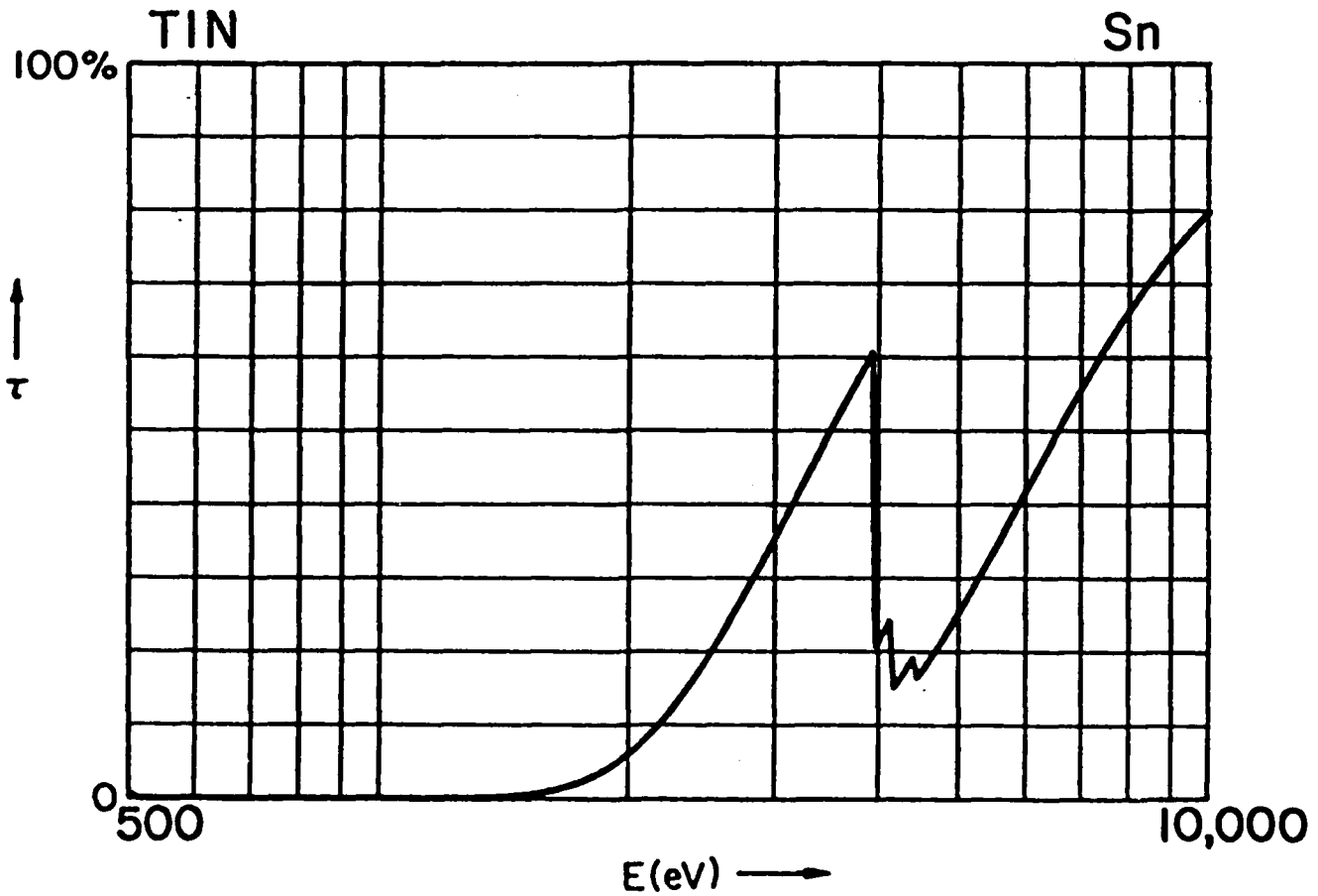
TIN
Sn
100%
τ
0
500
10,000
E(eV)

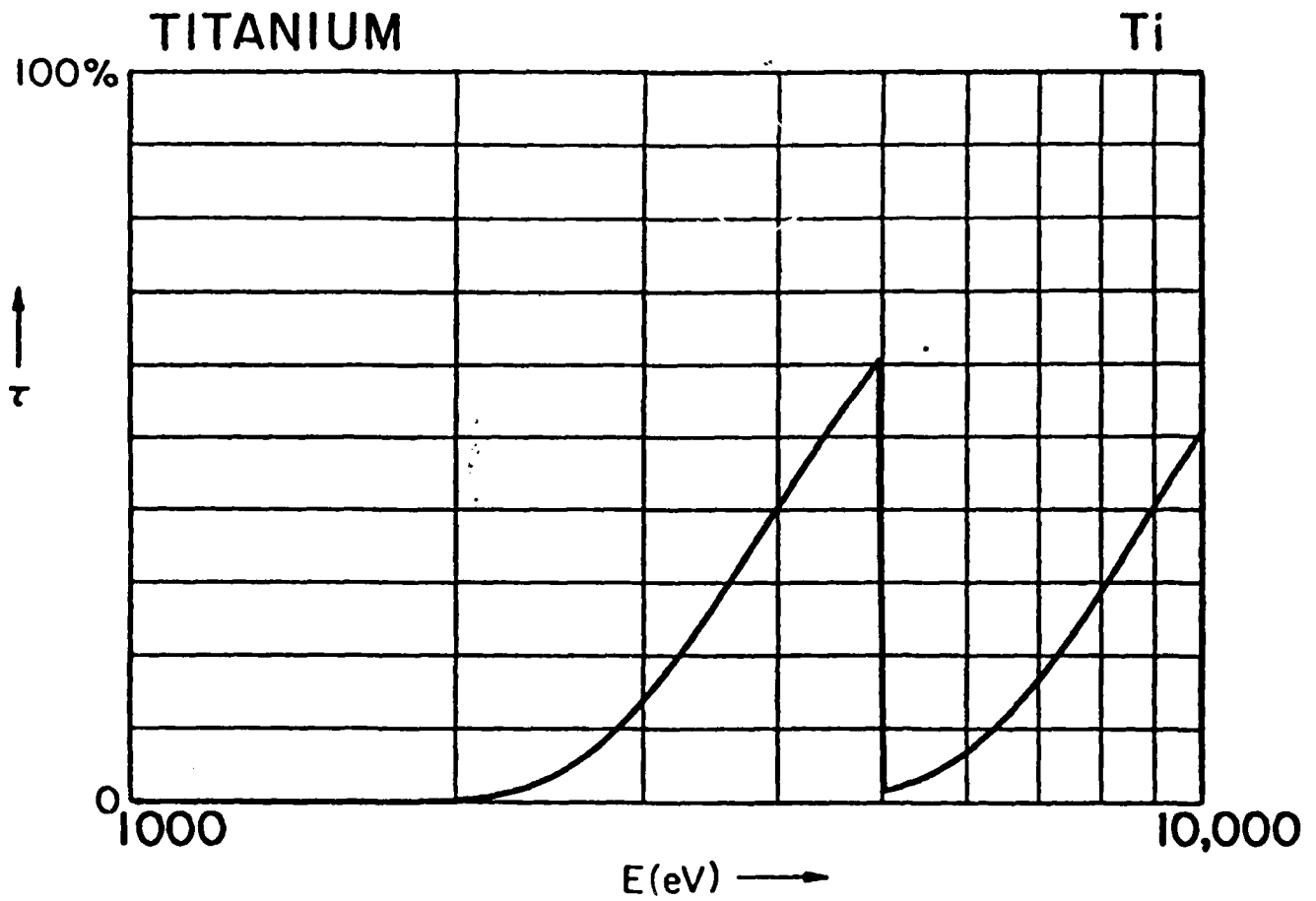
TITANIUM
Ti
100%
τ
0
1000
10,000
E(eV)

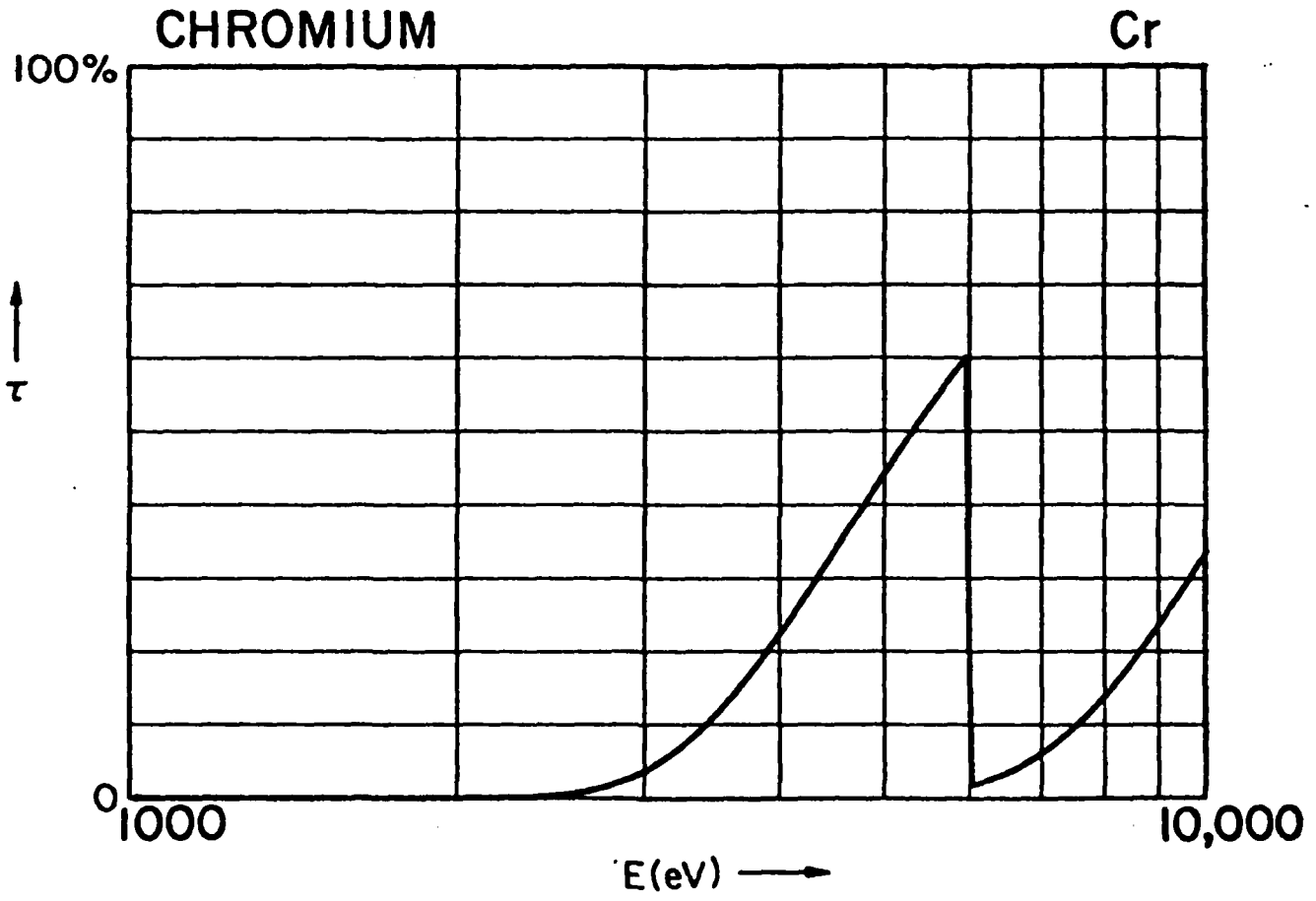
CHROMIUM
Cr
100%
τ
0
1000
10,000
E(eV)

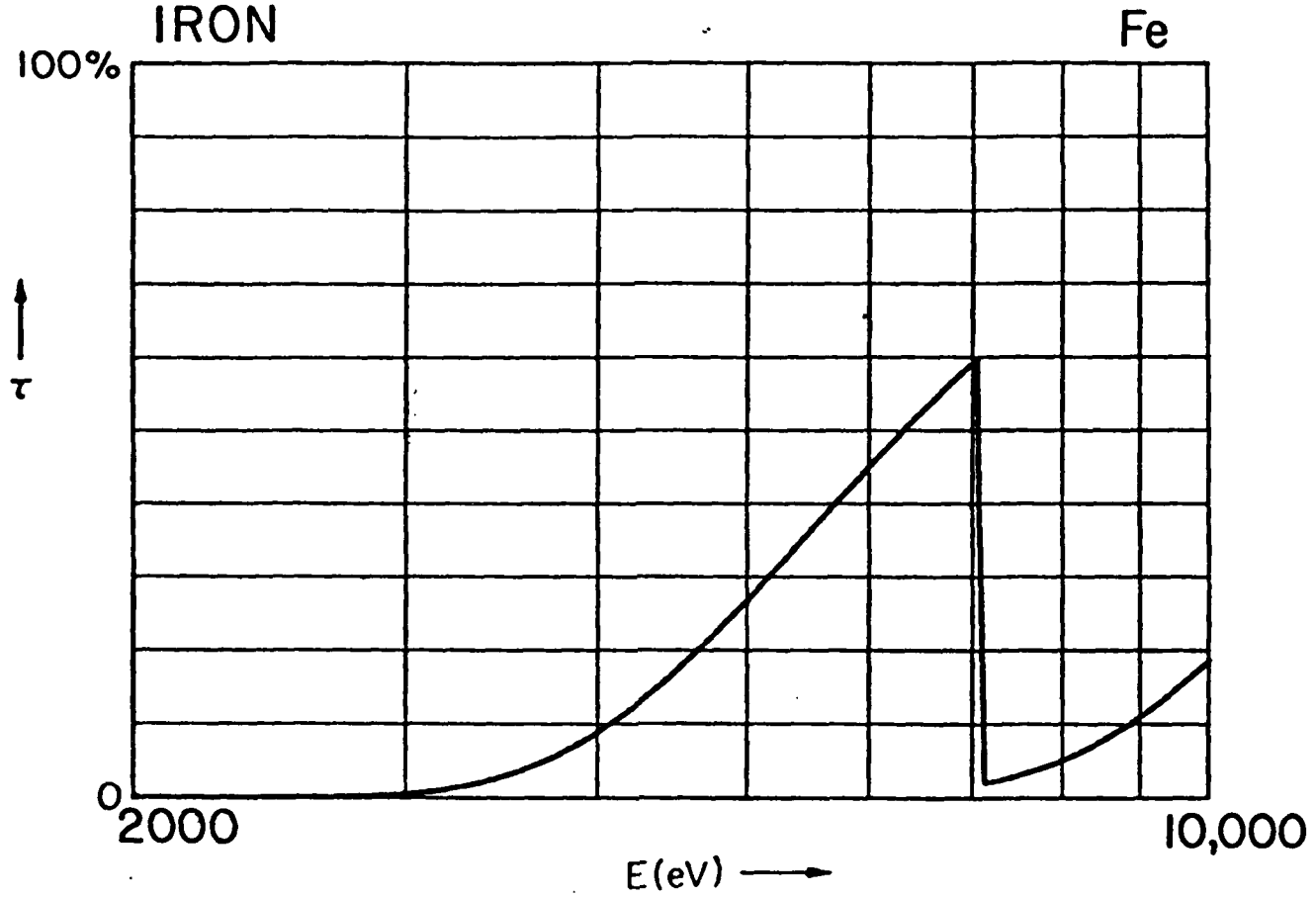
IRON
Fe
100%
τ
0
2000
10,000
E(eV)

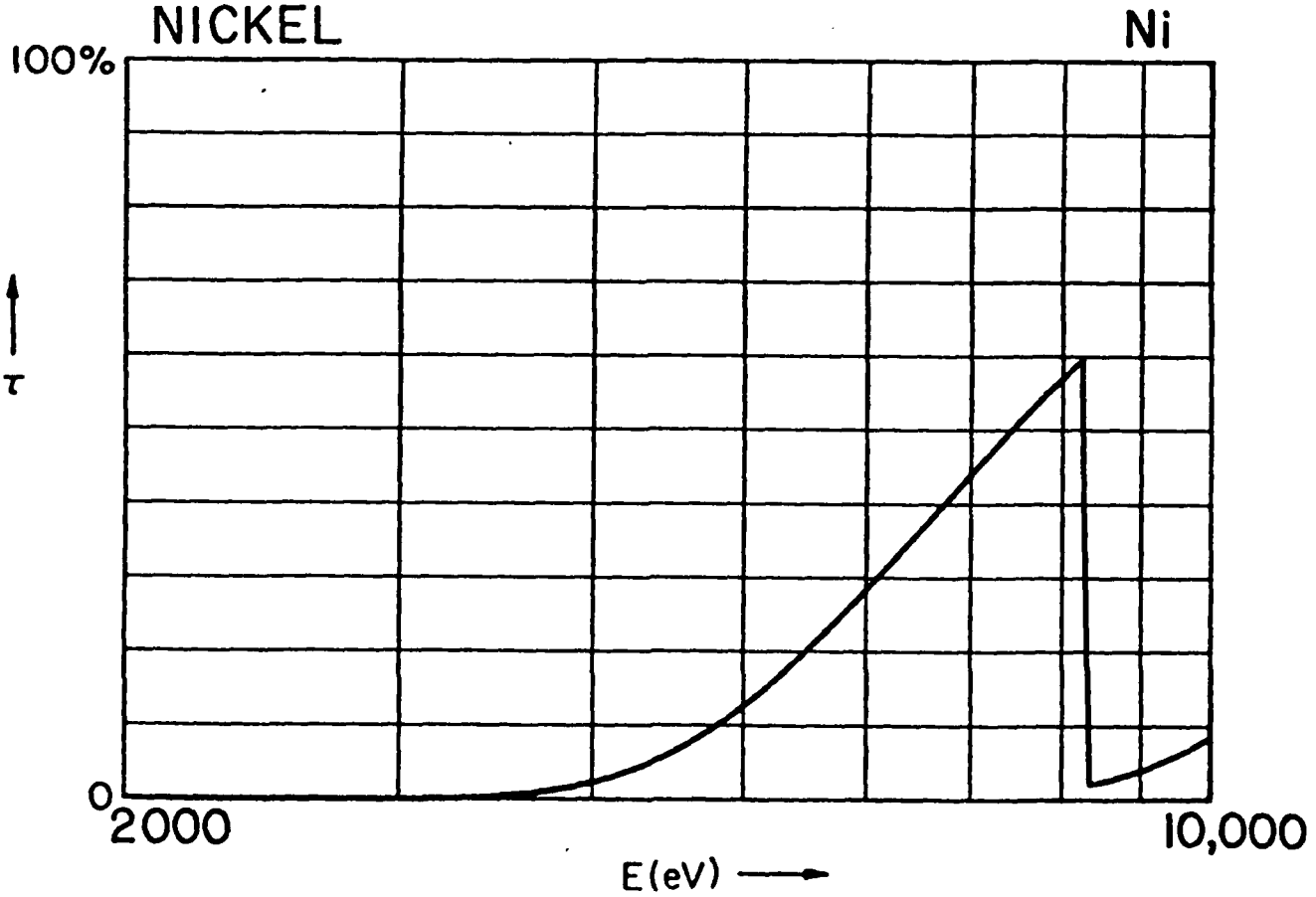
NICKEL
Ni
100%
τ
0
2000
10,000
E(eV)

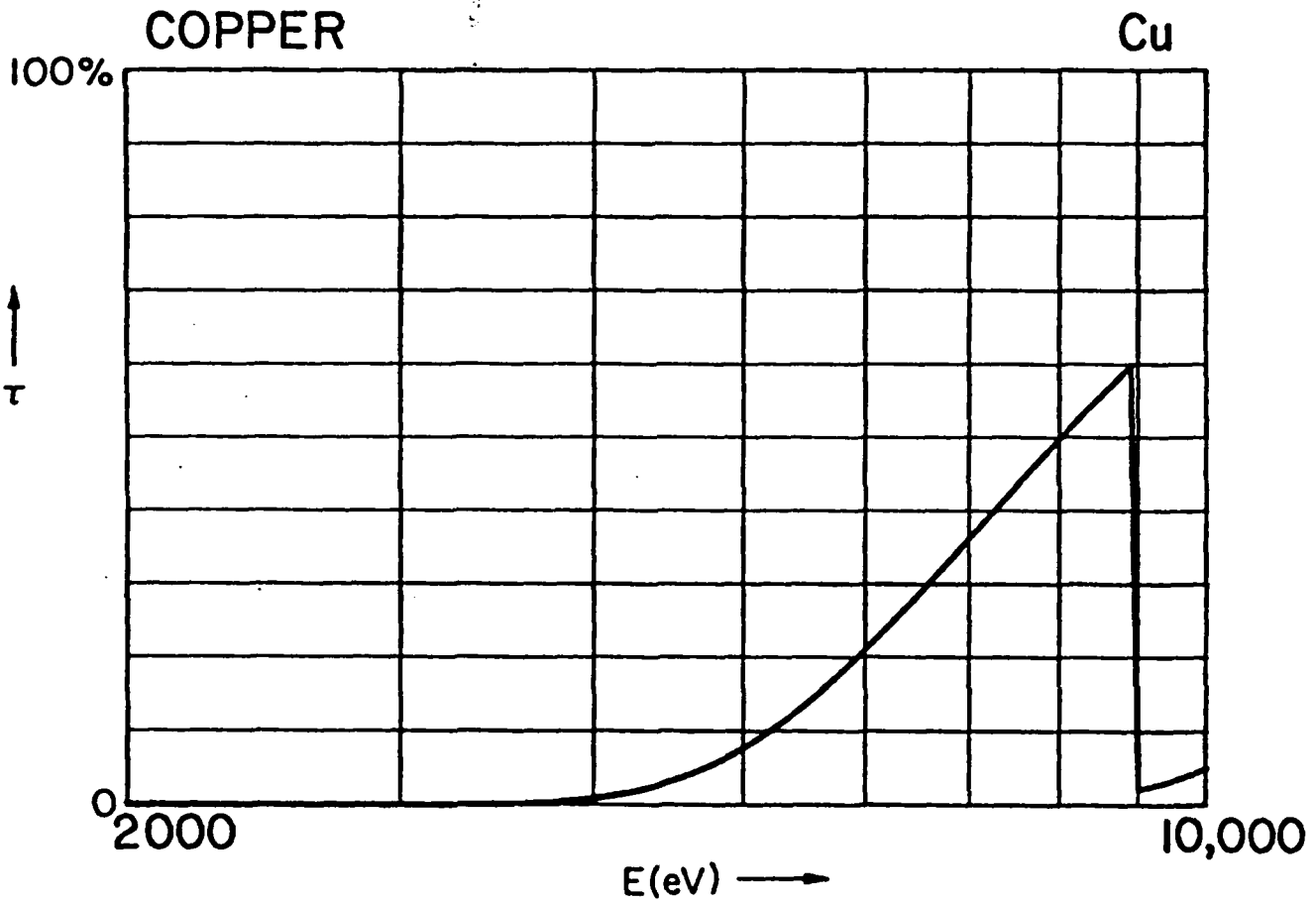
COPPER
Cu
100%
τ
0
2000
10,000
E(eV)

APPENDIX B

Integrated reflectivity, R (Darwin-Prins) vs photon energy, E(eV) for first- and second-order diffraction from the eleven crystal/multilayer analyzers that have been listed in Table 1 and described in Fig. 7. These calculated values were for "thick" crystals (setting number of layers, N, equal to infinity).

LEAD MELISSATE 2d--160 A 1st ORDER

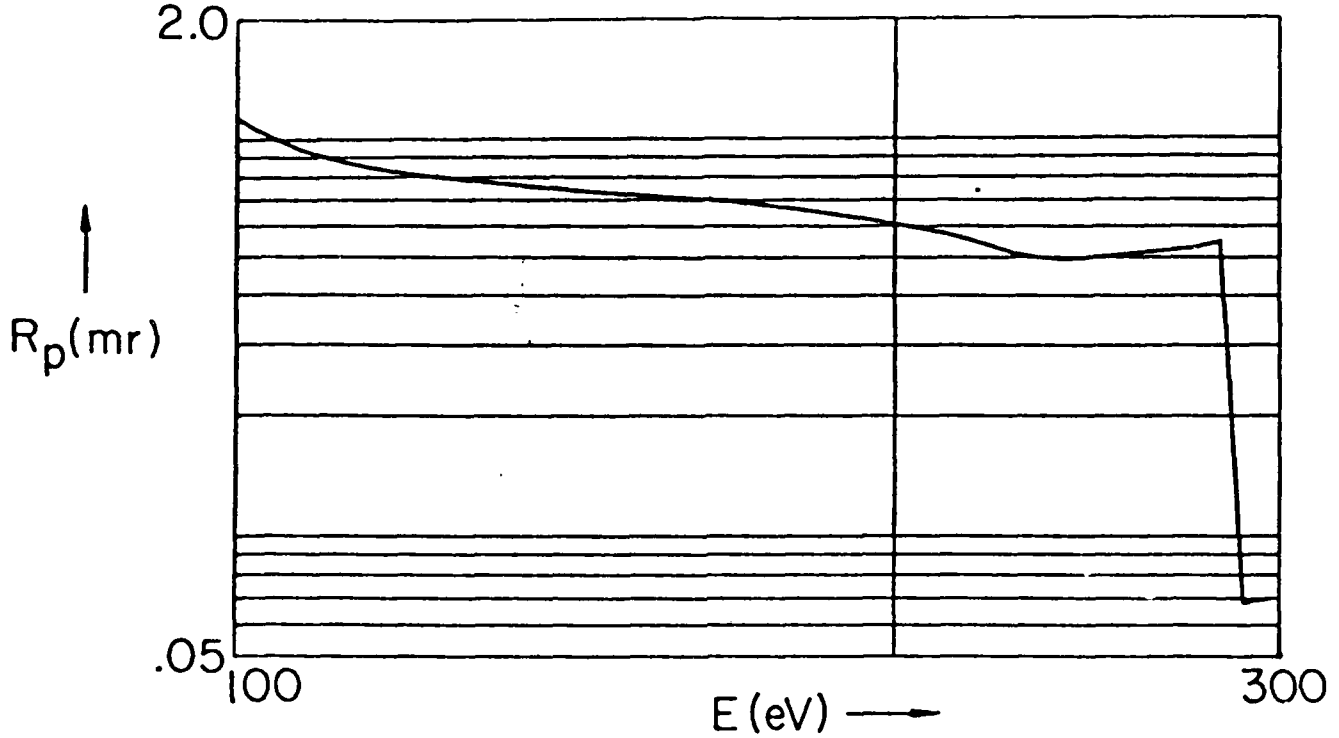

LEAD MELISSATE 2d--160 A 2nd ORDER

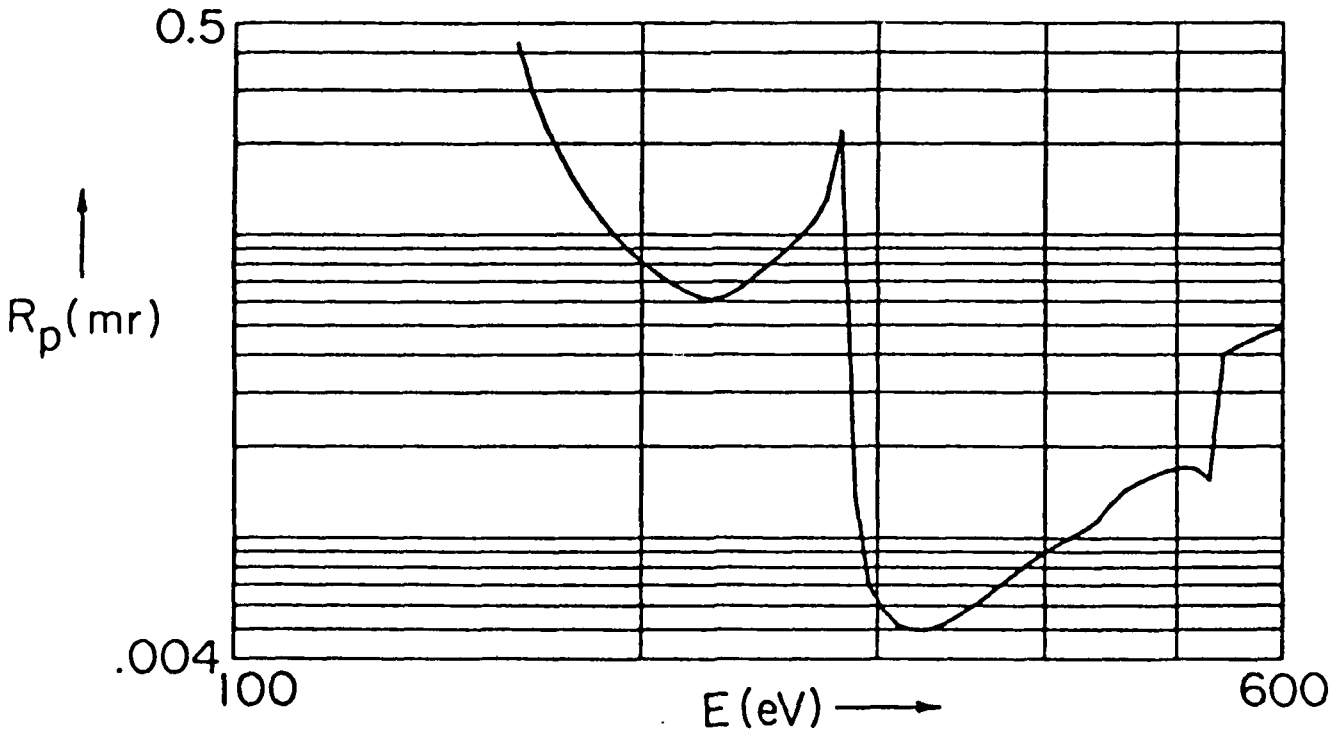

LEAD LIGNOCERATE 2d--130 A 1st ORDER

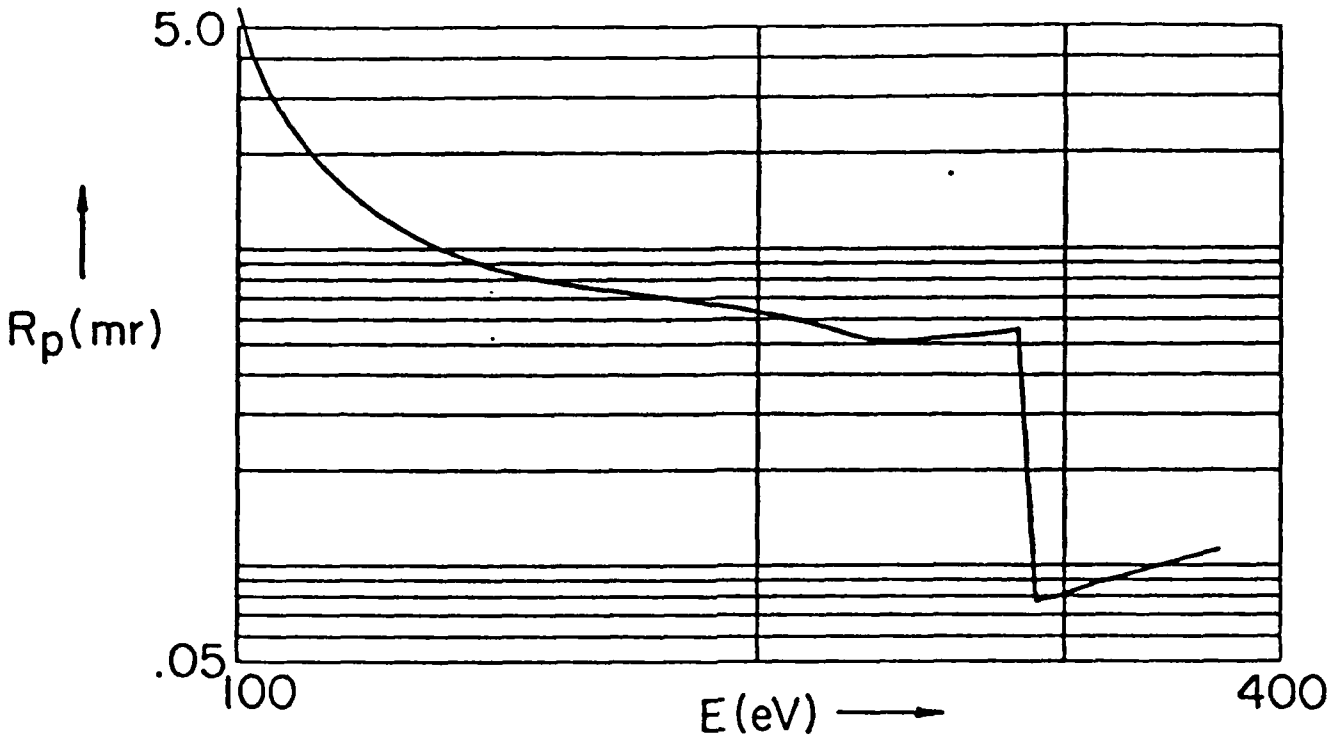

LEAD LIGNOCERATE 2d--130 A 2nd ORDER

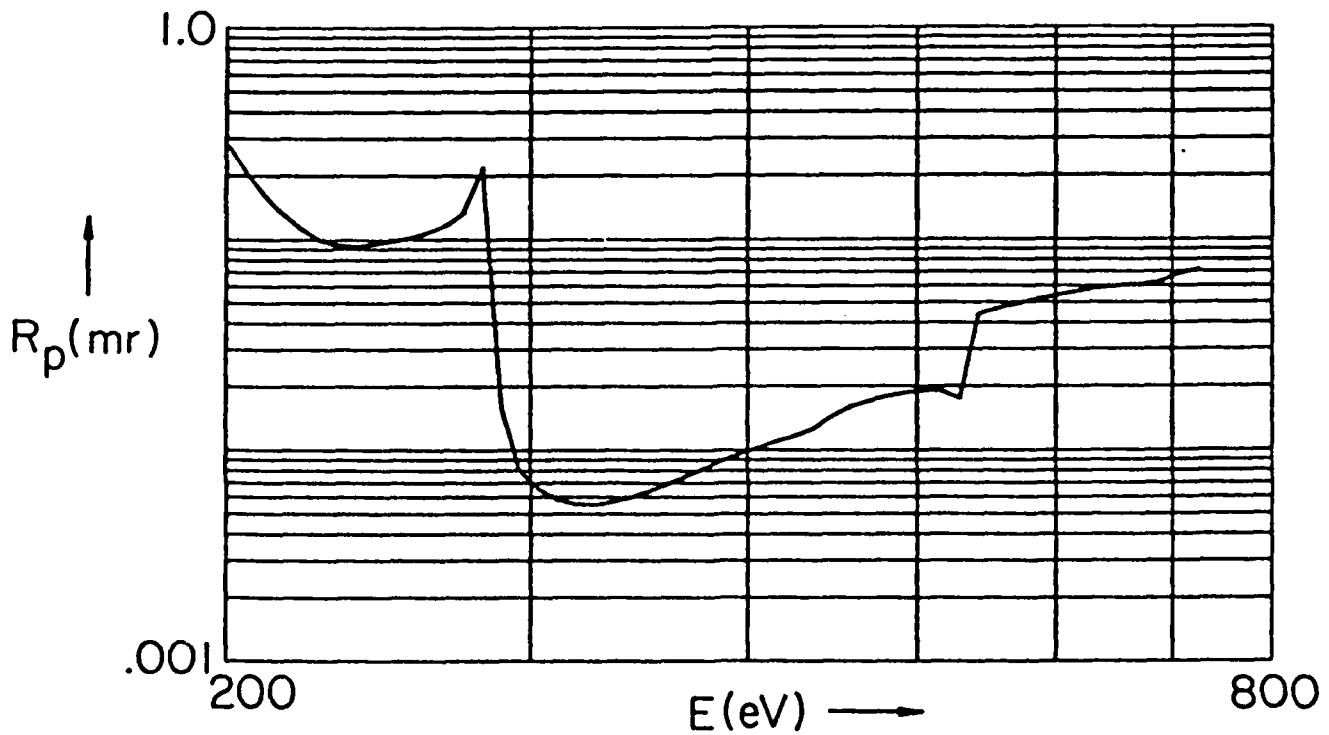

LEAD STEARATE 2d--100 A 1st ORDER

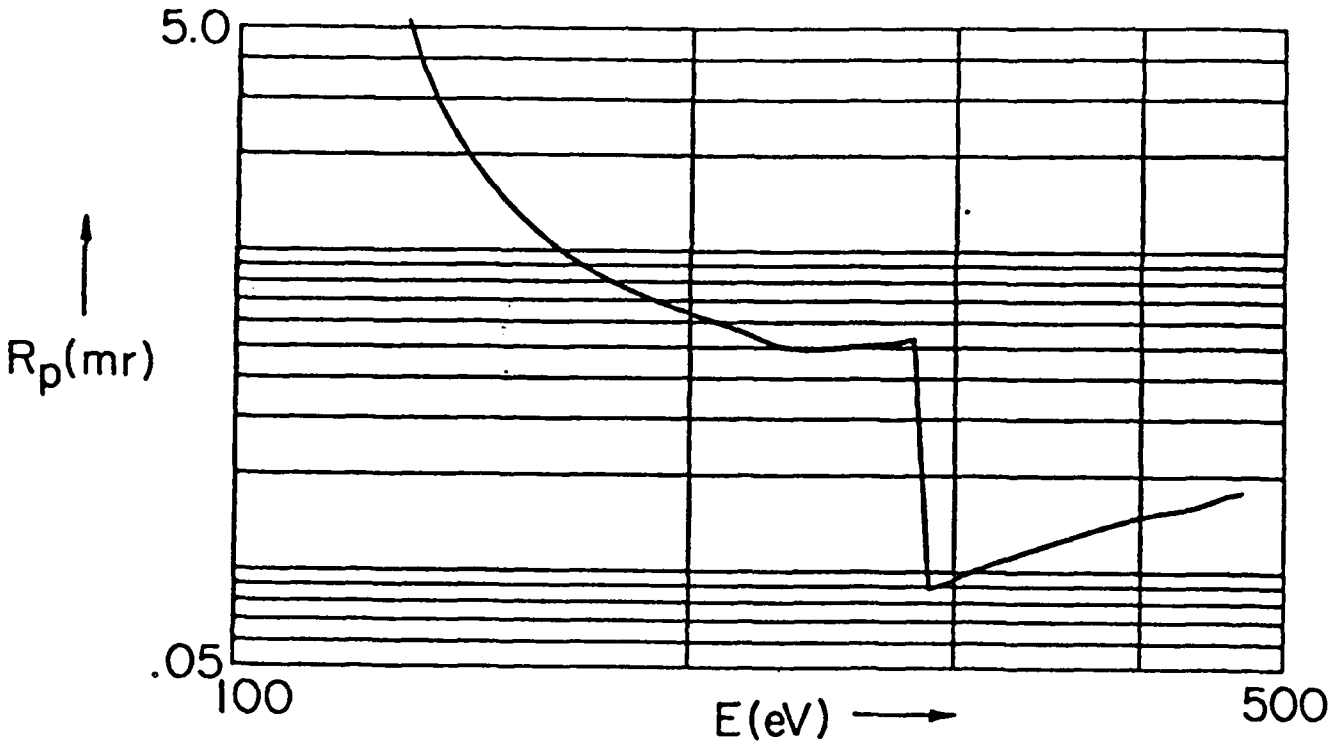

LEAD STEARATE 2d--100 A 2nd ORDER

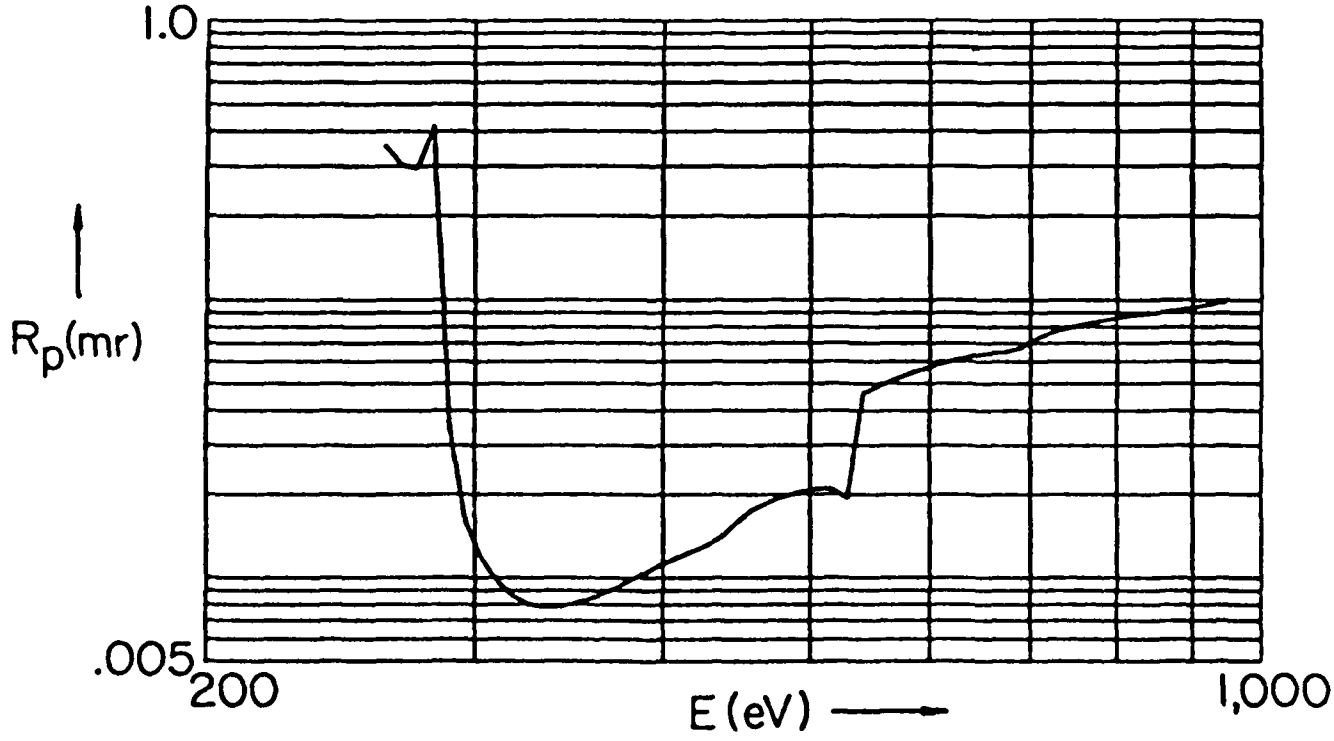

LEAD LAURATE 2d--70 A 1st ORDER

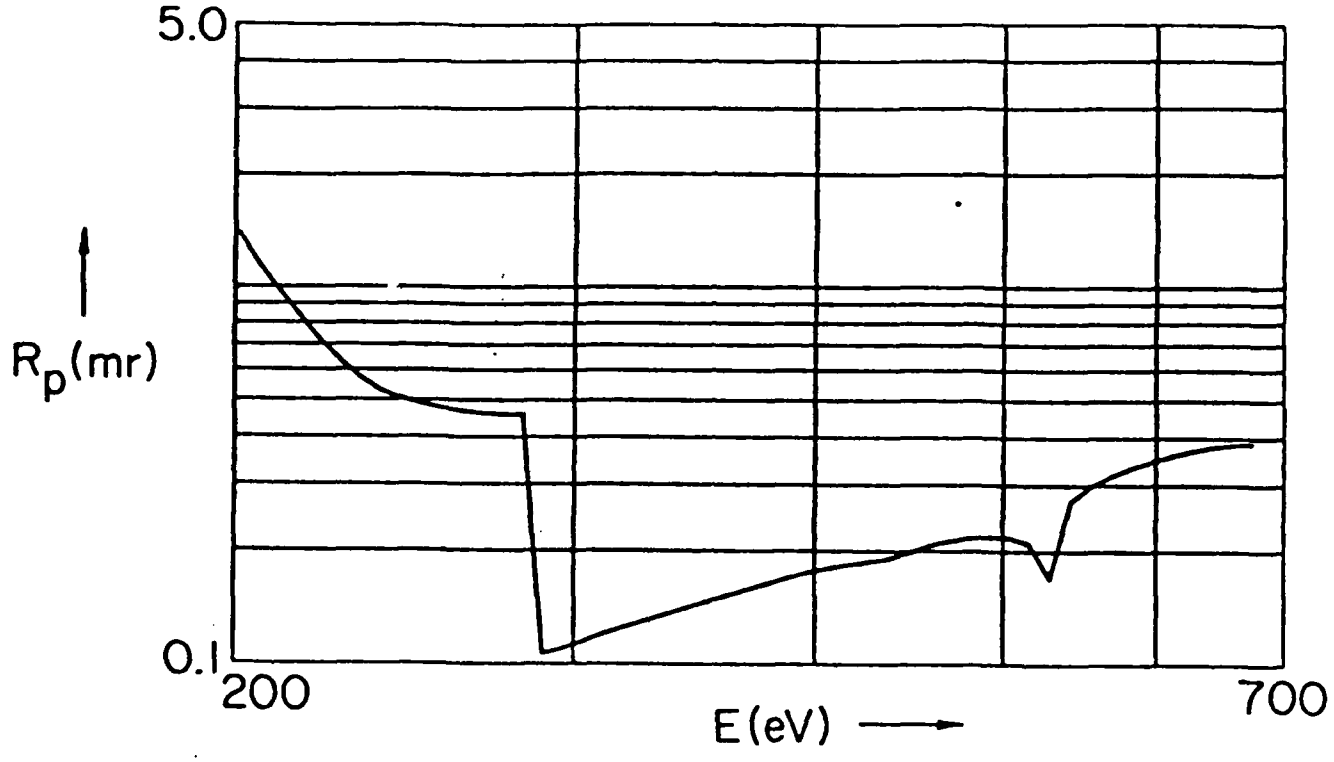

LEAD LAURATE 2d--70 A 2nd ORDER

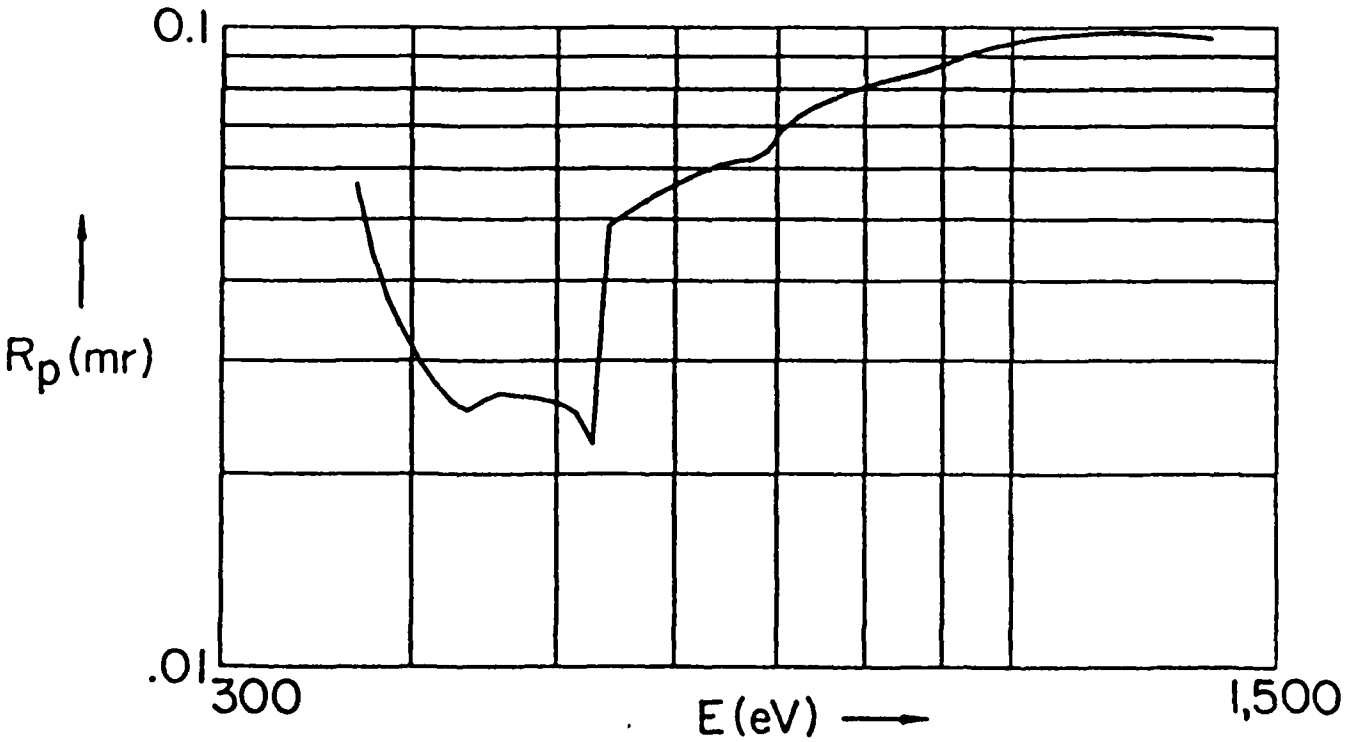

KAP ($10\bar{1}0$) 2d = 26.626 A 1st ORDER

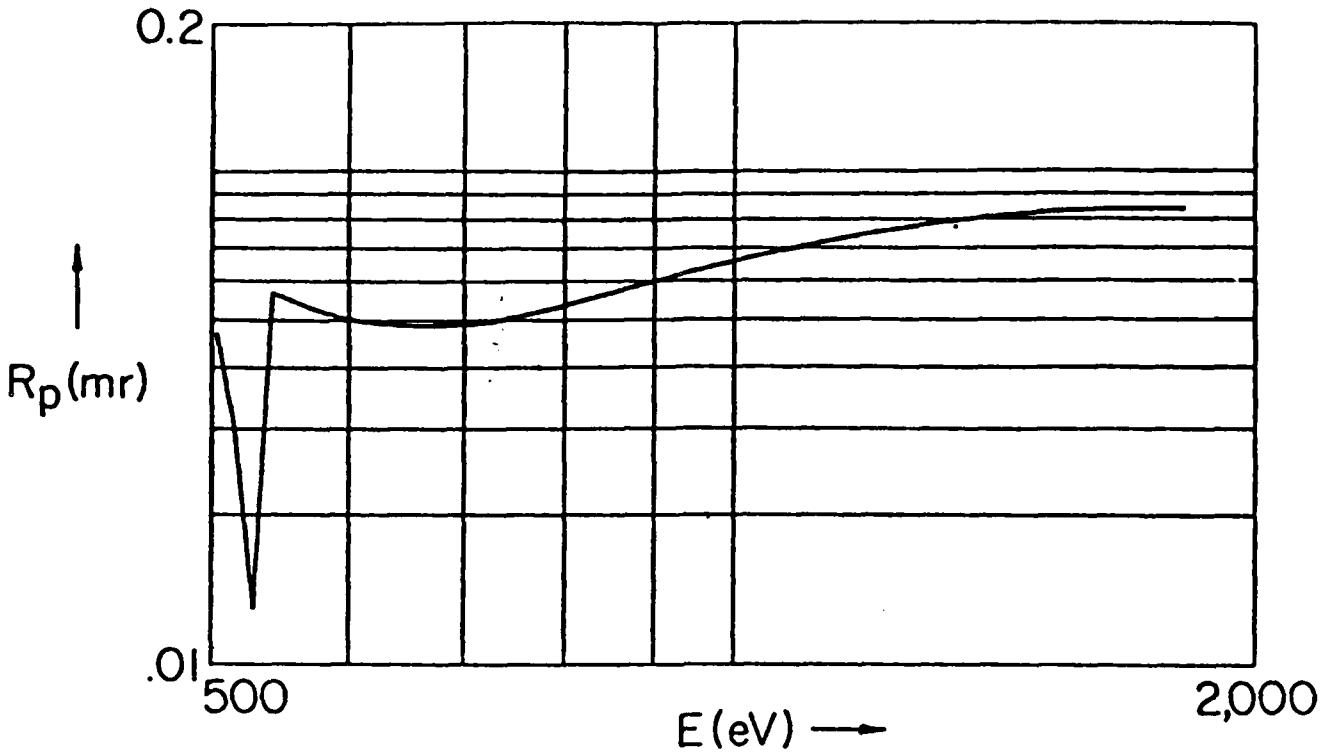

KAP ($10\bar{1}0$) 2d--26.626 A 2nd ORDER

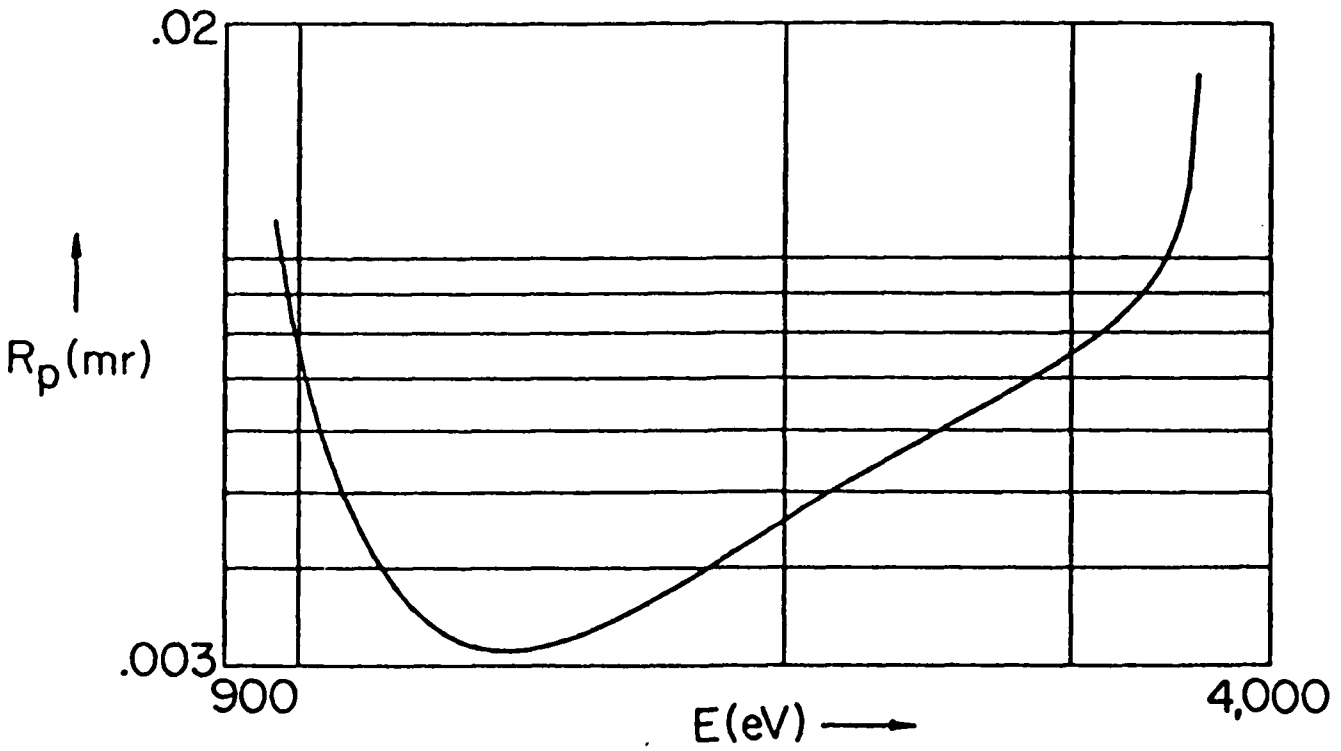

RAP ($10\bar{1}0$) 2d--26.121 A 1st ORDER

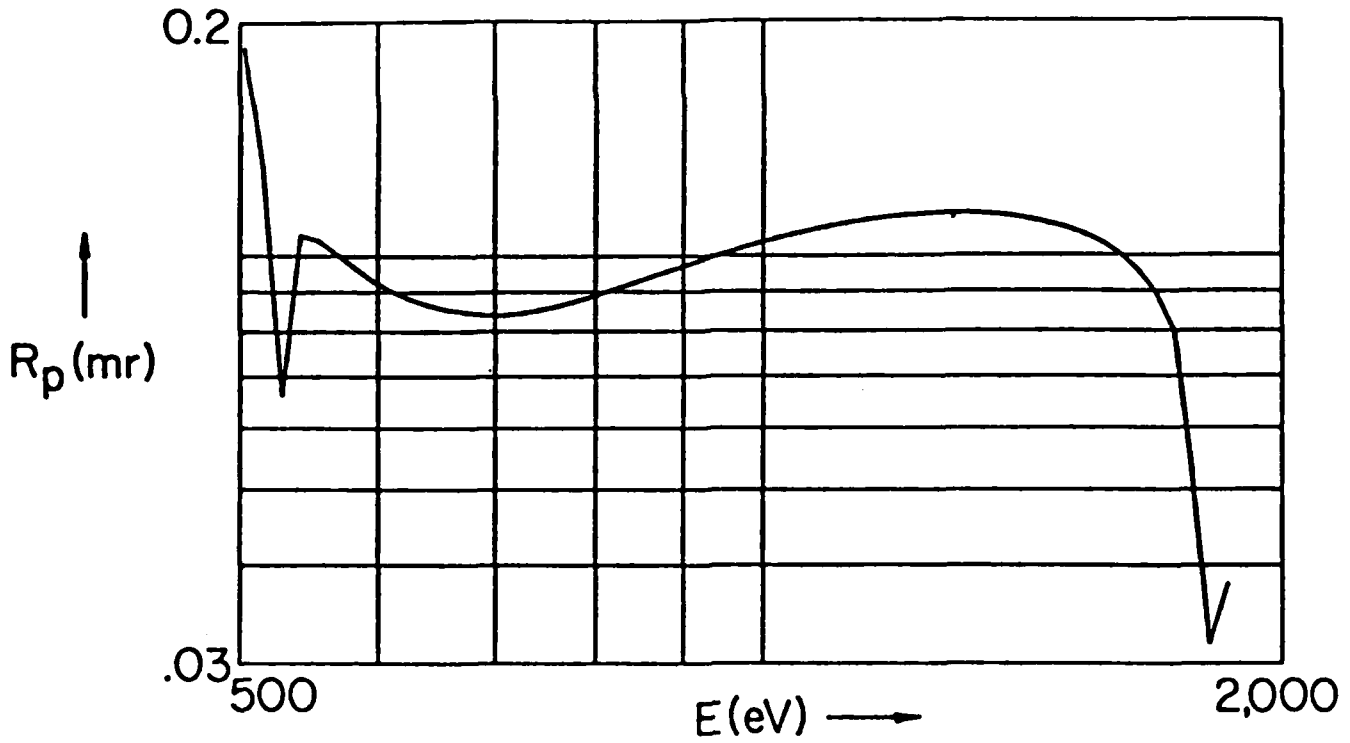

RAP ($10\bar{1}0$) 2d--26.121 A 2nd ORDER

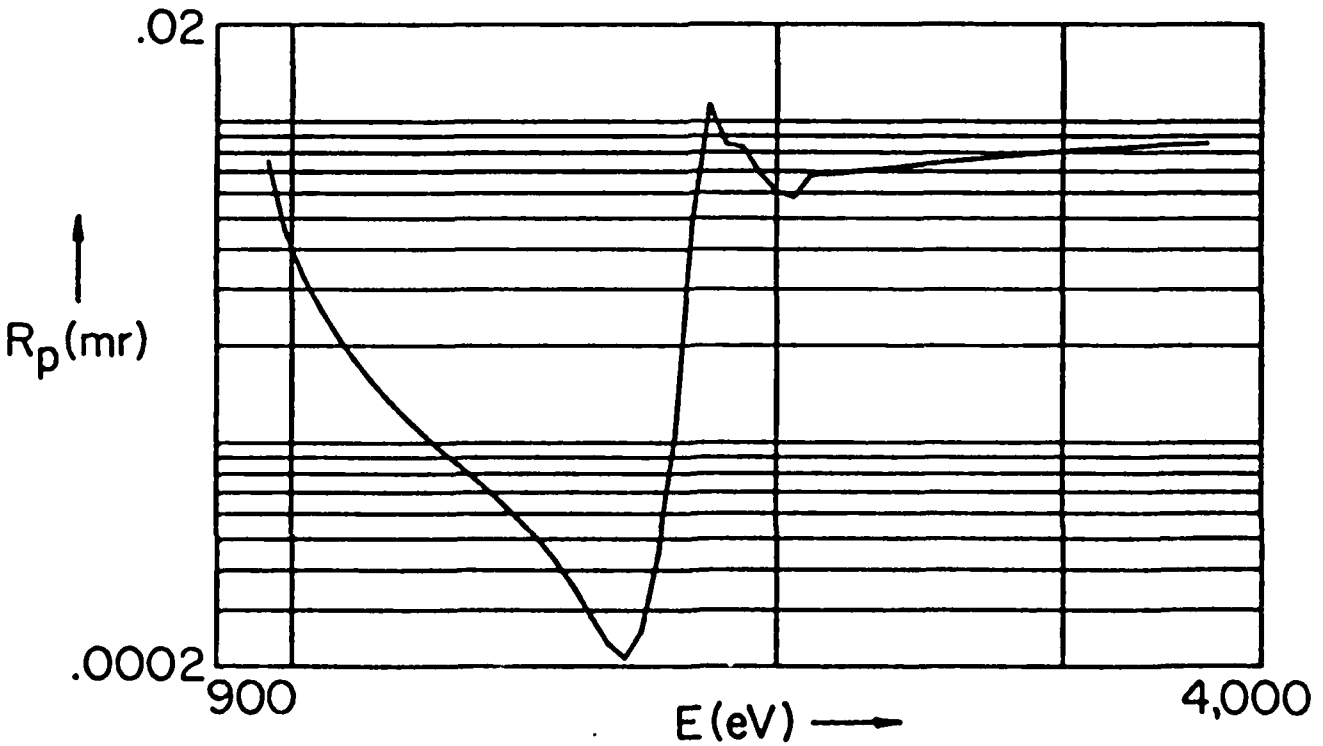

MICA (002) 2d--19.84 A 1st ORDER

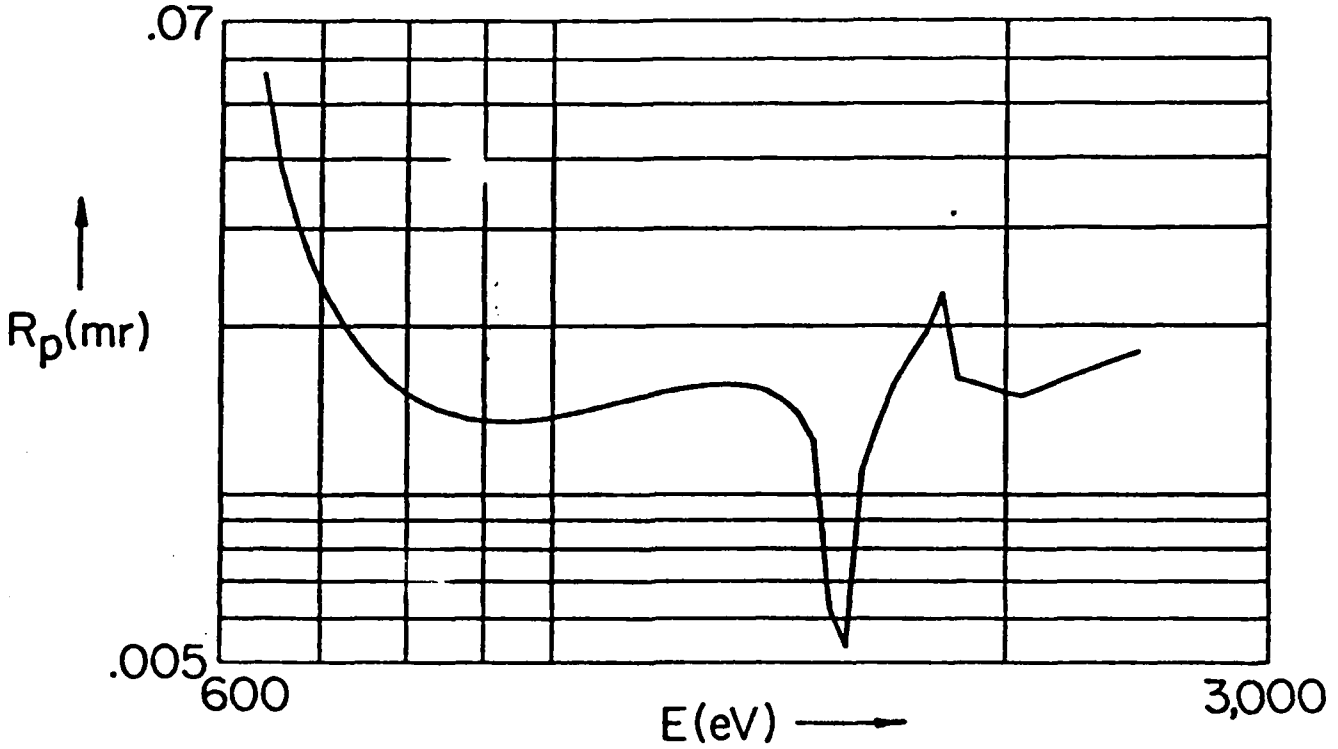

MICA (002) 2d--19.84 A 2nd ORDER

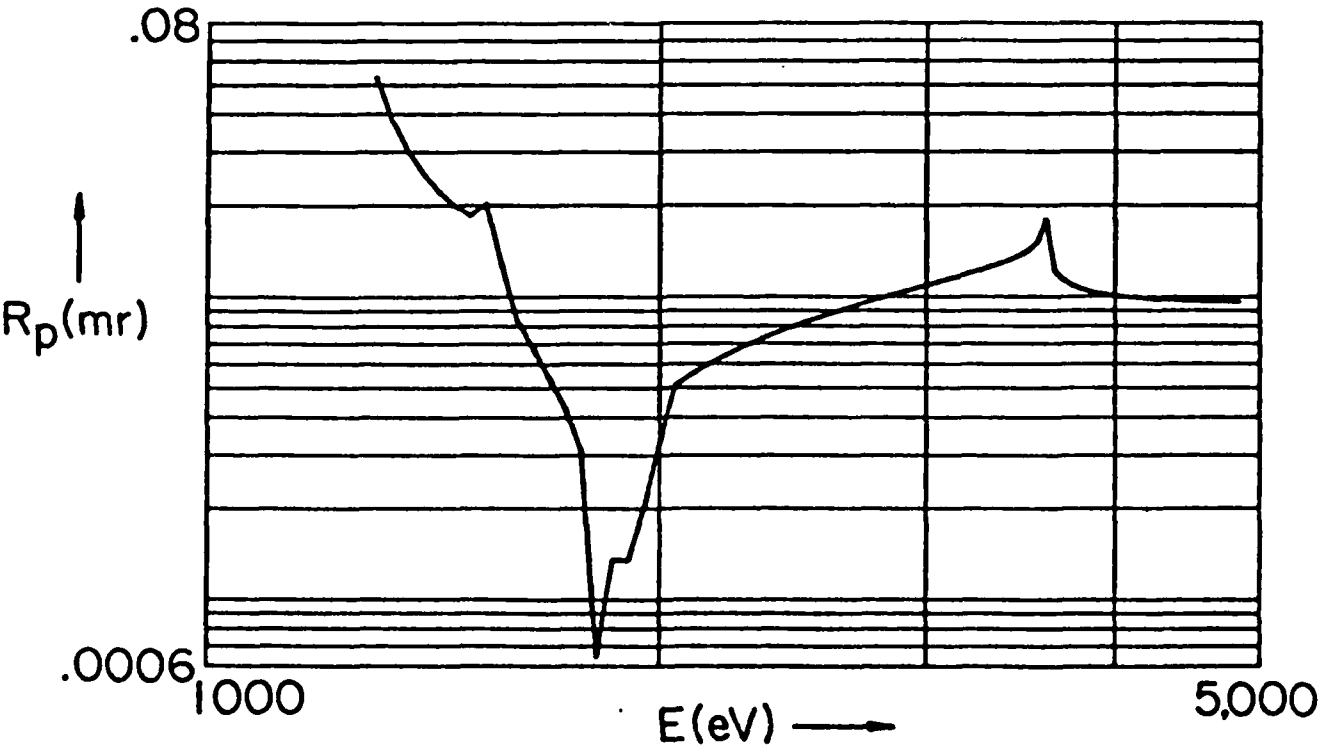

GYPSUM (020) 2d--15.185 A 1st ORDER

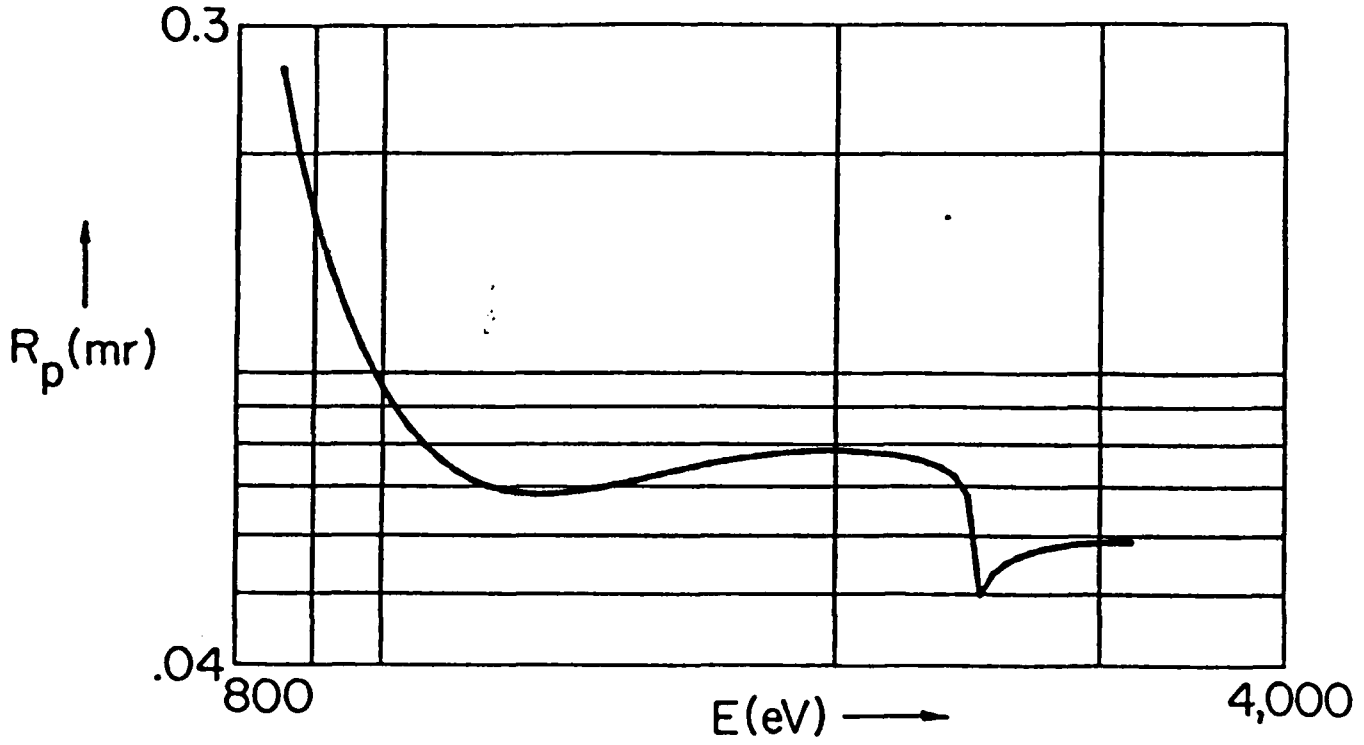

GYPSUM (020) 2d--15.185 A 2nd ORDER

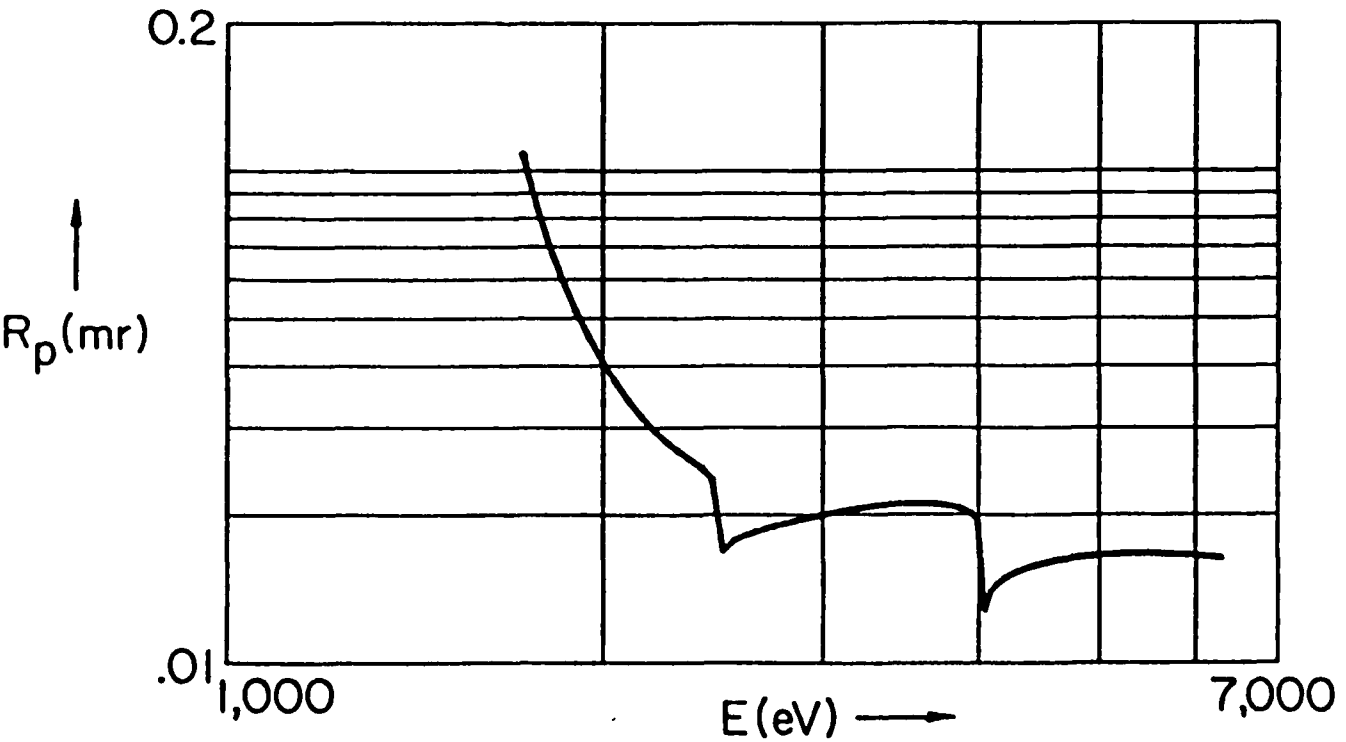

PET (002) 2d--8.742 A 1st ORDER

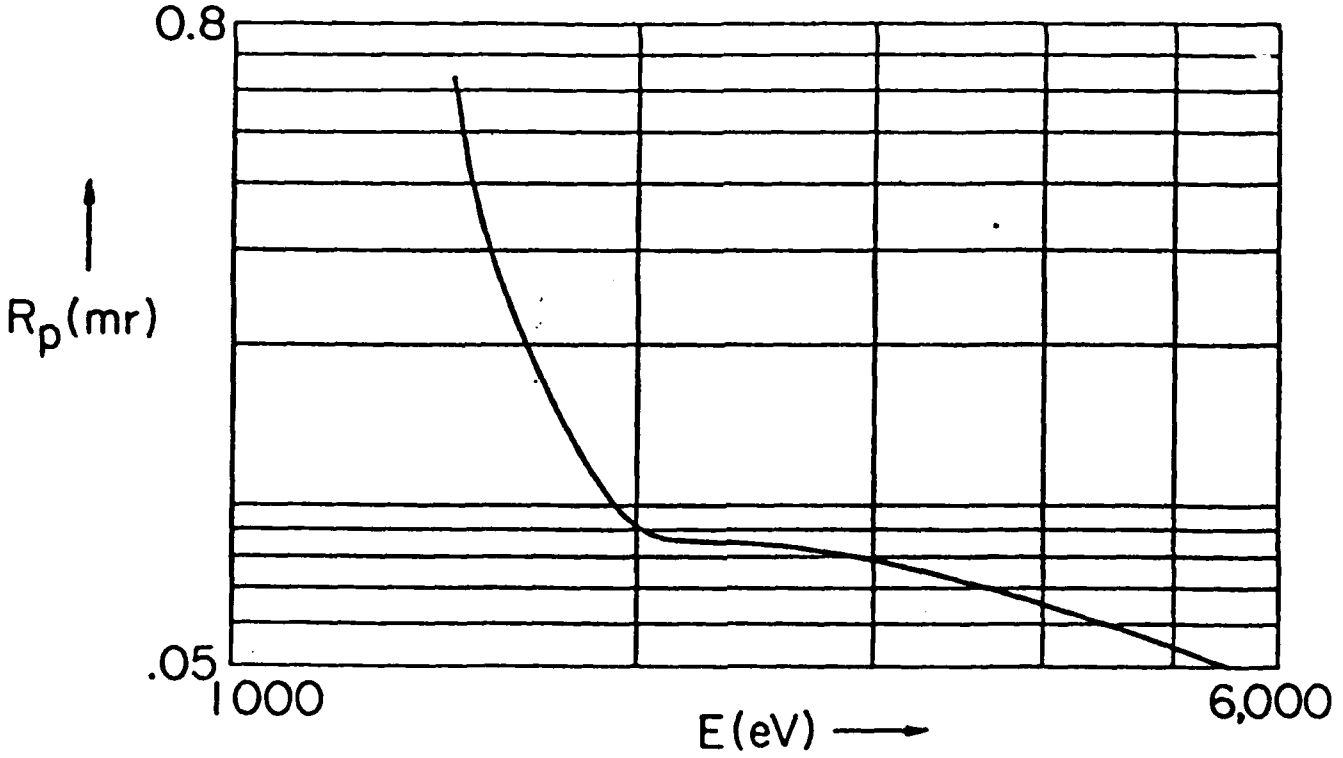

PET (002) 2d--8.742 A 2nd ORDER

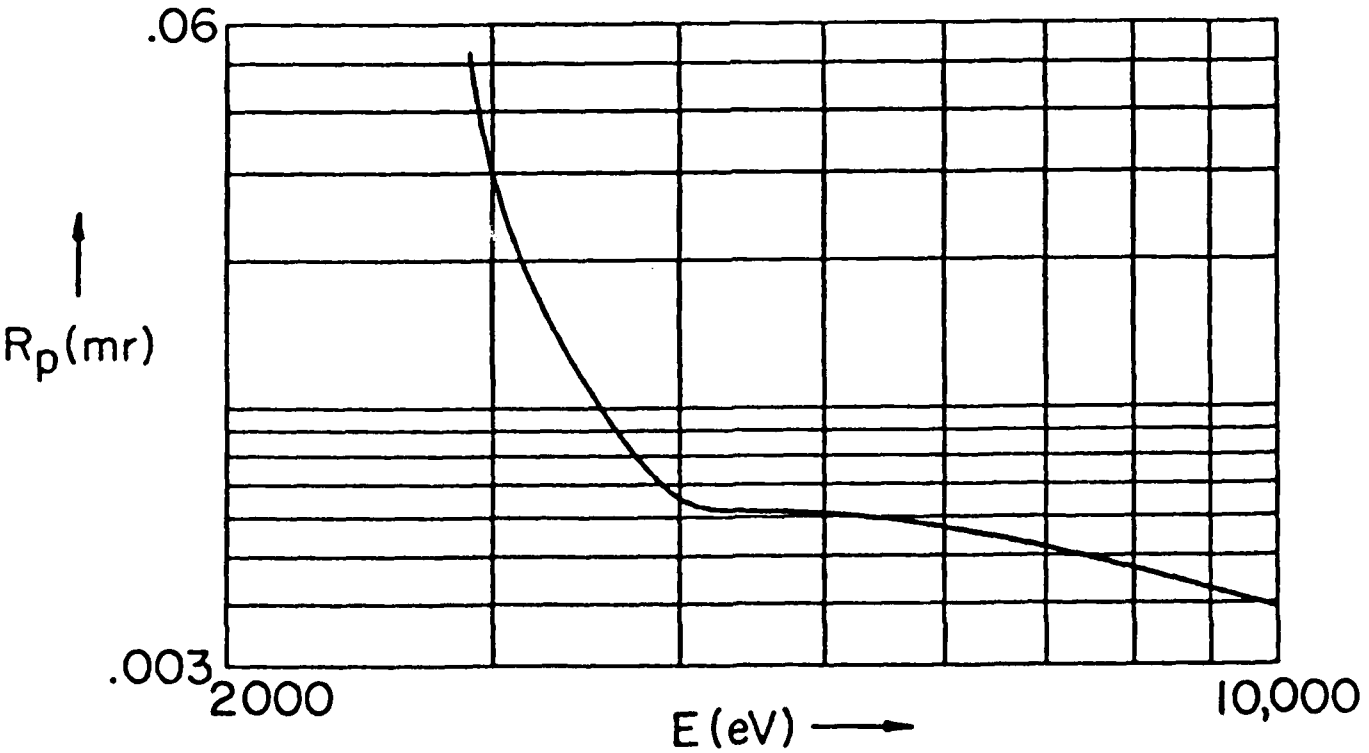

MICA (002) 2d--19.84 A 3rd ORDER

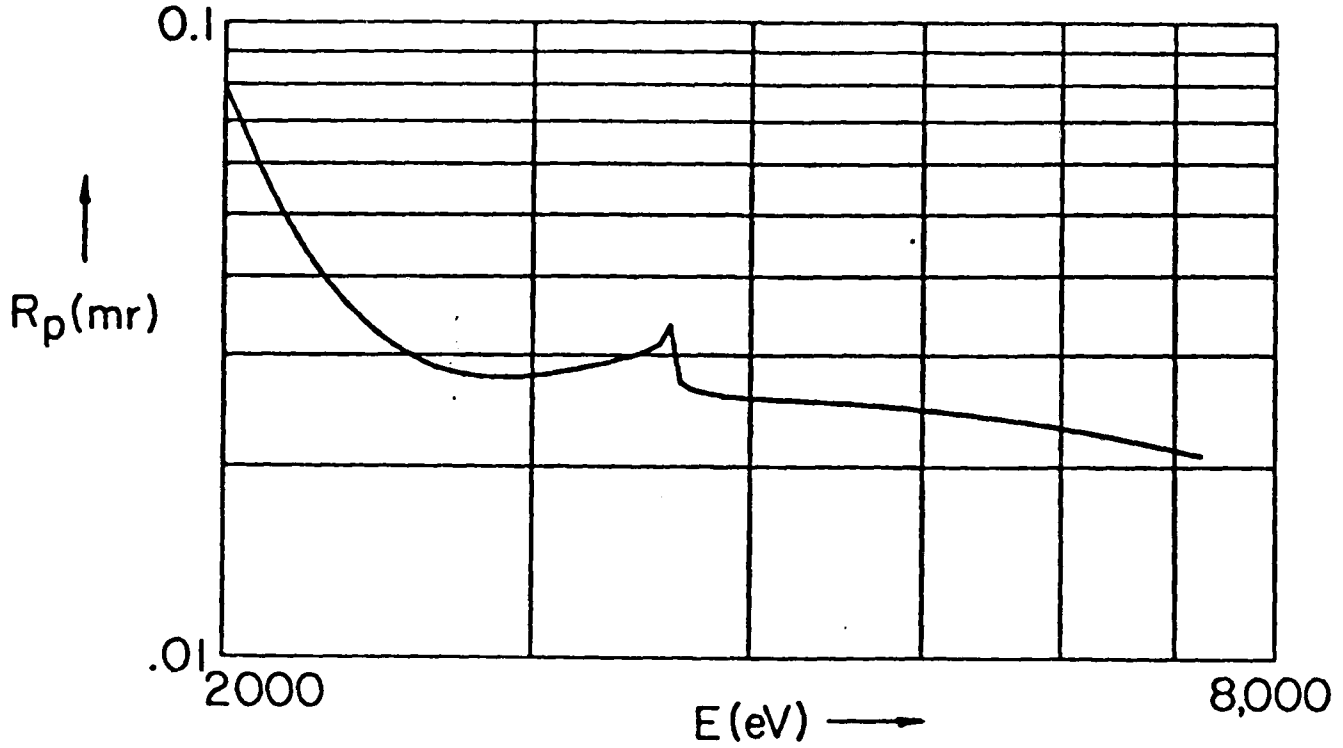

LiF (200) 2d--4.027 A 1st ORDER

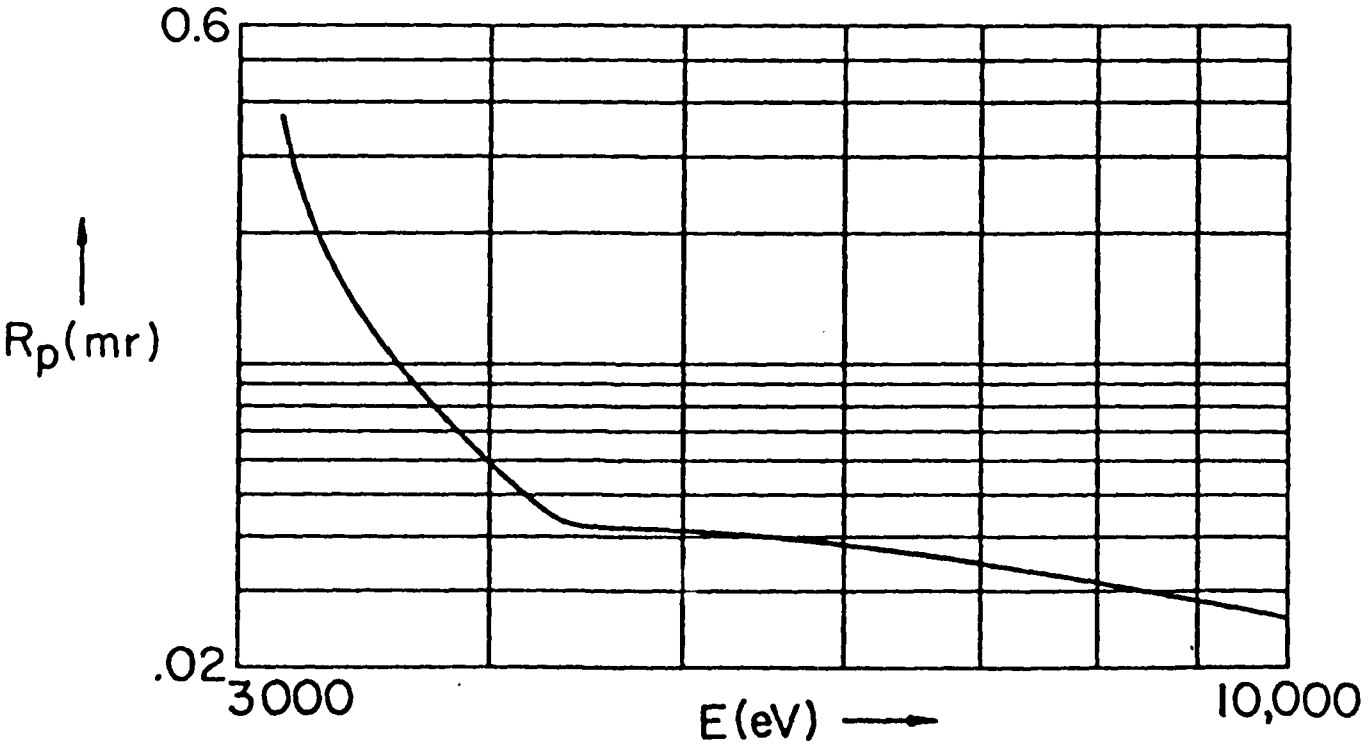

APPENDIX C. Table of density, D, vs exposure, I(photons/μm²) and photon energy, E(eV) for the RAR-2495 photographic film.

2495 FILM--EXPOSURE, I(photons/μm²)

NET DENSITY,D
(SPECULAR-0.1-0.1 mA)

D

PHOTON ENERGY,E(eV)
WAVELENGTH,λ(Å)

E(eV)	0.2	0.4	0.6	0.8	1.0	1.2	1.4	1.6	1.8	2.0	λ(Å)
A											
75	1.65 01	4.51 01	9.46 01	1.80 02	3.28 02	5.84 02	1.03 03	1.79 03	3.11 03	5.40 03	165.31
100	3.83 00	1.02 01	2.06 01	3.78 01	6.62 01	1.13 02	1.90 02	3.18 02	5.28 02	8.76 02	123.98
125	1.78 00	4.56 00	8.93 00	1.58 01	2.65 01	4.34 01	6.98 01	1.11 02	1.76 02	2.78 02	99.18
150	1.09 00	2.74 00	5.20 00	8.91 00	1.45 01	2.28 01	3.54 01	5.43 01	8.26 01	1.25 02	82.65
175	7.89-01	1.93 00	3.58 00	5.96 00	9.40 00	1.44 01	2.16 01	3.20 01	4.70 01	6.87 01	70.85
200	6.21-01	1.49 00	2.71 00	4.41 00	6.80 00	1.01 01	1.48 01	2.14 01	3.05 01	4.34 01	61.99
225	5.20-01	1.23 00	2.20 00	3.52 00	5.31 00	7.77 00	1.11 01	1.57 01	2.19 01	3.04 01	55.10
250	4.53-01	1.06 00	1.87 00	2.94 00	4.38 00	6.30 00	8.87 00	1.23 01	1.69 01	2.30 01	49.59
275	4.07-01	9.42-01	1.64 00	2.56 00	3.77 00	5.35 00	7.43 00	1.02 01	1.37 01	1.85 01	45.08
B											
300	1.72 00	4.40 00	8.58 00	1.51 01	2.53 01	4.13 01	6.62 01	1.05 02	1.66 02	2.61 02	41.33
325	1.36 00	3.45 00	6.63 00	1.15 01	1.89 01	3.02 01	4.75 01	7.39 01	1.14 02	1.76 02	38.15
350	1.13 00	2.83 00	5.36 00	9.15 00	1.48 01	2.33 01	3.59 01	5.48 01	8.30 01	1.25 02	35.42
375	9.75-01	2.40 00	4.49 00	7.56 00	1.20 01	1.86 01	2.82 01	4.23 01	6.29 01	9.31 01	33.06
C											
425	9.35-01	2.30 00	4.30 00	7.22 00	1.15 01	1.77 01	2.69 01	4.02 01	5.98 01	8.83 01	29.17
450	8.19-01	2.00 00	3.72 00	6.19 00	9.76 00	1.49 01	2.24 01	3.32 01	4.88 01	7.13 01	27.55
475	7.38-01	1.79 00	3.29 00	5.43 00	8.48 00	1.28 01	1.90 01	2.78 01	4.04 01	5.84 01	26.10
500	6.74-01	1.62 00	2.95 00	4.83 00	7.46 00	1.12 01	1.64 01	2.37 01	3.40 01	4.85 01	24.80
D											
550	9.92-01	2.45 00	4.61 00	7.78 00	1.25 01	1.94 01	2.95 01	4.45 01	6.66 01	9.92 01	22.54
600	8.29-01	2.02 00	3.73 00	6.20 00	9.74 00	1.48 01	2.21 01	3.27 01	4.78 01	6.95 01	20.66
650	7.17-01	1.72 00	3.14 00	5.13 00	7.92 00	1.18 01	1.74 01	2.51 01	3.60 01	5.13 01	19.07
700	6.38-01	1.52 00	2.72 00	4.39 00	6.68 00	9.83 00	1.42 01	2.01 01	2.83 01	3.97 01	17.71
750	5.85-01	1.37 00	2.44 00	3.87 00	5.80 00	8.41 00	1.19 01	1.67 01	2.30 01	3.16 01	16.53
800	5.45-01	1.27 00	2.22 00	3.48 00	5.14 00	7.34 00	1.02 01	1.41 01	1.92 01	2.59 01	15.50
850	5.14-01	1.18 00	2.05 00	3.17 00	4.63 00	6.52 00	8.97 00	1.22 01	1.63 01	2.17 01	14.59
900	4.91-01	1.12 00	1.92 00	2.94 00	4.24 00	5.90 00	8.03 00	1.07 01	1.42 01	1.87 01	13.78
950	4.73-01	1.07 00	1.81 00	2.75 00	3.93 00	5.42 00	7.29 00	9.64 00	1.26 01	1.63 01	13.05
1000	4.59-01	1.03 00	1.73 00	2.60 00	3.68 00	5.02 00	6.69 00	8.76 00	1.13 01	1.45 01	12.40
1050	4.48-01	9.85-01	1.66 00	2.48 00	3.49 00	4.71 00	6.22 00	8.07 00	1.04 01	1.32 01	11.81
1100	4.40-01	9.71-01	1.61 00	2.39 00	3.33 00	4.47 00	5.85 00	7.53 00	9.58 00	1.21 01	11.27
1150	4.34-01	9.52-01	1.57 00	2.31 00	3.20 00	4.27 00	5.56 00	7.11 00	8.98 00	1.13 01	10.78
1200	4.30-01	9.39-01	1.54 00	2.26 00	3.11 00	4.12 00	5.33 00	6.78 00	8.52 00	1.06 01	10.33
1250	4.28-01	9.30-01	1.52 00	2.21 00	3.03 00	4.01 00	5.16 00	6.53 00	8.17 00	1.01 01	9.92
1300	4.27-01	9.24-01	1.51 00	2.18 00	2.98 00	3.92 00	5.03 00	6.34 00	7.90 00	9.77 00	9.54
1350	4.28-01	9.23-01	1.50 00	2.17 00	2.95 00	3.86 00	4.93 00	6.20 00	7.70 00	9.50 00	9.18
1400	4.30-01	9.24-01	1.50 00	2.16 00	2.92 00	3.82 00	4.87 00	6.11 00	7.57 00	9.32 00	8.86
1450	4.33-01	9.29-01	1.50 00	2.16 00	2.92 00	3.80 00	4.84 00	6.05 00	7.49 00	9.20 00	8.55
1500	4.37-01	9.37-01	1.51 00	2.17 00	2.93 00	3.80 00	4.83 00	6.03 00	7.45 00	9.15 00	8.27
E											
1800	3.44-01	7.39-01	1.19 00	1.72 00	2.32 00	3.02 00	3.84 00	4.81 00	5.95 00	7.31 00	6.89
1900	3.49-01	7.47-01	1.20 00	1.72 00	2.33 00	3.03 00	3.84 00	4.79 00	5.92 00	7.26 00	6.53
2000	3.59-01	7.67-01	1.23 00	1.76 00	2.37 00	3.08 00	3.90 00	4.86 00	5.99 00	7.34 00	6.20
2100	3.70-01	7.88-01	1.26 00	1.80 00	2.43 00	3.14 00	3.97 00	4.94 00	6.09 00	7.46 00	5.90
2200	3.84-01	8.18-01	1.31 00	1.87 00	2.51 00	3.24 00	4.09 00	5.09 00	6.27 00	7.67 00	5.64
2300	4.01-01	8.52-01	1.36 00	1.94 00	2.60 00	3.36 00	4.24 00	5.28 00	6.49 00	7.95 00	5.39
2400	4.19-01	8.90-01	1.42 00	2.02 00	2.71 00	3.50 00	4.42 00	5.49 00	6.76 00	8.28 00	5.17
2500	4.40-01	9.33-01	1.49 00	2.12 00	2.84 00	3.66 00	4.62 00	5.74 00	7.07 00	8.66 00	4.96
2600	4.62-01	9.80-01	1.56 00	2.22 00	2.98 00	3.84 00	4.85 00	6.02 00	7.42 00	9.09 00	4.77
2700	4.87-01	1.03 00	1.64 00	2.34 00	3.13 00	4.04 00	5.10 00	6.33 00	7.80 00	9.56 00	4.59
2800	5.13-01	1.09 00	1.73 00	2.46 00	3.30 00	4.26 00	5.37 00	6.67 00	8.22 00	1.01 01	4.43
2900	5.41-01	1.15 00	1.83 00	2.60 00	3.48 00	4.49 00	5.66 00	7.04 00	8.67 00	1.06 01	4.28
3000	5.71-01	1.21 00	1.93 00	2.74 00	3.67 00	4.74 00	5.98 00	7.43 00	9.16 00	1.13 01	4.13
3100	6.04-01	1.28 00	2.04 00	2.90 00	3.88 00	5.01 00	6.32 00	7.86 00	9.69 00	1.19 01	4.00
3200	6.38-01	1.35 00	2.15 00	3.06 00	4.10 00	5.29 00	6.67 00	8.30 00	1.02 01	1.26 01	3.87
3300	6.74-01	1.43 00	2.27 00	3.23 00	4.33 00	5.59 00	7.06 00	8.78 00	1.08 01	1.33 01	3.76
F											
4000	4.97-01	1.05 00	1.68 00	2.39 00	3.19 00	4.12 00	5.20 00	6.46 00	7.96 00	9.78 00	3.10
5000	7.37-01	1.56 00	2.49 00	3.54 00	4.74 00	6.12 00	7.73 00	9.63 00	1.19 01	1.47 01	2.48
6000	1.09 00	2.30 00	3.67 00	5.22 00	7.00 00	9.05 00	1.14 01	1.43 01	1.77 01	2.18 01	2.07
7000	1.56 00	3.30 00	5.27 00	7.50 00	1.01 01	1.30 01	1.65 01	2.06 01	2.55 01	3.15 01	1.77
8000	2.17 00	4.59 00	7.33 00	1.04 01	1.40 01	1.81 01	2.29 01	2.87 01	3.56 01	4.41 01	1.55
9000	2.93 00	6.21 00	9.91 00	1.41 01	1.89 01	2.45 01	3.11 01	3.88 01	4.82 01	5.98 01	1.38
10000	3.86 00	8.18 00	1.31 01	1.86 01	2.50 01	3.23 01	4.10 01	5.13 01	6.37 01	7.90 01	1.24

Large Aperture Picosecond X-Ray Streak Camera

P. A. Jaanimagi* and B. L. Henke

Department of Physics and Astronomy
University of Hawaii
Honolulu, Hawaii 96822

ABSTRACT

We report the development of a new picosecond streak camera with a large aperture, 1 x 40 mm, photocathode slit. The streak tube features demagnified electron optics, an accelerating field at the cathode greater than 20 kV/cm and more than 300 spatial resolution elements. The tube design was tested in static mode with an x-ray sensitive photocathode. Preliminary dynamic tests are also presented.

---

*Current address: University of Rochester, Laboratory for Laser Energetics, 250 East River Road, Rochester, New York 14623.

I. INTRODUCTION

In recent years we have witnessed the development of a new generation of picosecond streak cameras;[1-3] in addition, there have been a series of modifications to or variations on past designs.[4-9] These efforts have been directed mainly toward achieving sub-picosecond time resolution, with secondary emphasis on the number of spatial resolution elements along the photocathode slit. Improvements in the time resolution capabilities of streak tubes have centered on increasing both the accelerating field at the photocathode and the axial potential throughout the rest of the tube. The resulting higher energy photoelectrons, however, are more difficult to focus and thus the imaging properties are degraded and/or the photoemission must be limited to the paraxial region. In order to effectively incorporate a streak camera with an imaging or spectrographically resolving system, one desires a large number of spatial resolution elements as well as a large aperture photocathode. The latter is especially important for x-ray streak cameras where the input signal cannot be demagnified to fit the photocathode dimensions in a simple manner.

The usable length of the photocathode for all of the current designs is in the range 8 to 20 mm, resulting in 100 to 200 spatial resolution elements. This number is of course dependent upon many factors, for example: recorded contrast level, input signal intensity, intensifier and recording system spatial resolution, and also upon the radial position on the photocathode. In this paper we report on a new streak tube which incorporates a 40 mm-long slit while maintaining the

large accelerating field at the photocathode necessary for picosecond time resolution. This streak tube was designed specifically for use with an elliptical crystal analyzer x-ray spectrograph[10,11] where we wish to diagnose a large spectral range on a single shot and not be limited by the spatial resolution of the streak camera.

The main problems associated with large aperture electron-optical lenses in streak tubes are field curvature distortion, accelerating field uniformity and iso-chromism. Iso-chromism is defined as the difference in transit time (cathode to phosphor screen) for off-axis trajectories with respect to axial trajectories and causes the well known phenomena of curved streak images. These problems were addressed in the new streak tube design. A curved photocathode was implemented to minimize non-iso-chromism. Accelerating field uniformity was established by a spherical diode electrode configuration with a long slot aperture opposite the photocathode. The focus and anode electrodes were designed to achieve a demagnified electron-optical imaging system. An astigmatism problem inherent in the streak tube design was corrected by shaping the end of the anode electrode into a double-lipped tube lens.[12]

An electron optics ray trace code was very useful in the preliminary design work. The computer program used was an upgraded version of the SLAC Electron Trajectory Program.[13] This is a two-dimensional code which can use either rectangular or cylindrically symmetric geometry. The program was modified to provide quantitatively more accurate results.[14] Laplace's equation was solved numerically with a line-successive-over-relaxation technique and used a finite difference equation on a 9-point cross stencil for a rectangular numerical mesh. Boundaries were handled by substituting the appropriate 4- or 5-point

(with non-equidistant spacing) formulas for the derivatives into the finite difference equation. The relativistic differential equations for the trajectories were solved with a fourth-order Runge-Kutte method, and 4 by 4 bivariate Lagrangian interpolation[15] was used to calculate the required fields and potentials.

II. STREAK TUBE DESIGN

The RCA 73435 image tube[16] was selected as an initial design which was to be modified for picosecond time resolution and a 40 mm photocathode. Preliminary modifications to this tube have been very encouraging, however, limitations on the magnitude of the accelerating field and the usable photocathode length had to be amended.[9]

Fig. 1 shows a cross section of the new streak tube front-end. The cathode and accelerator electrodes form a section of a spherical diode of radii 10.1 and 10.0 cm, respectively. The photocathode slit, 1 x 40 mm is cut directly into the cathode plate and is positioned on the tube axis. The slot in the accelerator plate is 2 x 64 mm and is positioned directly opposite the photocathode slit. These two plates are attached together on insulating spacers to within very strict mechanical tolerances, however the cathode plate is simply demountable for the quick exchange of photocathodes. The x-ray photocathode substrate, Be foil or thin plastic, is mounted directly on the concave surface of the cathode plate.

This front-end electrode configuration has many desirable features. The curvature of the photocathode surface is a major factor in correcting the iso-chromism problem of large aperture systems.[17] Our ray

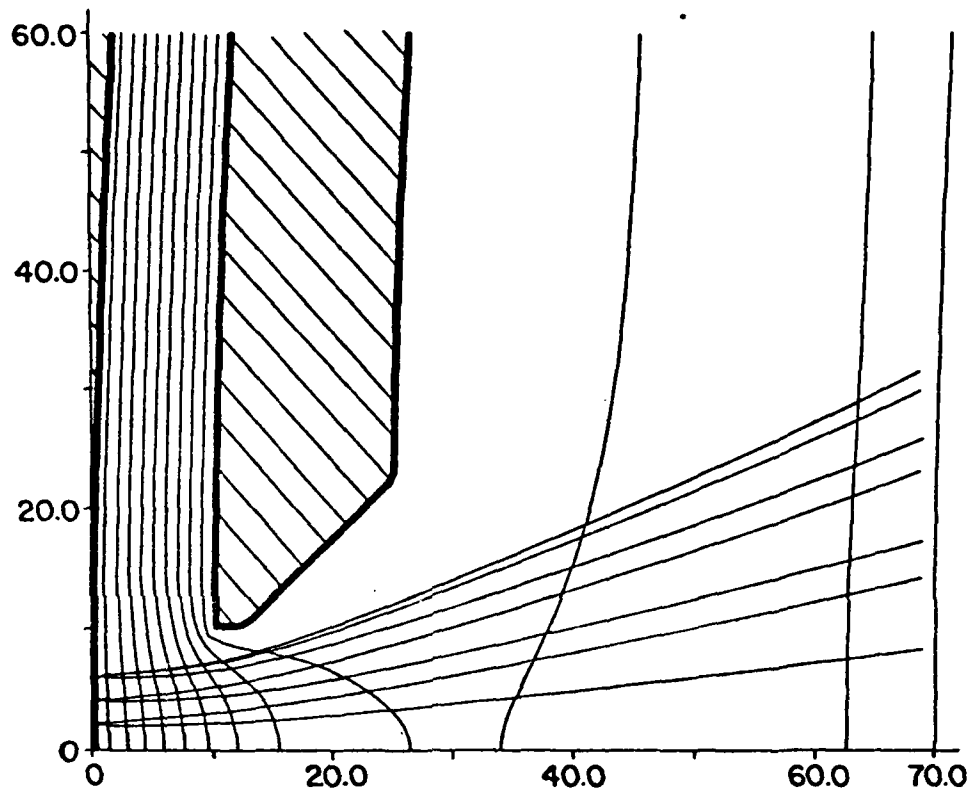

Figure 1. Cross section of the streak camera photocathode and the accelerating slot aperture. The scale is 0.1 mm. Equipotentials are drawn for every .1 V_{SLOT}. The potential on the right hand boundary is .76 V_{SLOT} and was chosen to simulate the potential in the focussing region. Photoelectron trajectories were calculated with transverse energies of 0 and +1 eV for positions .2 and .4 mm off-axis, and 0, +1, +2 eV from .6 mm off-axis.

trace code shows that for a planar cathode, photoelectrons emitted from a position 20 mm off-axis would arrive at the phosphor about 300 ps after a similar one emitted on-axis--certainly an unwieldy delay for streak cameras operating in the few picosecond time resolution regime. The accelerating field uniformity is limited only by the mechanical tolerances and the geometry. One can show that the field is uniform over the central 75% of the length of the acceleration plate aperture.[12] The magnitude of the accelerating field is limited by the surface finish of the electrodes and the geometry. For a slot width to electrode spacing ratio of two, the magnitude of the accelerating field on the tube axis is 70% of the interelectrode field. The slot aperture rather than a fine mesh is used to generate the large accelerating field at the photocathode for a number of reasons. The slot aperture is mechanically more rigid. The photoelectron transmission is 100%, compared with typically 40-70% for a mesh. The noise and ghost images caused by secondary electron emission generated by x-rays and photoelectrons impinging upon the electrode surfaces is eliminated. The minimum width of the slot aperture and also the bevel on the concave side of the accelerator plate are defined by requiring the elimination of this secondary electron generation.

The diverging lens effect of the slot aperture, clearly shown by the trajectories in Fig. 1, is used to advantage in this design. It introduces an asymmetry into the rectangular cross section of the photoelectron beam profile, but also astigmatic distortion into the electron imaging. The asymmetry in the beam profile results in different magnifications parallel and perpendicular to the photocathode slit.[9] Perpendicular to the slit, the image is demagnified by a factor

of four to eight, thereby allowing the use of very wide (~1 mm) input slits without compromising the time resolution. This is advantageous for situations where the x-ray photon flux is at a premium. Parallel to the slit, the magnification is in the range 1.2 to 1.5. When a mesh is used for the initial accelerating electrode on the RCA tube, the magnifications parallel and perpendicular to the slit are equivalent.[18] The magnitude of the astigmatism depends upon the accelerating fields and the geometry of the focus and anode electrodes.

Proper analysis of the electron optics of the streak tube requires a full three-dimensional ray trace code due to the nonrotational symmetry at the front-end electrodes. This problem was satisfactorily resolved at least for studying the focussing conditions and spatial resolution along the length of the photocathode slit by implementing a pseudo-electrode as an equipotential starting surface for the trajectories and using the two-dimensional code with circular symmetry. The cathode and pseudo-electrode surfaces form a section of a spherical diode with a 2 mm spacing over 75% of the length of the true slot aperture. The spacing decreases slightly towards the ends of the aperture. The potential for this pseudo-electrode was made equal to the axial potential 2 mm from the photocathode in Fig. 1, and an analytic paraxial solution for the diode was used for the trajectories in the region to the starting surface. Similar techniques for studying the focussing conditions in the direction of the slit width were not very successful since the numerical mesh dimensions was only half the slot aperture width.

Fig. 2a shows a photoelectron trajectory analysis for a standard RCA tube electrode configuration after replacing the usual cathode and grid wire structure with the slot aperture producing a 21 kV/cm

accelerating field. The focus electrode potential was adjusted for optimum spatial resolution in the paraxial region at the phosphor screen which is positioned at z = 230 mm. The anode aperture diameter was also increased from the standard 6 mm in order to facilitate numerical difficulties associated with small apertures. This had a very minor effect on the focussing properties of the tube.

Clearly the tube design presented in Fig. 2a cannot be used with a 40 mm photocathode. Extrapolating back to the true anode aperture diameter we should start observing a decrease in photoelectron throughput at cathode positions greater than about 7 mm off-axis with a complete cut-off at 13 mm off-axis. The cathode to phosphor magnification of the slit length is 1.36. This is in good agreement with our experimental observations and gives us confidence in our electron optics code and also the use of the pseudo-electrode starting surface. To increase the usable photocathode length, the cross-over point in front of the anode cone must be moved back toward the anode aperture.

In Fig. 2b we present the trajectory analysis after most of the anode cone has been removed. This increases the usable cathode length to 36 mm and decreases the magnification to unity. The potential at the cross-over point, however, is only 7.3 kV and this can present a possible space charge problem and limit the dynamic range. In Fig. 2c, with the smaller radius focus electrode the space charge problem at the cross-over is alleviated, the magnification is further reduced to 0.9 and the full 40 mm photocathode can be used.

The magnitude of the iso-chromism problem can be estimated from our electron optics program. The time differences as a function of photocathode position for the three electrode configurations in Fig. 2 are

presented in Fig. 3. The estimated streak curvature of 20 ps for electrons originating 20 mm off-axis is an acceptable figure. Further improvement can be made by implementing a curved phosphor screen. A smaller radius of curvature on the cathode could also be used, however this further magnifies any problems in imaging onto a convex photocathode surface.

III. TIME-OF-FLIGHT DISPERSION IN STREAK CAMERAS

Time-of-flight dispersion (Δt) due to a finite spread in the initial photoelectron energies ($\Delta\varepsilon$) is the primary limiting factor in the time resolution capabilities of all streak cameras. Most authors, when quoting time resolution specifications due to time-of-flight dispersion, consider only the cathode to mesh or accelerating aperture region and totally neglect the dispersion through the focussing, anode and drift regions. This can significantly increase Δt. Simple formulae to properly estimate the time-of-flight follow.

The axial potential in most streak tubes can be approximated as in Fig. 4. d_1 is the initial accelerating region; d_2 the focussing region; d_3 the final accelerating region; and d_4 the drift region to the phosphor screen. V_2 is the anode potential and V_1 is approximately equal to the focus voltage. Using the simple non-relativistic, constant acceleration formulae for the motion of an electron in a diode or drift region, one can easily calculate the transit time in each successive region for electrons with initial axial velocities corresponding to energies of zero and ε. Subtracting these numbers gives the time-of-flight dispersion in each region to order ε as

$$\Delta t_1 = k d_1 V_1^{-1} [\varepsilon^{\frac{1}{2}} - \varepsilon V^{-\frac{1}{2}}/2]$$

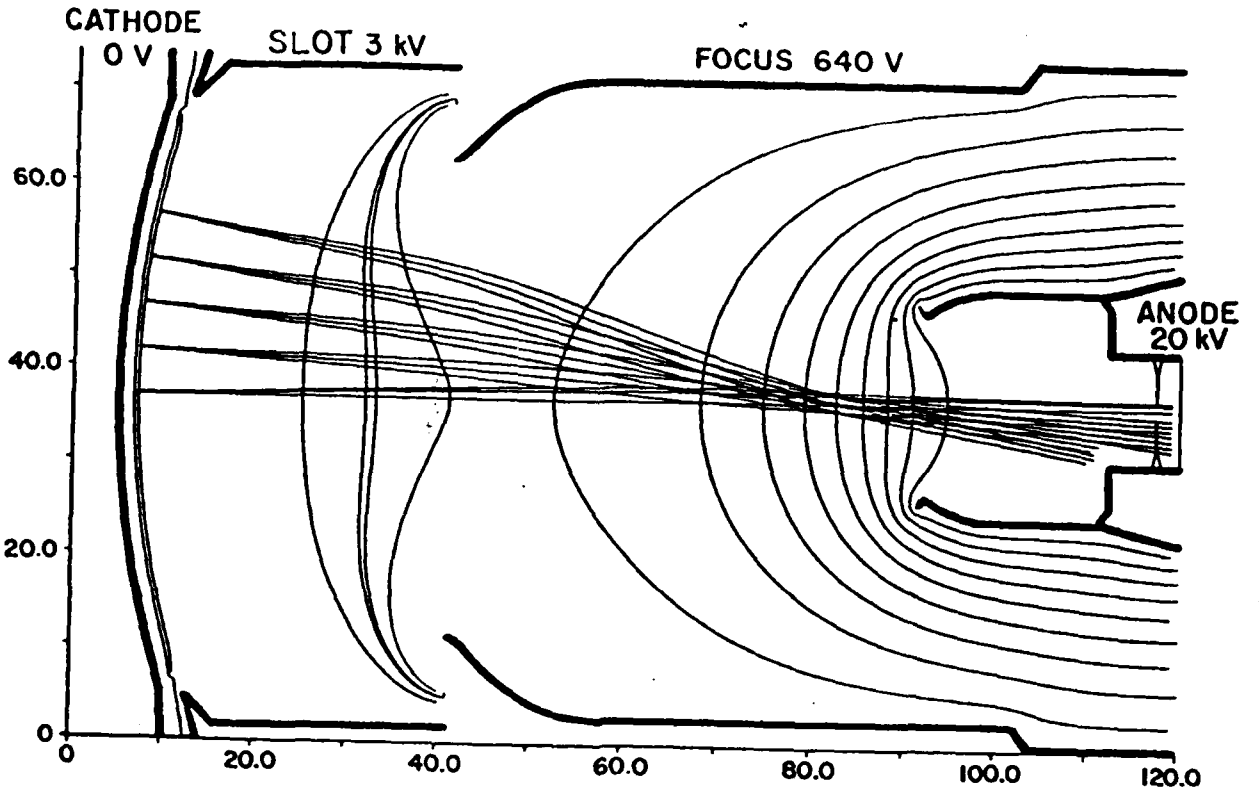

Figure 2a.

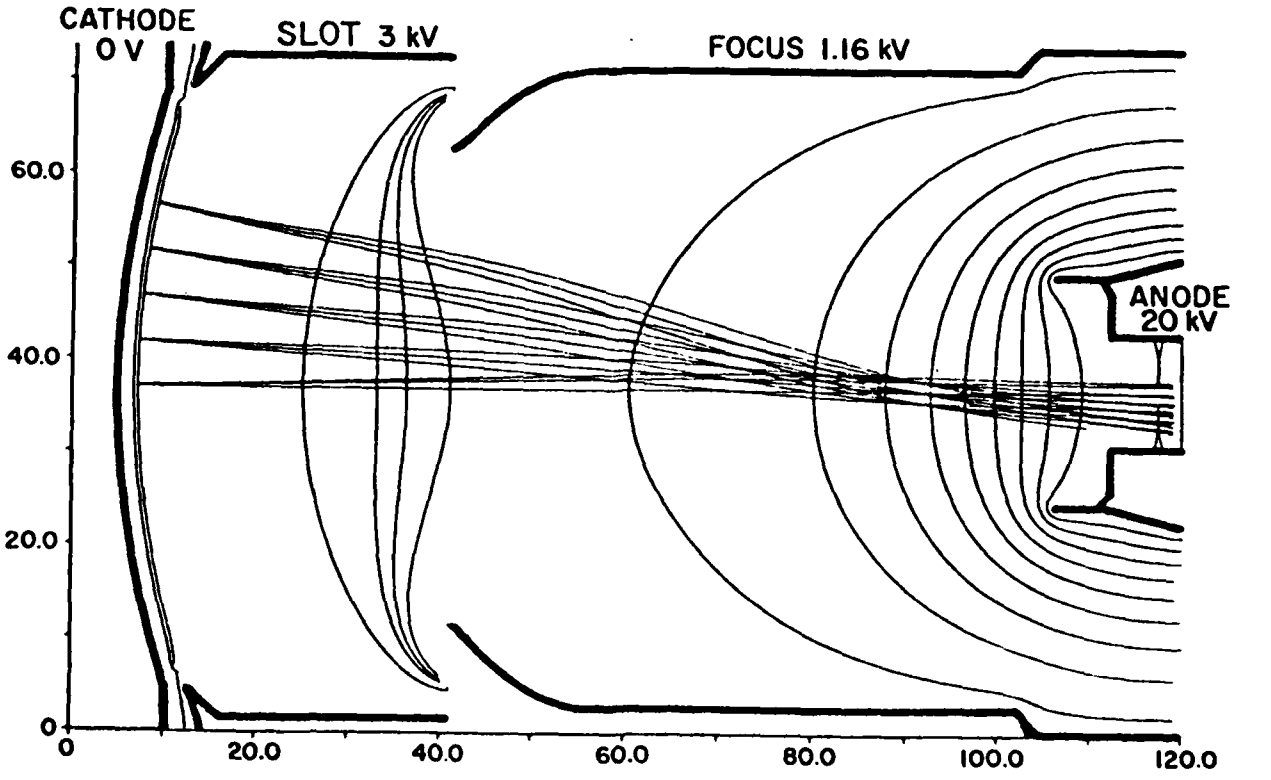

Figure 2b.

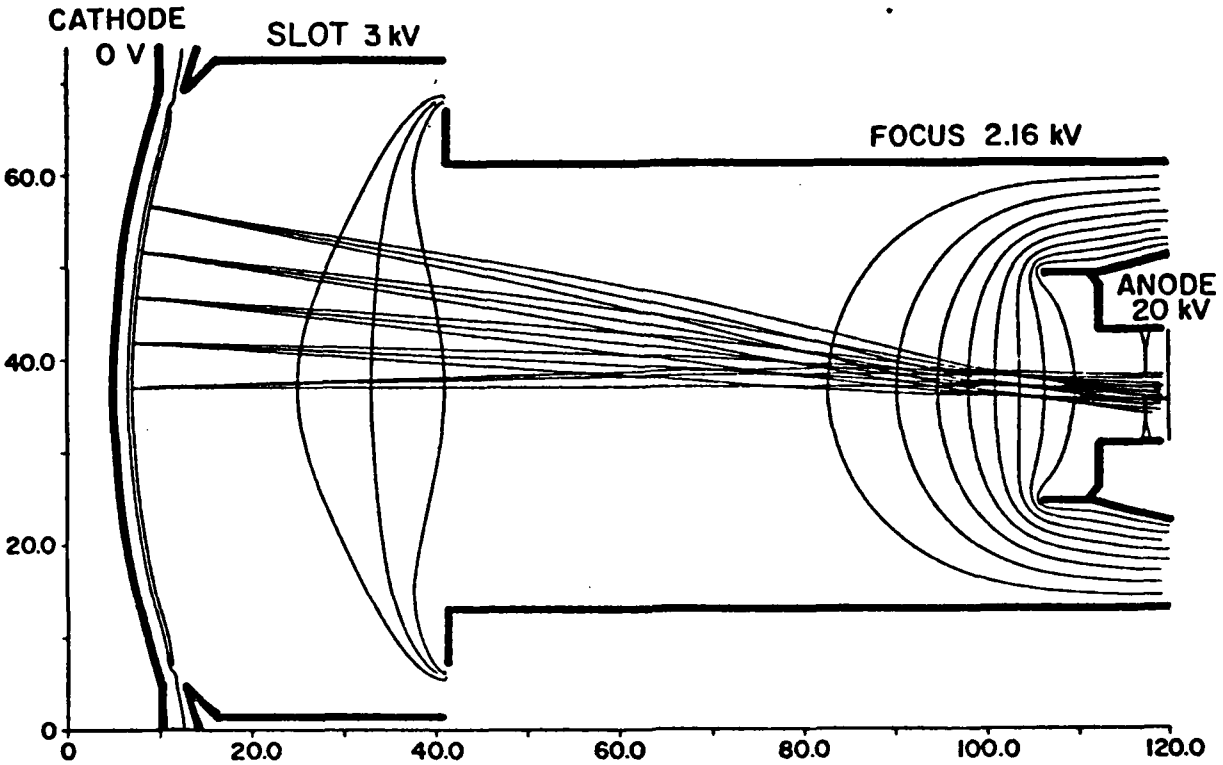

Figure 2c.

Figures 2a-2c. Photoelectron trajectory analysis of various streak tube designs. The scale is 1.0 mm. Equipotentials are drawn for every .1 V_{ANODE} and from z positions on-axis of 25, 33 and 41. Trajectories were calculated with transverse energies of -1, 0, +1 eV for positions 5, 10, 15 and 20 mm off-axis and 0, +1, +2 eV on-axis.

$$\Delta t_2 = k d_2 V_1^{-3/2} \varepsilon/4$$

$$\Delta t_3 = k d_3 (V_2 - V_1)^{-1} \varepsilon [V_1^{-\frac{1}{2}} - V_2^{-\frac{1}{2}}]/2$$

$$\Delta t_4 = k d_4 V_2^{-3/2} \varepsilon/4$$

where $k = (2m/e)^{\frac{1}{2}}$. The sum of all these contributions provide a more realistic estimate for the time resolution specification.

The time-of-flight dispersion for the tube design in Fig. 2c can be written as $\Delta t = 1.6\ \varepsilon^{\frac{1}{2}} + 0.7\ \varepsilon$ ps with ε in units of eV. This corresponds to a 6.0 ps time resolution for an x-ray streak camera with a Au photocathode, $\varepsilon \leq 4$ eV.

IV. STREAK TUBE TESTS

The streak tube as configured in Fig. 2C was built and assembled onto the back half of an RCA image tube. A stainless steel flange was welded to the central metal ring of the original tube. This flange was used to mount the new focus electrode which was held at ground potential and also to provide an O-ring surface for the vacuum seal. The accelerator electrode was attached to the focus electrode with a MACOR[19] ring. Static mode testing of the streak tube was performed using a 200 A Au on 25 μm Be photocathode and a Henke tube[20] with a Cu anode for the x-ray source. Actual static performance of the streak tube was very close to that predicted by the electron optics ray trace code. The focus voltage for optimum spatial resolution was within 20 V and the magnification was within 4%.

The astigmatism problem, focal position at the phosphor screen for optimum time resolution (narrowest slit image) being different than that

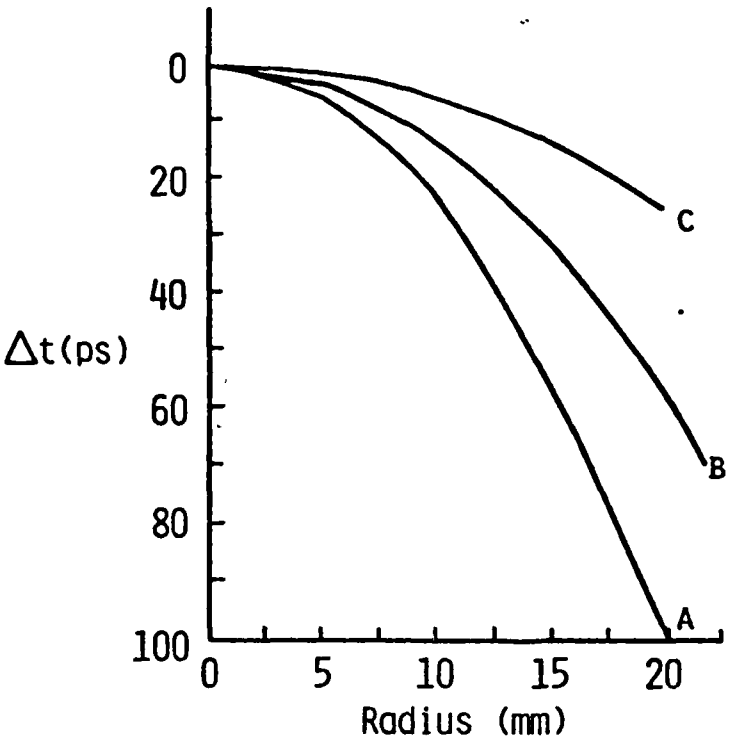

Figure 3. Transit time difference to the phosphor for electrons emitted from different positions on the photocathode(iso-chromism) for the tube designs in Fig. 2. No corrections for imaging onto a convex surface are included.

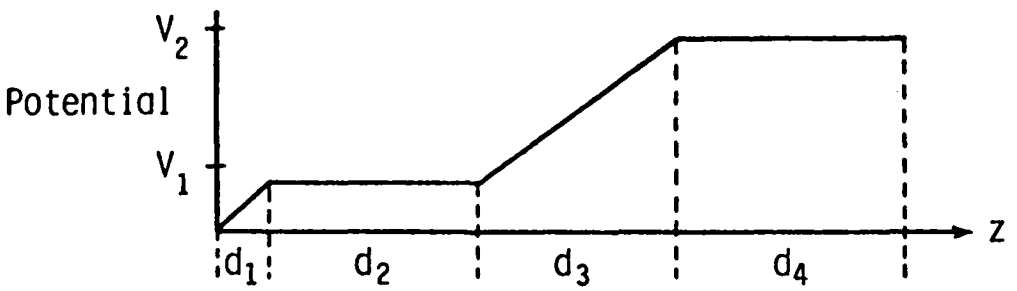

Figure 4. Simplified axial potential in the streak tube.

for best spatial resolution was very evident. The difference in focus electrode voltage for the two positions was 200 V, which corresponds to about 18 mm in image position at the screen. This error was corrected by contouring the end of the anode cone to form a double lipped tube lens,[12] (see Fig. 5). This type of lens is equivalent to two perpendicular cylindrical lenses, one positive and the other negative, thereby converging rays in one direction while diverging them in the other. The actual contouring required to correct the astigmatism was very small, the peak to valley dimension was .35 mm on a 25 mm diameter tube.

The potentials for best focus are summarized in Fig. 6. Note that the ratio V_{KF}/V_{KA} is approximately constant independent of the accelerating field 7 V_{KG}(V/cm), depending just upon the ratio of the diameter of the focus and anode electrodes. The magnification, cathode to phosphor increases with the accelerating field but decreases with increasing cathode to anode potential.

A 60 to 40 mm fiber optic taper and a 40 mm proximity focussed channel plate image intensifier were incorporated for conducting dynamic testing of the streak camera. The streaked images were recorded on either Polaroid or 35 mm negative film. The streak deflection circuit consisted of a double stack of 2N5551 transistors (seven per side) and LCR integrators were used to modify the streak speed.

In Fig. 7 we present a streak record of two 50 ps UV (λ = 266 nm) laser pulses separated by 900 ps. The laser pulses were generated by frequency quadrupling a single pulse from a mode-locked Nd:YAG laser and recombining the signals from a beam-splitter on the cathode with a fixed delay. A 200 A Au on 1000 A parylene transmission photocathode of dimensions 1 X 45 mm was used. Note that there is no streak curvature

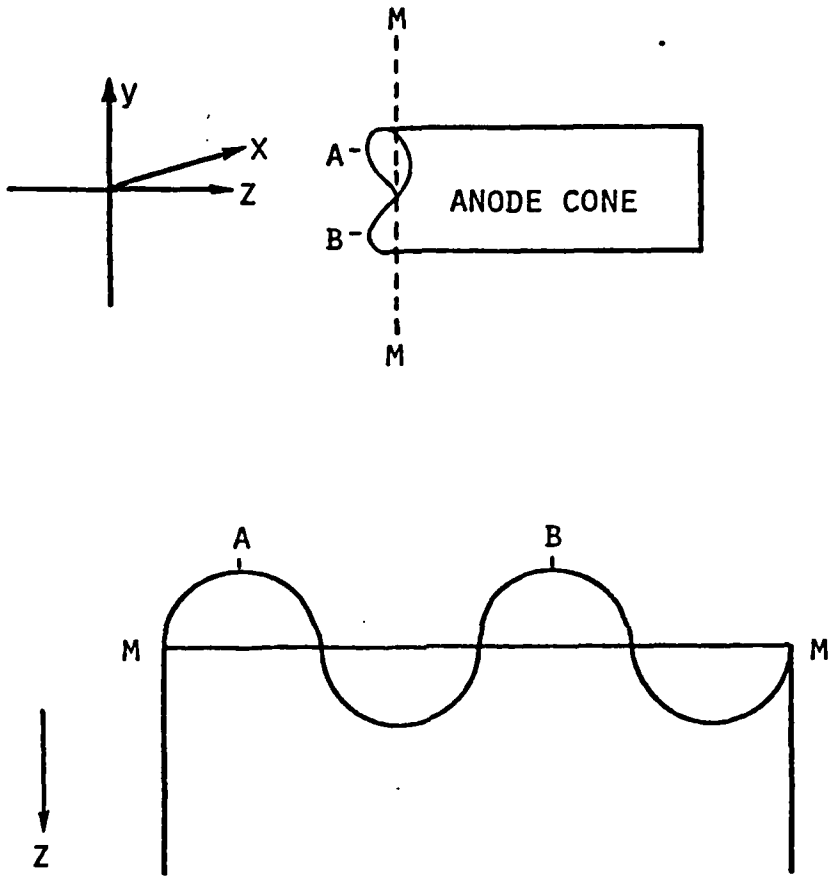

Figure 5. Schematic of the double lipped tube lens and its curved mid-surface that was used to correct the astigmatism.

evident in Fig. 7. This establishes an upper bound on the iso-chromism at 50 ps for a radial position of 22.5 mm in agreement with Fig. 3.

The primary application of this streak camera is time-resolved x-ray spectromety of laser fusion targets at the University of Rochester's OMEGA laser facility. In Fig. 8 we present a sample time-resolved x-ray spectrum. The target was a 225 μm diameter glass microballoon with a thin aluminum overcoat, illuminated uniformly with six UV (λ = 351 nm) beams at an intensity of 4 X 10^{14} W/cm^2. The x-ray spectrum was dispersed with an elliptical PET crystal analyzer and the streak camera had a 200 A Au photocathode on a 12.7 μm Be substrate. The H-like and He-like resonance lines of aluminum and silicon are well resolved.

Further characterization of the dynamic performance of this streak camera design will be reported in a subsequent paper. Of direct interest are the time and spatial resolution capabilities with various UV and x-ray sensitive photocathodes. Our estimates from the computer code for these quantities are 5-10 ps temporal resolution and 300-450 spatial resolution elements with either CsI or Au photocathode materials.

ACKNOWLEDGMENTS

We gratefully acknowledge the invaluable assistance of Priscilla Piano in the preparation of this report. This project is part of an overall program on Low-Energy X-Ray Physics and Technology supported by the Air Force Office of Scientific Research Grant No. 84-0001 and supplementally by the Department of Energy under Grant Nos. DE-AS08-83DP40181 (LANL/LLNL) and DE-AS08-82DP40175 (NLUF).

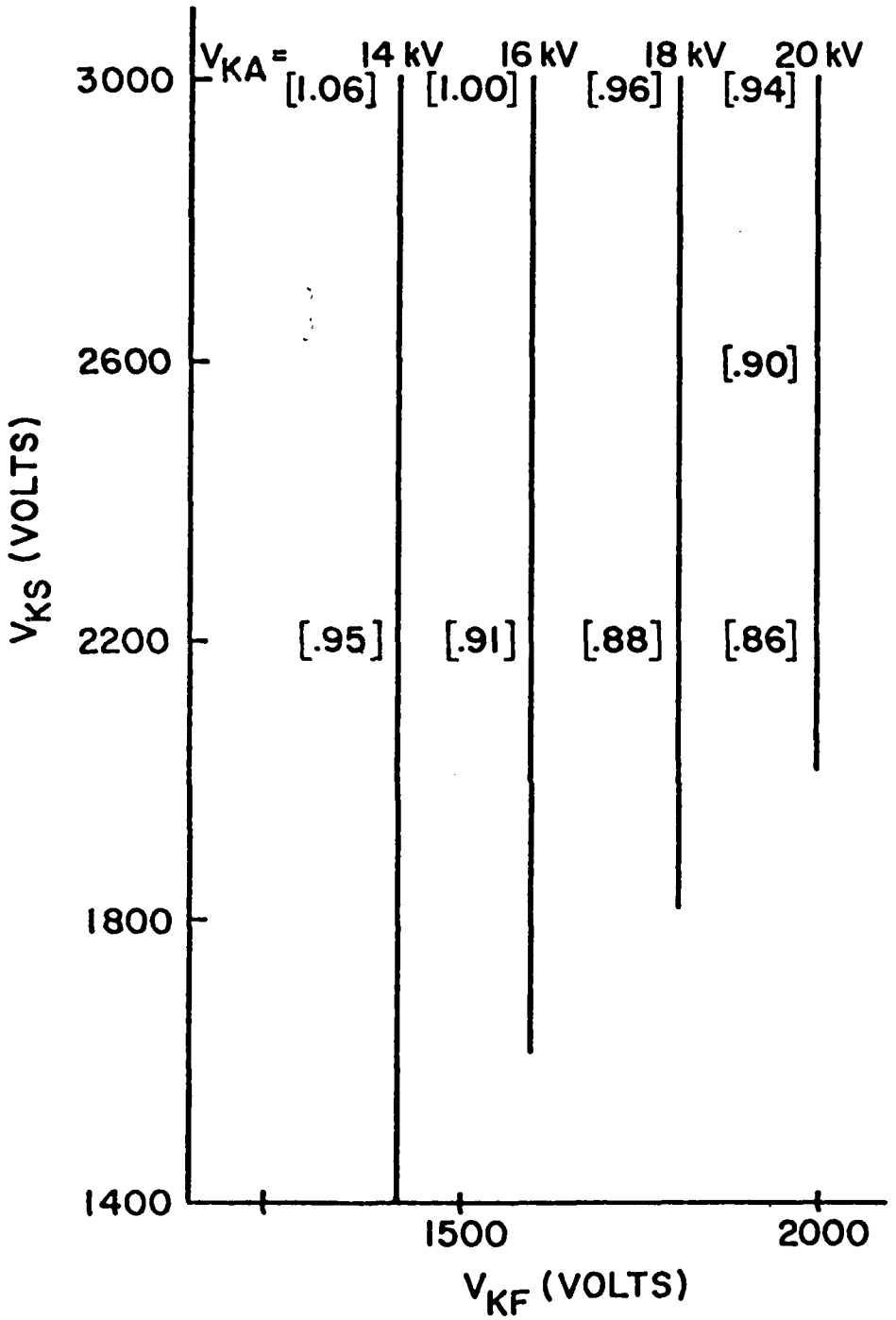

Figure 6. Electrode potentials for best focus imaging for streak tube design in Fig. 2c, V_{KS} V_{KF} and V_{KA} are the slot aperture, focus and anode electrode potentials with respect to the cathode, respectively. The streak tube electron-optical magnification is shown in square brackets at various potential configurations.

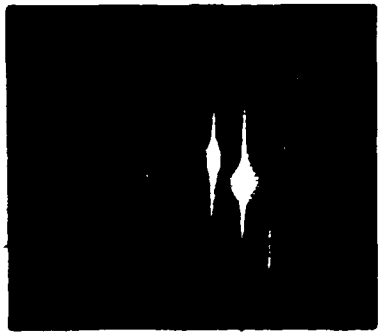

Figure 7. Streak record of two 50 ps UV laser pulses separated by 900 ps. The intensity blooming is caused by saturation of the Polaroid film. The third weak pulse at the bottom occurs on the retrace of the deflection ramps.

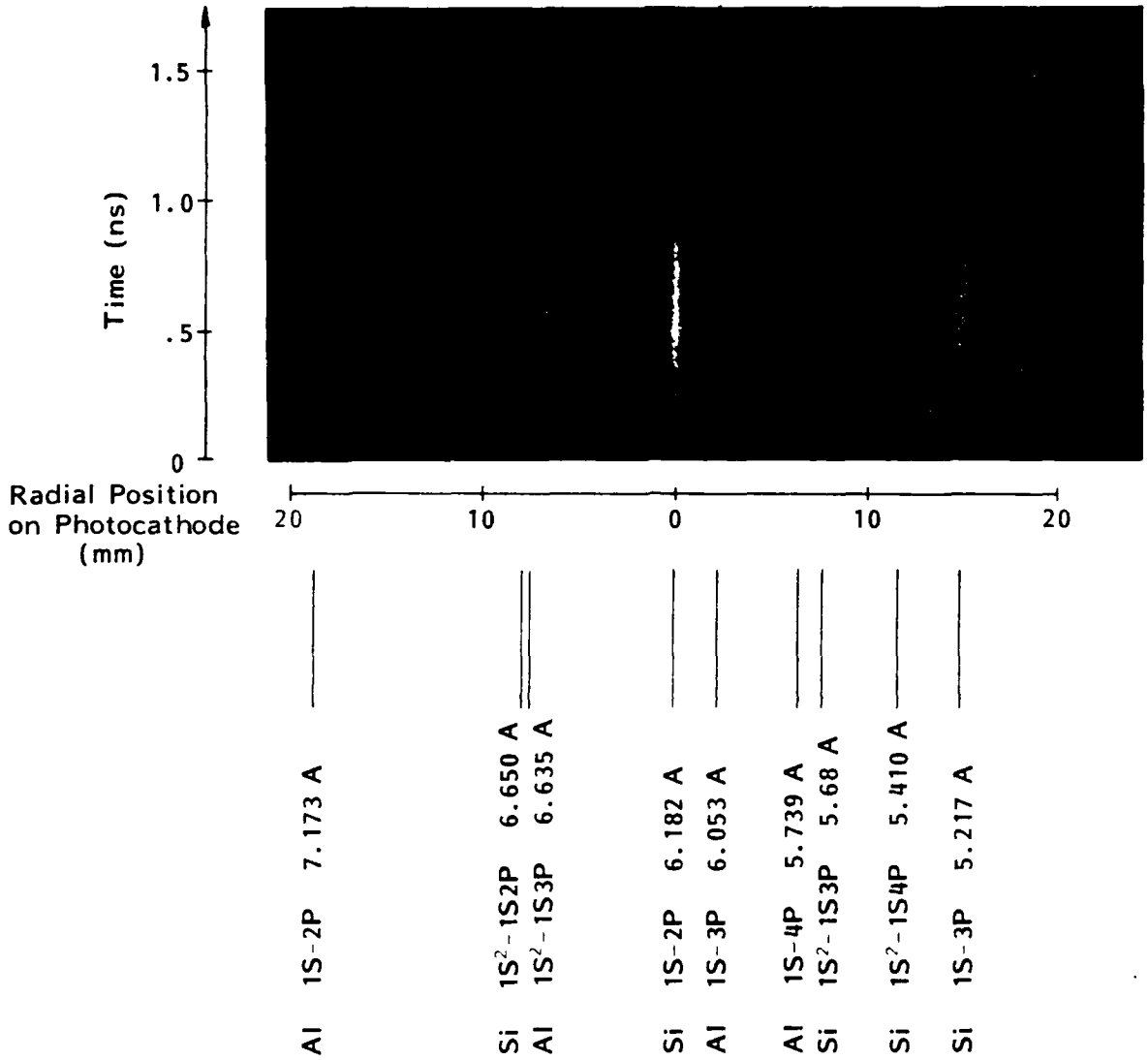

Figure 8. A sample time-resolved x-ray spectrum from an aluminum coated glass microballoon illuminated by the 6 UV beam OMEGA laser facility at the University of Rochester. The x-ray lines identified are clearly resolved on the original negative.

REFERENCES

1. A. J. Lieber, H. D. Sutphin, C. B. Webb, A. H. Williams, Electro Optical System Design, (Sept. 1976), p. 26.
2. H. Niu and W. Sibbett, Rev. Sci. Instrum. 52, 1830 (1981).
3. B. Boutry, C. Cavailler, N. Fleurot, SPIE 348, 766 (1983).
4. C. F. McConaghy and L. W. Coleman, Appl. Phys. Lett. 25, 268 (1974).
5. M. Ya Schelev, SPIE 189, 142 (1979).
6. S. Majumdar, P. A. Jaanimagi and M. C. Richardson, SPIE 189, 825 (1979).
7. N. H. Schiller, Y. Tsuchiya, E. Inuzuka, Y. Suzuki, K. Kinoshita, K. Kamiya, H. Lida, R. R. Alfano, Optical Spectra, (June 1980), p. 55.
8. Imacon 500 Streak Camera manufactured by Hadland Photonics, Ltd., England.
9. P. A. Jaanimagi and M. C. Richardson, Rev. Sci. Instrum. 54, 1095 (1983).
10. B. L. Henke, H. T. Yamada and T. J. Tanaka, Rev. Sci. Instrum. 54, 1311 (1983).
11. B. L. Henke and P. A. Jaanimagi, to be published.
12. O. Klemperer and M. E. Barnett, Electron Optics (Cambridge University Press, London, 1971), 3rd Ed.
13. W. B. Herrmannsfeldt, SLAC Report No. 166 (1973).
14. P. A. Jaanimagi, J. Comput. Phys., to be published.
15. C. F. Gerald, Applied Numerical Analysis (Addison-Wesley, Massachusetts, 1970).

16. R. G. Stoudenheimer and J. C. Moor, RCA Review 18, 322 (1957).

17. H. Niu, SPIE 348, 231 (1983).

18. S. W. Thomas and R. L. Peterson, SPIE 348, 190 (1983).

19. Machinable ceramic from Corning Glassworks, Corning, New York.

20. B. L. Henke, M. A. Tester, Advances in X-Ray Analysis (Plenum, New York, 1975), Vol. 18, p. 76.

Numerical Solution of Poisson's Equation

P. A. Jaanimagi*

Department of Physics and Astronomy
University of Hawaii
Honolulu, Hawaii 96822

ABSTRACT

A fourth-order finite difference formula for an iterative numerical solution of Poisson's equation in rectangular or cylindrical coordinates is described. The discretization is based upon a 9-point cross stencil for a nonequidistant numerical mesh spacing. These formulas can also be applied to handling irregular boundary conditions for problems using a regular square numerical mesh. The solution technique is the line-successive over-relaxation iterative method with red-black ordering.

---

* Current address: University of Rochester, Laboratory for Laser Energetics, 250 East River Road, Rochester, New York 14623.

I. INTRODUCTION

Numerical finite difference methods for calculating the electric potential in electrostatic lenses have been described by many authors.[1-10] In brief, the technique involved overlaying the area within a boundary with a set of numerical mesh points (typically configured as a regular square grid), replacing Poisson's equation with a finite difference formula, and performing an iterative relaxation calculation to solve for the potential at the mesh points. Generally, these methods have been used only for two-dimensional boundary value problems, in either Cartesian or circularly symmetric cylindrical coordinate systems.

Two of the main considerations for these numerical calculations are the computational time (i.e., the cost) required for the solution and the precision of the potential solution. The computational time is proportional to the square of the total number of mesh points in the problem, but it also depends on the convergence of the relaxation calculation. Successive-over-relaxation (SOR) [11-12] techniques have helped decrease costs immensely. The precision of the potential solution depends on the discretization error. The magnitude of this error is affected by many aspects of the problem. 1) The total number of mesh points since the error is proportional to some power of the mesh spacing. A rule of thumb is that the mesh spacing should be much less than the smallest dimension in the problem, whether this be an aperture size, an interelectrode distance, or the radius of curvature of a boundary. 2) The order of the finite difference formula for Poisson's equation; higher order schemes have smaller discretization errors. However, only second-order finite difference analogs are typically used to handle irregular

boundaries (not coincident with the mesh points). 3) Regions in the problem where the higher derivatives of the potential are large have correspondingly larger discretization errors.

In order to improve the precision of the potential solution, many authors have upgraded their programs by going from a second-order finite difference equation based on the standard 5-point stencil[1] to a higher order equation based on a 9-point stencil. The two forms of the 9-point stencil are the cross [5] and the square [6]; both generate a fourth-order finite difference equation when applied to regular square numerical mesh, and are equivalent in precision. As a single point algorithm the improvement in precision between a fourth- and a second-order difference equation can be two orders of magnitude. In an actual full test problem, however, this improvement is usually not realized. A degradation in precision stems from the lower order single point algorithms typically used at mesh points adjacent to an irregular boundary. The larger discretization error from these points propagates (although decreasing in magnitude) to the interior regions.

What is required to maintain good precision is a general set of finite difference equations of the highest order, configured on a rectangular numerical mesh of arbitrary spacing. Such a set of equations based on the 9-point square stencil has not been reported; also it would be very complex due to the many different ways for a boundary to intersect the stencil. [8] The problem is greatly simplified when based on the 9-point cross stencil. In the worst case the stencil is reduced to seven points, which generates a third-order finite difference equation.

Formulating a solution of Poisson's equation on a rectangular numerical mesh has the other advantage that with a judicious choice of

mesh spacing the total number of mesh points can be minimized. For a required precision one uses a high mesh density near boundaries, corners, apertures, etc., grading the mesh to larger spacings in regions of small gradients. Boundary configurations with large aspect ratios can be handled very neatly using graded meshes. The advantages of increasing the mesh density locally, while maintaining a regular square mesh has been demonstrated by Edwards [10] for the case of straight boundaries. But the programming to handle many of these regions (and to include irregular boundaries) in a general routine becomes overly complicated.

SINGLE-POINT ALGORITHMS

Poisson's equation is written as

$$\frac{\partial^2}{\partial y^2} + \frac{\partial^2}{\partial z^2} = -\frac{\rho}{\varepsilon_0} \tag{1}$$

in Cartesian coordinates and as

$$\begin{aligned} &\frac{1}{r}\ \frac{\partial V}{\partial r} + \frac{\partial^2 V}{\partial r^2} + \frac{\partial^2 V}{\partial z^2} = \frac{\rho}{\varepsilon_0} && \text{(off-axis)} \\ &2\ \frac{\partial^2 V}{\partial r^2} + \frac{\partial^2 V}{\partial z^2} = \frac{\rho}{\varepsilon_0} && \text{(on-axis)} \end{aligned} \tag{2}$$

in circularly symmetric cylindrical coordinates. To generate the finite difference analog to Poisson's equation using the 9-point cross stencil configured on a rectangular mesh of arbitrary spacing we start with the well-known general Lagrange interpolation formula.

$$f(x) = \sum_{i=0}^{n} \ell_i(x) f_i + R_n(x) \tag{3}$$

where

$$\ell_i(x) = \frac{(x-x_0)\cdots(x-x_{i-1})(x-x_{i+1})\cdots(x-x_n)}{(x_i-x_0)\cdots(x_i-x_{i-1})(x_i-x_{i+1})\cdots(x_i-x_n)}$$

and $R_n(x)$ is the remainder term. This formula is easily differentiated with respect to x to obtain formulas for the first and second derivatives. Then by equating x to z_0 and using the conventions outlined in Fig. 1, we may write the 4- and 5-point formulas for $f'(z_0)$ and $f''(z_0)$ as

4-point biased for positive z

$$f_0' = \frac{-s_2s_3f_1}{s_1(s_1+s_3)(s_1-s_2)} + \frac{s_1s_3f_2}{s_2(s_2+s_3)(s_1-s_2)} - \frac{[s_2s_3 - s_1(s_2-s_3)]f_0}{s_1s_2s_3} - \frac{s_1s_2f_3}{s_3(s_2+s_3)(s_1+s_3)} + \frac{s_1s_2s_3f_0^{iv}}{24} + \cdots \tag{4}$$

$$f_0'' = \frac{2}{(s_2+s_3)}\left\{\frac{-(s_2^2-s_3^2)f_1}{s_1(s_1+s_3)(s_1-s_2)} + \frac{(s_1-s_3)f_2}{s_2(s_1-s_2)} - \frac{(s_2+s_3)(s_1+s_2-s_3)f_0}{s_1s_2s_3} + \frac{(s_1+s_2)f_3}{s_3(s_1+s_3)}\right\} - \frac{[s_2s_3-s_1(s_2-s_3)]f_0^{iv}}{12} + \cdots \tag{5}$$

4-point biased for negative z

$$f_0' = \frac{s_3s_4f_2}{s_2(s_2+s_3)(s_2+s_4)} + \frac{[s_2s_3+s_4(s_2-s_3)]f_0}{s_2s_3s_4} + \frac{s_2s_4f_3}{s_3(s_2+s_3)(s_3-s_4)} - \frac{s_2s_3f_4}{s_4(s_2+s_4)(s_3-s_4)} - \frac{s_2s_3s_4f_0^{iv}}{24} - \cdots \tag{6}$$

$$f_0'' = \frac{2}{(s_2+s_3)}\left\{\frac{(s_3+s_4)f_2}{s_2(s_2+s_4)} + \frac{(s_2+s_3)(s_2-s_3-s_4)f_0}{s_2s_3s_4} + \frac{(s_2-s_4)f_3}{s_3(s_3-s_4)} - \frac{(s_2^2-s_3^2)f_4}{s_4(s_2+s_4)(s_3-s_4)}\right\} - \frac{[s_2s_3+s_4(s_2-s_3)]f_0^{iv}}{12} - \cdots \tag{7}$$

and the 5-point formulas.

$$f_0' = \frac{-s_2 s_3 s_4 f_1}{s_1(s_1+s_4)(s_1+s_3)(s_1-s_2)} + \frac{s_1 s_3 s_4 f_2}{s_2(s_2+s_3)(s_1-s_2)(s_2+s_4)} +$$

$$\frac{[s_2 s_3(s_1-s_4)+s_1 s_4(s_2-s_3)]f_0}{s_1 s_2 s_3 s_4} + \frac{s_1 s_2 s_4 f_3}{s_3(s_2+s_3)(s_1+s_3)(s_3-s_4)} - \qquad (8)$$

$$\frac{s_1 s_2 s_3 f_4}{s_4(s_1+s_4)(s_2+s_4)(s_3-s_4)} + \frac{s_1 s_2 s_3 s_4 f_0^{v}}{120} + \ldots$$

$$f_0'' = \frac{-2[s_2 s_3+s_4(s_2-s_3)]f_1}{s_1(s_1+s_4)(s_1+s_3)(s_1-s_2)} + \frac{2[s_1 s_4+s_3(s_1-s_4)]f_2}{s_2(s_2+s_3)(s_1-s_2)(s_2+s_4)} -$$

$$\frac{2[s_2 s_3-(s_2-s_3)(s_1-s_4)+s_1 s_4]f_0}{s_1 s_2 s_3 s_4} + \frac{2[s_2(s_1-s_4)-s_1 s_4]f_3}{s_3(s_2+s_3)(s_1+s_3)(s_3-s_4)} + \qquad (9)$$

$$\frac{2[s_2 s_3-s_1(s_2-s_3)]f_4}{s_4(s_1+s_4)(s_2+s_4)(s_3-s_4)} + \frac{[s_2 s_3(s_1-s_4)+s_1 s_4(s_2-s_3]f_0^{v}}{60} + \ldots$$

Eqs. (8) and (9) reduce to the familiar 5-point formulas with equally spaced abscissas when $s_2 = s_3 = h$ and $s_1 = s_4 = 2h$.

$$f_0' = \frac{1}{12h}\left\{-f_1 + 8f_2 - 8f_3 + f_4\right\} + \frac{h^4 f_0^{v}}{30} + \ldots \qquad (10)$$

$$f_0'' = \frac{1}{12h^2}\left\{-f_1 + 16f_2 - 30f_0 + 16f_3 - f_4\right\} + \frac{h^4 f^{vi}}{90} . \qquad (11)$$

The standard 5- or 9-point cross stencil finite difference equations are obtained by substituting the appropriate formulas for the derivatives Eqs. (3)-(11) into Poisson's equation, Eq. (1) or (2). We assume that the space charge term $-\rho/\varepsilon_0$ doesn't change much over a mesh unit.

For the case of vertical or horizontal boundaries where the first derivative of the potential is defined to be zero, the mesh points inside the boundary are mirrored in the plane of the boundary to obtai

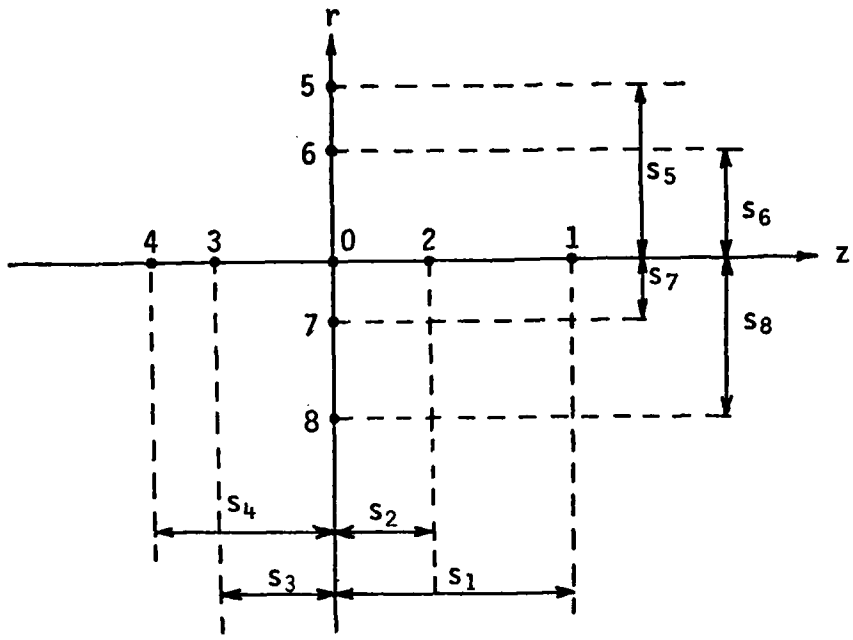

Fig. 1. Convention for numbering the mesh points for the 9-point cross stencil. The mesh point spacings, s_i, are positive in magnitude.

the complete 9-point stencil. For example, in the 5-point formulas at $r = 1$, which span the $r = 0$ axis, we equate $f_8 = f_0$ and $s_8 = 2s_7$.

A better difference equation can be derived for application to problems with circular symmetry in cylindrical coordinates. Following the formalism of Weber [3] which is essentially the same as that presented by Edwards [10]), we may write to fourth-order precision the potential at (r,z) which is a solution of Poisson's equation as

$$V(r,z) = V_0 + r_0 \ell n \frac{r}{r_0} V^{(1,0)} + \left\{\frac{r_0^2}{2} \ell n \frac{r}{r_0} - \frac{r_0(r-r_0)}{2} - \frac{(r-r_0)^2}{4}\right\}\left\{\frac{\rho}{\epsilon_0} + V^{(0,2)} + (z-z_0)V_0^{(0,3)} + \left(\frac{(z-z_0)^2}{2} - \frac{(r-r_0)^2}{12}\right)V_0^{(0,4)}\right\} + (z-z_0)V_0^{(0,1)} + \frac{(z-z_0)^2}{2} V_0^{(0,2)} + \frac{(z-z_0)^3}{6} V_0^{(0,3)} + \frac{(z-z_0)^4}{24} V_0^{(0,4)} - \left(\frac{(r-r_0)^2}{6} r_0 \ell n \frac{r}{r_0}\right) V_0^{(1,1)} + (z-z_0)\ell n \frac{r}{r_0} \{\text{other terms}\} \qquad (12)$$

where

$$V_0^{(i,j)} = \left(\frac{\partial^{i+j} V}{\partial r^i \partial z^j}\right)_{(r_0,z_0)} .$$

The difference equation is obtained by evaluating Eq. (12) at points 1 to 8 in Fig. 1 and solving for V by eliminating the derivative terms. We also use the expansion $(\ell n \frac{r}{r_0})^{-1} = (\ell n(1 \pm \frac{s}{r_0}))^{-1} = \pm (\frac{r_0}{s})(1 \pm \frac{s}{2r_0} - \frac{s^2}{12r_0^2} \pm \ldots)$. The off-axis formulas are

$$\frac{-2\, V_5(s_6-s_7)}{s_5(s_5-s_6)(s_5+s_7)}\left[1 + \frac{s_5}{2R} - \frac{s_5^2}{12R^2}\right] + \frac{2V_6(s_5-s_7)}{s_6(s_6+s_7)(s_5-s_6)}\left[1 + \frac{s_6}{2R} - \frac{s_6^2}{12R^2}\right] + \frac{2V_7(s_5+s_6)}{s_7(s_6+s_7)(s_5+s_7)}\left[1 - \frac{s_7}{2R} - \frac{s_7^2}{12R^2}\right] - P_0 V_0 + V^{(0,2)} = \frac{-\rho}{\epsilon_0} \qquad (13)$$

$$\frac{2V_6(s_7+s_8)}{s_6(s_6+s_7)(s_6+s_8)}\left[1+\frac{s_6}{2R}-\frac{s_6^2}{12R^2}\right]+\frac{2V_7(s_6-s_8)}{s_7(s_6+s_7)(s_7-s_8)}\left[1-\frac{s_7}{2R}-\frac{s_7^2}{12R^2}\right]-$$

$$\frac{2V_8(s_6-s_7)}{s_8(s_6+s_8)(s_7-s_8)}\left[1-\frac{s_8}{2R}-\frac{s_8^2}{12R^2}\right]-P_0V_0+V^{(0,2)}=\frac{-\rho}{\varepsilon_0} \qquad (14)$$

$$\frac{-2V_5[s_8(s_6-s_7)+s_6s_7]}{s_5(s_5-s_6)(s_5+s_7)(s_5+s_8)}\left[1+\frac{s_5}{2R}-\frac{s_5^2}{12R^2}\right]+\frac{2V_6[s_5s_8+s_7(s_5-s_8)]}{s_6(s_6+s_7)(s_5-s_6)(s_6+s_8)}$$

$$\left[1+\frac{s_6}{2R}-\frac{s_6^2}{12R^2}\right]+\frac{2V_7[s_6(s_5-s_8)-s_5s_8]}{s_7(s_6+s_7)(s_5+s_7)(s_7-s_8)}\left[1-\frac{s_7}{2R}-\frac{s_7^2}{12R^2}\right]-$$

$$\frac{2V_8[s_5(s_6-s_7)-s_6s_7]}{s_8(s_5+s_8)(s_6+s_8)(s_7-s_8)}\left[1-\frac{s_8}{2R}-\frac{s_8^2}{12R^2}\right]-P_0V_0+V^{(0,2)}=\frac{-\rho}{\varepsilon_0} \qquad (15)$$

for 4-point bias, 4-point negative bias and 5-point in the r direction, respectively. And on axis as

$$\frac{-4s_6^2V_5}{s_5^2(s_5^2-s_6^2)}+\frac{4s_5^2V_6}{s_6^2(s_5^2-s_6^2)}-P_0V_0+V^{(0,2)}=\frac{-\rho}{\varepsilon_0}\,. \qquad (16)$$

The appropriate formula, Eq. 5, 7, or 9 is substituted for $V^{(0,2)}$. In Eqs. (13)-(16), the coefficient of V_0 is the sum of the coefficients of the other potentials.

$P_0 = \sum_{i=1}^{8} P_i$, where the difference equation is written as

$$\sum_{i=1}^{8} P_iV_i - P_0V_0 = \frac{-\rho}{\varepsilon_0}\,. \qquad (17)$$

For the case of a rectangular mesh of unit h, the terms in $\frac{s_i^2}{12R^2}$ are dropped if $s_5 = 2h$ in Eq. (13), $s_8 = 2h$ in Eq. (14), $s_5 = s_8 = 2h$ in Eq. (15) resulting in the standard 9-point cross formulas.

II. SOLUTION TECHNIQUES

A block iterative technique [2,12] is used to solve the set of single point algorithms for the potential solution. The line SOR formula described below is quite efficient and easy to implement. An examination of Eqs. (13)-(16) shows that the set of difference equations for a vertical column of mesh points in the problem can be written as a pentadiagonal matrix equation.

$$\begin{bmatrix} c_1 & d_1 & e_1 & & & 0 \\ b_2 & & & & & \\ a_3 & & & & & \\ & & & & & e_{n-2} \\ & & & & & d_{n-1} \\ 0 & & & & a_n & b_n & c_n \end{bmatrix} \begin{bmatrix} u_1 \\ \vdots \\ u_n \end{bmatrix} = \begin{bmatrix} k_1 \\ \vdots \\ k_n \end{bmatrix} \tag{18}$$

where $-a_i$, $-b_i$, c_i, $-d_i$, $-e_i$ are the coefficient P_i of V_5, V_6, V_0, V_7, V_8, respectively, and $k_i = \rho/\epsilon_0 + \sum_{j=1}^{4} P_j V_j$. The algorithm for solution is as follows

$$v_1 = \frac{d_1}{c_1}, \quad w_1 = \frac{e_1}{c_1}, \quad g_1 = \frac{k_1}{c_1},$$

$$q_2 = c_2 - b_2 v_1 \qquad v_2 = \frac{d_2 - b_2 w_1}{q_2}, \quad w_2 = \frac{e_2}{q_2} \qquad g_2 = \frac{k_2 - b_2 g_1}{q_2}$$

$$t_i = b_i - a_i v_{i-2}, \quad q_i = c_i - a_i w_{i-2} - t_i v_{i-1}, \quad v_i = \frac{d_i - t_i w_{i-1}}{q_i}$$

$$w_i = \frac{e_i}{q_i}, \quad g_i = \frac{k_i - a_i g_{i-2} - t_i g_{i-1}}{q_i}, \quad 3 \le i \le n$$

with back substitution as

$$u_n = g_n, \quad u_{n-1} = g_{n-1} - v_{n-1} u_n, \quad u_i = g_i - v_i u_{i+1} - w_i u_{i+2}, \quad 1 \le i \le n-2$$

Note that for the top and bottom of the column the boundary values are known and fixed, and terms such as $b_1 V_{Boundary}$ are added to k_1.

The old values of the potential in a column are replaced as

$$V_0^{(n+1)} = V_0^{(n)} + W^{(n)}(u_0^{(n+1)} - V_0^{(n)}) ,$$

where W is an over-relaxation factor with values $1. \leq W < 2$, and n is the iteration count. Optimization of this over-relaxation factor has been discussed by many authors.[6,11,12]

An additional feature of the iterative solution to Poisson's equation is red-black ordering, [12] where two passes are made through the potential distribution per iteration. First the odd numbered columns are solved and new potential values substituted, then the even numbered columns are solved. This aids in speeding up the convergence of the solution.

No proof is offered for the convergence of the potential solution using this relaxation techniques on a rectangular mesh of arbitrary spacing. It has been noted on some test problems, however, that if the mesh spacing is graded gradually, such that the absolute value of the ratio of any two of the coefficients P_i in Eq. 17 remains below ~150, the solution converges quickly and smoothly.

III. TEST PROBLEMS

Two test problems are given to illustrate the application of these formulas for solving Laplace's equation. For simplicity we use a regular square mesh to solve for the potential between two infinitely long coaxial cylinders, but impose irregular boundaries in the r-direction. In Tables 1 and 2 are a comparison of the solutions obtained using a 5-point cross stencil, the standard 9-point cross stencil and the 9-point cross stencil outlined in Eqs. (13)-(16).

AD-A149 983 DEVELOPMENT AND APPLICATION OF LOW ENERGY X-RAY AND ELECTRON PHYSICS(U) HAWAII UNIV HONOLULU DEPT OF PHYSICS AND ASTRONOMY B L HENKE 06 DEC 84 2/3

UNCLASSIFIED AFOSR-TR-84-1270 AFOSR-84-0001 F/G 14/5 NL

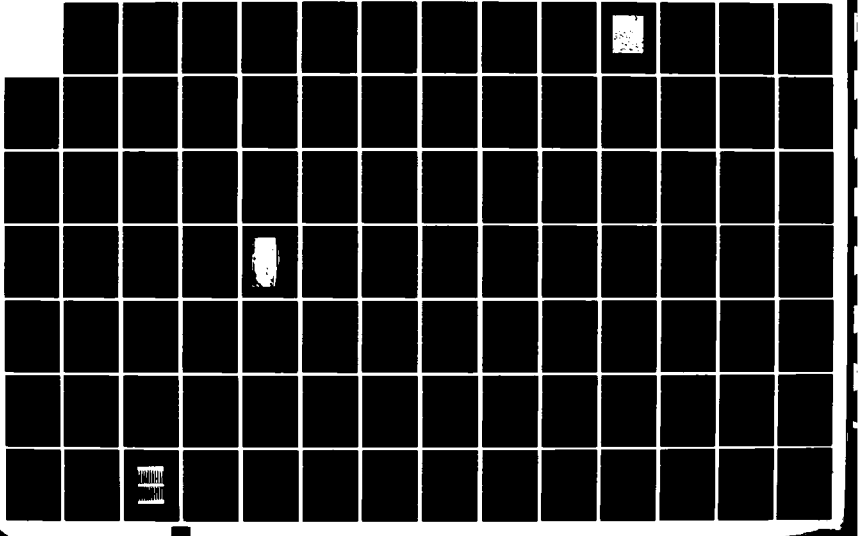

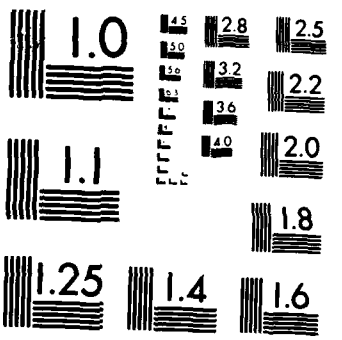

The problem for Table I has the boundary conditions $V(0.5) = 0$ and $V(10.5) = 100$ with the analytic solution $V(r) = 100\ \ell n2r/\ell n21$. The precision of the solution is not very good. The main difficulty here is that the mesh spacing is only twice the smallest dimension in the problem. In Table II we have increased the diameter of both cylinders and achieved a marked improvement in the precision of the solution. Case 2 has boundary conditions $V(9.5) = 0$ and $V(18.5) = 100$ with the solution $V(r) = 100\ \ell n(r/9.5)/\ell n(18.5/9.5)$.

In both cases the 9-point cross stencil described in this paper is the most precise. Note also the improvement in going from a 5-point to a 9-point stencil. Also for these simple problems the line-SOR technique of solution gives the final result on the first iteration.

IV. SUMMARY

We have derived the finite difference equations for a solution of Poisson's equation using a rectangular numerical mesh of arbitrary spacing. These formulas permit the use of a graded mesh to minimize the total number of points required in the problem as well as improved handling of irregular boundaries. With graded meshes problems requiring full three-dimensional treatment become solvable since the total number of mesh points can be kept to reasonable levels. The line-successive-over-relaxation algorithm outlined in this paper provides a fast and efficient convergence for the iterative solution.

TABLE I

r	V(r)	5-pt Std.	9-pt Std.	9-pt (this paper)
10.5	100.000	100.000	100.000	100.000
10	98.397	98.448	98.418	98.405
9	94.937	95.105	95.002	94.959
8	91.068	91.368	91.183	91.108
7	86.682	87.134	86.853	86.741
6	81.619	82.248	81.854	81.700
5	75.630	76.474	75.941	75.738
4	68.301	69.416	68.702	68.438
3	58.852	60.342	59.360	59.018
2	45.534	47.638	46.142	45.687
11	22.767	26.466	23.386	22.712
0.5	0.0	0.0	0.0	0.0

TABLE II

r	V(r)	5-pt Std.	9-pt Std.	9-pt (this paper)
18.5	100.0000	100.0000	100.0000	100.0000
18	95.8890	95.8857	95.8892	95.8890
17	87.3128	87.3094	87.3132	87.3129
16	78.2166	78.2134	78.2170	78.2167
15	68.5331	68.5305	68.5337	68.5332
14	58.1812	58.1799	58.1819	58.1814
13	47.0619	47.0625	47.0627	47.0621
12	35.0521	35.0557	35.0530	35.0523
11	21.9967	22.0049	21.9977	21.9969
10	7.6962	7.7111	7.6971	7.6963
9.5	0.0	0.0	0.0	0.0

ACKNOWLEDGEMENTS

This research has been supported by DOE/NLUF Contract No. DE-AS08-82DP40175 and is part of an on-going program on Low-Energy X-Ray Physics and Technology at the University of Hawaii supported by Air Force Office of Scientific Research Grant No. 84-0001 and supplementally by the Department of Energy under Contract No. DE-AS08-83DP40181.

REFERENCES

1. G. Shortley, P. Darby, E. H. Gamble, J. Appl. Phys. 18 (1947), 116.
2. P. H. Rose, A. Galejs, L. Peck, Nucl. Instrum. Methods 31 (1964), 262.
3. A. Septier, "Focusing of Charged Particles" Academic Press, New York, 1967, see Ch. 1.2 by C. Weber in Vol. I.
4. G. Birkhoff, "Numerical Analysis of Elliptic Equations," Society of for Industrial and Applied Mathematics, Philadelphia, Pennsylvania (1971).
5. S. Natali, D. DiChio, C. E. Kuyatt, J. Research National Bureau of Standards 76A (1972), 17.
6. E. Kasper, Optic 46 (1976), 27.
7. A. Skollermo, G. Skollermo, J. Computational Phys. 28 (1978), 103.
8. E. Kasper in "Magnetic Electron Lenses," Topics in Current Physics (Springer, Berlin/Heidelberg/New York, 1982), Vol. 18, Ch. 2, P. W. Hawkes, ed.
9. A. Skollermo, J. Computational Phys. 47 (1982), 160.
10. D. Edwards, Jr., Rev. Sci. Instrum. 54 (1983), 1729.
11. B. A. Carre, Computer J. 4 (1963), 73.
12. L. A. Hageman and D. M. Young, "Applied Iterative Methods," Academic Press, New York, 1981.

Low-energy x-ray response of photographic films: part I. mathematical models.

B.L. Henke, S. L. Kwok, J. Y. Uejio,
H. T. Yamada and G. C. Young

University of Hawaii
Honolulu, Hawaii 96822

ABSTRACT

Relatively simple mathematical models are developed for optical density as a function of the x-ray intensity, its angle of incidence and photon energy in the 100-10,000 eV region for monolayer and emulsion types of photographic films. Semi-empirical relations have been applied to characterize a monolayer film, Kodak 101-07, and an emulsion type film, Kodak RAR 2497, which fit calibration data at nine photon energies well within typical experimental error.

I. INTRODUCTION

Photographic film is used extensively as the time-integrating, position-sensitive detector for x-ray spectrometry of pulsed, high temperature plasma sources.[1] These sources include the inertially and magnetically confined plasmas studied in fusion energy research, and others such as the Z-pinch, the exploding wire and imploding linear plasma sources. Photographic detection is often chosen for the fixed analyzer spectroscopy of such sources because of its relatively high sensitivity, wide latitude of response and simplicity of implementation as compared with the alternative position-sensitive electronic detection array systems.

For the diagnostics of high temperature plasma sources there is considerable need for well calibrated, absolute spectrometry. The spectral analysis that is required demands a precise knowledge of peak-and-integrated intensities and shapes of spectral lines and of the intensity distributions in continua. Such information can be deduced from the measured optical density vs position along the film and its quantitative relationship to the incident intensity for a given photographic emulsion of appropriate sensitivity and resolution.

Because the optical density is a function of not

only the intensity of the x-radiation but also of its angle of incidence and of its photon energy, it is important to supplement experimental calibration with theoretical modeling. Semi-empirical, "universal" mathematical relations may then be established which yield detailed photometric information (including the effects of x-ray absorption edge structure) as based upon a minimum set of experimental data. An optimum design for the experimental calibration may be effectively guided by these model relations.

In this Part I of the present work, we develop relatively simple mathematical models for the photographic response of monolayer and thick and thin emulsion films for the low-energy x-ray region of 100-10,000 eV. Their validity is established by applying them to the description of two examples of photographic films, Kodak 101-07, a monolayer, and Kodak RAR 2497, an emulsion-type system.

II. SIMPLE MODELS FOR THE PHOTOGRAPHIC X-RAY RESPONSE

A. The Monolayer Model

In Fig. 1 is depicted a photographic film for which the sensitive region is essentially a monolayer of densely packed AgBr grains of average film thickness, t_1, and with a packing density of M_0 (AgBr grains per unit area).

MONOLAYER MODEL

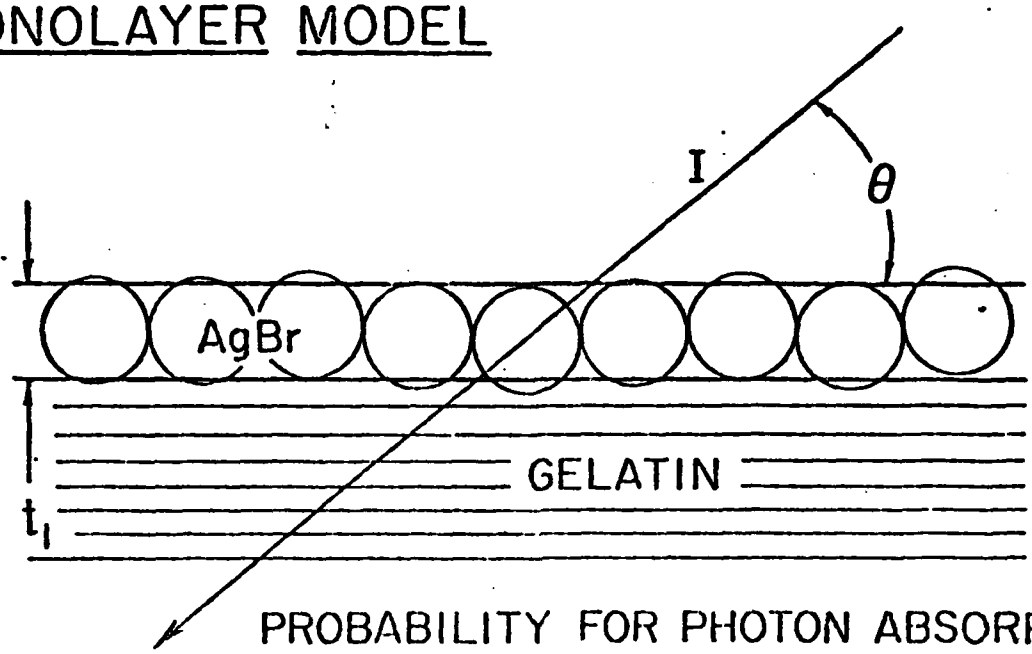

PROBABILITY FOR PHOTON ABSORPTION WITHIN AgBr GRAIN

$$= I[\sin\theta(1-\exp(-\mu_1 t_1/\sin\theta))]/M_0$$

Figure 1. Monolayer model for an effective film thickness, t_1, of M_0, densely packed, nearly spherical AgBr grains per unit area, and of linear x-ray absorption coefficient equal to μ_1 (for AgBr).

A scanning electron microscope photograph of this type of film (Kodak 101-07) is shown in Fig. 2. As suggested by this photograph, the grains may be considered as being nearly spherical with a mean diameter of about one μm.

The probability that a AgBr grain will absorb a photon under an exposing radiation intensity, I (photons/μm^2), of photon energy E(eV), and at an angle of incidence, θ, is simply the total number of photons absorbed per unit area within the monolayer divided by the number of grains per unit area, M_0, viz.,

$$\frac{I\sin\theta(1 - \exp(-\mu_1 \frac{t_1}{\sin\theta}))}{M_0},$$

where μ_1 is the linear x-ray absorption coefficient of AgBr (which parameter introduces the only dependence upon photon energy, E). For the low-energy x-ray region of interest here (100-10,000 eV), it may be assumed that the absorption of a single photon is sufficient to render the AgBr grain developable and therefore any additional absorption events within that grain cannot contribute to its effective exposure process.[2] We may therefore write the differential equation that determines the increase in the number of grains per unit area, dM, that have been rendered developable when the radiation intensity is increased by an amount dI by equating dM to the number of grains within the layer as yet not rendered developable, viz., M_0-M, multiplied by the probability of a photon being absorbed within a given grain for an increment of

Figure 2. Scanning electron microscope photograph of the Kodak 101-07 film showing nearly spherical AgBr grains of about one micron average diameter.

intensity, dI. Hence

$$dM = (M_0 - M)\left(\frac{\sin\theta(1 - \exp(-\mu_1 \frac{t_1}{\sin\theta}))}{M_0}\right)dI. \qquad (1)$$

This may be immediately integrated to yield the number of grains per unit area, M, rendered developable under a total exposure of incident beam of intensity, I photons per unit area at incident angle, θ, obtaining

$$M = M_0\left[1 - \exp(-\sigma\sin\theta(1 - e^{-\mu_1 \frac{t_1}{\sin\theta}})I)\right]. \qquad (2)$$

Here we have substituted for $(M_0)^{-1}$ in the argument of the exponential an effective average cross sectional area of the AgBr grain, σ.

In the development process, the exposed grain is reduced chemically to a cluster of silver usually of somewhat increased cross sectional area which we shall define here as S. This silver cluster strongly absorbs and scatters the light beam in a densitometer measurement of the exposed grain density.

In microdensitometry, as required for the quantitative analysis of spectroscopic line images, a relatively small angle cone of illuminating light is focussed and transmitted at a small optically defined "slit" region area of the film and the transmitted beam is received by a nearly matched, small-angle acceptance aperture of an objective lens, imaged at a fixed slit, and then delivered to a photocell. We designate by i_0 the photo-

cell current that is measured for the transmitted rays that pass through an unexposed section of the film and by i that for the same small angle light cone system passing through a similar section of an exposed region of the film having M silver cluster grains per unit area. We may relate the fraction transmitted, τ, (i.e., i/i_0) to the grain density, M, using the fraction of the area that is "blocked" by the silver grains, MS, obtaining

$$\tau = i/i_0 = 1 - MS. \qquad (3)$$

Rather than using the transmission, τ, this measurement is conventionally expressed using an alternative variable, the optical density, D, which is defined as the log-to-base-ten of the reciprocal of the transmission, τ. Thus

$$D = \log_{10}(1/\tau) = -\log_{10}(1 - MS)$$

And

$$D = -\log_{10}\{1 - M_0S(1 - \exp[-\sigma\sin\theta(1 - \exp(-\frac{\mu_1 t_1}{\sin\theta}))I])\}. \qquad (4)$$

For usual spectroscopic exposures on the monolayer films it is expected that the value of MS be small as compared with unity and consequently Eq. (4) may be simplified to obtain

$$D = \frac{M_0S}{2.30}(1 - \exp\{-\sigma\sin\theta[1 - \exp(-\mu_1 t_1/\sin\theta)]I\}). \qquad (5)$$

(In the density measurement defined here using illumination and objective lenses of small and nearly matched

numerical apertures, D is essentially specular density. This optical density may be related to the smaller value, diffuse density, that is measured when all of the forward scattered light in the transmitted beam is included in the measurement. The relationship between specular and diffuse density will be discussed in Part II of this work.)

An important implication of this analysis in deriving Eq. (4) is that the monolayer film density, D, is a function of the single variable, $\beta_1 I$ where β_1 introduces the total dependence upon the photon energy, E, and upon the incidence angle, θ, and is defined by

$$\beta_1 = \sin\theta(1 - \exp(\frac{-\mu_1 t_1}{\sin\theta})). \qquad (6)$$

To test this universal model relationship for the monolayer film we have plotted in Fig. 3 for Kodak 101-07 film the specular densities (which have been measured as described in Part II) for normal incidence exposures and for eight photon energies in the 100-1500 eV region. This plot is presented as density, D, versus the universal variable $(1 - \exp(-\mu_1 t_1))I$. The value of the effective layer thickness, t_1, was chosen as that for which the data for the entire range of photon energies "best fit" a single "universal" curve. This data for Kodak 101-07 film yielded the empirical value for t_1 equal to two microns. An efficient, two-parameter empirical equation, suggested by this model (see Eq. (5))

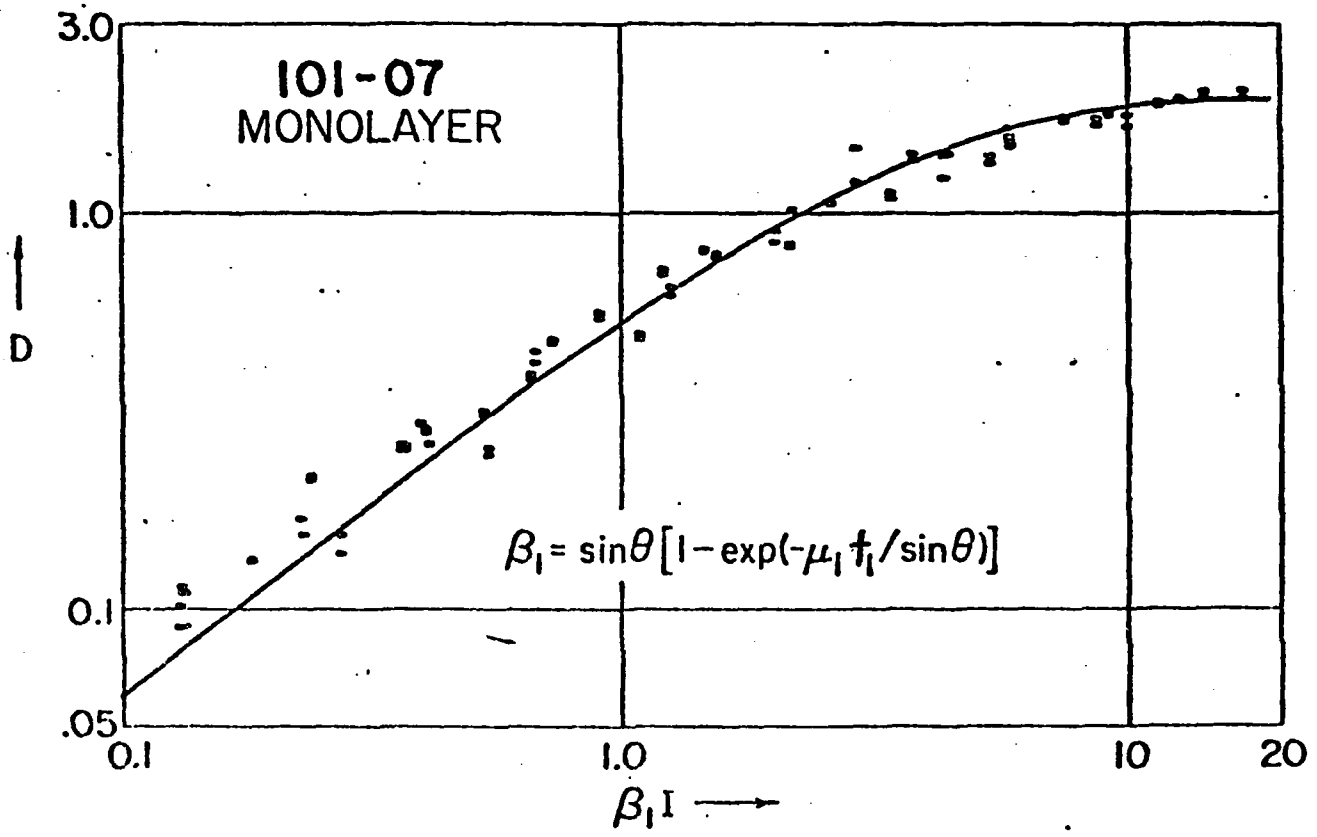

Figure 3. The universal plot of D vs β_1 I for the Kodak 101-07 monolayer using D vs I calibration data as measured at eight photon energies in the 100-1500 eV region. The smooth curve is from fitting the semi-empirical Eq. (7) derived here for the monolayer film. The photon energy dependence is introduced by the scaling factor, β_1 .

has been chosen as

$$D = a_1[1 - \exp(-b_1\beta_1 I)]. \qquad (7)$$

For the Kodak 101-07 monolayer film, the constants a_1 and b_1 have been determined by least squares fitting of this D vs $\beta_1 I$ data for photon energies in the 100-1500 eV region to be 1.96 and .313 $(\mu m)^2$, respectively. This empirically fit curve is also plotted in Fig. 3. In Fig. 4 a comparison of the measured data and of the semi-empirical curve is presented for D vs log I for the Kodak 101-07 film at the photon energy of 277 eV. Also, as will be described in Part II, the optical film density, D, was measured with an essentially constant incident intensity at a range of incidence angles, θ, of 5 to 90 degrees. In Fig. 5 is presented the optical density, D, for a constant incident intensity, for two ranges of exposure, along with that angular dependence as predicted by the semi-empirical model relation using Eqs. (6) and (7) for this monolayer film. (Note: in the relation for density, D, given in Eq. (7), the intensity, I, should be multiplied by a factor $(1 - F(\theta))$ to account for a reduction in exposure at the very small angles of incidence ($\theta < 5°$). $F(\theta)$ is the fraction of the incident radiation intensity that is low-angle scattered and/or totally reflected outward from the monolayer surface and therefore not allowed to be photoelectrically absorbed within the AgBr grains.)

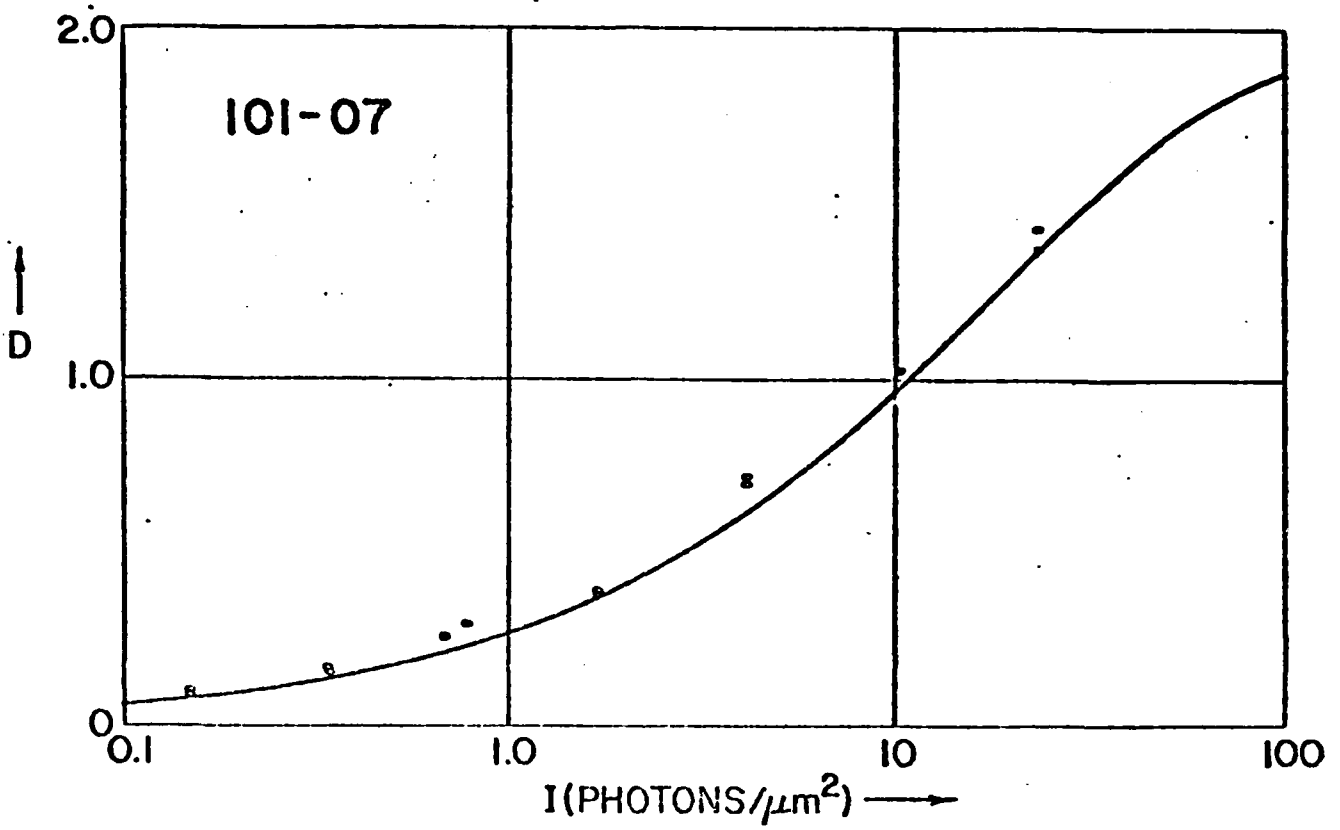

Figure 4. Comparing the experimental D vs log I calibration data for the Kodak 101-07 film at the C-Kα (277 eV) photon energy with the averaged, semi-empirical universal response predicted by Eq. (7).

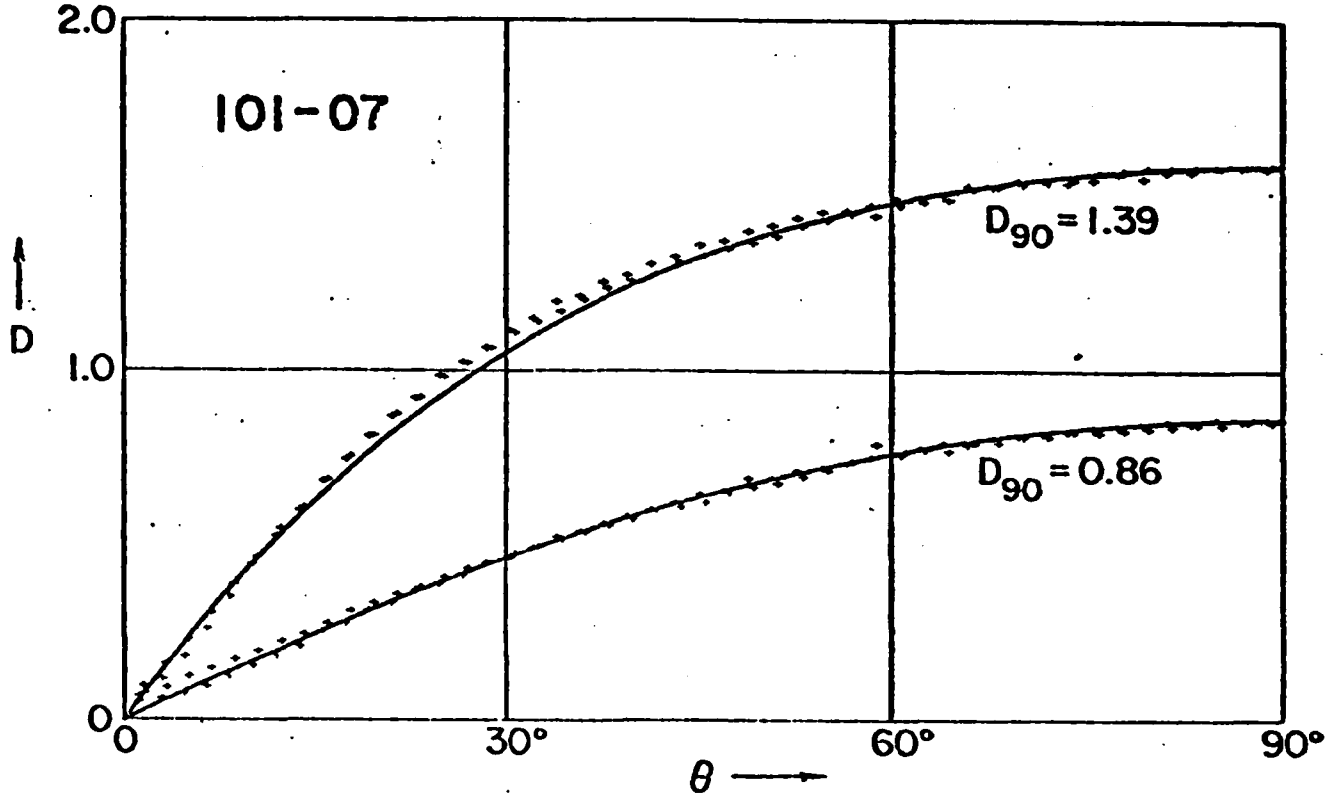

Figure 5. Comparing D vs θ plots (at constant I and measured as described in Part II) with those obtained from the universal response function given by Eq. (7).

The prediction accuracy of this simple mathematical model relation, using empirically determined values of t_1 and of a_1 and b_1 seems to be well within the experimental errors associated with the D vs I measurements. Most of this error is attributed to that of the measurement of the absolute intensity, I (photons/μm^2) and to a variation of the optical density with development conditions. The effect of development is expressed here entirely through the developed silver grain cluster cross section, S (to which parameter the constant a_1 is proportional according to Eq. (5)).

Finally, we may solve for the exposing intensity, I (photons/μm^2) in Eq. (7) to obtain

$$I = (1/b_1\beta_1)\ln(a_1/(a_1-D)). \qquad (8)$$

Using the values of $\mu_1(E)$ as calculated from the absorption data for Ag and Br given by Henke et al.,[4] we have plotted in Fig. 6 the intensity, I(photons/μm^2), as a function of photon energy, E(eV), in the 100-10,000 eV region for normal incidence exposures which result in optical densities, D, equal to 0.5 and 1.0 for the Kodak 101-07 monolayer film. (The reciprocal of these intensities for a given density value is conventionally defined as the film sensitivity.)

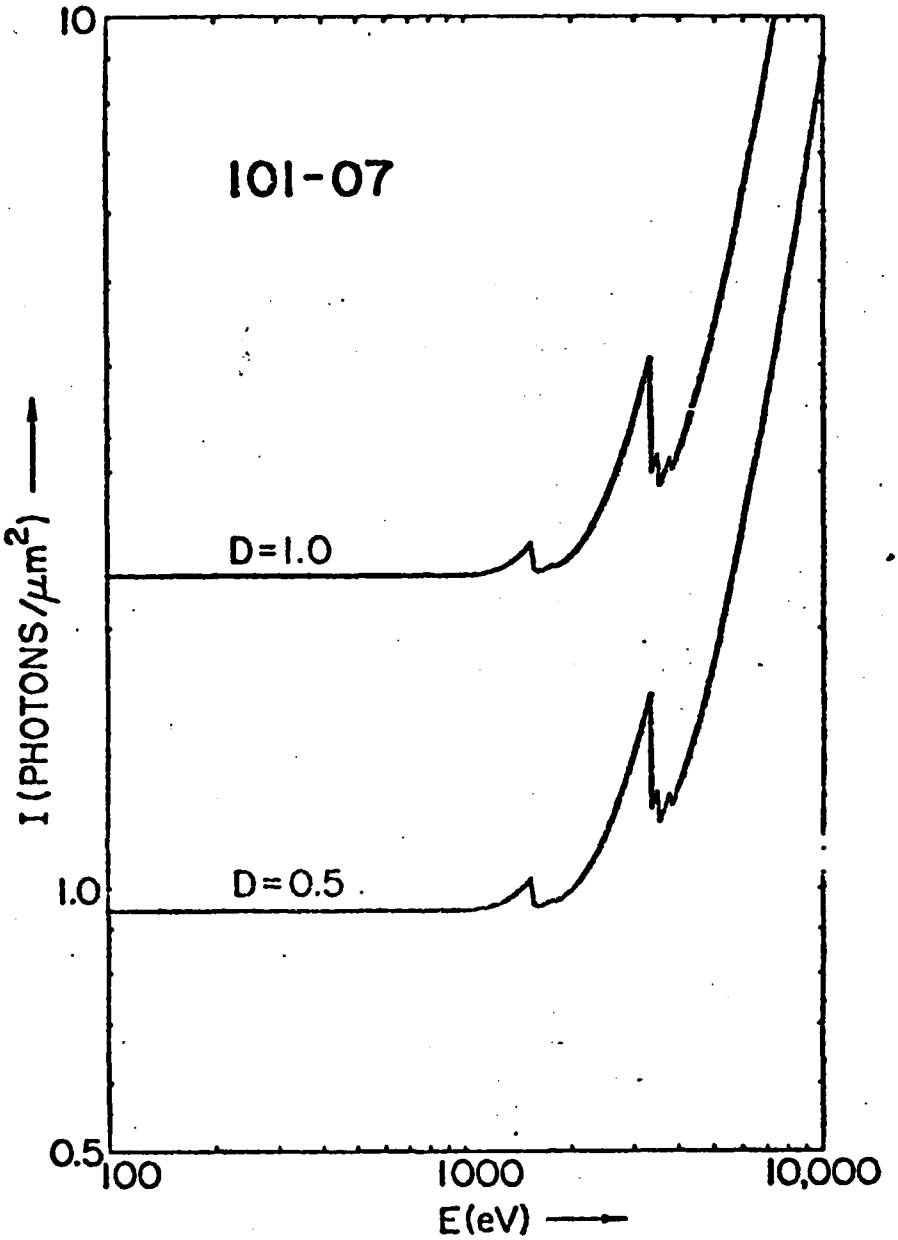

Figure 6. The intensity, I (photons/μm^2) required to establish a specular density of 0.5 and of 1.0 in the Kodak 101-07 monolayer film. These I vs E plots were derived using the semi-empirical relation given in Eq. (8) and illustrate the "flat", high sensitivity response for the 100-1000 eV region and the reduced sensitivity along with the absorption edge structure (Br-L and Ag-L) in the 1000-10,000 eV region.

B. Thick Emulsion Model

We now consider the more complicated problem, that of establishing an optical density relation for a thick emulsion in which the photons are completely absorbed within a heterogeneous system of AgBr grains imbedded in gelatin. The total volume fraction, V, of the AgBr is relatively small (typically < 20%). The thick emulsion film will usually have a protective overcoat of thickness, t, which we assume here to be gelatin-like. We consider (as for the monolayer film analysis above) the AgBr grains to be approximately spherical with a cross section equal to σ and with an effective absorbing thickness equal to d.

In Fig. 7 is depicted a monolayer section within this emulsion, with low-density packing and with gelatin that is assumed to be only between the grains. The probability that an incident photon will be absorbed within an individual AgBr grain in this monolayer section, at depth x within the emulsion, may be written as

$$I\{\sigma(1 - e^{-\mu_1 d})e^{-\mu' x/\sin\theta}e^{-\mu_0 t/\sin\theta}\} = \gamma I$$

which is the product of the number of incident photons per unit area, I; the AgBr grain cross section, σ; the probability of a photon which reaches the AgBr grain is absorbed within that grain; the transmission fraction through the emulsion of thickness, x; and the

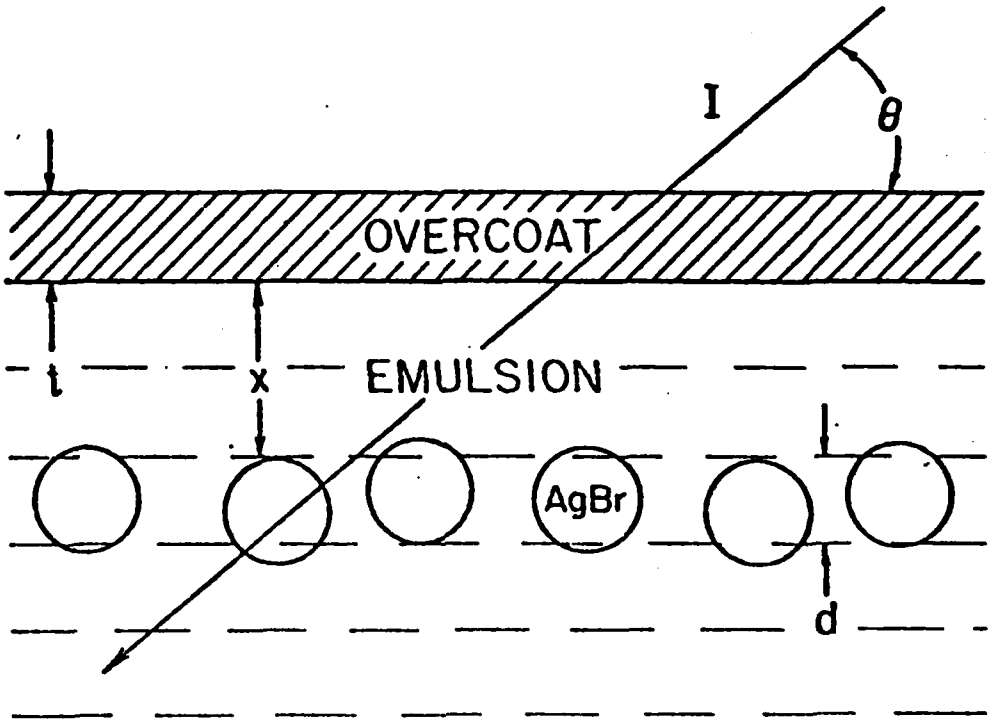

PROBABILITY FOR ABSORPTION WITHIN AgBr GRAIN AT DEPTH, x

$$\sigma I \left[1 - \exp(-\mu_1 d)\right] \exp\left[\frac{-(\mu_0 t + \mu' x)}{\sin\theta}\right]$$

Figure 7. Emulsion film model for an overcoat of thickness, t, and a heterogeneous emulsion consisting of V volume fraction of AgBr, spherical grains distributed within a (1-V) volume fraction of gelatin. Noted here is the probability for photon absorption of an AgBr grain within an assumed monolayer section of average, effective absorption thickness, d, at a depth x within the emulsion.

transmission fraction through the overcoat of thickness, t, for a beam at incidence angle, θ. (μ_0 and μ_1 are the linear absorption coefficients of the gelatin and AgBr, respectively, and μ' is the heterogeneous linear absorption coefficient for the emulsion.) Defining the quantity in this probability expression within the brackets as γ, we may write the differential equation for the additional number of grains rendered developable resulting from an additional increment of incident exposure intensity, dI (similarly as for Eq. (1) above) to be

$$dM = (M_0 - M)\gamma dI,$$

where again the quantity (M_0-M) is the number of grains not as yet rendered developable by at least one photon absorption. Integrating, we obtain for the total exposing intensity of I at θ-incidence with the film surface the relation for the number of grains rendered developable within the monolayer section at depth x

$$M = M_0(1 - e^{-\gamma I}). \tag{9}$$

Upon development, the exposed grains are reduced to silver clusters of average cross section equal to S. The fraction, τ, of a light beam that is transmitted through this monolayer section can be written as described in Sec. II-A as

$$\tau_n = 1 - \text{'S} = 1 - M_0 S[1 - \exp(-\gamma I)]$$

$$= 1 - M_0 S(1 - e^{-\sigma\beta I e^{-\mu' x/\sin\theta}})$$

with

$$\beta = (1 - e^{-\mu_1 d})e^{-\mu_0 t/\sin\theta}. \qquad (10)$$

This is the transmission for a narrow cone system of light through the nth monolayer section of thickness, d, and at a depth, x, equal to nd.

We assume, as a first consideration, that the total optical transmission for the thick emulsion may be given by simply the product of the monolayer section transmissions. This assumption is valid only for relatively small values of MS and d so that the probability for "shadowing" (one grain blocking another in the light beam) is negligible. Then the total transmission is simply

$$\tau = \prod_1^\infty \tau_n = \prod_1^\infty [1 - M_0 S(1 - e^{-\sigma\beta I e^{-\mu' nd/\sin\theta}})]. \qquad (11)$$

And since the optical density, D, is defined as $\log_{10}(1/\tau)$, we may then write for D

$$D = -\log_{10}(\prod_1^\infty(\tau_n)) = -(1/2.30)\sum_1^\infty \ell n[1-M_0 S(1-\exp(-\sigma\beta I e^{-\mu' nd/\sin\theta}))]. \qquad (12)$$

With the assumption that MS is small, this expression for D may then be approximated as simply

$$D = (1/2.30)\sum_1^\infty M_0 S(1 - \exp(-\sigma\beta I e^{-\mu' nd/\sin\theta})). \qquad (13)$$

It is useful here to re-express Eq. (13) as an integral, allowing M_0 to be replaced by $N_0 dx$ with N_0 equal to the

number of AgBr grains per unit volume (and therefore equal to M_0/d), and nd to be replaced by x. We may then write for the optical density

$$D = (1/2.30)\int_0^\infty N_0 S[1 - \exp(-\sigma\beta I e^{-\mu' x/\sin\theta})]dx. \qquad (14)$$

This integral may be easily evaluated as a converging series solution. It is considered here, however, that the assumptions made in its derivation (low AgBr grain density and exposures are too restrictive for many practical applications of photographic measurement. A more detailed, (but more complicated) expression for the transmission through a dense, heterogeneous system of light absorbing silver grain clusters could be derived. Nevertheless, for this more precise description, the resulting transmission, in any event, must also be a function of the intrinsic exposed AgBr grain density, N, at depth x and consequently of the variable

$$z = \sigma\beta I e^{-\mu' x/\sin\theta},$$

which determines the number of grains rendered developable within a differential monolayer section of the emulsion. Here β is defined in Eq. (10). With no assumptions as to the details of the light absorption process within the thick emulsion we may write a general expression for the optical density as

$$D = \int_0^\infty F(z)dx, \qquad (15)$$

where F(z) is a function that may be determined

empirically, for example, from D vs I data for photons of such energy as to be completely absorbed within the given emulsion's total thickness. F(z) has a constant, "saturation" value for large z (at small penetration depths with large exposure, I) ($N_0S/2.30$ in Eq. (14)). F(z) approaches zero value as z becomes small (for small exposure, I, and/or at large depth, x). Differentiating the variable z we have

$$dz = -(\mu'/\sin\theta)\sigma\beta I e^{-\mu' x/\sin\theta} dx$$
$$= -(\mu'/\sin\theta) z dx$$

and we may therefore rewrite Eq. (14) completely in the dimensionless variable, z, as

$$D = \left(\frac{\sin\theta}{\mu'}\right) \int_0^{\sigma\beta I} \frac{F(z)}{z}\, dz. \qquad (16)$$

We conclude, therefore, that the integral must simply be a function of the integration limit $\sigma\beta I$, and we may write for D vs I the "universal" relation of the form

$$D = \left(\frac{\sin\theta}{\mu'}\right) \phi(\beta I). \qquad (17)$$

We note that the factor $(\sin\theta/\mu')$ is a mean penetration depth in the x direction of the incident beam inside the emulsion, and, for a given exposure, I, the function $\phi(\beta I)$ yields the optical density, D, per unit mean penetration depth.

Now for the very low-energy x-radiations of

particular interest here, this penetration depth will approach effectively the thickness of the surface monolayer section (see Fig. 7). For such a "surface" exposure, the transmission factor $\exp(-\mu' x/\sin\theta)$ is not involved, and we consider the contribution to the density, D, for this surface region to be an amount equal to $d_0\phi(\beta I)$, where d_0 will be an empirically determined parameter that measures the effective surface monolayer depth. We add this limiting surface layer contribution to D in Eq. (17) to finally obtain for the optical densit. contributions for both "surface" and "volume" generation of optical density

$$D = \left(\frac{\sin\theta}{\mu'} + d_0\right)\phi(\beta I). \tag{18}$$

Eq. (18) may then be written as a function of the universal variables, αD and βI, viz.,

$$\left(\frac{\mu'/\sin\theta}{1 + \mu' d_0/\sin\theta}\right)D = \alpha D = \phi(\beta I) \tag{19}$$

(thus defining the universal variables that establish the scaling for D and I as the photon energy and the angle of incidence of the exposing radiation are varied.)

The heterogeneous absorption coefficient, μ', may be appreciably different from that which is calculated as $\bar{\mu}$ for a homogeneous absorbing system with the same volume fractions of AgBr and gelatin. We have derived an expression for the linear heterogeneous absorption coefficient in Appendix A, which may be written as

follows:

$$\mu' = \mu_0 - (1/d)\ln[1 - V(1 - e^{-(\mu_1-\mu_0)d})]. \qquad (20)$$

For the same volume fraction, V, for AgBr, and hence (1 - V) for the gelatin, the linear homogeneous absorption coefficient, $\bar{\mu}$, may be given by

$$\bar{\mu} = (1 - V)\mu_0 + V\mu_1. \qquad (21)$$

It may be noted that this relation given for the heterogeneous linear coefficient in Eq. (20) does reduce to this expression for the homogeneous coefficient, $\bar{\mu}$, for small values of the grain size, d.

In Fig. 8 we have plotted for comparison the linear absorption coefficients, μ' and $\bar{\mu}$, given in Eqs. (20) and (21), for Kodak RAR 2497 film, assuming a value for d equal to 0.3 μm.

In order to illustrate the accuracy of prediction of a universal curve as defined by Eq. (19) and of the associated description for the heterogeneous absorption coefficient, given in Eq. (20) we have plotted in Fig. 9 the variables $\mu'D/(1+\mu' d_0)$ and $(1-e^{-\mu_1 d})e^{-\mu_0 t}I$ using D vs I data for the Kodak RAR 2497 film measured at $\theta = 90°$ (and as described in Part II). These data have been measured at eight photon energies in the 100-1500 eV region for which we can assume complete absorption within this emulsion. The overcoat thickness, t, the mean grain size, d, the volume fraction, V, and the surface layer

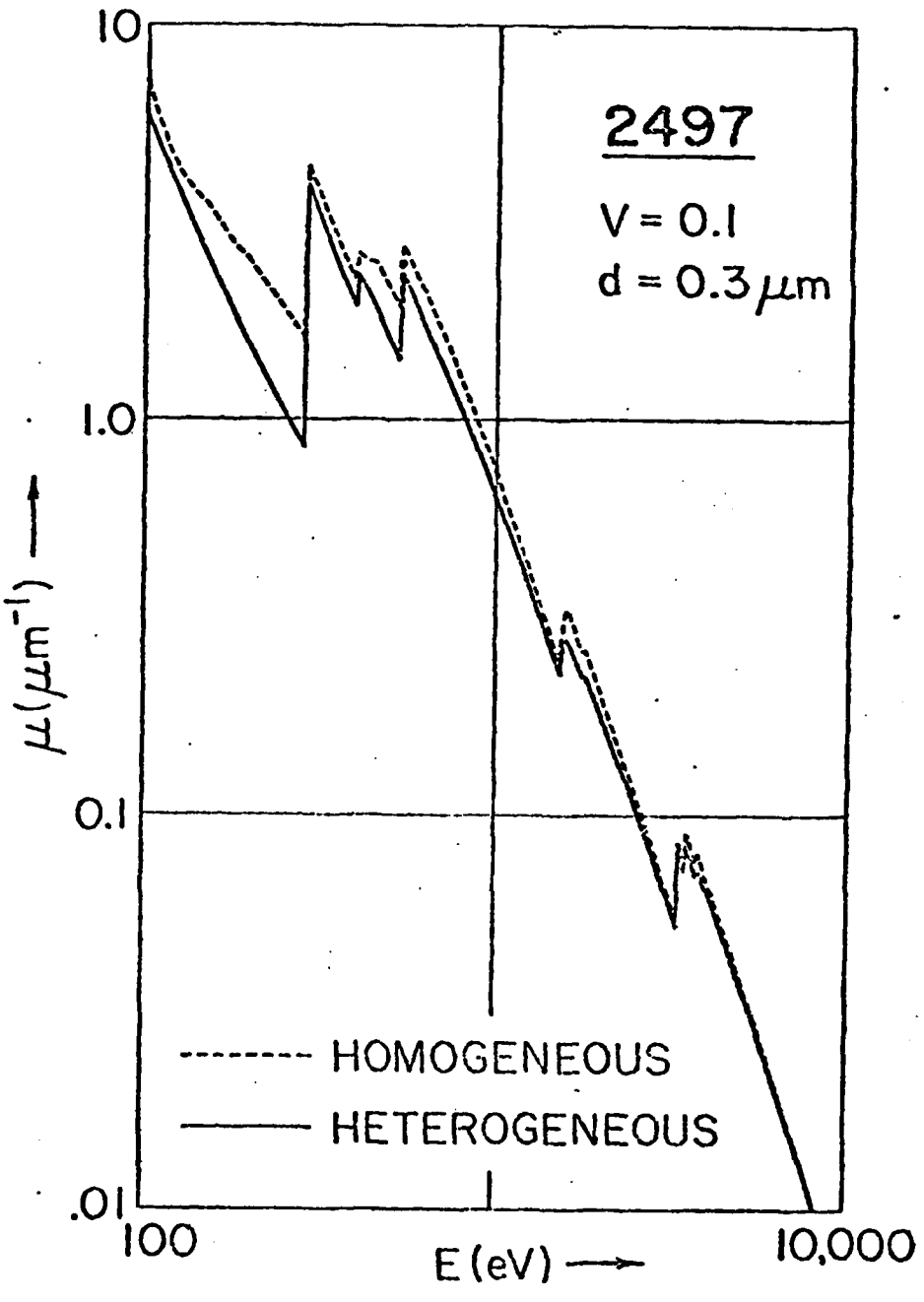

Figure 8. Comparing the linear absorption coefficient as calculated for the heterogeneous RAR 2497 emulsion film system with an amorphous system of the same volume fraction of AgBr. (See Appendix A.) Note the appreciable differences in the low-energy x-ray region.

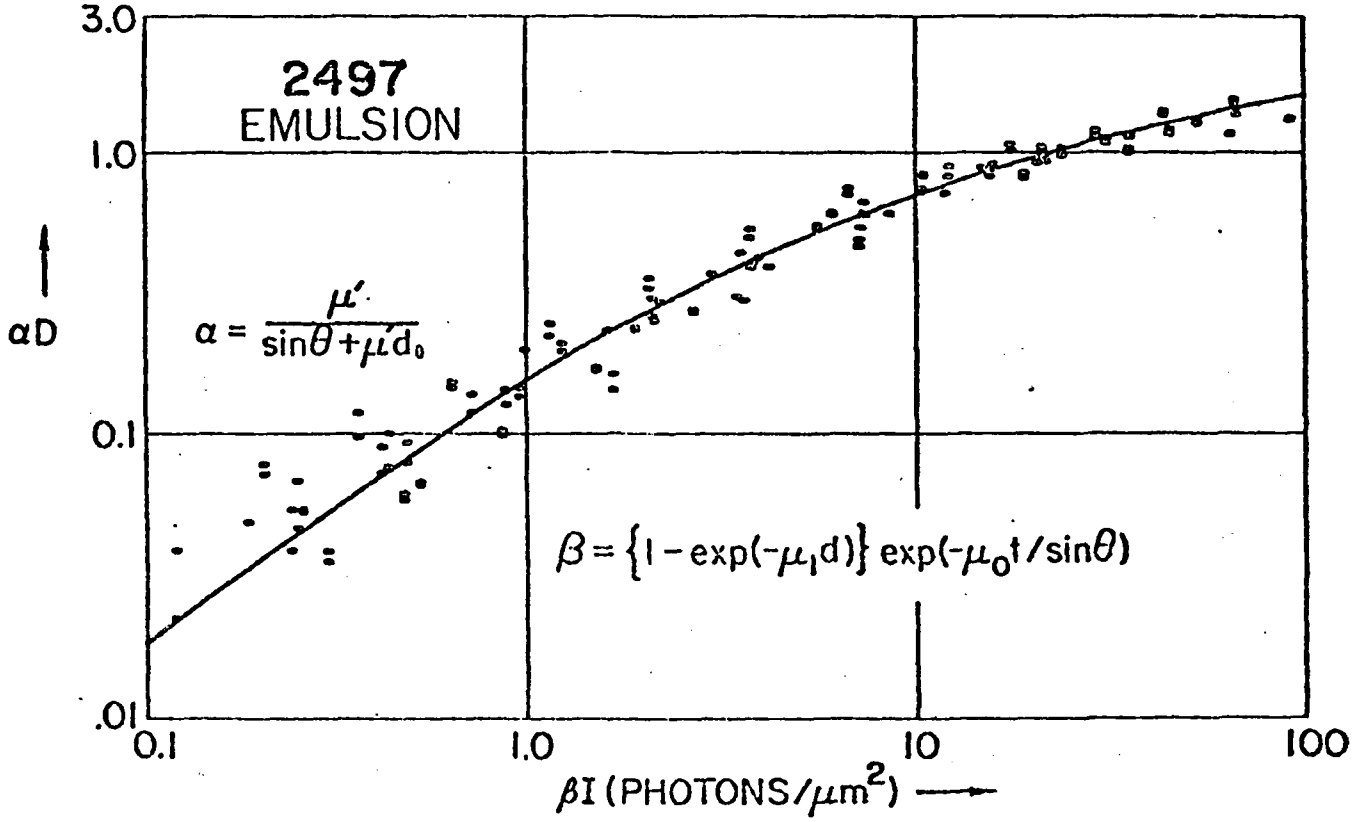

Figure 9. The universal plot of αD vs βI for the Kodak RAR 2497 emulsion film using D vs I calibration data as measured at eight photon energies in the 100-1500 eV region. The smooth curve is obtained by fitting to these points the semi-empirical Eq. (26) derived here for the emulsion type film. The photon energy dependence is introduced through the scaling factors α and β .

thickness, d_0, were chosen so as to yield a minimum variation from a universal curve for the entire photon energy range (see Sec. III). The values so determined for t, d, d_0 and V were 0.3 μm, 0.3 μm, 0.6 μm and 0.1 respectively. Again we consider the departures from a universal curve among these data points as plotted here to be well within experimental error.

We have plotted also in Fig. 9 a semi-empirical equation for the universal curve, the derivation for which will now be described.

Early in the exposure process, the first layers that are encountered within the emulsion may become saturated, i.e., all of the AgBr grains within these layers are rendered developable. And, as the exposure increases, the depth, x_s of this saturation region increases. The corresponding growth in optical density is depicted in Fig. 10 along with a plot of F(z), which function has been defined in Eq. (15), where $z = \beta I \exp(-\mu' x/\sin\theta)$. For sufficiently large values of z and, correspondingly, for sufficiently small values of penetration depth, x, and/or for large values of I, F(z) is equal to a constant "saturation" value F_S. For relatively low densities of AgBr grains within the emulsion, this saturation value is simply $N_0 S/2.30$, as suggested in Eq. (14) and F(z) may then be interpreted as the optical absorption cross section per unit volume of developed silver grain clusters for an exposure that initiates saturation. For

FORMATION OF OPTICAL DENSITY

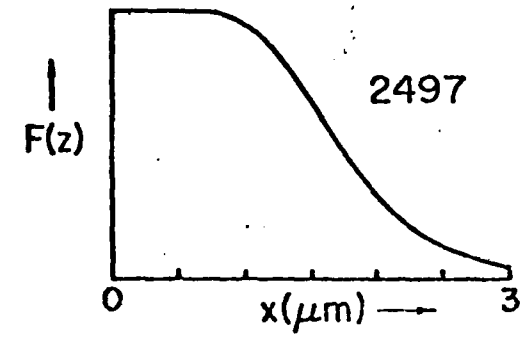

F(z) ≈ LIGHT SCATTERING CROSS SECTION/UNIT VOLUME

$$F(z) \approx F_s(1 - e^{-z})$$

WHERE

$$z = \sigma\beta I \exp\left(\frac{-\mu' x}{\sin\theta}\right)$$

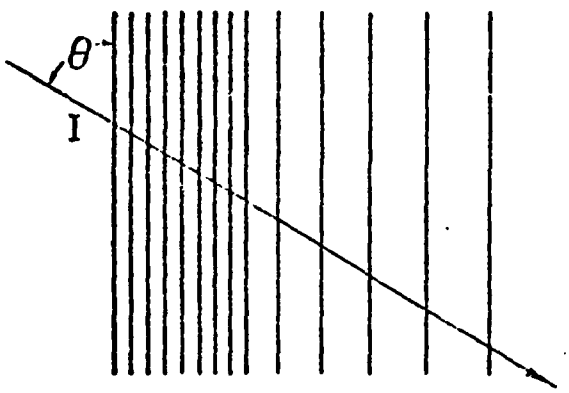

Figure 10. Plotted here is the approximate function, F(z), for the light scattering cross section per unit volume associated with the developed silver grain clusters and resulting from an intermediate exposure, I (calculated for the RAR 2497 film). An exposure was chosen so as to render all grains developable within the first half-thickness of the emulsion. As the exposure, I, increases, this saturation region increases in depth s, and according to this model, this process accounts for the linear relationship between D and log I after the onset of the saturation process.

small z, F(z) approaches zero value. We shall define by z_s that value of z for which F(z) reaches its constant, saturation value, defined here as F_s, (within, say, a few percent). The corresponding saturation depth, x_s, may then be related to z_s by

$$z_s = \sigma\beta I \exp(-\mu' x_s/\sin\theta)$$

and (22)

$$x_s = \left(\frac{\sin\theta}{\mu'}\right) \ell n(\sigma\beta I/z_s).$$

We may now write Eq. (15) as follows:

$$D = \int_0^{x_s} F(z)dx + \int_{x_s}^{\infty} F(z)dx$$

$$= F_s x_s + \sin\theta/\mu' \int_0^{x_s} F(z)/z \, dz$$

and by using Eq. (22), (16) and (17), we obtain

$$D = (\sin\theta/\mu')\left[F_s \ell n(\sigma\beta I/z_s) + \phi(z_s)\right]. \qquad (23)$$

Including the parameter d_0 in order to account for the surface layer exposure (as has been described for Eq. (18)), we may rewrite Eq. (23) as

$$D = \left(\frac{\sin\theta}{\mu'} + d_0\right)(F_s \ell n\sigma\beta I + \text{constant}). \qquad (24)$$

We therefore predict that after an initial exposure that will initiate the onset of saturation in the first layers, the optical density, D, should vary linearly with the logarithm of the exposure, I. This is indeed what is usually observed as is illustrated, for example, in the D

vs log I plot for the Kodak RAR 2497 film presented in Fig. 11.

Eq. (24) may be written as a universal, semi-empirical equation of the form

$$\left(\frac{\mu'/\sin\theta}{1 + \mu' d_0/\sin\theta}\right)D = \alpha D = a\ell n(b\beta I). \qquad (25)$$

However, for exposure, I, below that which may induce saturation, it is expected that D be directly proportional to I. This may be deduced, for example, by integrating Eq. (14) after expanding the exponential for small values of its argument ($\sigma\beta I\exp(-\mu' x/\sin\theta)$) obtaining

$$D \approx \left(\frac{\sin\theta}{\mu'}\right)\frac{N_0 S}{2.30}\sigma\beta I \text{ for small I.}$$

In order to require that our model relation for the optical density, D, does increase initially as I in the "toe" region of the D vs I response, we make a simple addition to the argument of the logarithmic term in Eq. (25) to obtain finally the semi-empirical relation for D vs I as

$$\alpha D = a\ell n(1 + b\beta I). \qquad (26)$$

For the RAR 2497 film, the constants a and b have been determined by least square fitting of the αD vs βI data as plotted in Fig. 9, yielding the values of 0.414 μm^{-1} and 0.454 μm^2, respectively. This least squares fit function has been plotted as the universal curve in Fig. 9 and it has been applied to yield the D vs log I curve presented

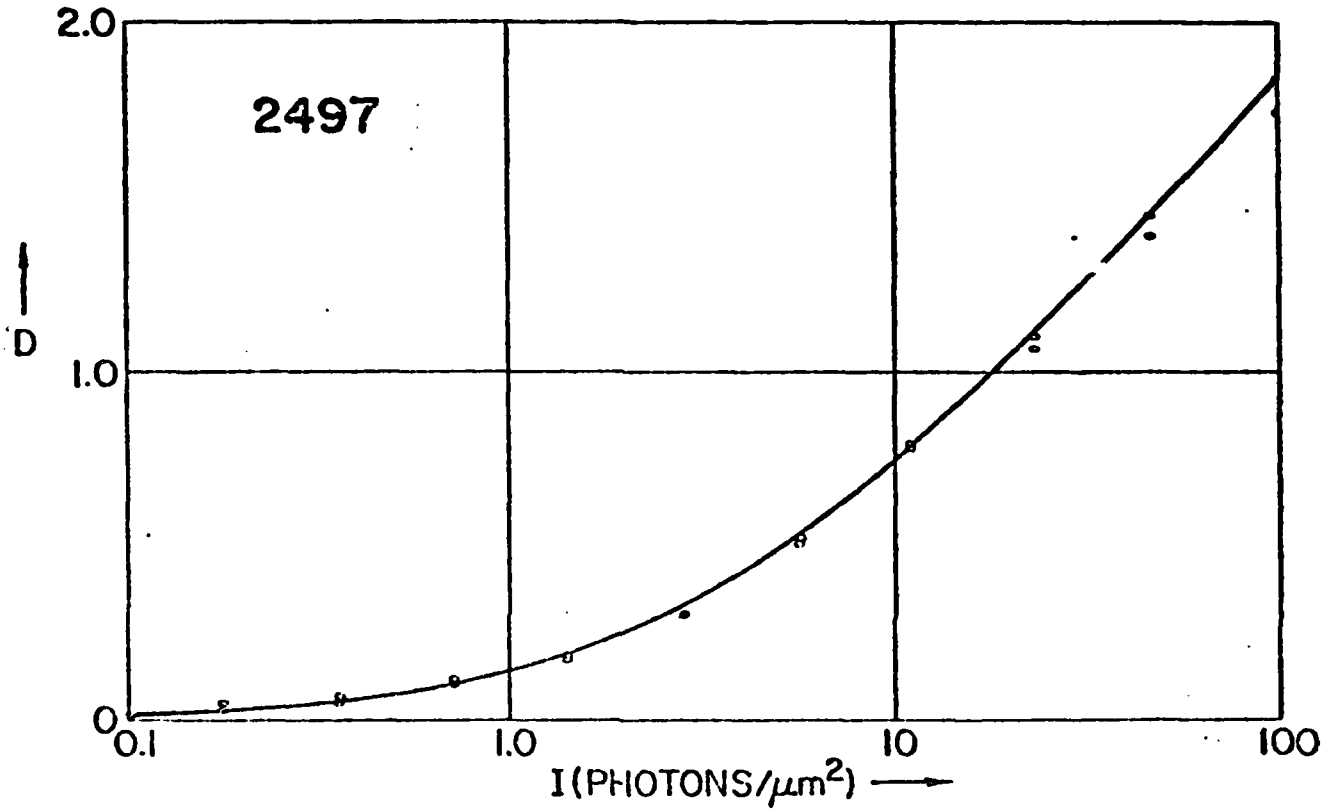

Figure 11. Comparing the D vs log I calibration data for the RAR 2497 film at the O-Kα (525 eV) photon energy with the averaged universal response function given by the semi-empirical Eq. (26).

in Fig. 11, as an example, at the particular photon energy of 525 eV.

C. THIN EMULSION MODEL

For the thick emulsion model described above it was assumed that all of the incident photons were absorbed in the overcoating and emulsion layers. For the thin emulsion model it is required that the predicted contribution to the optical density for emulsion depths greater than the value, T (the actual emulsion thickness) be subtracted from the density, D, as predicted for the thick emulsion as given by Eq. (18).

For the thin emulsion case, therefore, we rewrite Eq. (16) (after including the surface exposure correction parameter, d_0) as follows:

$$D = \left(\frac{\sin\theta}{\mu'} + d_0\right) \int_{\beta I e^{-\mu' T/\sin\theta}}^{\beta I} \frac{F(z)}{z}\, dz$$

yielding, for emulsion thickness, T, a predicted universal relation

$$\alpha D = \int_{\beta I e^{-\mu' T/\sin\theta}}^{\beta I} \frac{F(z)dz}{z} = \phi(\beta I) - \phi(\beta I e^{-\mu' T/\sin\theta}). \quad (27)$$

And, correspondingly, we may rewrite Eq. (26) for the thin emulsion case as

$$\alpha D = a \ \ell n \ \left(\frac{1 + b\beta I}{1 + b\beta I e^{-\mu' T/\sin\theta}}\right). \quad (28)$$

Note: It has been assumed here that the universal function (and its semi-empirical description given in Eq. (28) defined through the parameters a and b) are established using calibration data for which the emulsion is "thick", i.e., for photons that are completely absorbed within the emulsion.

The photographic response function presented in Eq. (28) is applicable in the photon energy region for which the primary assumption made in its derivation obtains, viz., that each AgBr grain will be rendered developable by a single photon absorption within the grain. It has been thus assumed that the effective cross section for photon excitation, σ, is constant, i.e., independent of the photon energy. For photons of energy above about ten keV it is expected that the photoelectrons that are generated within the emulsion in the vicinity of a given AgBr grain may have sufficient range to contribute, along with the direct photon absorption, to the excitation cross section of that AgBr grain. The effective cross section, σ, may then be energy dependent at the higher photon energies, requiring that the relatively simple analysis presented here be modified for $E > 10$ keV.[2]

In Fig. 12 we have applied Eq. (28) to predict, for this 100 to 10,000 eV region, the number of photons/μm^2 required to yield optical, specular densities of 0.5 and 1.0 for normal incidence upon the RAR 2497 film.

In many practical spectrographic measurements, the

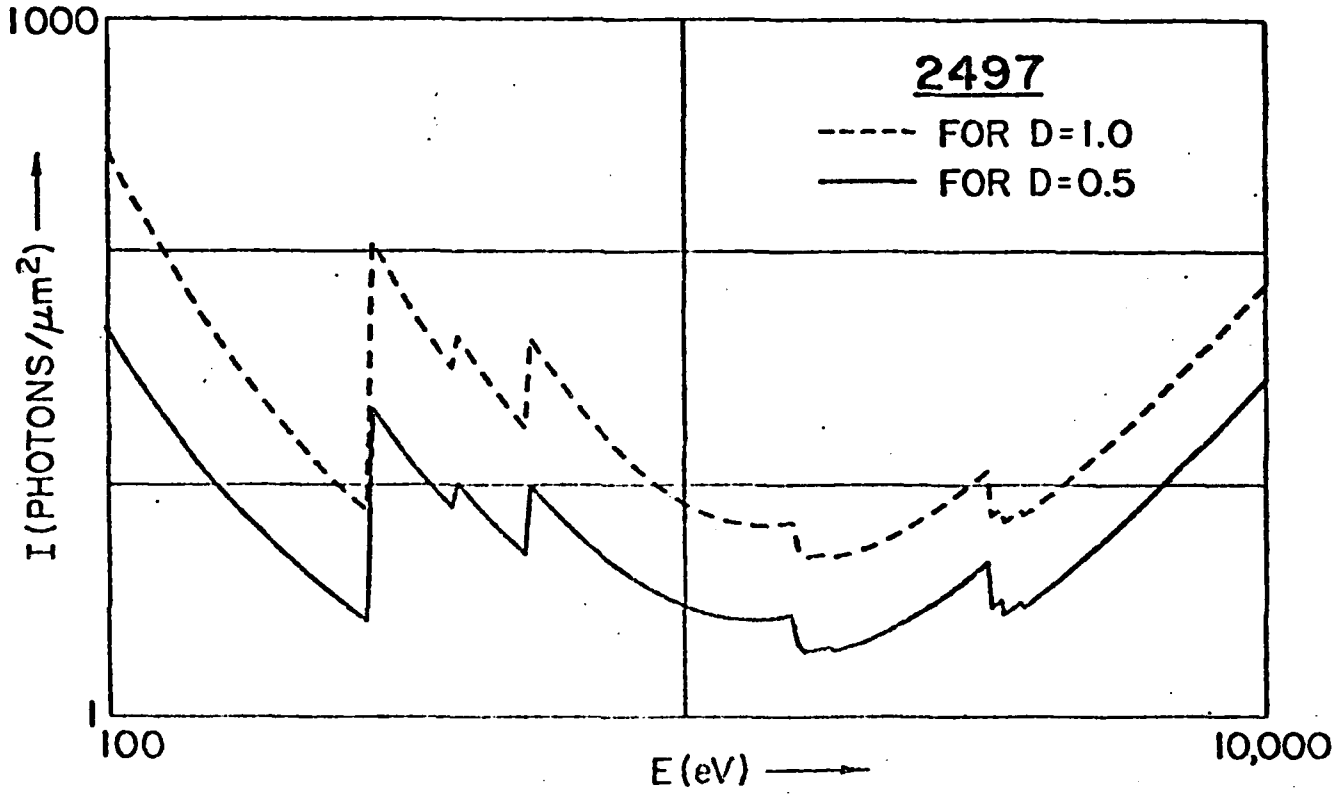

Figure 12. The intensity I (photons/μm^2) required to establish a specular density of 0.5 and of 1.0 in the RAR 2497 emulsion film.

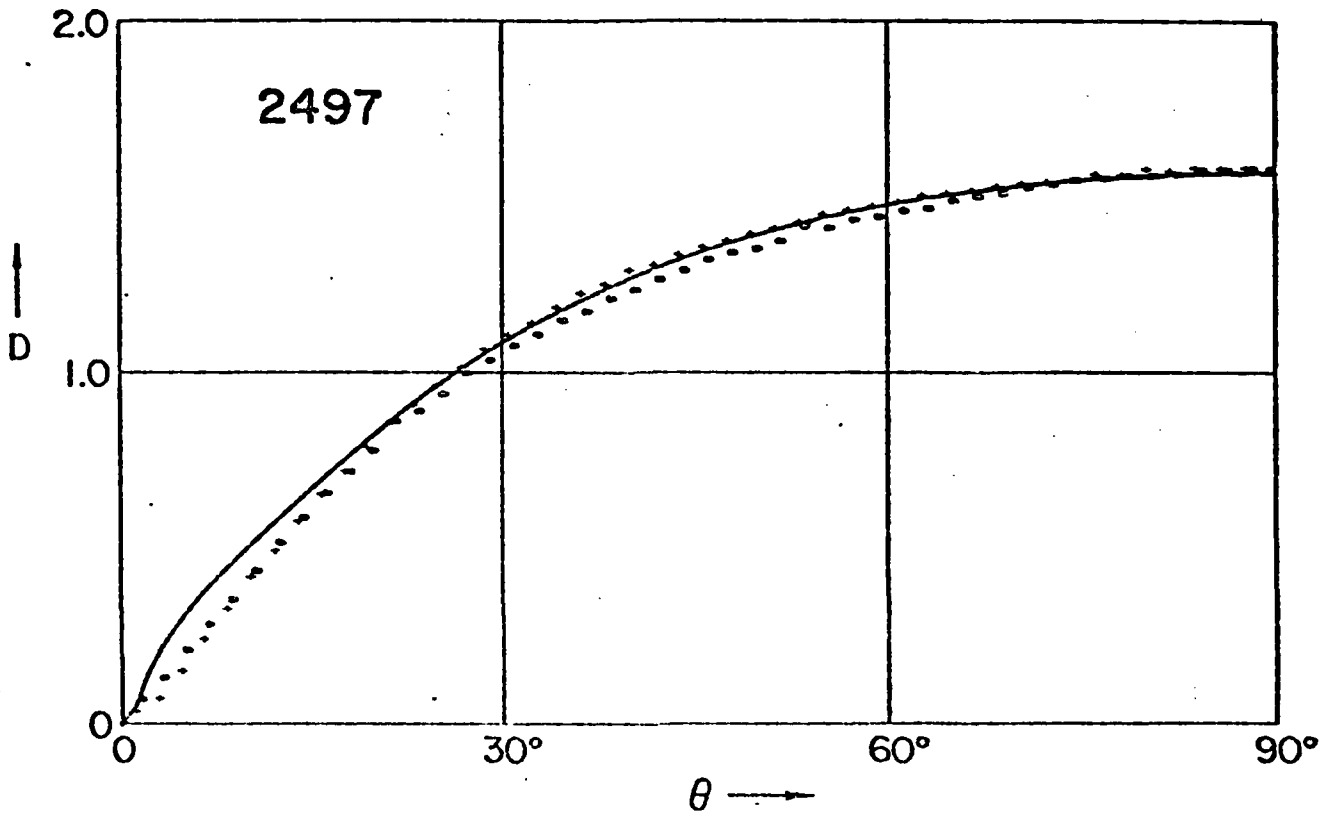

Figure 13. Comparing experimentally measured D vs θ plots (measured as described in Part II for constant incident intensity, I, and energy Al-K α (1487 eV)) with those predicted by the semi-empirical, universal response function given in Eq. (28) for the RAR 2497 film.

x-ray intensity is not incident at 90° upon the film. Nevertheless, the density-exposure-photon energy characterizations presented in Figs. 11 and 12 can be presented for angles of incidence other than 90° through the θ-dependence of Eq. (28). The optical density, D, has been measured (as described in Part II) for θ values in the 5° to 90° range for essentially constant incident intensity, I, and for several photon energies. As is suggested in Fig. 13, the θ-dependence as predicted by Eq. (28) for a photon energy equal to 1487 eV is demonstrated to be well within the limits of the experimental errors for the RAR 2497 film.

III. SUMMARY AND APPLICATION

In this section we summarize the results of the foregoing analysis of the low-energy x-ray response of photographic films. These are expressed as semi-empirical equations which relate the specular optical density, D, the incident intensity, I(photon/μm^2), the angle of incidence, θ, and the photon energy, E(eV) (through the linear absorption coefficients, μ_0 for gelatin, μ_1 for AgBr and μ' for the heterogeneous emulsion mixture.)

A. The Monolayer - Defined as a densely packed layer of AgBr grains of effective thickness, t_1.

$$D = a_1\{1 - \exp(-b_1\beta_1 I)\}$$

or

$$I = 1/(b_1\beta_1)\ell n(\frac{a_1}{a_1-D})$$

In which

$$\beta_1 = \sin\theta\{1 - \exp(-\mu_1 t_1/\sin\theta)\} .$$

($\underline{a_1}$ varies approximately as S/d^2 and $\underline{b_1}$ as d^2).

B. The Thick Emulsion - Defined as completely absorbing with an effective AgBr grain thickness, d, AgBr volume fraction, V, and with a gelatin-like overcoat of thickness, t.

$$\alpha D = a\ell n(1 + b\beta I)$$

or

$$\beta I = (1/b)\{\exp(\alpha D/a)-1\} .$$

In which

$$\beta = \{1 - \exp(-\mu_1 d)\} \exp(-\mu_0 t/\sin\theta)$$

$$\alpha = \mu'/(\sin\theta + \mu' d_0)$$

where

$$\mu' = \mu_0 - (1/d)\ell n\{1 - V(1 - \exp[-(\mu_1 - \mu_0)d])\}$$

and d_0 is an effective emulsion surface layer thickness ($\underline{a}$ varies approximately as S/d^3 and $\underline{b}$ as d^2).

C. Thin Emulsion - Defined as for the thick emulsion case for the lower energy photons but modified to account for the incomplete absorption of higher energy photons within a finite emulsion thickness, T.

$$\alpha D = a \ell n \frac{1+b\beta I}{1+b\beta I \exp(-\mu' T/\sin\theta)}$$

or

$$\beta I = (1/b) \frac{\exp(\alpha D/a)-1}{1 - \exp(-\mu' T/\sin\theta)\exp(\alpha D/a)}$$

In order to efficiently apply photographic materials as absolute x-ray detectors, it is very helpful to have at least approximate information about the film's physical and chemical structure, particularly the volume fraction, V, the emulsion thickness, T, the overcoat thickness, t, and the constituency of the overcoating material if it is not gelatin. Ideally, these parameters would be supplied by the film manufacturers. Unfortunately, at this time, these data were not shared with the user. Many of the larger laboratories do have the facilities to measure directly these parameters, but it would seem important to avoid such an expenditure of additional time and effort.

Alternatively, if these film characteristics are not available from the manufacturer or by independent analytical means, their effective values may be determined through more extensive calibration measurements of D vs I at additional photon energies. This has been the approach adopted in this work.

For the monolayer film this procedure is not so difficult. A minimum of two photon energies is required for which D vs I data are chosen so that the absorption within AgBr is appreciably different. Because it is

predicted that D is a function of the single, universal variable, $\beta_1 I$, the ratio of the I values for the two photon energies that yield the same D values is a constant and equal to the corresponding ratio of the β_1-values. The average value for this ratio, r, may then be applied to determine the effective AgBr monolayer thickness, t_1. Thus

$$r = \frac{1 - \exp[-\mu_1(E')t_1]}{1 - \exp[-\mu_1(E'')t_1]}$$

in which E' and E'' are the two photon energies for which the two D vs I curves are measured. This expression may be solved numerically for the value of t_1. With this parameter determined, the universal curve, $D = \phi(\beta_1 I)$ is established and a least squares fit to this curve, based upon D vs I data at the different photon energies, may then be applied to determine the parameters, a_1 and b_1. These define the semi-empirical equation given above which relates I(photons/μm^2) to the values of D, θ, and photon energy, E. This equation allows a very straightforward microcomputer analysis of the densitometer data to yield an absolute spectrum in I.

In order to similarly characterize an overcoated, thick emulsion film, at least three D vs I sets of data are required at appreciably different photon energies for which complete absorption within the film is obtained. This is because two parameters, d and t are required to define β; and V and d_0 also need to be determined to

define the scaling factor, α.

Finally, for the thin emulsion type film of thickness, T, this parameter must be determined using at least one more D vs I data set at a higher photon energy of a radiation that is appreciably transmitted through the emulsion.

We have found that by using a small computer-plotter system, a graphical, iterative determination of the film structure parameters was usually rapid and efficient with an accuracy commensurate with that of the experimental calibration data. Log-Log plots of αD vs βI were generated in order 1) to obtain values of t and d that establish a set a β-values for a series of photon energies that translate the corresponding αD vs βI curves along the $\log\beta I$ axis to form a parallel set, and 2) to vary d_0 and V parameters to establish the values of α for the different photon energies in order that the set of parallel curves be then reduced to a single universal curve by so shifting then along the $\log\alpha D$ axis. Examples of such universal curves for the monolayer film, Kodak 101-07 and the thick emulsion film, Kodak RAR 2497 film were presented in Figs. 3 and 9. These curves were then least-square fit to yield the complete semi-empirical equations, as based upon the normal incidence D vs I data which yield the parameters a and b that define the complete θ-dependent semi-empirical relations described above.

In Part II of this work, the calibration and characterization of five films considered to be appropriate for absolute low-energy x-ray spectroscopic analysis is described. These calibrations will be shown to be well described by the semi-empirical equations that have been developed here.

ACKNOWLEDGEMENTS

The authors gratefully acknowledge the invaluable assistance in this program of Priscilla Piano, and the helpful advice throughout this work of David Dixon of the Technical Photography Group, Lawrence Livermore National Laboratory, and his preparation of the scanning electron microscope film studies. This program in Low-Energy X-Ray Physics and Technology is supported by the Air Force Office of Scientific Research under Grant No. 84-0001 and supplementally by the Department of Energy under Contract No. DE-AS08-83DP40181.

APPENDIX A--Linear Absorption Coefficient, μ', for Heterogeneous Materials

In our analysis for the number of AgBr grains that are rendered developable at emulsion depth, x (derivation for Eq. (9)), it was necessary to introduce a transmission factor, $\exp(-\mu' x/\sin\theta)$, in which μ' is the effective linear absorption coefficient for the heterogeneous system of finite size AgBr grains imbedded within a gelatin matrix. For AgBr grain sizes that are small as compared with reciprocal linear absorption

coefficient of AgBr, the heterogeneous coefficient will approach the homogeneous absorption coefficient, $\bar{\mu}$, as given by

$$\bar{\mu} = (1 - V)\mu_0 + V\mu_1 , \qquad \text{(A1)}$$

where μ_0 and μ_1 are the linear absorption coefficients for gelatin and for AgBr, respectively, and V is the volume fraction for the AgBr component.

In Fig. 14 we present an SEM photo of the cross section of the SB-392 film (described in Part II) which illustrates the heterogeneity of the photographic emulsions.

In order to determine μ', we shall again assume that it is sufficiently accurate to model this heterogeneous system as a system of s layers of thickness, d, equal to the effective grain size, with the grains ordered completely within each layer (absorbing as equivalent aligned cubes). This geometry is depicted in Fig. 15. We define the x-ray transmission factor, τ, for the heterogeneous absorber (an averaged value for a large number of incident photons) as follows:

$$\tau = \sum_0^s p_n \tau_n = \exp(-\mu' x), \qquad \text{(A2)}$$

where n is the number of AgBr grain encounters for a given photon passing through the s layers ranging from zero to s, as possible values (for n); p_n is the probability of having n encounters and τ_n is the associated

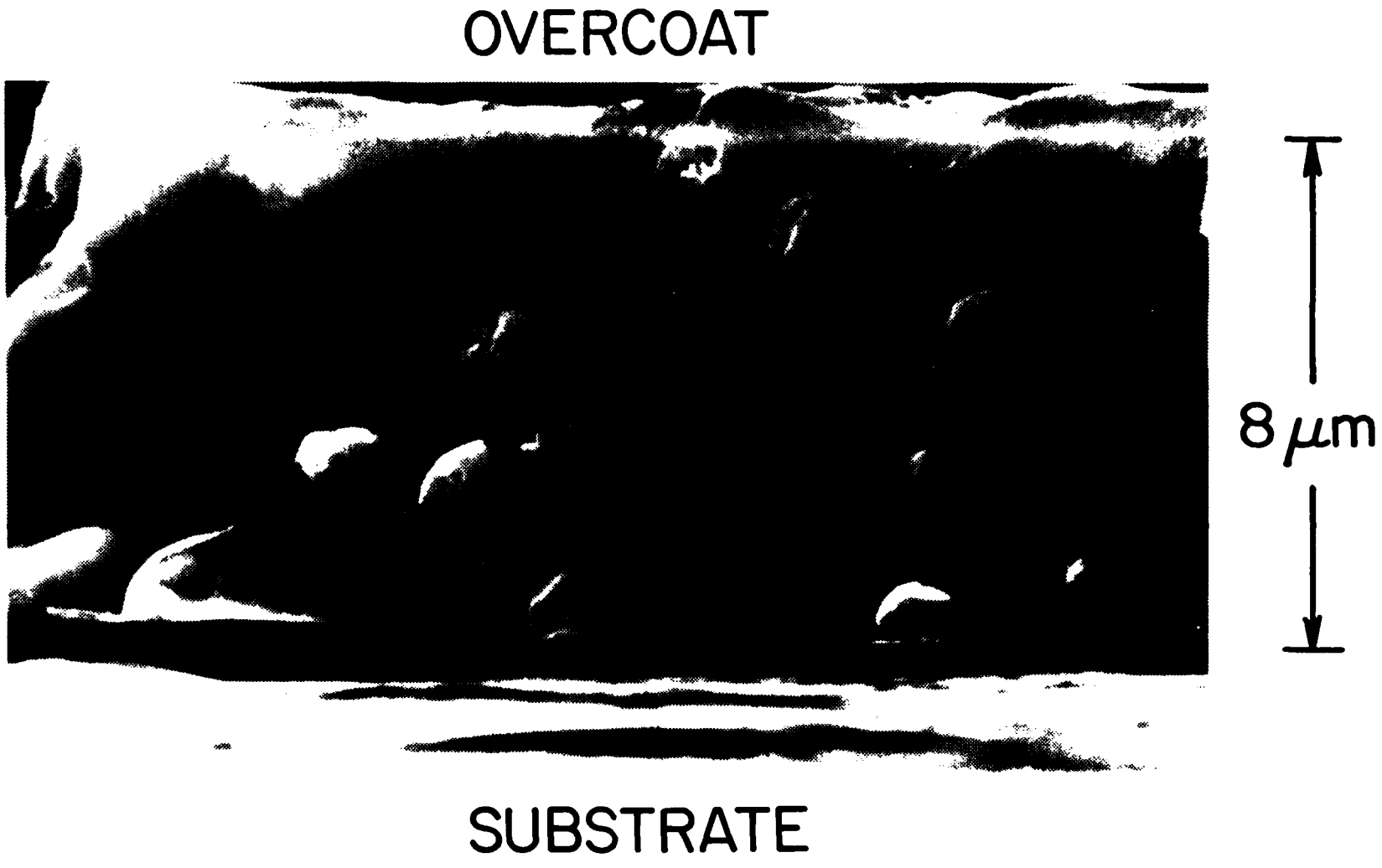

Figure 14. A scanning electron microscope photograph of a cross section of an undeveloped SB-392 film. Illustrated here is the heterogeneous quality of this photographic emulsion.

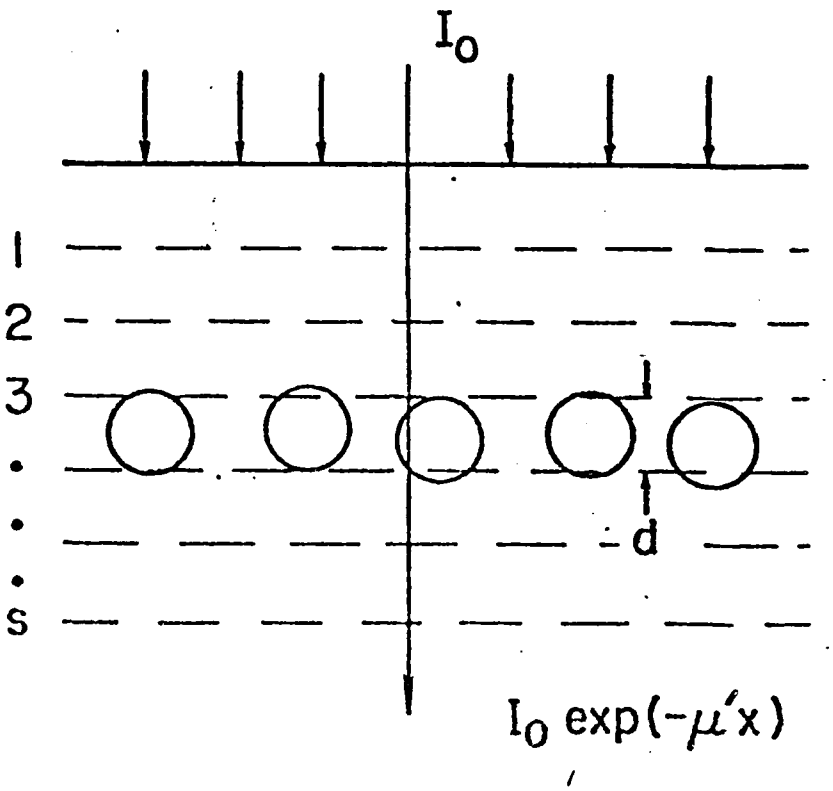

Figure 15. Model for the calculation of the transmission of photons through a thickness, x, of heterogeneous emulsions which consist of s monolayer sections of thickness equal to an effective grain absorption thickness, d, and with a fraction, V, of AgBr grains and of (1-V) of gelatin.

transmission factor for a photon passing through nd thickness of AgBr, multiplied by that for passing through (s - n)d thickness of gelatin. We shall write expressions for p_n and τ_n for the first few values of n in order to establish the general expression for $\Sigma p_n \tau_n$. (Note: the area fraction occupied by the AgBr grains within this single layer is the same as the volume fraction, V; and therefore the probability for encountering one or no AgBr grains for a single photon passing through this layer is V or (1-V), respectively.)

n = 0:

$$p_0 = (1-V)^s$$

$$\tau_0 = e^{-\mu_0 x}$$

n = 1:

$$p_1 = s(1-V)^{s-1}V$$

$$\tau_1 = e^{-\mu_1 d} e^{-\mu_0 (x-d)} = e^{-\mu_0 x} e^{-(\Delta\mu)d}$$

where $\Delta\mu = (\mu_1 - \mu_0)$

n = 2:

$$p_2 = s(s-1)/2 \quad (1-V)^{s-2}(V)^2$$

$$\tau_2 = e^{-2\mu_1 d} e^{-\mu_0 (x-2d)} = e^{-\mu_0 x} e^{-2\Delta\mu d}$$

$n = 3$:

$$p_3 = s(s-1)(s-2)/3! \quad (1-V)^{s-3}(V)^3$$

$$\tau_3 = e^{-3\mu_1 d_e - \mu_0(x-3d)} = e^{-\mu_0 x_e - 3\Delta\mu d} .$$

It is evident therefore that

$$p_n = \frac{s!}{(s-n)!n!}(1-V)^{s-n}V^n \qquad \text{(A3)}$$

and

$$\tau_n = e^{-\mu_0 x_e - n\Delta\mu d} \qquad \text{(A4)}$$

and that

$$\tau = e^{-\mu_0 x} \sum_0^s \frac{s!}{(s-n)!n!}(1 - V)^{s-n}(Ve^{-\Delta\mu d})^n . \qquad \text{(A5)}$$

Recalling that the Binomial Equation may be written as

$$(A + B)^s = \sum_0^s \frac{s!}{(s-n)!n!} A^{s-n}B^n , \qquad \text{(A6)}$$

we note that

$$\sum_0^s p_n = \sum_0^s \frac{s!}{(s-n)!n!}(1 - V)^{s-n}(V)^n = 1 \qquad \text{(A7)}$$

and that

$$\tau = e^{-\mu_0 x}[1 - V(1 - e^{-\Delta\mu d})]^s = e^{-\mu' x}. \qquad \text{(A8)}$$

Finally, we may solve Eq. (A8) for μ' and letting $s = x/d$, we obtain

$$\mu' = \mu_0 - (1/d)\ell n(1-V(1 - e^{-\Delta\mu d})). \qquad \text{(A9)}$$

This result is essentially the same expression for the heterogeneous absorption coefficient as has been applied by Brown et al.[2] and by Toor[3] in their photographic film models.

In Fig. 8, we have for the RAR 2497 film compared the homogeneous linear absorption coefficient, $\bar{\mu}$, and this heterogeneous linear absorption coefficient, μ', for photon energies in the 100 to 10,000 eV region (using the atomic absorption data recently reported by Henke et al.[4]).

REFERENCES

[1]B. L. Henke, H. T. Yamada, and T. J. Tanaka, "Pulsed plasma source spectrometry in the 80-8000 eV x-ray region," Rev. Sci Instrum. 54, 1311-1330 (1983).

[2]D. B. Brown, J. W. Criss, and L. S. Birks, "Sensitivity of x-ray films. I. A model for sensitivity in the 1-100 keV region," J. Appl. Phys. 47, 3722-3731 (1976).

[3]A. Toor, Lawrence Livermore National Laboratory, private communication.

[4]B. L. Henke, P. Lee, T. J. Tanaka, R. L. Shimabukuro, and B. K. Fujikawa, "Low-energy x-ray interaction coefficients: photoabsorption, scattering, and reflection. E=100-2000 eV Z=1-94," Atomic Data and Nuclear Data Tables 27, No. 1, 1-144 (1982).

Low-energy x-ray response of photographic films: part II. experimental characterization

B. L. Henke, F. G. Fujiwara, M. A. Tester

University of Hawaii
Honolulu, Hawaii 96822

C. H. Dittmore

Lawrence Livermore National Laboratory
Livermore, California 94550

M. A. Palmer

Sandia National Laboratory
Albuquerque, New Mexico 87185

ABSTRACT

Optical density vs exposure data have been obtained at nine photon energies in the 100-2000 eV x-ray region for five spectroscopic films (Kodak's 101-07, SB-392, RAR 2492, 2495 and 2497). These data were determined operationally by a direct comparison of the peak absolute intensities of spectral lines measured with a calibrated proportional counter and the microdensitometer tracings of the corresponding photographically recorded spectral lines. Film resolution limits were deduced from an analysis of contact microradiograms of linear zone plates constructed of gold bars. The relationship between the specular densities as measured here and the diffuse

densities have been experimentally determined for the five films. Finally, experiment surements of the optical density vs the angle c ence of exposing radiation of constant intensity obtained. These data, relating density to the x intensity, its photon energy and angle of incidence are shown to be fit very satisfactorily in the 100-10,000 eV region by the semi-empirical mathematical model relations which have been derived in Part I of this work.

I. INTRODUCTION

In the work that is described here, we have characterized photographic films for absolute spectrographic analysis in particularly the low-energy x-ray photon energy region of 100-2000 eV. Five films have been calibrated which were chosen as being appropriate for low-energy x-ray spectroscopy because of their proven quality, vacuum compatibility and range of sensitivity/resolution. These are Kodak's films, 101-07, SB-392, and RAR films 2492, 2495 and 2497. The first four are currently available. The RAR 2497 film is no longer manufactured but has been included here because of its past and present very extensive application at the National Laboratories. The 2497 film (and its predecessor, RAR 2490) have very similar characteristics as those of the newer RAR 2492 and 2495. A very comprehensive study of the RAR 2490 film has been reported by Benjamin et al.[1] An early work on the calibration of the 101 type film for the low-energy x-ray region has been presented by Koppel[2] who has recently also reported some calibrations for the RAR 2492 and SB-5 film (which is the sheet film version of the 35 mm, SB-392 film that is characterized here).[3] (We would like also to refer the reader to another excellent report by Dozier et al.[4] on film calibration for the higher photon energies than those particularly addressed here.) In Fig. 1 we present

a comparison of the sensitivity vs photon energy curves for the 101, SB-392 and RAR films as determined by the work described here.

In the following Sec. II, we describe a method for the absolute sensitometric calibration of x-ray spectroscopic films and present graphs and tables for density vs normal-incidence exposure data at nine photon energies for the five film types. Also presented here are semi-empirical equations derived from the mathematical models developed in Part I of this work which introduce generally the dependence upon photon energy and upon the angle of incidence of the exposing x-radiation. In Sec. III, we present a relatively simple definition and method of measurement for spectroscopic film resolution and suggest resolution limits for the film types studied. In Sec. IV, we discuss the effect of batch-to-batch variation of film characteristics, concluding that each new batch should be calibrated at a few normalizing points for precise, absolute spectrometry. We present comparisons of our film calibrations with those reported from other laboratories for similar film types. In Appendix A is presented data which relates the specular densities, as required for spectroscopic film calibration (and as measured directly in this work) to diffuse density values that may be alternatively applied in comparing ours to other film

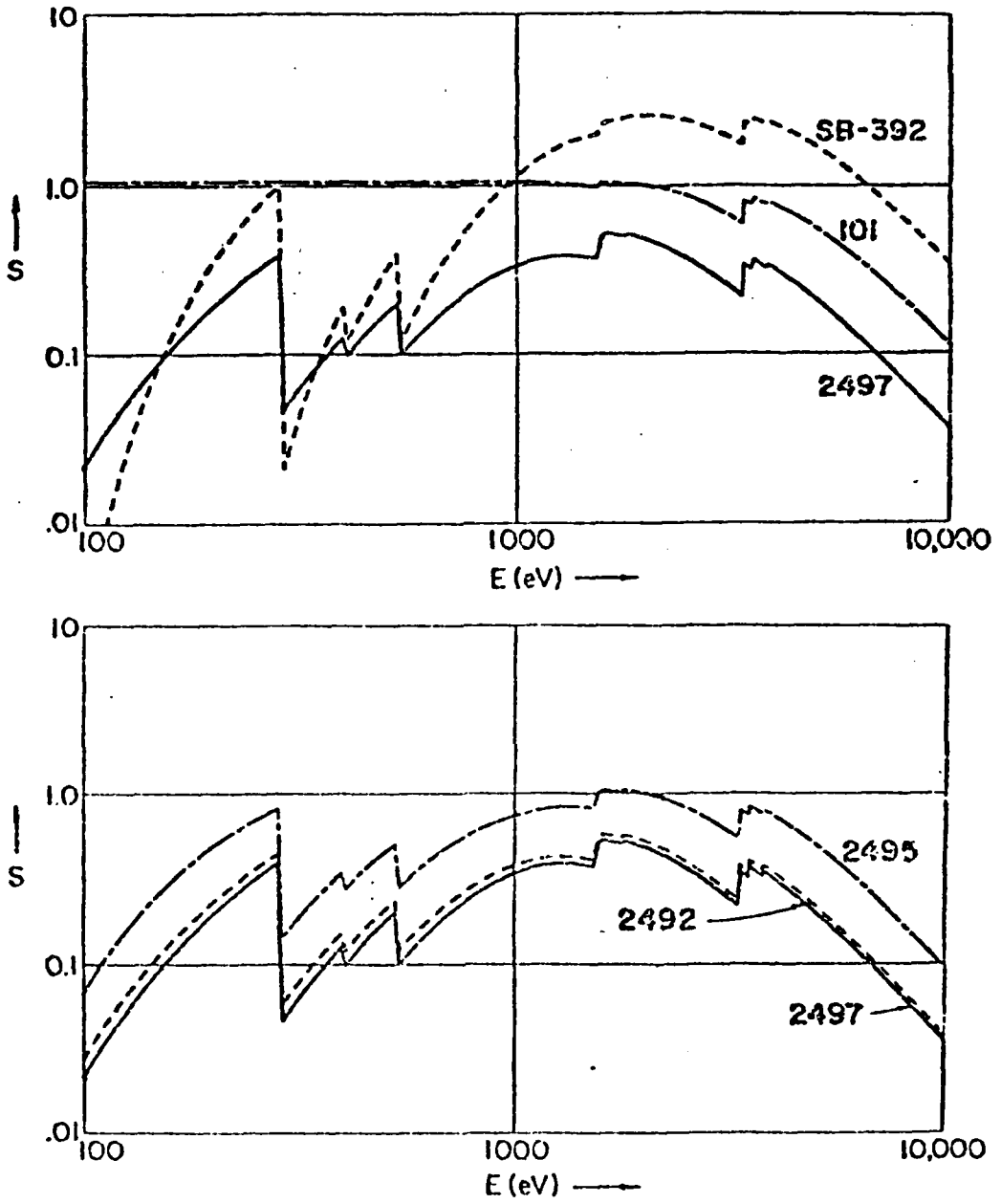

Figure 1. Comparison of the sensitivities of the five investigated spectroscopic films for the 100-10,000 eV photon energy region. Sensitivity is defined here as the reciprocal of the exposure, I (photons/μm^2) that is required to establish a specular density of 0.5. These curves have been developed in this work.

characterizations. In Appendix B the film processing procedures that have been followed are described. Finally, in Appendix C are presented tables for the five films of density vs exposure data calculated at regularly fine-spaced intervals in photon energy.

II. SENSITOMETRIC CALIBRATION OF X-RAY SPECTROSCOPIC FILMS

For quantitative low-energy x-ray spectroscopy, an accurate relationship must be established between the microdensity values (within slit widths of 20-100 μm) and the corresponding exposures (in units presented here as photons/μm^2) and the photon energy. Generally this requires microdensitometer measurements using numerical apertures for the objective and the illumination lenses of about 0.1-0.25 values. For such densitometry, effectively all of the absorbed and scattered light is subtracted from the incident light beam to define the resulting transmitted beam. The measured ratio of the transmitted to incident light, τ, then yields essentially the specular optical density value, D, which is defined by the relation

$$D = \log_{10}(1/\tau) \ . \qquad (1)$$

If all of the light that is scattered in the forward direction is included in the measurement of the transmitted beam, the corresponding diffuse optical density that is calculated using Eq. (1) is a somewhat

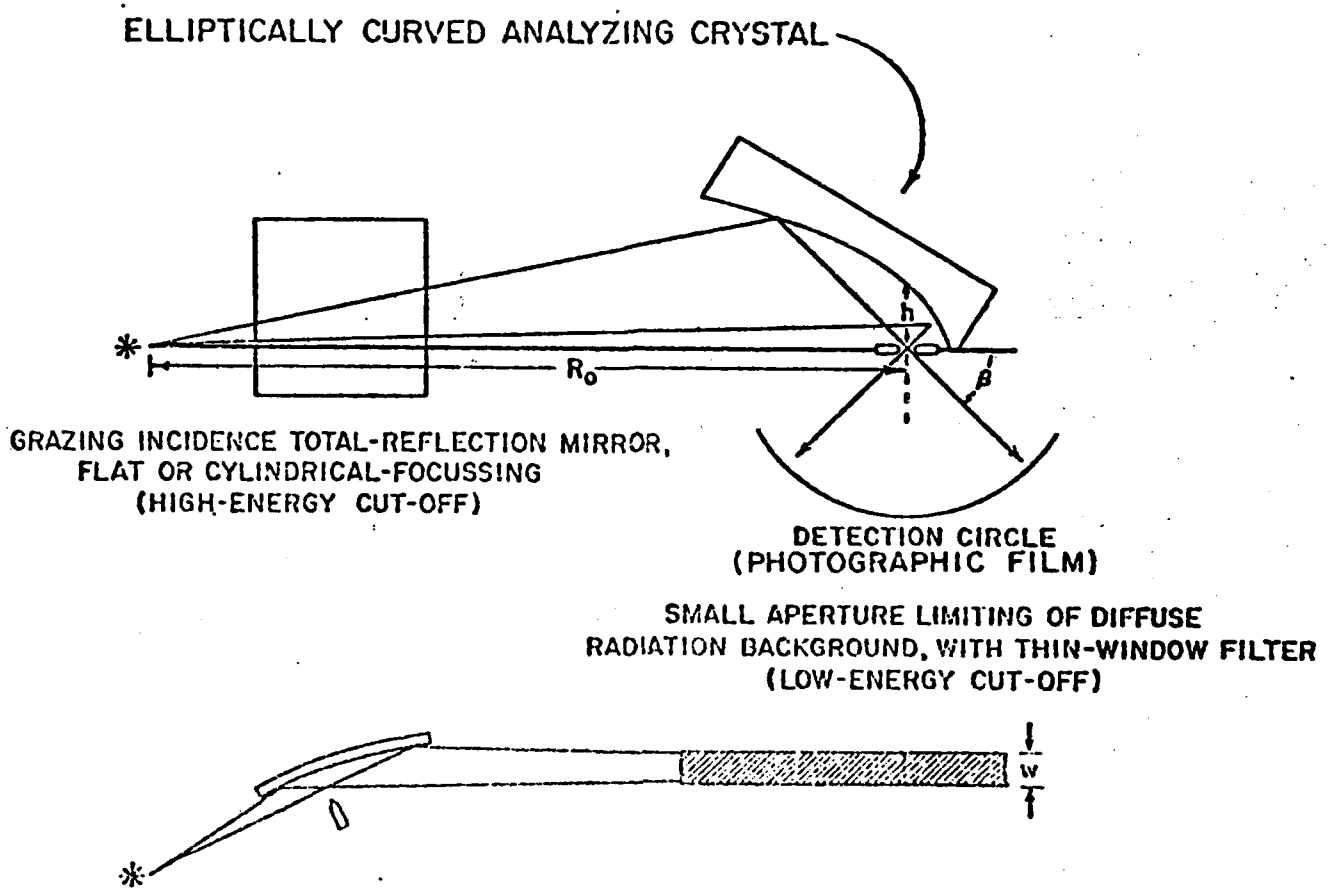

Figure 2. The elliptical analyzer spectrograph that has been used to generate a normal-incidence line spectra in the 100-10,000 eV x-ray region. (An x-ray line source and the scatter aperture are located at the respective focal points for an elliptically curved cylindrical crystal analyzer.) A spectrum is recorded on a film located along the detection circle. A corresponding absolute intensity spectrum is measured by translating a flow-proportional counter along the same circle. The specular density on a photographically recorded peak is related to the absolute intensity (photons/μm^2) and are measured using matched microdensitometer and proportional counter slits of widths that are small as compared with the spectral line width. (For the measurements described here the mirror monochromator was not required.)

smaller value. Often the diffuse densities are reported in the literature that characterizes a particular photographic material. For the five films studied here, the relationship between specular and diffuse densities have been experimentally determined and are presented in Appendix A. It should be emphasized, however, that it is specular density that is directly measured in most analyses of photographically recorded spectra.

An "operational" method has been developed for the specular microdensity calibration of spectroscopic films which is based upon a direct comparison of the photographically recorded spectrum to the corresponding measured absolutely calibrated (photons/sec-μm^2) spectrum. As illustrated in Fig. 2, this is accomplished by establishing along a normal incidence detection circle a Bragg reflected spectrum by means of an elliptically curved, cylindrical crystal. A small slit x-ray source and a scatter aperture are located at respective focal points for the given elliptical analyzer profile. A detailed description of this elliptical analyzer spectrograph, including that of the crystals and multilayers employed for establishing the normal-incidence detection of spectra in the 100-10,000 eV region, has been recently presented in another report.[5] Also described there are the procedures by which the absolute spectral intensities are obtained using a calibrated, flow proportional counter that is scanned along the detection circle (using

a goniometer with its axis through the focal point at the scatter aperture). The flow proportional counter is "pressure tuned" and calibrated for absolute photon counting by a method which has also been described previously.[6] Peak intensities and corresponding microdensities are measured with matched microdensitometer and proportional counter slit systems, with slit widths that are set to be small as compared with the instrumental spectral line widths (~100 μm). Peak intensities and microdensities are compared on spectral lines that are recorded at a series of exposure times under constant and known x-ray spectral line intensities.

Characteristic x-radiations at nine photon energies in the 100-2000 eV region were obtained using demountable x-ray tube anodes[6] which provided broad source, large-angle illumination of the source slit. The anodes were of pure metals except for the graphited and anodized aluminum anodes which provided the characteristic C-Kα (277 eV) and the O-Kα (525 eV) radiations. The other characteristic photon energies were Be-Kα (109 eV), Mo-Mζ (193 eV), Cr-Lα (573 eV), Fe-Lα (705 eV), Cu-Lα (930 eV), Al-Kα (1487 eV) and Mo-Lα (2293 eV). Appropriate filters and x-ray tube anode voltages were selected to minimize any high-order Bragg reflected line or continuum background that might be associated with the measured spectral lines. An analysis of the proportional counter pulse-height spectrum was applied to

establish that any background remaining at a given spectral line was first-order diffracted and essentially of the same photon energy as that of the line itself. For this reason, peak intensities and microdensities did not require correction for extraneous x-ray background and were considered totally characteristic of the given spectral line photon energy.

The measurement procedure was as follows: The absolute photons/sec-μm^2 counting rates on the spectral lines were set by adjusting the x-ray tube power to yield line intensities of the order of several thousand counts per second. The source was then monitored for constancy by moving the counter to the direction of zero -angle, stopping the beam down in this position by means of a fine slit at the counter window to yield approximately the same counting rate levels as those for the reflected lines. A film cassette was then moved into place with the film to be exposed along the same detection circle and a multiple exposure series was made using a spooled film transport controlled through a flexible cable and magnetic coupled feedthrough to outside the vacuum chamber. After each exposure, the diffracted line intensities were measured again, and, if necessary, a small drift correction for this intensity was made. Ten or more density vs exposure points were taken at each of the nine photon energies for each film. (It was found necessary to spray a thin film of static charge

eliminating solution upon the back surface of the 101-07 film which has no overcoat protection in order to eliminate the static discharge background exposure associated with transporting this type of film in vacuum.) Manufacturer-recommended film processing procedures were followed and these are described in Appendix B.

Repeated microdensitometer measurements were made using instruments with 0.1 numerical apertures for both the illumination and the transmission beam cones. One set was measured at the University of Hawaii on a microdensitometer with a 100 μm slit (Boller & Chivens Microphotometer, Model 14213). Other sets were measured at the Sandia National Laboratories, Albuquerque, and at the Lawrence Livermore National Laboratory using a 30 μm slit and integrating to the same total slit size as that of the first measurements. (The instruments used for these measurements were the Photometric Data Systems Model 1010 Microdensitometer.) We found no significant differences among these independent measurements of film densities.

These data were computer-plotted as log D vs log I, D vs I and D vs log I. Examples of these initial plots for the five films exposed to O-Kα (525 eV) are shown in Figs. 3 through 7. The onset region, plotted as D vs I, must allow a linear extrapolation to the origin and this constitutes a check on the background subtraction that yielded these net densities from the measured gross

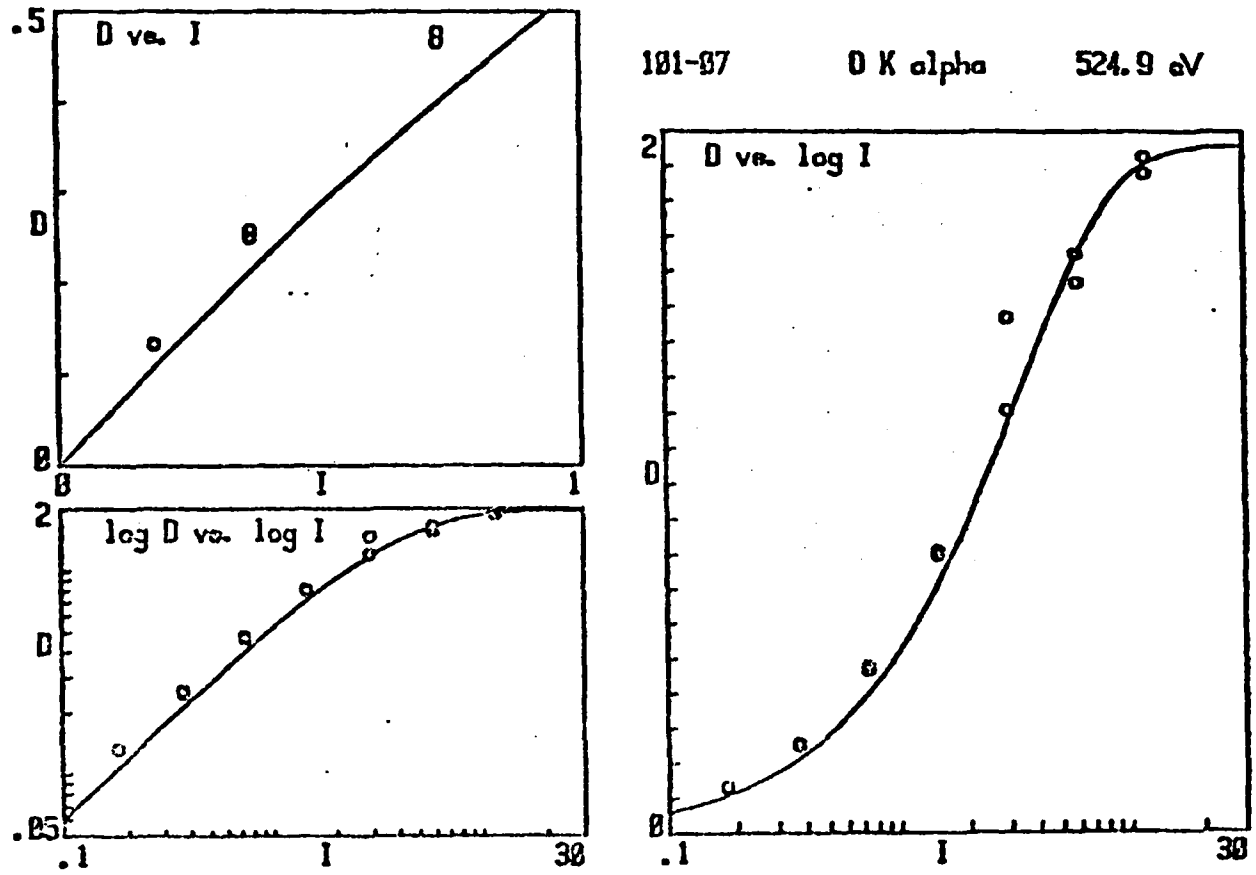

Figure 3. The measured D vs I data were obtained for the five films at nine photon energies and were computer-plotted as illustrated here for the 101-07 film at the O-K α (525 eV) photon energy The smooth curves have been generated by the universal, semi-empirical equation developed in this work for this particular film.

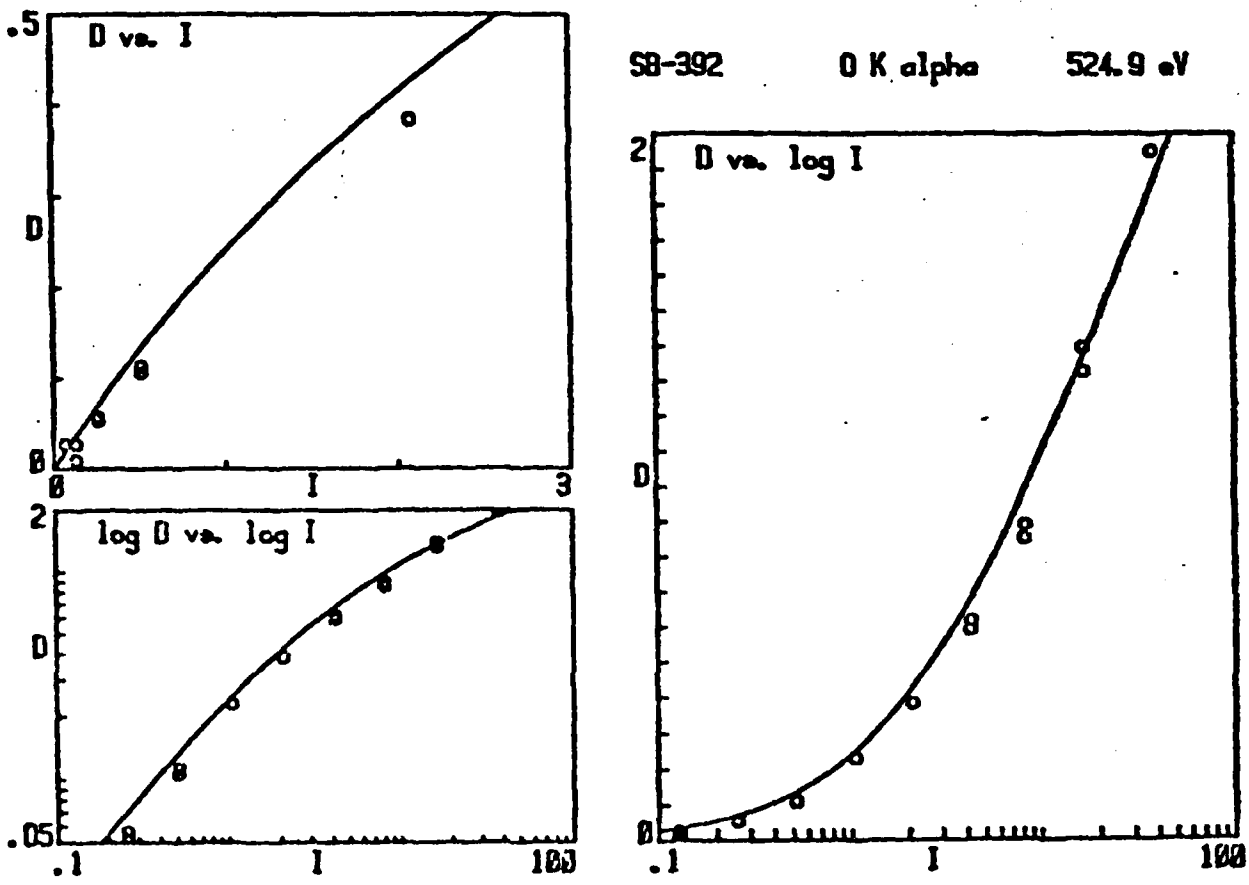

Figure 4. For the SB-392 film and as described for Figure 3.

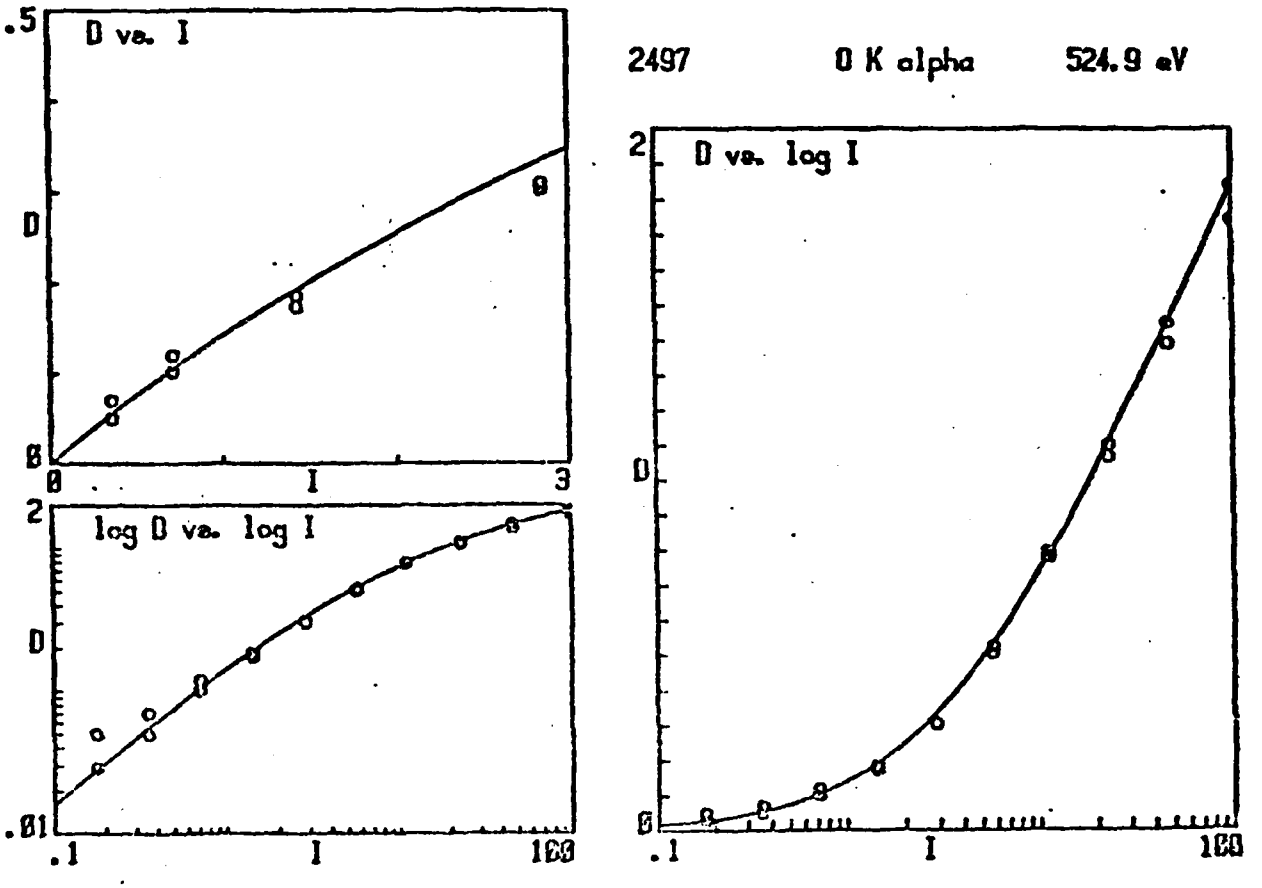

Figure 5. For the RAR-2497 film and as described for Figure 3.

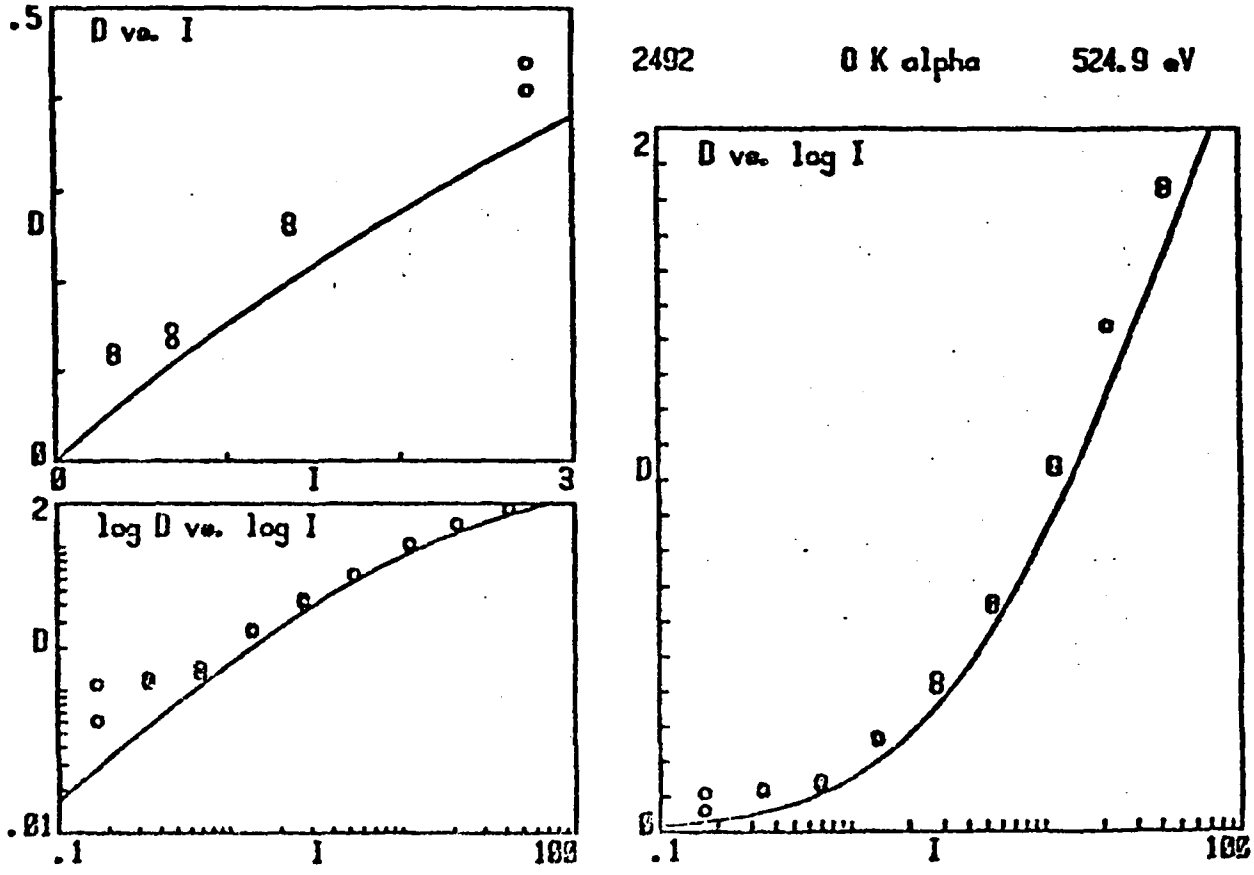

Figure 6. For the RAR-2492 film and as described for Figure 3.

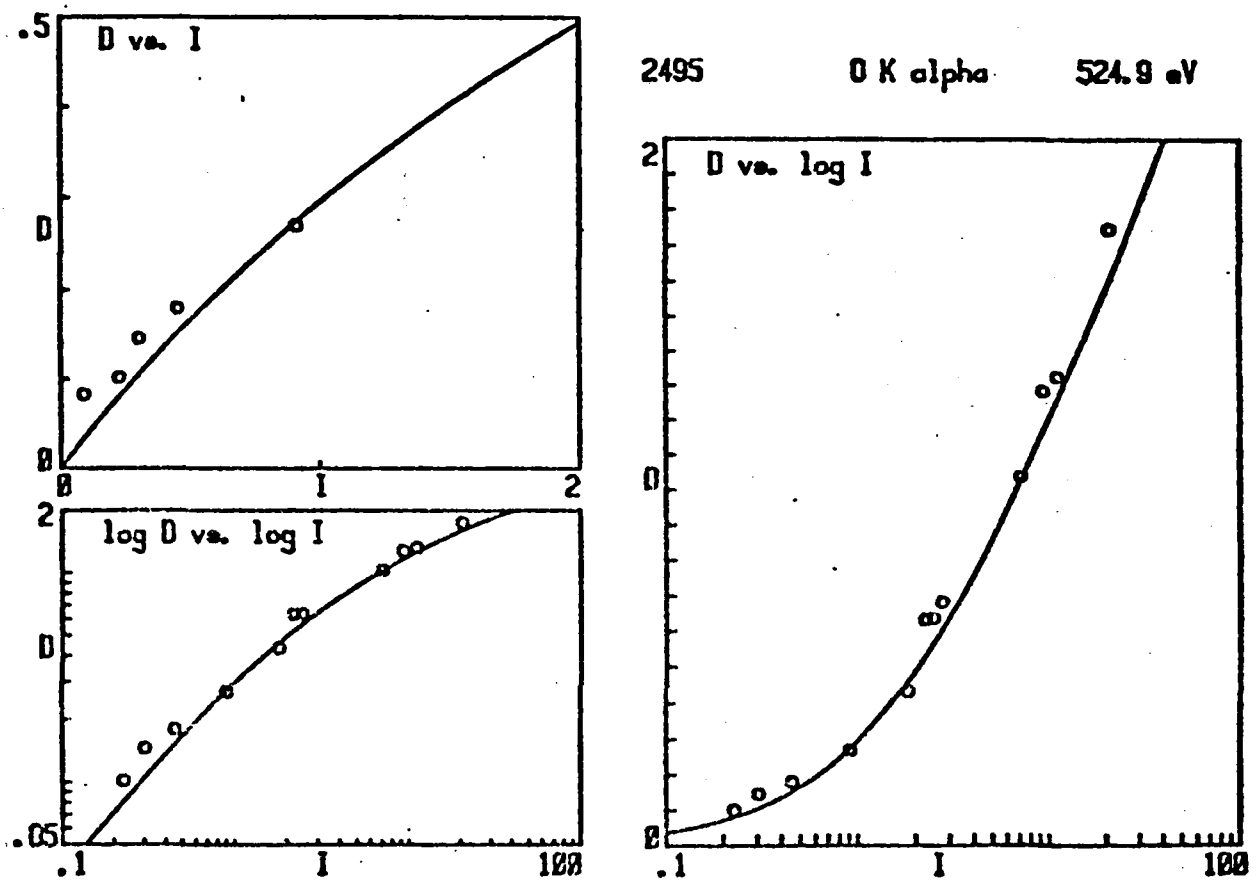

Figure 7. For the RAR-2495 film and as described for Figure 3.

densities. The correction to net densities involved cancelling from the measured transmission the transmission of an unexposed portion of film in order that the resulting transmission, τ, be the result of only the effect of the exposed and developed grain density as defined by Eq. (1). (Also plotted in Figs. 3 through 7 are the semi-empirical model curves obtained as described below.)

In Tables 1 through 5, we present for the five films the averaged density vs normal incidence exposure data for the nine photon energies in the 100-2000 eV region. (Also presented in Tables 10-14 in Appendix C at regularly spaced energy intervals in the extended 100-10,000 eV region.) Listed on these tables are letters referring to the characteristic abosorption edge energies given in Table 6 for the silver bromide and for the carbon, nitrogen and oxygen constituents of the gelatin in the photographic emulsion. At these photon energies, significant discontinuities may occur in the film sensitivity vs photon energy curve. As may be noted in Fig. 1, the C, N and O edges are not in evidence for the 101 type film which consists of essentially a monolayer of silver bromide grains with no absorbing overcoat of gelatin (as is present for the emulsion film types).

The significant systematic errors occurring in these calibrations were usually in the determination of the absolute photon intensities. Such errors were discovered be comparing plots of I vs E at constant density, D, for the five films. If calibration errors

TABLE 1.

101-07 FILM--EXPOSURE, I(photons/μm²)

NET DENSITY, D
(SPECULAR-0.1×0.1 nA)

PHOTON ENERGY, E(eV)
WAVELENGTH, λ(Å)

D

E(eV)	0.2	0.4	0.6	0.8	1.0	1.2	1.4	1.6	1.8	λ(Å)	
A											A
109	0.34	0.73	1.17	1.68	2.29	3.04	4.02	5.44	8.07	114.27	
193	0.34	0.73	1.17	1.68	2.29	3.04	4.02	5.44	8.07	64.37	
277	0.34	0.73	1.17	1.68	2.29	3.04	4.02	5.44	8.07	44.76	
C											C
525	0.34	0.73	1.17	1.68	2.29	3.04	4.02	5.44	8.07	23.62	
573	0.34	0.73	1.17	1.68	2.29	3.04	4.02	5.44	8.07	21.64	
705	0.34	0.73	1.17	1.68	2.29	3.04	4.02	5.44	8.07	17.59	
930	0.34	0.73	1.17	1.68	2.29	3.04	4.02	5.44	8.07	13.34	
1487	0.37	0.78	1.25	1.80	2.45	3.25	4.30	5.83	8.64	8.34	
E											E
2293	0.39	0.83	1.33	1.91	2.60	3.45	4.56	6.18	9.16	5.41	

TABLE 2.

SB-392 FILM--EXPOSURE, I(photons/μm²)

NET DENSITY, D
(SPECULAR-0.1×0.1 nA)

PHOTON ENERGY, E(eV)
WAVELENGTH, λ(Å)

D

E(eV)	0.2	0.4	0.6	0.8	1.0	1.2	1.4	1.6	1.8	2.0	λ(Å)	
A												A
109	3.82 01	9.59 01	1.83 02	3.14 02	5.12 02	8.12 02	1.26 03	1.94 03	2.97 03	4.52 03	114.27	
193	9.83-01	2.34 00	4.22 00	6.82 00	1.04 01	1.54 01	2.23 01	3.18 01	4.49 01	6.31 01	64.37	
277	3.41-01	7.78-01	1.34 00	2.06 00	2.98 00	4.16 00	5.68 00	7.63 00	1.01 01	1.33 01	44.76	
B												B
C												C
525	8.06-01	1.91 00	3.42 00	5.48 00	8.30 00	1.22 01	1.74 01	2.46 01	3.45 01	4.80 01	23.62	
D												D
573	1.83 00	4.43 00	8.13 00	1.34 01	2.09 01	3.15 01	4.67 01	6.82 01	9.88 01	1.42 02	21.64	
705	7.57-01	1.79 00	3.19 00	5.10 00	7.71 00	1.13 01	1.61 01	2.27 01	3.17 01	4.39 01	17.59	
930	3.41-01	7.76-01	1.33 00	2.05 00	2.96 00	4.13 00	5.62 00	7.53 00	9.99 00	1.31 01	13.34	
1487	1.82-01	3.97-01	6.50-01	9.49-01	1.30 00	1.73 00	2.24 00	2.86 00	3.62 00	4.55 00	8.34	
E												E
2293	1.45-01	3.12-01	5.06-01	7.33-01	1.00 00	1.32 00	1.70 00	2.17 00	2.75 00	3.48 00	5.41	

TABLE 3.

2497 FILM--EXPOSURE, I(photons/μm²)

NET DENSITY, D
(SPECULAR-0.1×0.1 nA)

PHOTON ENERGY, E(eV)
WAVELENGTH, λ(A)

D

E(eV)	0.2	0.4	0.6	0.8	1.0	1.2	1.4	1.6	1.8	2.0	λ(A)	
A												A
109	7.45 00	2.11 01	4.61 01	9.17 01	1.75 02	3.28 02	6.08 02	1.12 03	2.06 03	3.77 03	114.27	
193	1.60 00	3.98 00	7.53 00	1.28 01	2.07 01	3.24 01	4.99 01	7.59 01	1.15 02	1.72 02	64.37	
277	8.48-01	1.97 00	3.45 00	5.40 00	7.99 00	1.14 01	1.60 01	2.20 01	3.01 01	4.09 01	44.76	
B												B
C												C
525	1.48 00	3.64 00	6.77 00	1.13 01	1.80 01	2.76 01	4.17 01	6.22 01	9.19 01	1.35 02	23.62	
D												D
573	2.31 00	5.93 00	1.16 01	2.05 01	3.46 01	5.66 01	9.11 01	1.45 02	2.30 02	3.64 02	21.64	
705	1.51 00	3.68 00	6.80 00	1.13 01	1.78 01	2.70 01	4.04 01	5.97 01	8.73 01	1.27 02	17.59	
930	1.05 00	2.41 00	4.16 00	6.41 00	9.33 00	1.31 01	1.80 01	2.44 01	3.27 01	4.37 01	13.34	
1487	9.42-01	2.04 00	3.34 00	4.87 00	6.71 00	8.84 00	1.17 01	1.51 01	1.95 01	2.54 01	8.34	
E												E
2293	8.59-01	1.85 00	3.01 00	4.38 00	6.02 00	8.01 00	1.05 01	1.36 01	1.77 01	2.33 01	5.41	

TABLE 4.

2492 FILM--EXPOSURE, I(photons/μm²)

NET DENSITY, D
(SPECULAR-0.1×0.1 nA)

PHOTON ENERGY, E(eV)
WAVELENGTH, λ(A)

D

E(eV)	0.2	0.4	0.6	0.8	1.0	1.2	1.4	1.6	1.8	2.0	λ(A)	
A												A
109	6.67 00	1.74 01	3.46 01	6.23 01	1.07 02	1.78 02	2.93 02	4.78 02	7.75 02	1.25 03	114.27	
193	1.47 00	3.48 00	6.22 00	9.98 00	1.51 01	2.21 01	3.17 01	4.48 01	6.28 01	8.73 01	64.37	
277	7.89-01	1.77 00	2.99 00	4.51 00	6.41 00	8.77 00	1.17 01	1.54 01	2.00 01	2.57 01	44.76	
B												B
C												C
525	1.36 00	3.19 00	5.65 00	8.95 00	1.34 01	1.93 01	2.73 01	3.80 01	5.24 01	7.17 01	23.62	
D												D
573	2.11 00	5.11 00	9.38 00	1.55 01	2.41 01	3.65 01	5.41 01	7.92 01	1.15 02	1.66 02	21.64	
705	1.39 00	3.24 00	5.70 00	8.98 00	1.33 01	1.91 01	2.68 01	3.71 01	5.08 01	6.89 01	17.59	
930	9.85-01	2.18 00	3.65 00	5.43 00	7.62 00	1.03 01	1.35 01	1.75 01	2.25 01	2.85 01	13.34	
1487	8.89-01	1.89 00	3.03 00	4.32 00	5.81 00	7.51 00	9.49 00	1.18 01	1.45 01	1.78 01	8.34	
E												E
2293	8.13-01	1.72 00	2.75 00	3.90 00	5.23 00	6.75 00	8.51 00	1.06 01	1.30 01	1.60 01	5.41	

TABLE 5.

2495 FILM--EXPOSURE, I(photons/μm²)

NET DENSITY, D
(SPECULAR-0.1×0.1 mA)

PHOTON ENERGY, E(eV)
WAVELENGTH, λ(A)

D

E(eV)	0.2	0.4	0.6	0.8	1.0	1.2	1.4	1.6	1.8	2.0	λ(A)
A											A
109	2.73 00	7.14 00	1.43 01	2.59 01	4.46 01	7.50 01	1.24 02	2.04 02	3.33 02	5.41 02	114.27
193	6.62-01	1.60 00	2.92 00	4.79 00	7.42 00	1.11 01	1.64 01	2.38 01	3.43 01	4.92 01	64.37
277	4.04-01	9.34-01	1.63 00	2.54 00	3.73 00	5.29 00	7.34 00	1.00 01	1.36 01	1.82 01	44.76
B											B
C											C
525	6.22-01	1.49 00	2.68 00	4.35 00	6.66 00	9.88 00	1.43 01	2.05 01	2.92 01	4.11 01	23.62
D											D
573	9.08-01	2.23 00	4.16 00	6.97 00	1.11 01	1.70 01	2.57 01	3.84 01	5.68 01	8.36 01	21.64
705	6.32-01	1.50 00	2.69 00	4.33 00	6.59 00	9.68 00	1.39 01	1.98 01	2.78 01	3.88 01	17.59
930	4.80-01	1.09 00	1.85 00	2.83 00	4.05 00	5.61 00	7.57 00	1.01 01	1.32 01	1.72 01	13.34
1487	4.36-01	9.34-01	1.51 00	2.16 00	2.92 00	3.80 00	4.83 00	6.03 00	7.46 00	9.16 00	8.34
E											E
2293	4.01-01	8.52-01	1.36 00	1.94 00	2.60 00	3.36 00	4.25 00	5.28 00	6.50 00	7.95 00	5.41

TABLE 6. Absorption Edges

EDGE	E (eV)
A. Br M_4	71
B. C K	284
C. N K, Ag $M_{4,5}$	398 - 402
D. O K	532
E. Br $L_{3,2}$	1553 - 1599
F. Ag $L_{3,2}$	3351 - 3526

were made, the corresponding I-point would be systematically off an average I vs E plot for all five films. (All films were measured at the same calibrated line intensities.) After correcting for these systematic errors, the residual statistical errors in the D vs I data were averaged out by least squares fitting of the D vs I data to polynomials of the form

$$\log D = A + B \log I + C(\log I)^2$$

The averaged density data were then plotted as "universal" curves (for an appropriate range of photon energies) by a procedure which has been developed in Part I of this work. These curves, along with the definitions of the appropriate scaling factors that account for the dependence upon photon energy, E, are presented in Figs. 9 through 12. For the determination of these scaling factors, β_1, α and β, (defined in Figs. 8 through 12) the linear absorption coefficients, μ_0 for gelatin, μ_1 for AgBr, and μ' for the heterogeneous emulsion, absorption data were calculated using data recently compiled by Henke et al.[7] The heterogeneous absorption coefficient has been derived in Part I to be

$$\mu' = \mu_0 - (1/d)\,\ln\{1 - V(1 - \exp[-(\mu_1 - \mu_0)d])\} . \quad (2)$$

This reduces to the linear absorption coefficient for a homogeneous system for which AgBr grain size, d, approaches a small value, viz.,

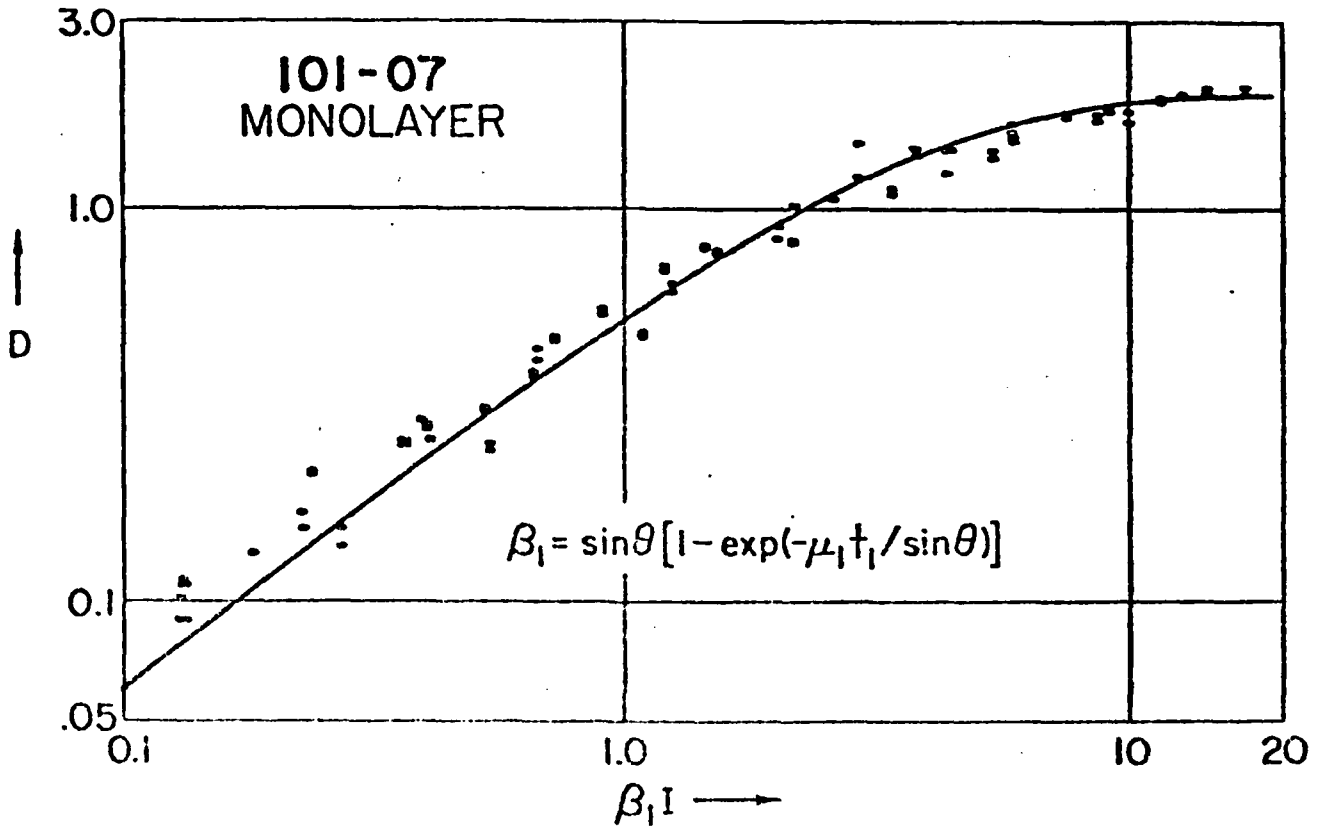

Figure 8. Universal plot, D vs $\beta_1 I$ for the 101-07 film in which the scaling factor, β_1, noted here, introduces the entire photon energy dependence. D-I data were used as measured at eight photon energies in the 100-1500 eV region. The smooth curve was obtained using the universal, semi-empirical Eq. (4).

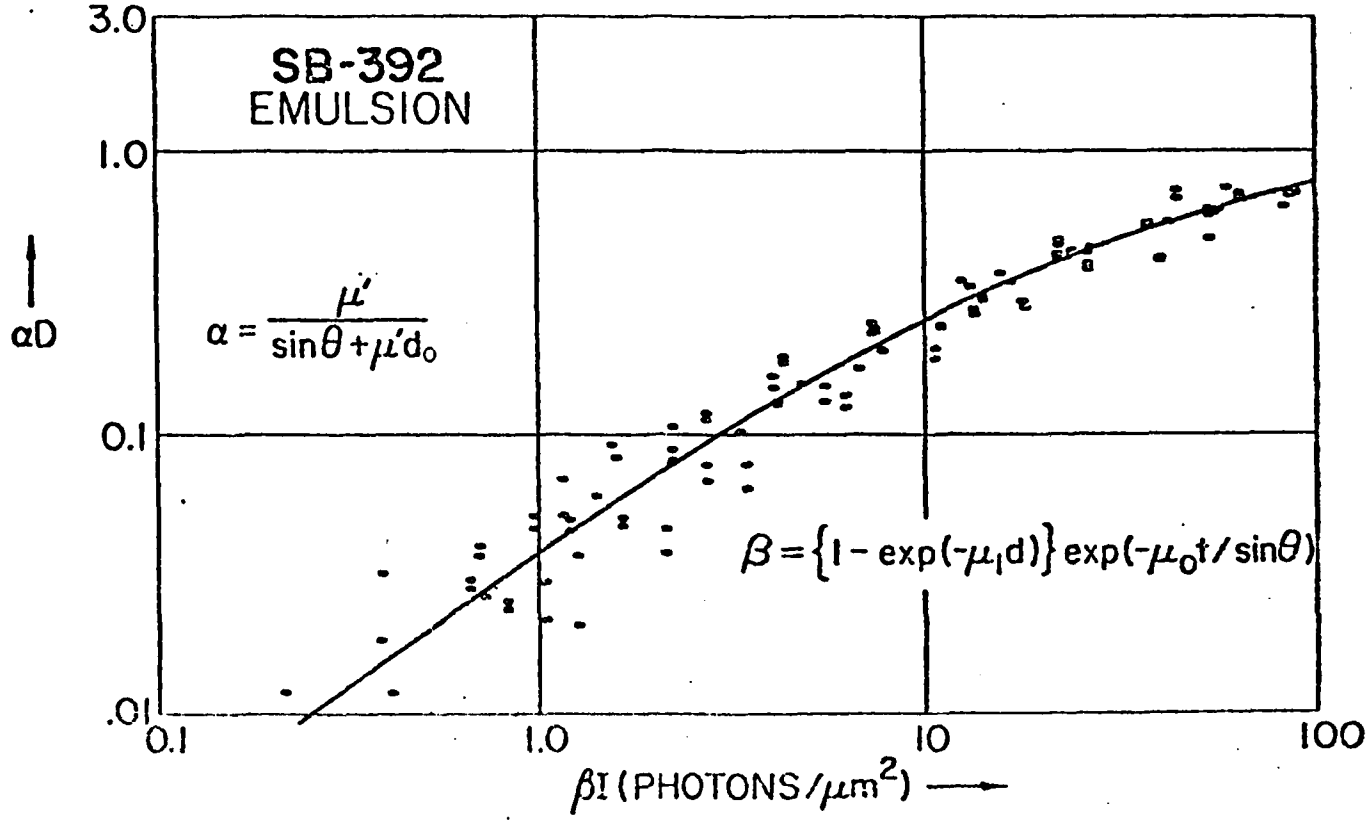

Figure 9. The universal plot for the SB-392 films, using D-I data measured at eight photon energies in the 100-1500 eV region and the energy-dependent scaling factors noted here, α and β. The smooth curve is a least squares fit of the semi-empirical Eq. (5).

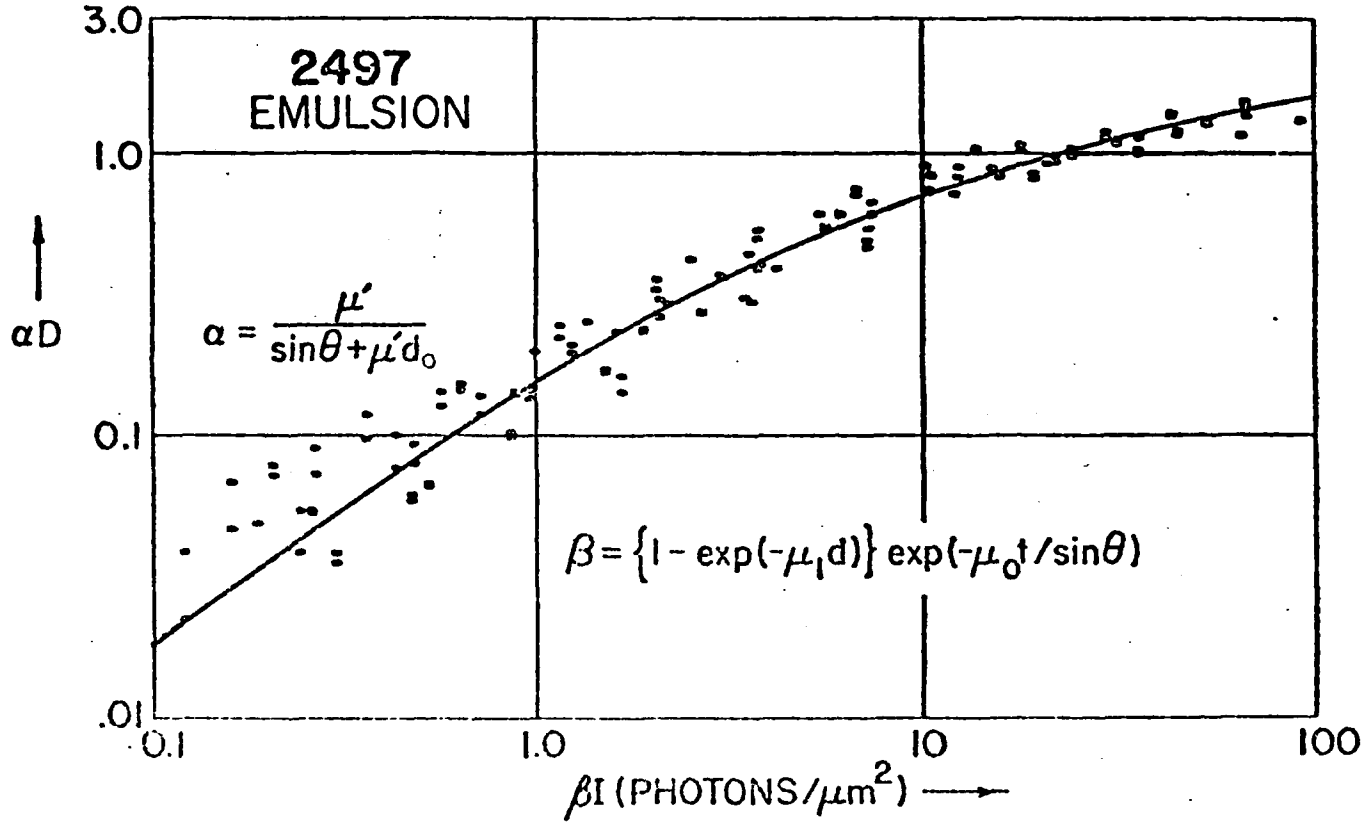

Figure 10. Universal plot for the RAR 2497 film and as described for Figure 9.

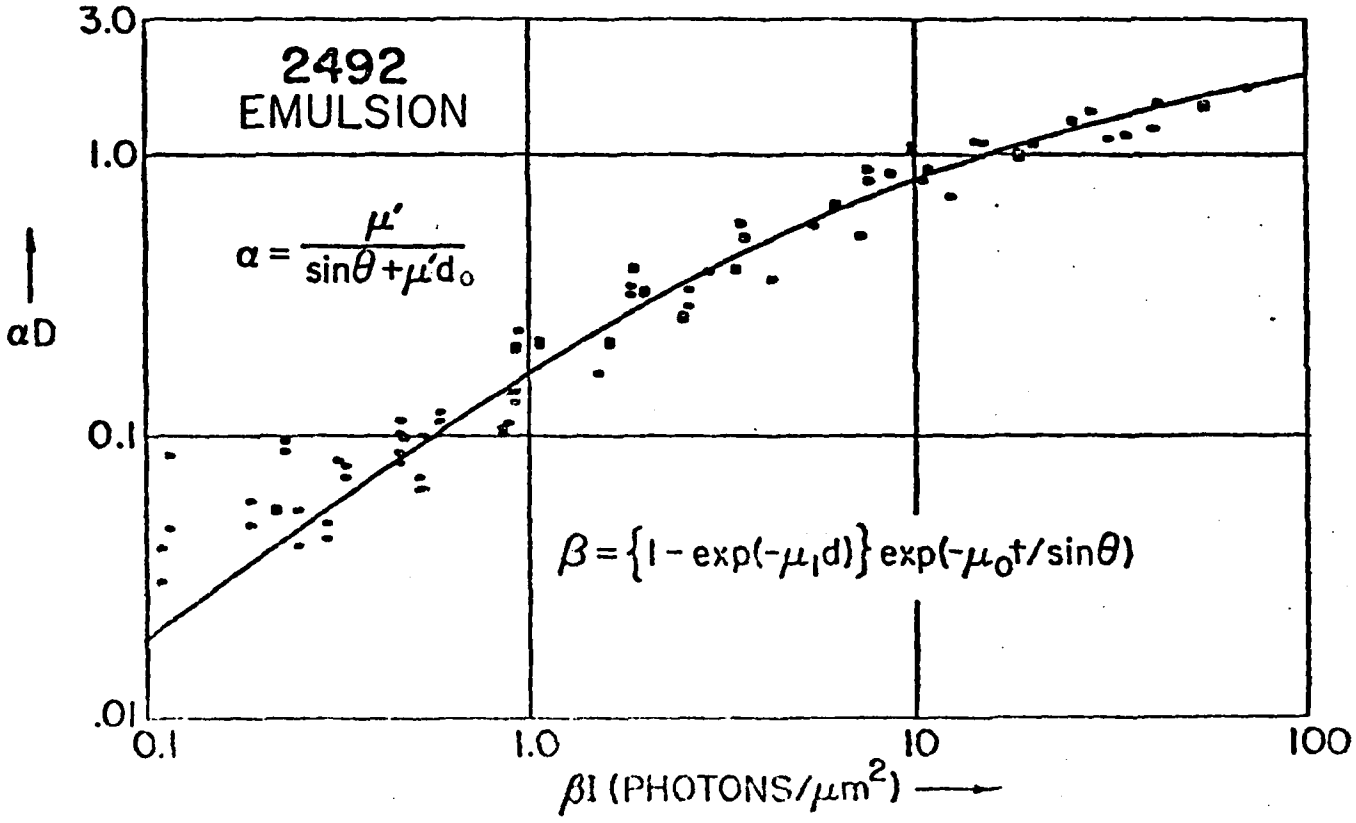

Figure 11. Universal plot for the RAR 2492 film and as described for Figure 9.

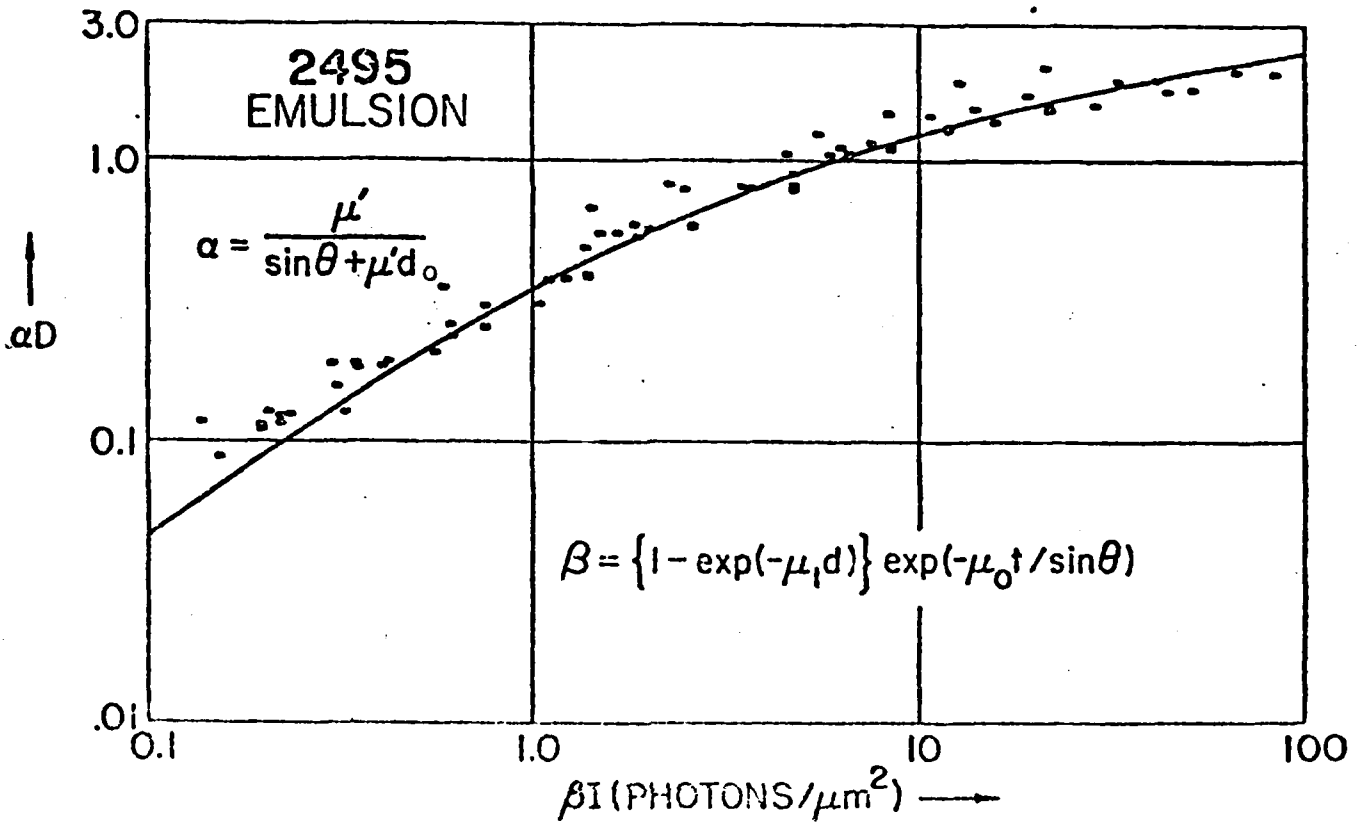

Figure 12. Universal plot for the RAR 2495 film and as described for Figure 9.

$$\bar{\mu} = (1 - V)\mu_0 + V\mu_1. \qquad (3)$$

A comparison of μ' and $\bar{\mu}$ for the heterogeneous and homogeneous models of the RAR 2492 film is presented in Fig. 13.

The film structure parameters, the grain size, d, the effective surface layer thicknesses, d_0 and t_1, and the AgBr volume fractions, V, that appear in the scaling factors α, β, andβ_1 were determined as described in Part I of this work by an iterative computer plotting technique in the generation of the universal curves.

As a test of the validity of the semi-empirical model equations that were derived in Part I, these were fit to the universal plots of Figs. 8 through 12, and presented therein as the smooth curves. For the monolayer type film (Kodak 101-07) the model equation is

$$D = a_1[1 - \exp(-b_1\beta_1 I)] \qquad (4)$$

And for the thick emulsion film, the model equation is

$$\alpha D = a\ell n\ (1 + b\beta I). \qquad (5)$$

(Note: To apply this relation, as for Figs. 9 through 12, only D vs I data for photon energies below 1500 eV were used for which it could be assumed that the photons were essentially absorbed within the emulsion.)

In establishing these least-squares fits, the parameters a_1, b_1, a and b were determined. In Table 7

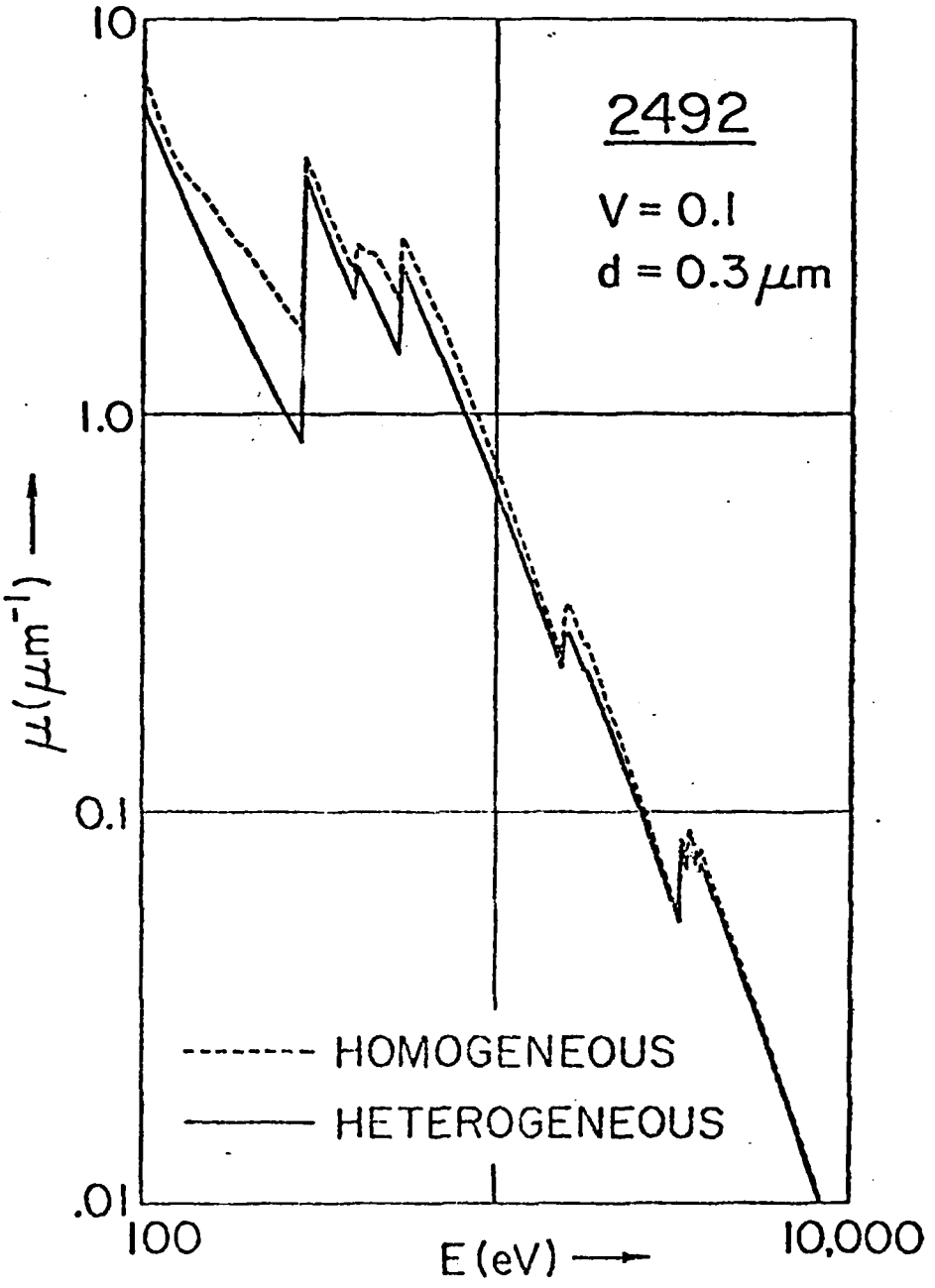

Figure 13. Comparing the heterogeneous linear absorption coefficient for the RAR 2492 film with the linear absorption coefficient for an amorphous system of the same volume fraction of AgBr. Note the appreciable difference in the low-energy x-ray region.

these parameters along with the empirical film structure parameters are presented for the five films that have been characterized in this study.

Finally, the semi-empirical equation that has been derived in Part I for thin emulsions (of thicknesses, T, such that not all of the incident photons are absorbed within the emulsion) becomes

$$\alpha D = a\ell n \frac{1 + b\beta I}{1 + b\beta I \exp(-\mu' T/\sin\theta)} \quad . \qquad (6)$$

The fitting described above was on the D vs I data that were directly measured for normal incidence intensities (for θ in the above equations set to 90°.) Because for many spectroscopic applications the incident intensities on the photographic films are not at 90°, the θ-dependence that has been included in these semi-empirical equations is essential. In order to test the accuracy of this predicted θ-dependence, we have measured, for a given photon energy, the D vs I data at a series of incidence angles. The method of measurement is illustrated in Fig. 14. A small line source of monochromatic radiation was generated by placing a thin wire (source of characteristic fluorescent line radiation) near the window of a demountable x-ray excitation source. The characteristic line radiation from this wire source was isolated by using an excitation radiation of energy only slightly higher than that excited and with

TABLE 7. Empirical Universal Equation Parameters

FILM	t(μm)	d(μm)	d_o(μm)	V	T(μm)	a(μm^{-1})	b(μm^2)
2497	0.3	0.3	0.6	0.1	7.0	.414	.454
2492	0.3	0.3	0.6	0.1	7.0	.527	.372
2495	0.3	0.3	0.6	0.2	7.0	.528	.926
SB-392	1.0	1.0	1.5	0.2	10.0	.285	1.41
		t_1(μm)				a_1	b_1(μm^2)
101-07		2.0				1.957	.3128

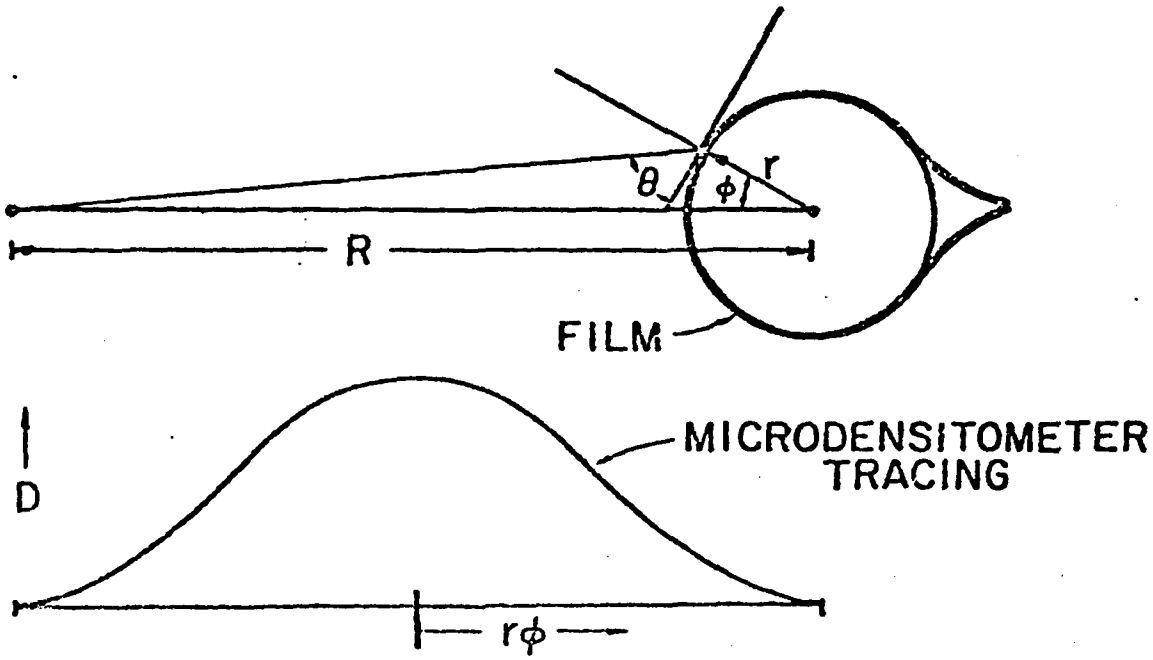

Figure 14. Experimental method for the determination of the effect of the angle of incidence, θ, upon exposure. The film, wrapped around a one-inch cylinder, is exposed by a filtered, flourescent line radiation source. The source is a thin wire placed near the window of an x-ray tube of effective excitation photon energy just sufficient to excite the desired characteristic flourescent line from the wire source.

appropriate filtering. It exposes a film which is wrapped under tension around a cylinder as shown. The variable angle of incidence, θ, is related to the distance $r\phi$ as measured along the developed film density pattern by the relation

$$\theta = \tan^{-1} \frac{\cos\phi + r/R}{|\sin\phi|} . \qquad (7)$$

And the intensity, I, at a given position along the film is given by

$$I = I(90^\circ) \frac{(R - r)^2}{R^2 + r^2 - 2Rr\cos\phi} . \qquad (8)$$

The normal intensity, $I(90^\circ)$, is determined from the value of the optical density, D, as measured at the center of the densitometer tracing, using the normal incidence D vs I calibration curves. With these relations, D vs θ plots may be generated for constant I and for a given photon energy. Such plots were presented in Part I of this work for the 101-07 and RAR 2497 films. Presented here in Fig. 15 is a D vs θ plot for the Kodak RAR 2492 film at the photon energy of Al-Kα (1487 eV). On all of these plots we have also presented the D vs θ curves for constant incident intensity, I, as predicted by the semi-empirical relations given above. It may be noted that the agreement between the experimental data and the predictions of the model relations is very satisfactory.

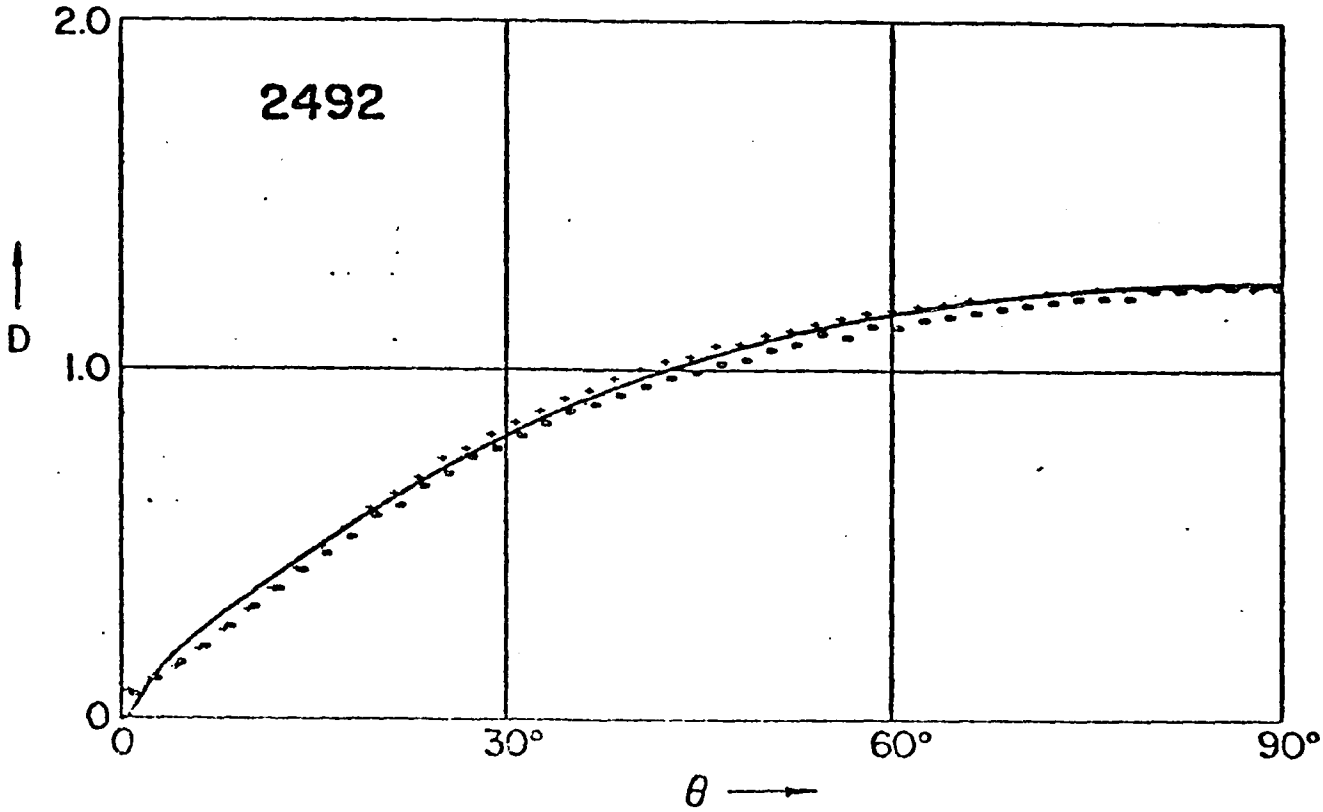

Figure 15. Comparing the D vs θ data (measured as illustrated in Figure 14) for constant incident intensity, I, and energy Al-K α(1487 eV)) with that predicted by the universal, semi-empirical relation, Eq. (6) for the RAR 2492 film.

III. DETERMINATION OF SPECTROSCOPIC FILM RESOLUTION LIMITS

For the calibrations described above, the proportional counter and microdensitometer slits were set equal to 100 μm and were small as compared with the spectral line widths generated by the low-energy x-ray spectrograph. (In a few instances, the x-ray source slit was broadened in order to ensure that the spectral line widths did satisfy this criterion.) It was then assumed that measured peak densities were precisely related to the corresponding absolute peak intensities through these D vs I calibrations for not only the measured lines but also for any that are broader. It is also important to know for how narrow the line and/or for how closely spaced adjacent lines may be before the effect of line spreading within the emulsion prevents an accurate determination of peak intensity when using the D vs I calibrations that have been presented here.

A simple test has been applied for the spectroscopic film resolution limits which is based upon an analysis of contact microradiograms that are made using a linear zone plate of gold bars to simulate an appropriate range of spectral line widths and spacings. The spacings between bars varied according to the Fresnel relation for the position of the bar edges of the zone plate that was

chosen

$$x \approx 100\sqrt{n}$$

These microstructures were provided for this work by Ceglio et al.[8] and were constructed by photolithographic techniques similar to those currently used in the microelectronics industry for the generation of integrated circuitry. A final electroplating procedure was applied to produce relatively thick gold bar microstructures. The gold bar structures, of about 8 μm thickness, are essentially opaque to the low-energy x-rays that were used to generate the contact microradiograms. The spacings and openings between the bars, x_2-x_1, and $x_{100}-x_{99}$, for the original 100-line zone plate mask were about 40 and 5 μm, respectively. After the final gold plating, the openings were accurately measured and were somewhat narrower (3-38 μm range). In Fig. 16 is shown a photomicrograph of a small section of the 2 x 4 mm zone-plate structure. In Fig. 17 is shown a microdensitometer tracing upon a contact microradiogram of this linear zone plate on RAR 2497 film with an exposure from a filtered flourescent source of Mg-Kα (1254 eV) radiation excited by Al-Kα (1487 eV) anode radiation. A microdensitometer slit width of 2 μm was used. It may be noted that as the openings in the zone plate became narrower, the peak densities decrease and the densities within the regions obstructed by the gold bars increase as a result of the line spreading. The difference between these densities, $D_{max}-D_{min}$, should be a constant for line widths above a defined spectroscopic film resolution limit and equal to

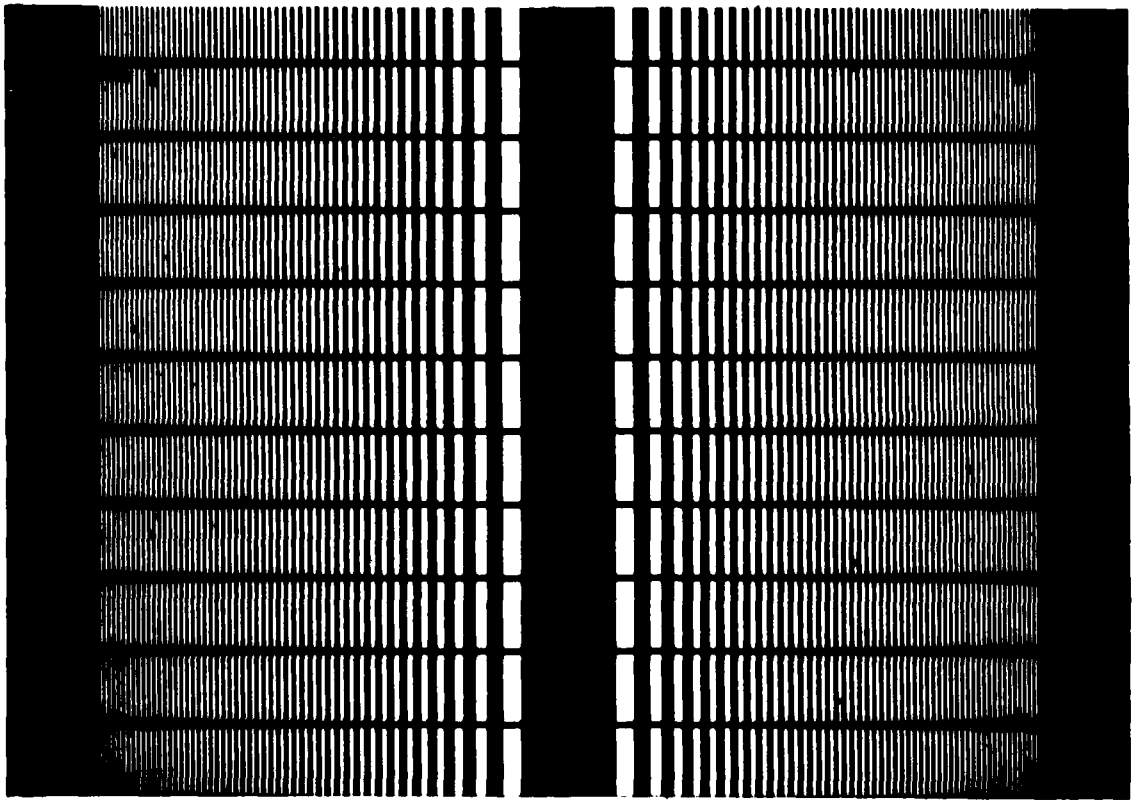

Figure 16. Photomicrograph of a section of the linear zone plate that has been applied to simulate exposures to spectral lines of varying width and spacing. The zone plate is formed by eight μm thick gold bars with openings that vary from 3 to 38 μm. The bars are essentially opaque to the x-radiation that have been used to generate the contact microradiograms (Mg-Kα (1254 eV)).

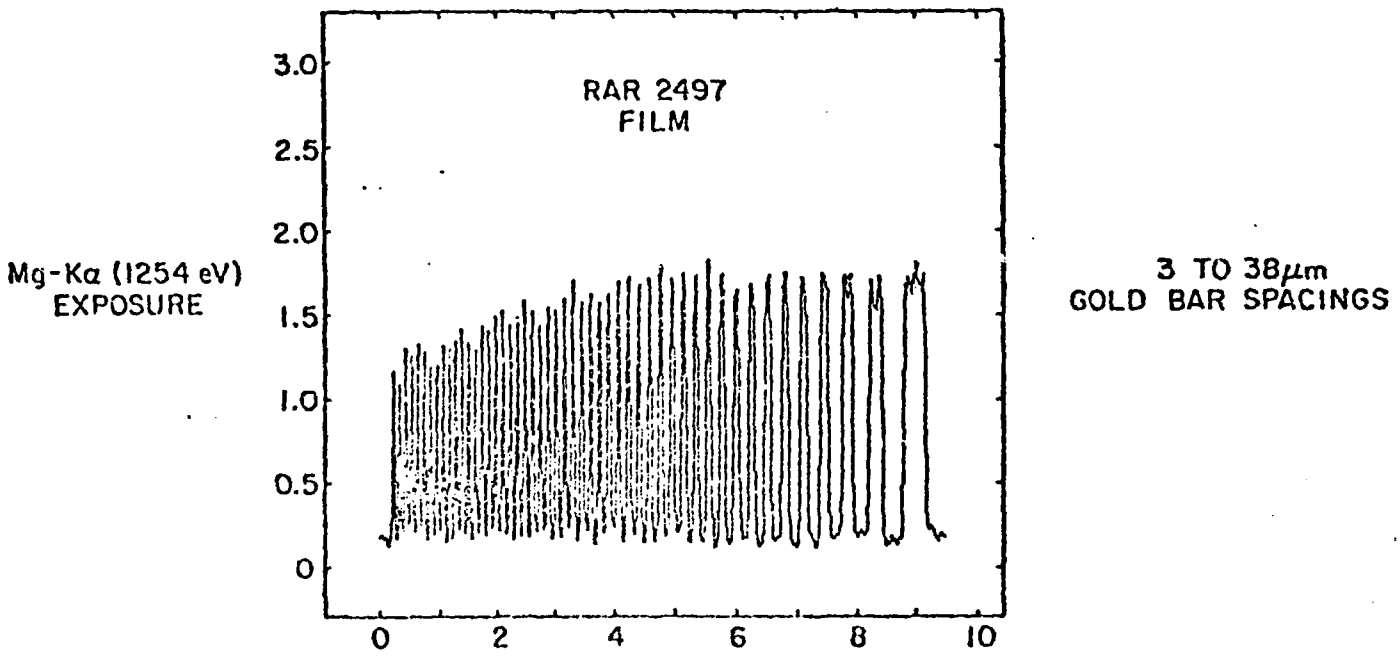

Figure 17. Densitometer tracing (with a 2 μm microdensitometer slit) upon a contact microradiogram of the linear zone plate using a uniform exposure of Mg-K α(1254 eV) filtered, flourescent radiation of small effective source size on the RAR 2497 film. The onset of the reduction of the peak densities as the slit widths decrease indicates the spectroscopic film resolution limit.

the net density as determined by the exposure, I, from the D vs I calibration. In Figs. 18, 19 and 20 we present plots of the $D_{max}-D_{min}$ values vs line width for contact microradiograms on the three film types, RAR 2497, 101-07 and SB-392. These have indicated spectroscopic film resolution limits of approximately 5, 10 and 15 μm, respectively at a density of about 1.5. Although this "operational" criterion for spectroscopic resolution is not precise, it does establish that all of the films that have been chosen here for low-energy x-ray spectroscopy can be applied to determine the absolute intensity distributions of typical spectral lines as generated by Bragg spectrographs in the 100-2000 eV region (widths > 20 μm).

IV. ACCURACY OF FILM CALIBRATIONS: CONCLUSIONS

Absolute x-ray spectrometry demands an accurate knowledge of the D vs I relation continuously with photon energy in order to translate a microdensitometer record of a spectrum into an absolute intensity distribution vs photon energy. In order to minimize the considerable amount of effort that is usually involved in the experimental calibration of spectroscopic films for the low-energy x-ray region, the approach that has been adopted here is to apply semi-empirical model equations which introduce the effect of the photon energy through the accurately known energy dependence of the x-ray

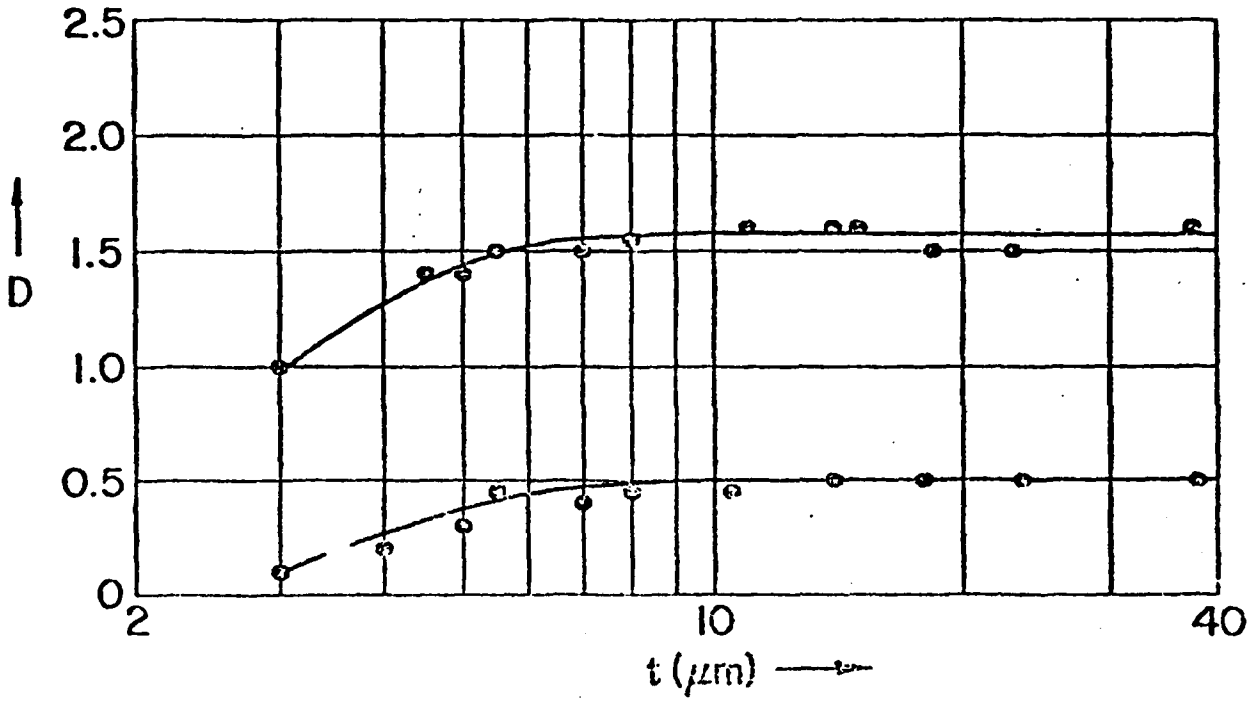

Figure 18. Plots of net microdensity values, $D_{max}-D_{min}$, vs zone plate slit width, t, for two contact microradiogram exposures on the RAR 2497 film as that described in Figure 17. The indicated spectroscopic film resolution limit was about 5 μm.

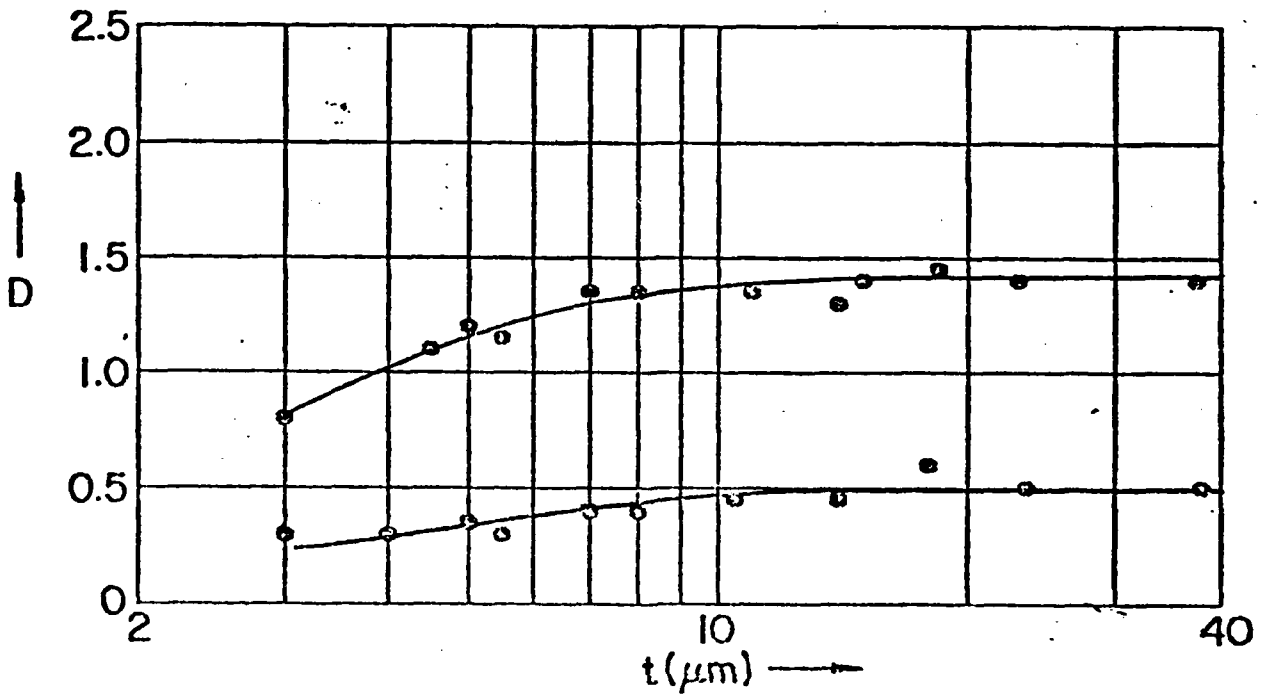

Figure 19. Plots of $D_{max}-D_{min}$ vs zone plate slit width, t, for two contact microradiogram exposures on the 101-07 film as that described in Figure 17. The indicated spectroscopic film resolution limit is about 10 μm.

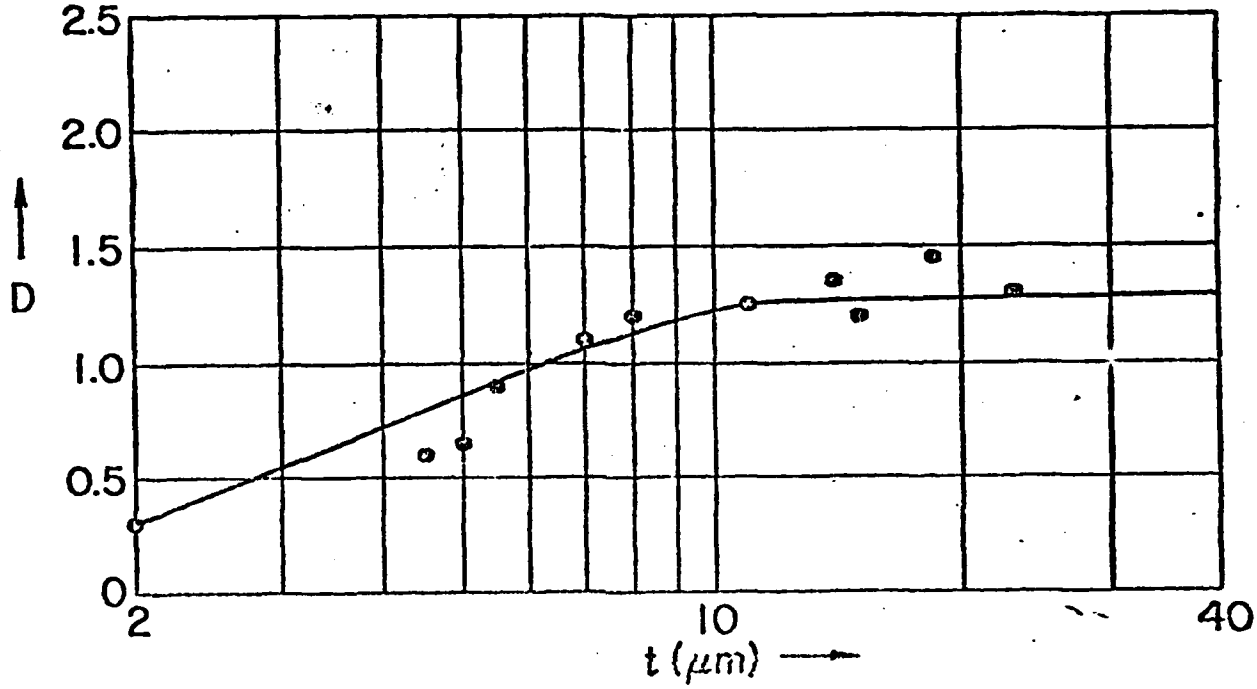

Figure 20. Plot of $D_{max}-D_{min}$ vs zone plate width, t, for a contact microradiogram exposure on the SB-392 film as that described in Figure 17. The indicated spectroscopic film resolution limit was about 15 μm.

absorption coefficients that characterize the film response. If the manufacturer would make available the approximate values for the required model parameters such as the average grain size, emulsion and overcoat thicknesses and volume fraction of the AgBr, the semi-emiprical method that has been presented in this work would require the measurement of D vs I at only a few photon energies. Unfortunately these data were not available and it was necessary to make these measurements at an extended number of photon energies. Nevertheless, it has been demonstrated in this work that: 1) universal plots that fully account for the photon energy dependence can be established, and 2) that these can be precisely fitted by relatively simple, semi-empirical equations involving only two adjustable parameters (a_1, b_1 or a,b). In Figs. 3-7, examples of experimental D vs I data are presented along with that predicted by the universal semi-empirical equations which indicate the typical accuracy of the present calibrations.

In Part I of this work it was noted that these parameters have the following, approximate theoretical dependence upon the film structure parameters:

For the monolayer film--

$$a_1 \sim M_0 S \sim S/d^2 \qquad b_1 \sim d^2$$

For the emulsion-type film--

$$a \sim N_0 S \sim V(S/d^3) \qquad b \sim d^2$$

(Here M_0 is the number of monolayer AgBr grains per unit area and N_0 is the number of AgBr grains per unit volume in the emulsion. V is the volume fraction of AgBr in the emulsion. S is an effective light absorption cross section of the developed silver grain clusters and d is an effective average diameter of the AgBr grain.) The implication of these approximate proportionalities are: 1) the only effect of the development process upon the sensitometric response is through the parameter a_1 or a by the growth of the cross section S; and 2) the effect of grain size, d, is most sensitively reflected in the values of a_1, b_1 and a, b.

In a batch-to-batch variation of film parameters, we would expect that the volume fraction V to be reasonably constant, but that the effective grain size could significantly vary. A small such variation may only slightly affect the values of the scaling factors (β_1, α and β) but could cause relatively large changes in the empirical parameters a_1, b_1, or a, b. It is therefore suggested here that for precise film calibration the following procedure be followed:

1) For a given film type the scaling factors be established as has been described in this work.

2) Then, for each new batch of film, a minimum set of D vs I data be obtained which permits, with the pre-established scaling factors, the generation of the universal plots of αD vs βI (or D vs $B_1 I$ for the monolayer).

3) Finally, a least-squares fitting of this universal plot then yields a new pair of fitting parameters, a_1, b_1, or a, b, which establish the universal, semi-empirical equations, $D = f(I,E,\theta)$ for the monolayer and the emulsion types of films. To assist in the above procedure for the description of the five films that have been characterized here, we have presented in Appendix C tables at regularly spaced intervals in photon energy, μ_0 for gelatin, μ_1 for AgBr; the scaling factors, β_1, α and β; and the universal functions relating D, I and E (for the particular film batches studied in this work).

Finally we would like to compare our film calibrations with those obtained independently upon similar photographic materials as reported from other laboratories.

The Kodak 101-01 film has been calibrated for the 100-1000 eV x-ray region using three characteristic line series from copper, iron and graphite targets which were excited by proton beam bombardment using the ion accelerator (IONAC) at the Lawrence Livermore National Laboratory [9] and flow proportional counter detectors. In Fig. 21 we present these experimental data, for each photon energy, as the number of photons required to establish a specular density of 0.5, 0.7 and 0.9. These densities corresponded to the reported diffuse densities of .35, .50 and .65 which were determined using the diffuse-to-specular density calibration curves presented

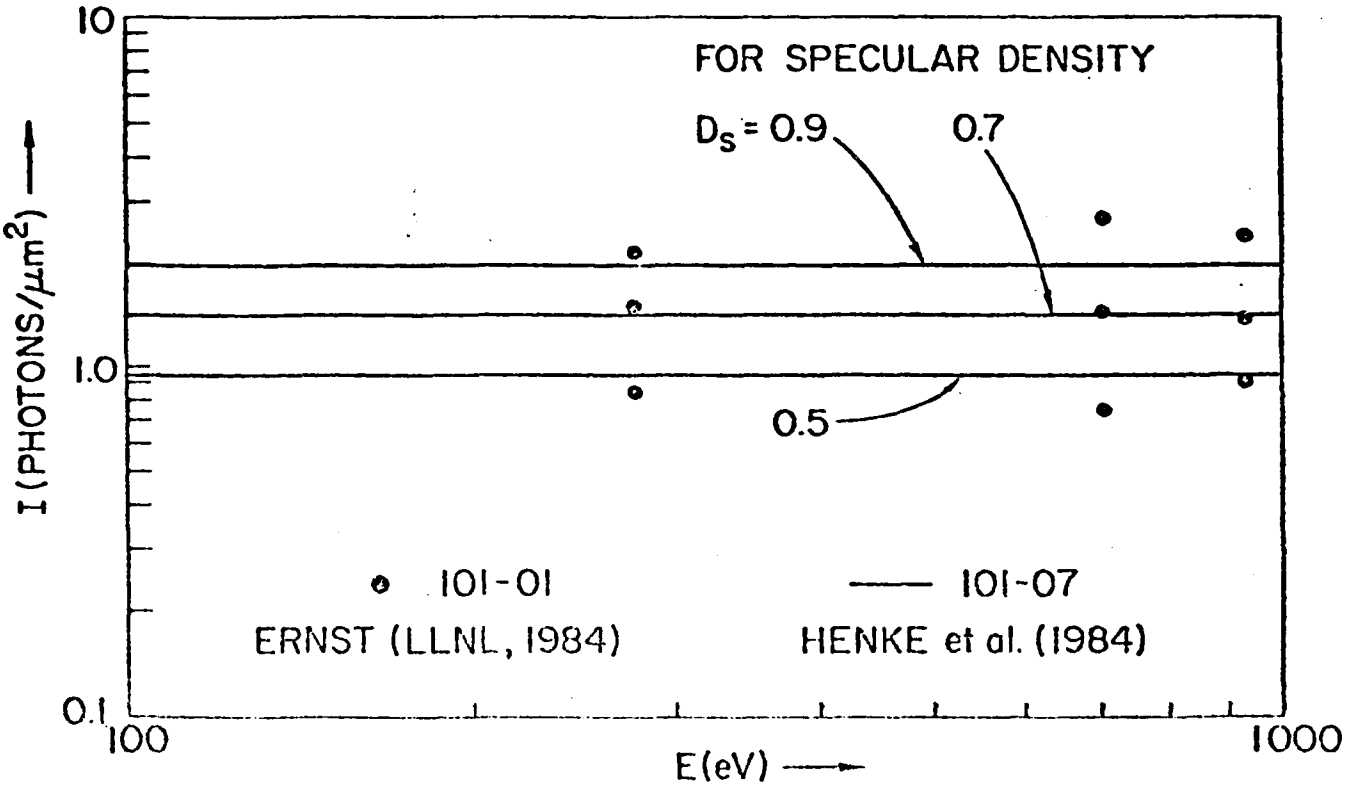

Figure 21. Comparing the intensities required to establish specular densities of 0.5, 0.7 and 0.9 as measured independently upon the similar film types 101-01 and 101-07 for the 100-1000 eV photon energy region.

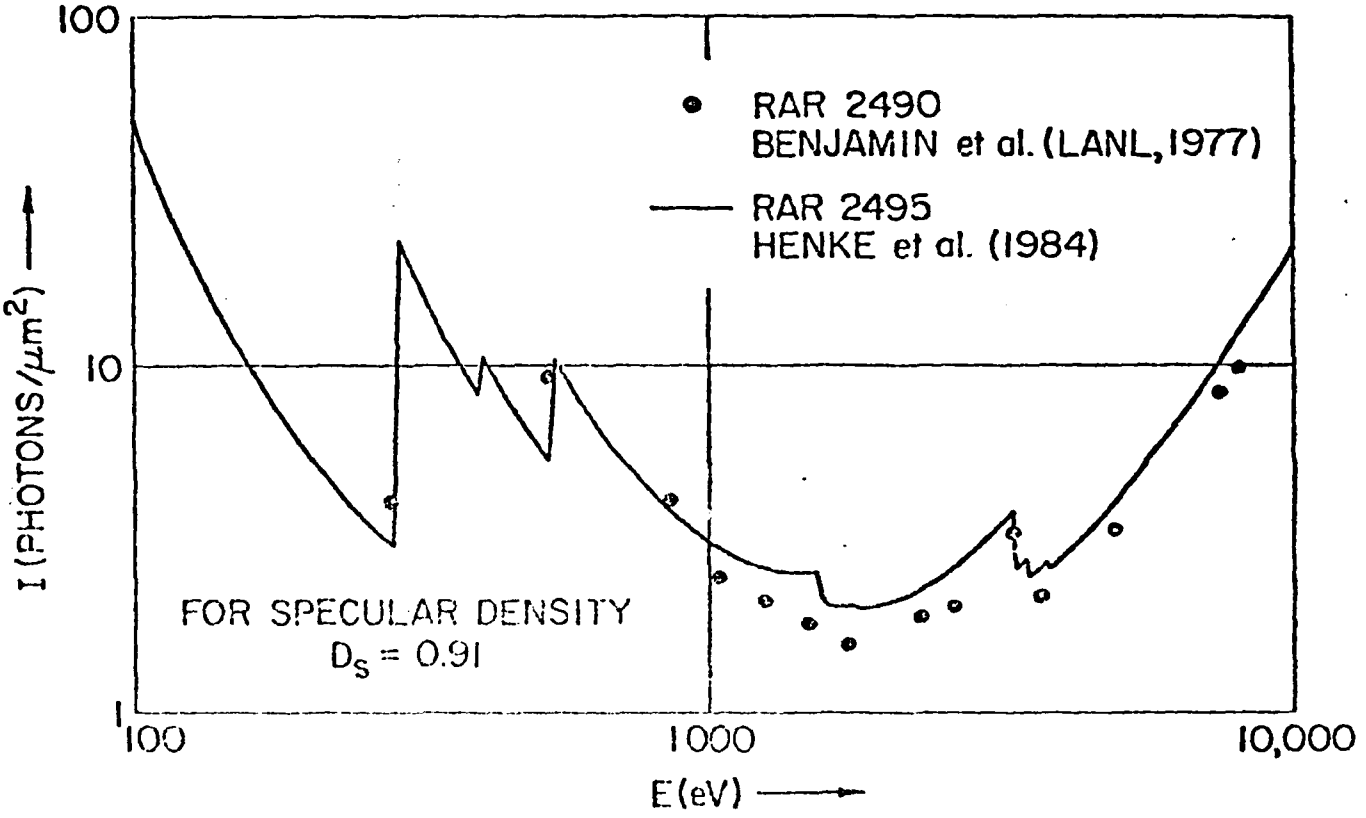

Figure 22. Comparing the intensities required to establish a specular density of 0.9 as measured independently upon the similar film types RAR 2490 and RAR 2495 for the 100-10,000 eV photon energy region.

in Appendix A. Along with these experimental points are our semi-empirical predicted curves (smooth) for the Kodak 101-07 film which was studied in this work. The principal difference between these film systems is that the 101-07 film is upon a 4 mil ESTAR base and the 101-01 film is upon a 5 mil acetate base.

The Kodak RAR 2490 film has been calibrated using filtered fluorescent x-radiations excited in a low-energy x-ray calibration facility at the Los Alamos National Laboratory. Averaged data was reported for the 100-10,000 eV region for the exposure required to establish a diffuse density of 0.5. This corresponds to our specular density value of 0.9 as determined for a similar type emulsion, the Kodak RAR 2495. In Fig. 22 we present these data along with our semi-empirical equation prediction for the RAR 2495 film. Although an absolute comparison is not possible here because two film types are involved, it should be noted that the model-prediction photon energy dependence for E > 2000 eV for such similar systems seems to be satisfactorily verified.

ACKNOWLEDGEMENTS

The authors gratefully acknowledge the invaluable assistance in this program of Priscilla Piano. Our thanks also to Robert Anwyl of Eastman-Kodak Company, Rochester, for his help in the initial planning of this

AD-A149 983 DEVELOPMENT AND APPLICATION OF LOW ENERGY X-RAY AND ELECTRON PHYSICS(U) HAWAII UNIV HONOLULU DEPT OF PHYSICS AND ASTRONOMY B L HENKE 06 DEC 84 3/3

UNCLASSIFIED AFOSR-TR-84-1270 AFOSR-84-0001 F/G 14/5 NL

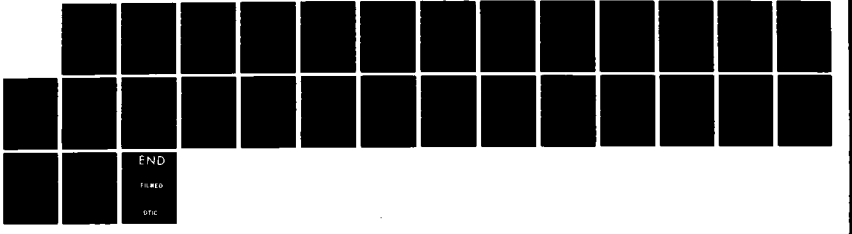

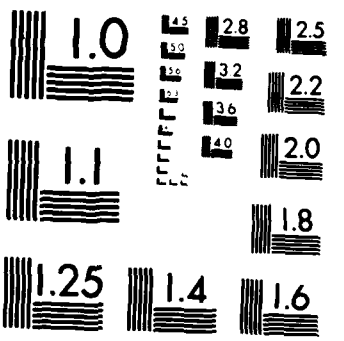

study, and to Al Widman of the Sandia National Laboratory for his help in the microdensitometer measurements. This program in Low-Energy X-Ray Physics and Technology is supported by the Air Force Office of Scientific Research under Grant No. 84-0001 and supplementally by the Department of Energy under Contract No. DE-AS08-83DP40181.

APPENDIX A: Specular Density vs Diffuse Density Calibrations

The density measured and referred to in the body of this work has been "specular density," D_s. Many laboratories use "diffuse density", D_d, and this appendix presents data to allow translation from one type of density to the other. The data presented here are in the form of plots of the ratio D_s/D_d vs D_d. (Figures A1-A10). Similar types of plots have been presented by others[10] for different types of films and there have been some theoretical and empirical treatments of the problem of relating specular to diffuse densities for different types of films[11]. The data presented here are directed specifically to the five types of films used and processed as described in Appendix B. The processing is important because of the dependence of these type of plots upon the light scattering cross section, S, as discussed above.[12] The specular density data were taken

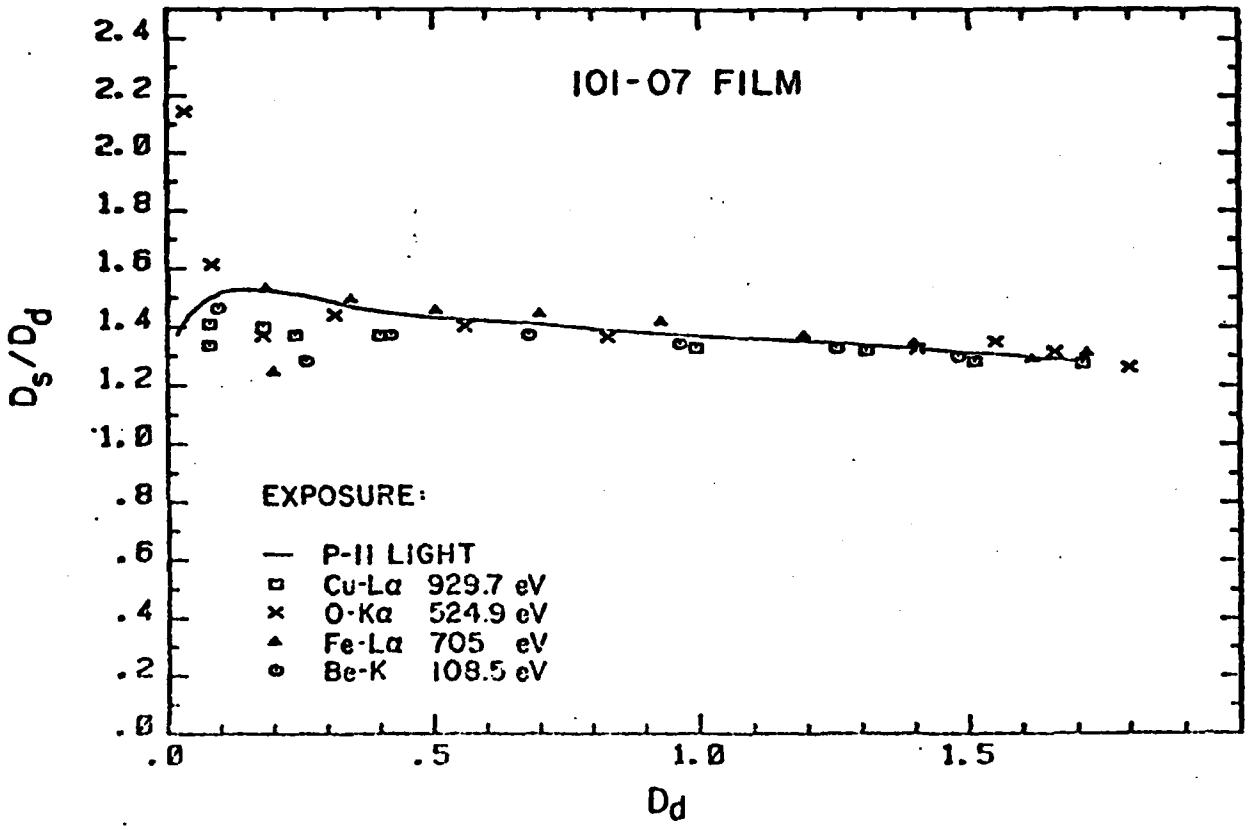

Figure A1. Specular density measured with matched 0.1 numerical apertures.

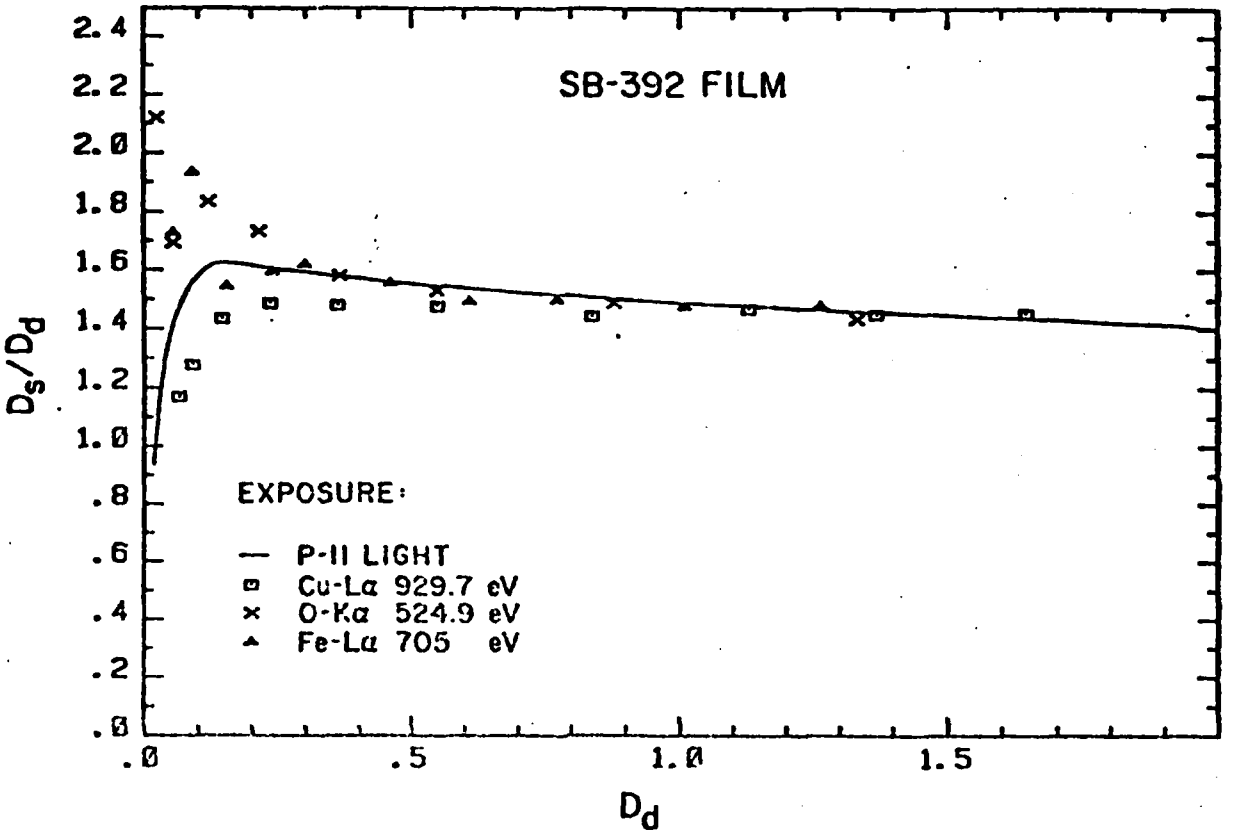

Figure A2. Specular density measured with matched 0.1 numerical apertures.

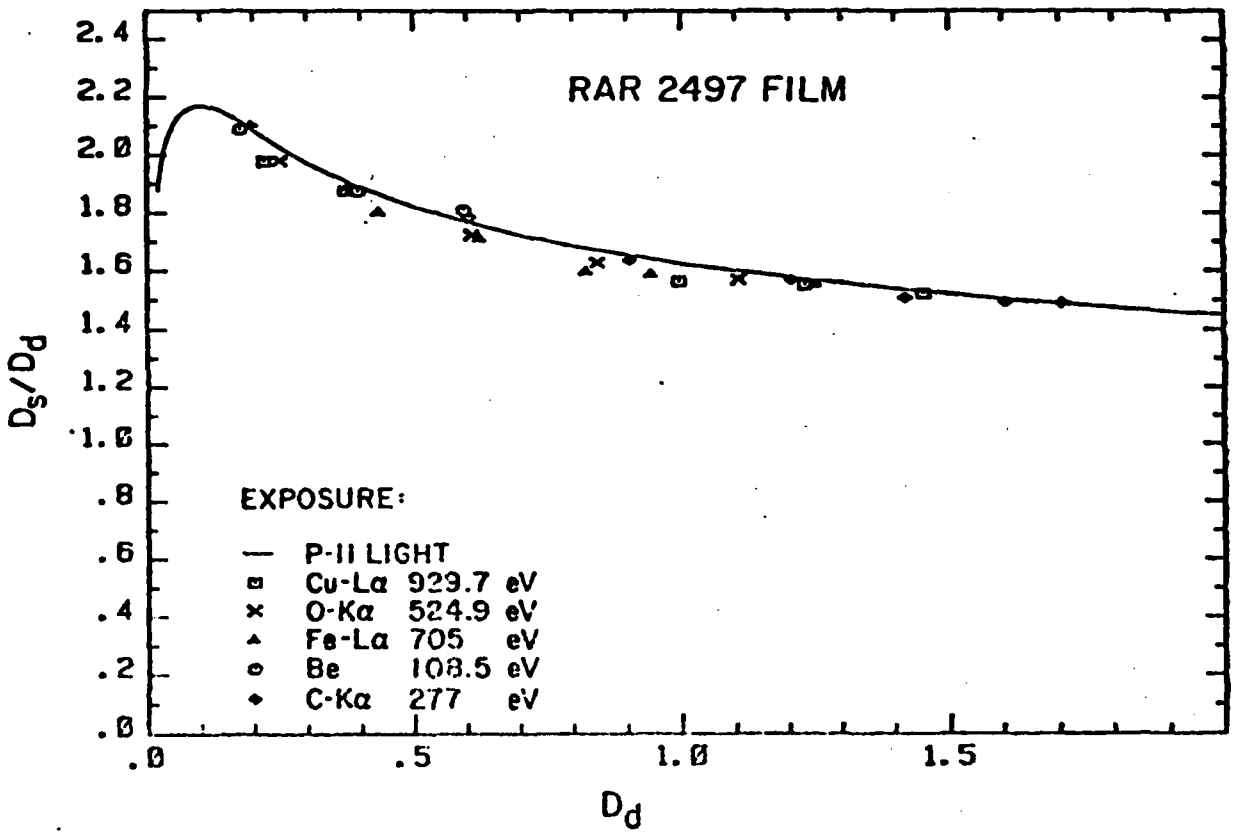

Figure A3. Specular density measured with matched 0.1 numerical apertures.

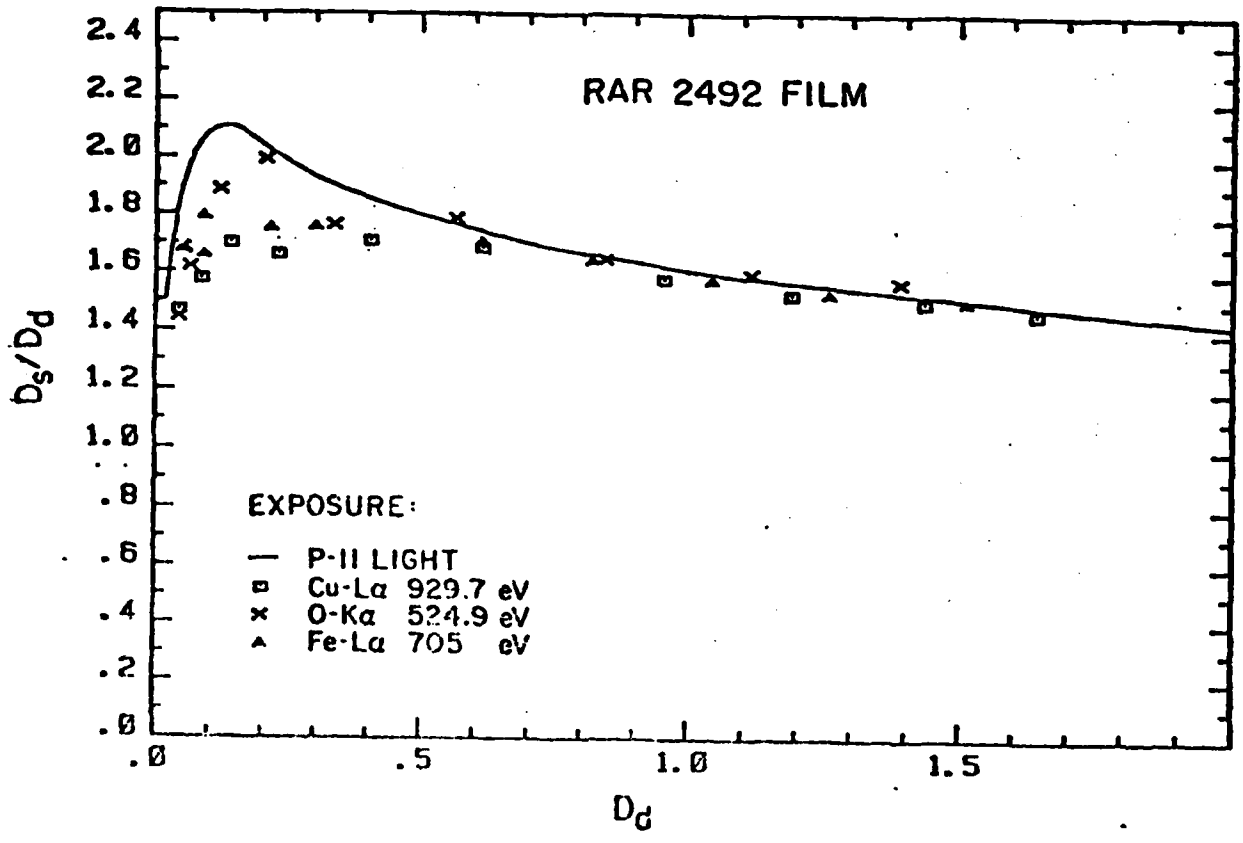

Figure A4. Specular density measured with matched 0.1 numerical apertures.

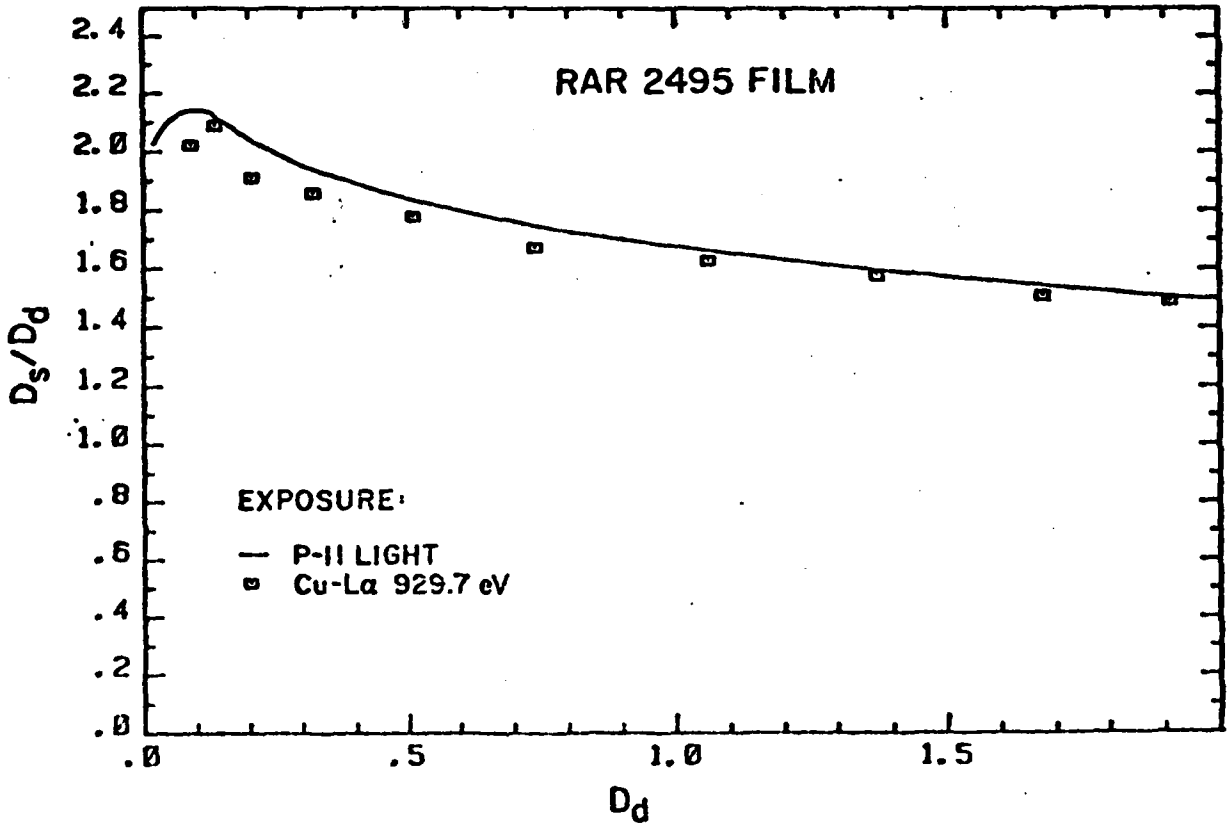

Figure A5. Specular density measured with matched 0.1 numerical apertures.

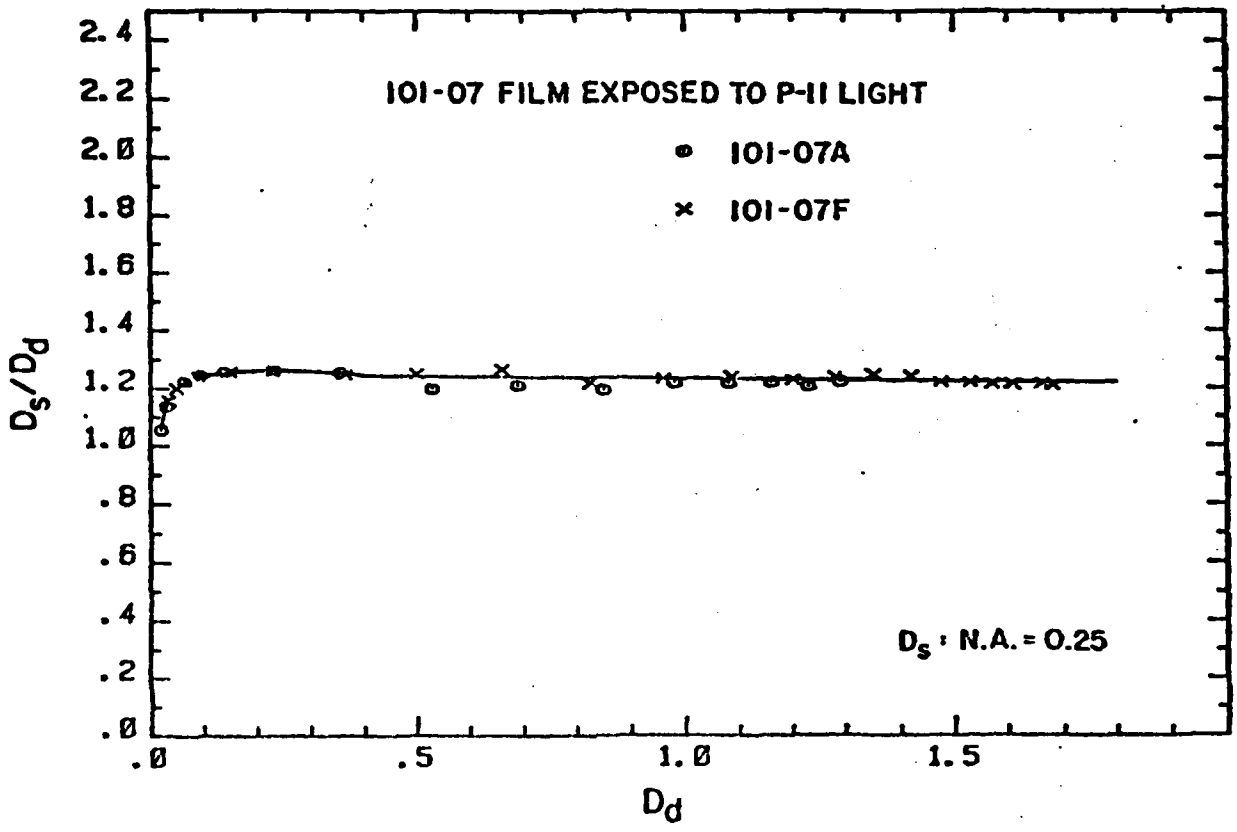

Figure A6. Specular denstiy measured with matched 0.25 numerical apertures.

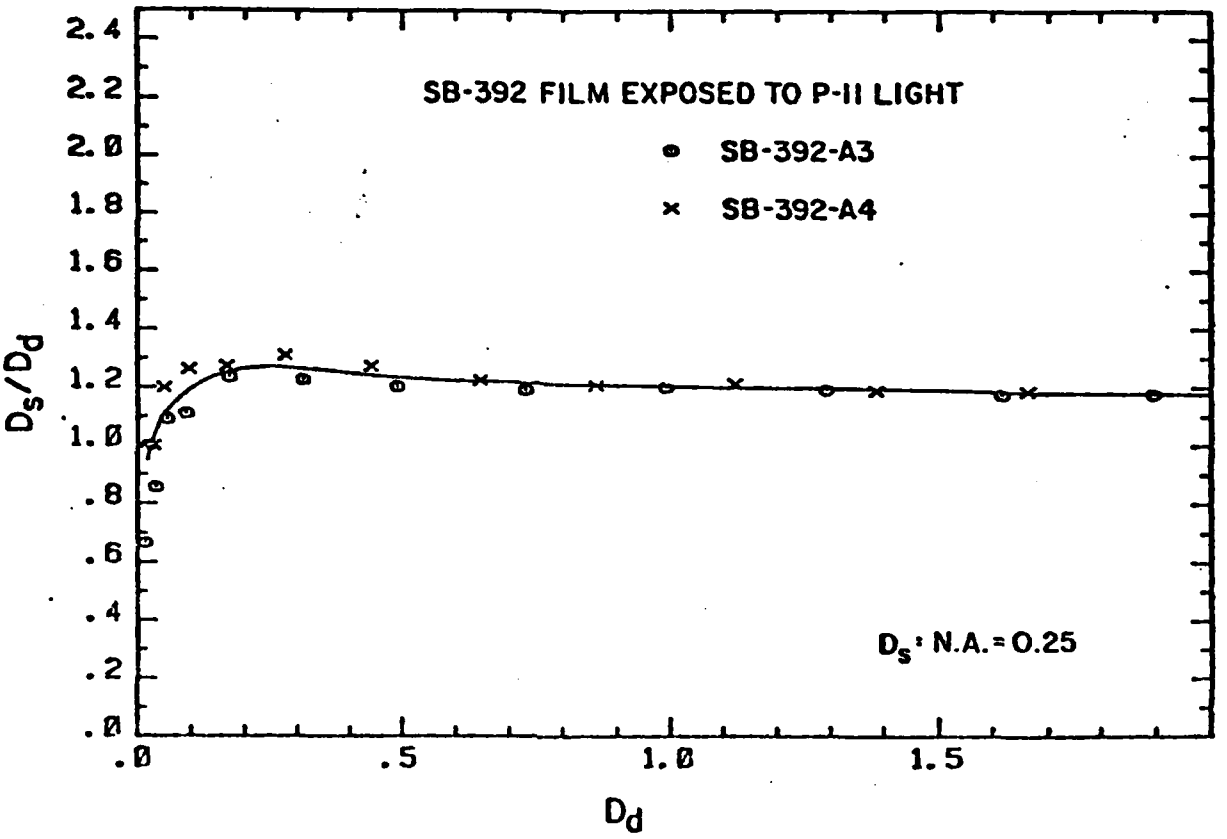

Figure A7. Specular density measured with matched 0.25 numerical apertures.

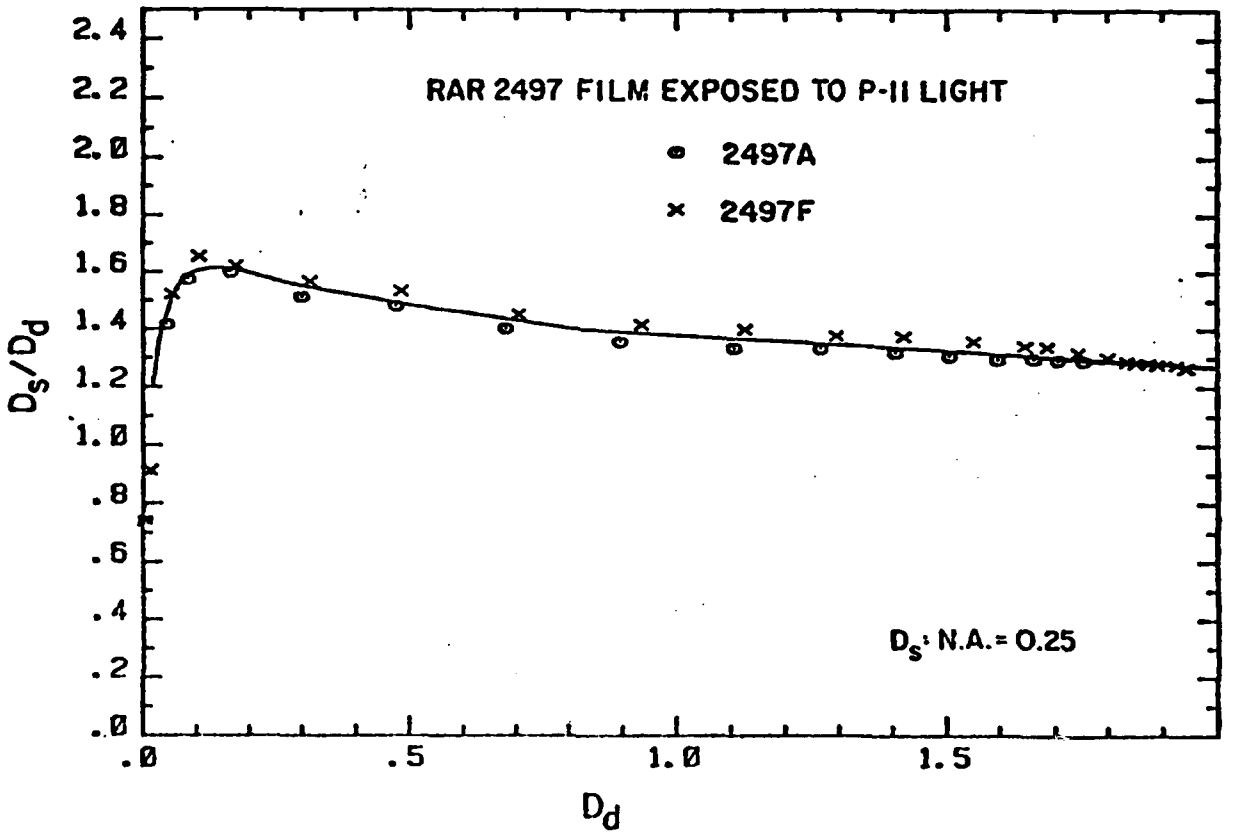

Figure A8. Specular density measured with matched 0.25 numerical apertures.

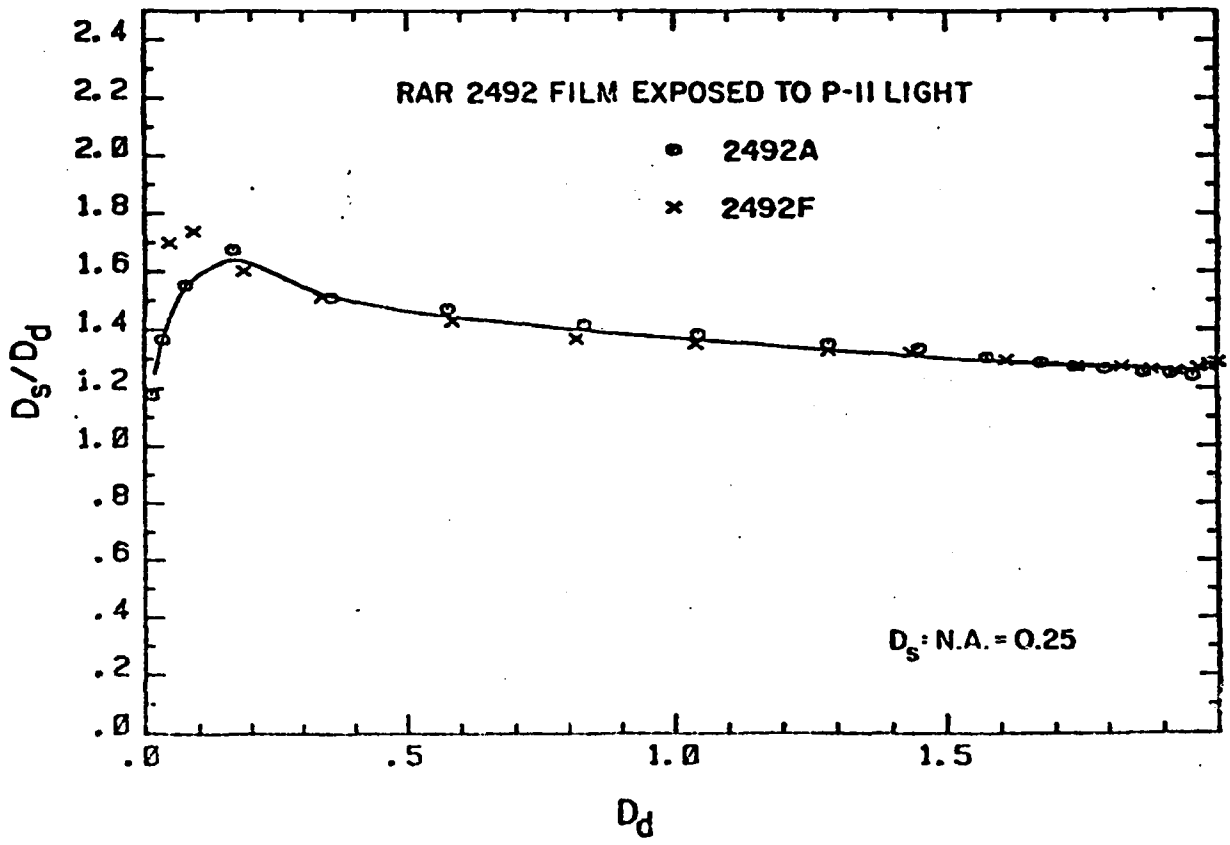

Figure A9. Specular density measured with matched 0.25 numerical apertures.

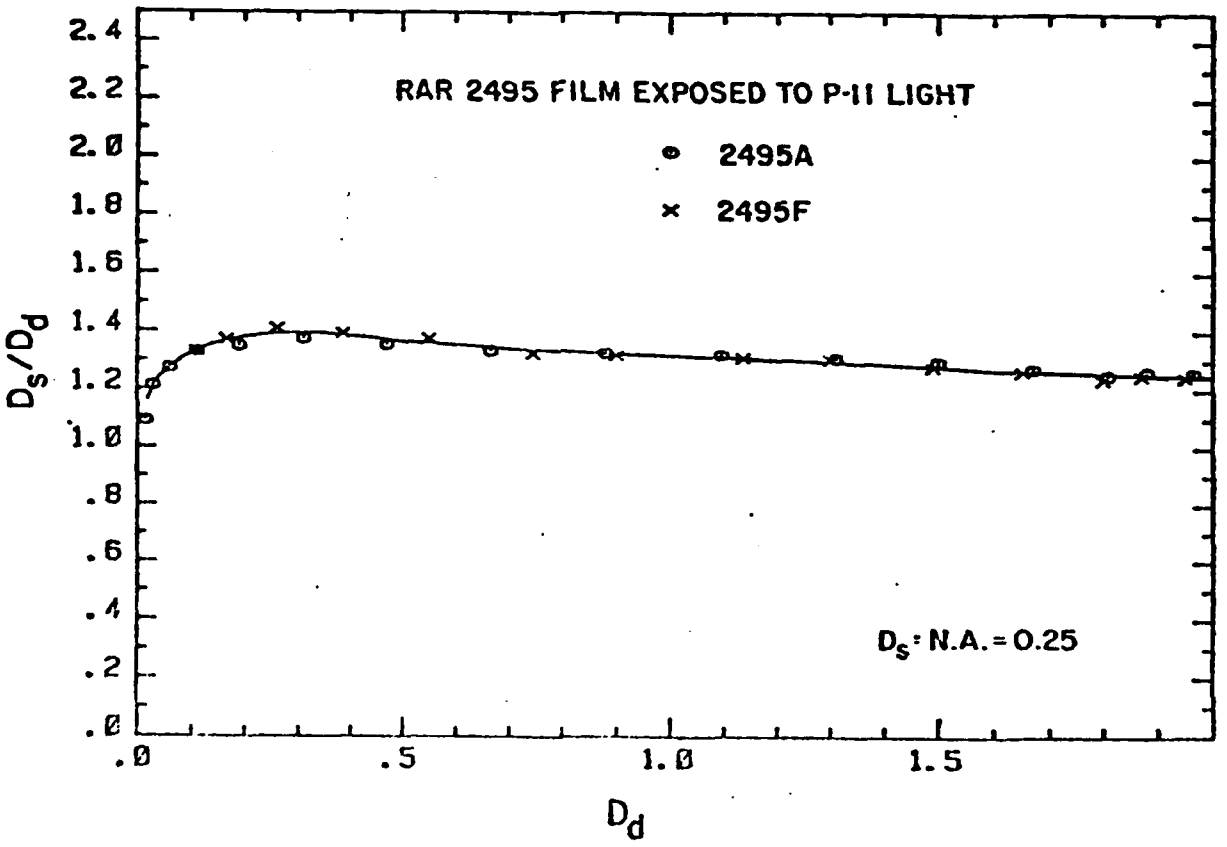

Figure A10. Specular density measured with matched 0.25 numerical apertures.

at two different matched numerical apertures (NA) for the optical system of the densitometer. One of these was the standard NA of 0.1. These data were used in Figures A1-A5 which give the D_s/D_d vs D_d plots for each of the five films used. In addition, in order to accomodate very fine spectral lines which necessitate increasing the optical apertures, data were also taken at the matched NA's of 0.25. These NA = 0.25 data are shown in Figures A6-A10 for the five films used.

The densities were measured using the following set-ups:

1) Specular density, D_s: A Photometric Data Systems Model 1010 microdensitometer system equipped with Hamamatsu R213 end-on photo-multiplier and operating with matched objective and "illumination" optical systems at a NA of 0.1 was used. Readings were taken at NA = 0.25 also. The effective objective aperture, (i.e., scanned sample dimensions,) for NA = 0.1 was 0.286 mm X 4.416 mm and 0.400 mm X 4.416 mm for NA = 0.25. A mean D_s density was determined for this sample area.

2) Diffuse density, D_d (totally diffuse visual density type V 1-b, in conformance with ANSI Standard pH 2.19): A Westrex RA-1100-H

Integrating Sphere Diffuse Densitometer with a reading aperture of 0.356 mm X 4.420 mm was used.

The x-ray films measurements were on the same exposures used to obtain the film calibration curves. Film density samples from exposure to P-11 simulated phosphor light source were also measured. The curves in the plots are those fitted to the P-11 data and the x-ray exposure data are plotted as points for NA = 0.1. The plots for NA = 0.25 portray P-11 simulated phosphor data only. As this and other studies have shown,[13] however, these plots tend to be independent of the energy of the exposing soft x-rays and similar to those for P-11 light.

APPENDIX B: Film Handling and Development Procedures

Kodak RAR 2492, 2495, and 2497 Films. These three films were handled and developed in the same manner with the exception that RAR 2495 required a Kodak Safelight Filter No. 2 while the RAR 2492 and 2497 could be handled with either a No. 1 or 2 filter. The exposed film was processed as follows in a developing tank at 68 $\pm$ 1°F:

1. Presoak: 2 minutes in distilled water. (This presoaking was done for all five films used in this study because of the varying times

during which the films were kept in vacuum.)

2. Development: 6 minutes in Kodak Developer D-19 with constant agitation.
3. Rinse: 30 seconds in Kodak SB-5 Indicator Stop Bath with constant agitation.
4. Fixing: 5 minutes in Kodak Rapid Fixer with constant agitation.
5. Wash: 10 minutes minimum in running water, then 30 seconds in Kodak Photo-Flo 200 Solution.
6. Drying: At room temperature in still air.

Kodak SB-392 (or SB-5): The Kodak SB-392 or SB-5 film, the difference between the two being merely their format, was handled under Kodak Safelight Filter No. 1. Special care was taken not to bend the film too sharply since that resulted in many minute cracks in the film. The processing of this film was as follows at 68 $\pm$ 1°F in a developing tank:

1. Presoak: 2 minutes in distilled water.
2. Development: 5 minutes in Kodak Liquid X-ray Developer or Kodak GBX Developer with constant agitation.
3. Rinse: 30 seconds in Kodak SB-5 Indicator Stop Bath with constant agitation.
4. Fixing: 2 minutes in Kodak Rapid Fixer with

constant agitation.

5. Wash: 30 minutes in running water, then 30 seconds in Photo-Flo 200 Solution.
6. Drying: At room temperature in still air.

Kodak Special Film Type 101-07: Great care was taken in the handling of this film since the emulsion lacks a protective overcoat of gelatin and is very easily marred. It was handled using Kodak Safelight Filter No. 1. It was found necessary to lightly spray the back-side of the film with a commercially available brand of "static guard" just prior to loading the film into the camera in order to prevent dark streaks on the developed film due to static electricity. The processing of this film at 68 ± 1° F follows:

1. Presoak: 2 minutes in distilled water.
2. Development: 4 minutes in Kodak D-19 Developer diluted 1:1 with distilled water and constantly agitated.
3. Rinse: 30 seconds in Kodak SB-5 Indicator Stop Bath with constant agitation.
4. Fixing: 2 minutes in Kodak Rapid Fixer with constant agitation.
5. Wash: 7 or more minutes in running water followed by 30 seconds in Kodak Photo-Flo 200 Solution.
6. Drying: At room temperature in still air.

APPENDIX C

Presented here in Table 9 are the energy-dependent scaling factors, β_1, α and β which have been applied to generate the universal photographic response functions for the five films studied in this work. (In Table 8 we have listed the calculated values for the linear absorption coefficients for gelatin, (μ_0), and for AgBr (μ_1), which were used in the generation of the scaling factors.) With these factors, the universal plots that have been presented in Figs. 8 through 13 were obtained. These plots were then least-squares fitted to our semi-empirical model equations to obtain the relatively sensitive pair-parameters a_1, b_1 or a,b in order to establish the "best average" characterizations (over photon energies in the 100-2000 eV region) for the investigated monolayer and emulsion type films (These parameters are listed above in Table 7.) The "averaged" characterizations have also been presented earlier in Tables 1 through 5 as exposure, I vs density, D at the nine characteristic photon energies which have been used for the D vs I calibrations. Presented here in Tables 10-14 are the averaged film response characteristics predicted by the semi-empirical relations for the extended photon energy region of 100-10,000 eV as calculated at regularly spaced intervals in energy for the five films.

As has been discussed in Sec. IV, the data presented here can be directly applied along with additional calibration data upon new batches of these films to obtain corrected values of the fitting parameters a_1, b_1 , or a,b.

TABLE 8

LINEAR ABSORPTION COEFFICIENTS

μ_g(Gelatin) For ρ = 1.40 gm/cm^3

μ_i(AgBr) For ρ = 6.47 gm/cm^3

	E (eV)	μ_g (μm^{-1})	μ_i (μm^{-1})	λ (A)	
A					A
	75	1.01 01	4.63 01	165.19	
	100	5.65 00	2.11 01	123.89	
	125	3.45 00	1.22 01	99.11	
	150	2.30 00	1.48 01	82.59	
	175	1.61 00	1.46 01	70.79	
	200	1.17 00	1.47 01	61.95	
	225	8.83-01	1.37 01	55.06	
	250	6.82-01	1.29 01	49.56	
	275	5.40-01	1.21 01	45.05	
B					B
	300	3.34 00	1.09 01	41.30	
	325	2.74 00	9.88 00	38.12	
	350	2.28 00	9.00 00	35.40	
	375	1.92 00	8.26 00	33.04	
C					C
	425	1.87 00	9.10 00	29.15	
	450	1.64 00	1.07 01	27.53	
	475	1.44 00	1.06 01	26.08	
	500	1.27 00	1.02 01	24.78	
D					D
	550	2.00 00	9.42 00	22.53	
	600	1.61 00	8.60 00	20.65	
	650	1.32 00	7.84 00	19.06	
	700	1.09 00	7.19 00	17.70	
	750	9.17-01	6.23 00	16.52	
	800	7.74-01	5.43 00	15.49	
	850	6.59-01	4.78 00	14.58	
	900	5.68-01	4.23 00	13.77	
	950	4.93-01	3.76 00	13.04	
	1000	4.29-01	3.36 00	12.39	
	1050	3.76-01	3.01 00	11.80	
	1100	3.32-01	2.71 00	11.26	
	1150	2.94-01	2.44 00	10.77	
	1200	2.62-01	2.22 00	10.32	
	1250	2.34-01	2.02 00	9.91	
	1300	2.10-01	1.84 00	9.53	
	1350	1.89-01	1.69 00	9.18	
	1400	1.71-01	1.55 00	8.85	
	1450	1.55-01	1.43 00	8.54	
	1500	1.41-01	1.33 00	8.26	
E					E
	1800	8.44-02	1.87 00	6.88	
	1900	7.24-02	1.69 00	6.52	
	2000	6.25-02	1.49 00	6.19	
	2100	5.28-02	1.32 00	5.90	
	2200	4.62-02	1.18 00	5.63	
	2300	4.06-02	1.05 00	5.39	
	2400	3.59-02	9.46-01	5.16	
	2500	3.19-02	8.53-01	4.96	
	2600	2.85-02	7.72-01	4.77	
	2700	2.55-02	7.01-01	4.59	
	2800	2.29-02	6.39-01	4.42	
	2900	2.07-02	5.84-01	4.27	
	3000	1.87-02	5.35-01	4.13	
	3100	1.70-02	4.92-01	4.00	
	3200	1.55-02	4.53-01	3.87	
	3300	1.41-02	4.18-01	3.75	
F					F
	4000	7.94-03	6.36-01	3.10	
	5000	4.01-03	3.60-01	2.48	
	6000	2.28-03	2.23-01	2.06	
	7000	1.41-03	1.47-01	1.77	
	8000	9.27-04	1.02-01	1.55	
	9000	6.38-04	7.43-02	1.38	
	10000	4.55-04	5.56-02	1.24	

TABLE 9

FILM:	2492 , 2497		2495		SB-392		101-07
E(eV)	α	β	α	β	α	β	β,
A							A
75	1.44 00	4.76-02	1.45 00	4.76-02	6.26-01	3.91-05	1.000
100	1.30 00	1.83-01	1.32 00	1.83-01	5.99-01	3.51-03	1.000
125	1.16 00	3.46-01	1.19 00	3.46-01	5.64-01	3.16-02	1.000
150	1.02 00	4.96-01	1.07 00	4.96-01	5.27-01	1.00-01	1.000
175	8.99-01	6.10-01	9.72-01	6.10-01	4.89-01	2.00-01	1.000
200	7.94-01	6.95-01	8.88-01	6.95-01	4.51-01	3.10-01	1.000
225	7.06-01	7.55-01	8.19-01	7.55-01	4.16-01	4.14-01	1.000
250	6.34-01	7.98-01	7.62-01	7.98-01	3.84-01	5.05-01	1.000
275	5.76-01	8.28-01	7.17-01	8.28-01	3.56-01	5.83-01	1.000
B							B
300	1.14 00	3.53-01	1.18 00	3.53-01	5.62-01	3.54-02	1.000
325	1.08 00	4.17-01	1.12 00	4.17-01	5.44-01	6.45-02	1.000
350	1.01 00	4.70-01	1.06 00	4.70-01	5.26-01	1.02-01	1.000
375	9.52-01	5.14-01	1.01 00	5.14-01	5.09-01	1.46-01	1.000
C							C
425	9.44-01	5.34-01	1.00 00	5.34-01	5.05-01	1.54-01	1.000
450	9.03-01	5.87-01	9.72-01	5.87-01	4.91-01	1.94-01	1.000
475	8.58-01	6.22-01	9.36-01	6.22-01	4.76-01	2.36-01	1.000
500	8.15-01	6.51-01	9.00-01	6.51-01	4.61-01	2.81-01	1.000
D							D
550	9.69-01	5.16-01	1.02 00	5.16-01	5.13-01	1.35-01	1.000
600	8.91-01	5.70-01	9.58-01	5.70-01	4.89-01	2.00-01	1.000
650	8.20-01	6.10-01	8.97-01	6.10-01	4.65-01	2.68-01	1.000
700	7.57-01	6.37-01	8.43-01	6.37-01	4.43-01	3.35-01	1.000
750	6.95-01	6.42-01	7.88-01	6.42-01	4.21-01	3.99-01	1.000
800	6.38-01	6.37-01	7.36-01	6.37-01	3.99-01	4.59-01	1.000
850	5.86-01	6.25-01	6.87-01	6.25-01	3.79-01	5.13-01	1.000
900	5.40-01	6.06-01	6.42-01	6.06-01	3.60-01	5.58-01	1.000
950	4.97-01	5.84-01	6.00-01	5.84-01	3.43-01	5.97-01	0.999
1000	4.57-01	5.59-01	5.60-01	5.59-01	3.26-01	6.29-01	0.999
1050	4.21-01	5.31-01	5.23-01	5.31-01	3.11-01	6.53-01	0.998
1100	3.88-01	5.03-01	4.88-01	5.03-01	2.96-01	6.70-01	0.996
1150	3.58-01	4.76-01	4.55-01	4.76-01	2.82-01	6.81-01	0.992
1200	3.31-01	4.49-01	4.25-01	4.49-01	2.69-01	6.86-01	0.988
1250	3.06-01	4.23-01	3.98-01	4.23-01	2.56-01	6.86-01	0.982
1300	2.84-01	3.99-01	3.72-01	3.99-01	2.44-01	6.82-01	0.975
1350	2.63-01	3.76-01	3.48-01	3.76-01	2.33-01	6.75-01	0.966
1400	2.44-01	3.54-01	3.26-01	3.54-01	2.22-01	6.65-01	0.955
1450	2.27-01	3.34-01	3.06-01	3.34-01	2.12-01	6.52-01	0.943
1500	2.12-01	3.15-01	2.87-01	3.15-01	2.02-01	6.38-01	0.929
E							E
1800	1.98-01	4.18-01	3.04-01	4.18-01	1.90-01	7.77-01	0.976
1900	1.81-01	3.89-01	2.82-01	3.89-01	1.80-01	7.58-01	0.966
2000	1.63-01	3.54-01	2.56-01	3.54-01	1.70-01	7.28-01	0.949
2100	1.46-01	3.22-01	2.33-01	3.22-01	1.59-01	6.96-01	0.929
2200	1.32-01	2.93-01	2.13-01	2.93-01	1.49-01	6.61-01	0.905
2300	1.20-01	2.68-01	1.94-01	2.68-01	1.40-01	6.25-01	0.878
2400	1.09-01	2.44-01	1.78-01	2.44-01	1.31-01	5.90-01	0.849
2500	9.92-02	2.24-01	1.63-01	2.24-01	1.23-01	5.56-01	0.818
2600	9.06-02	2.05-01	1.50-01	2.05-01	1.15-01	5.23-01	0.786
2700	8.29-02	1.88-01	1.38-01	1.88-01	1.08-01	4.91-01	0.754
2800	7.60-02	1.73-01	1.27-01	1.73-01	1.01-01	4.61-01	0.721
2900	6.98-02	1.60-01	1.17-01	1.60-01	9.49-02	4.33-01	0.689
3000	6.43-02	1.47-01	1.08-01	1.47-01	8.91-02	4.07-01	0.657
3100	5.93-02	1.36-01	1.00-01	1.36-01	8.36-02	3.82-01	0.626
3200	5.49-02	1.26-01	9.30-02	1.26-01	7.85-02	3.59-01	0.596
3300	5.08-02	1.17-01	8.64-02	1.17-01	7.38-02	3.37-01	0.567
F							F
4000	6.32-02	1.73-01	1.16-01	1.73-01	9.13-02	4.67-01	0.720
5000	3.71-02	1.02-01	6.92-02	1.02-01	5.98-02	3.01-01	0.513
6000	2.33-02	6.45-02	4.40-02	6.45-02	4.01-02	1.99-01	0.359
7000	1.56-02	4.32-02	2.95-02	4.32-02	2.77-02	1.37-01	0.255
8000	1.09-02	3.03-02	2.07-02	3.03-02	1.98-02	9.73-02	0.185
9000	7.89-03	2.20-02	1.51-02	2.20-02	1.46-02	7.15-02	0.138
10000	5.91-03	1.65-02	1.13-02	1.65-02	1.11-02	5.41-02	0.105

TABLE 10

101-07 FILM--EXPOSURE, I(photons/μm^2)

NET DENSITY, D
(SPECULAR-0.1-0.1 mA)

PHOTON ENERGY, E(eV)
WAVELENGTH, λ(A)

D

E(eV)	0.2	0.4	0.6	0.8	1.0	1.2	1.4	1.6	1.8	λ(A)
A										A
75	0.34	0.73	1.17	1.68	2.29	3.04	4.02	5.44	8.07	165.31
150	0.34	0.73	1.17	1.68	2.29	3.04	4.02	5.44	8.07	82.65
225	0.34	0.73	1.17	1.68	2.29	3.04	4.02	5.44	8.07	55.10
300	0.34	0.73	1.17	1.68	2.29	3.04	4.02	5.44	8.07	41.33
375	0.34	0.73	1.17	1.68	2.29	3.04	4.02	5.44	8.07	33.06
C										C
475	0.34	0.73	1.17	1.68	2.29	3.04	4.02	5.44	8.07	26.10
600	0.34	0.73	1.17	1.68	2.29	3.04	4.02	5.44	8.07	20.66
750	0.34	0.73	1.17	1.68	2.29	3.04	4.02	5.44	8.07	16.53
900	0.34	0.73	1.17	1.68	2.29	3.04	4.02	5.44	8.07	13.78
950	0.34	0.73	1.17	1.68	2.29	3.04	4.02	5.44	8.07	13.05
1000	0.35	0.73	1.17	1.68	2.29	3.04	4.02	5.45	8.08	12.40
1050	0.35	0.73	1.17	1.68	2.29	3.04	4.03	5.45	8.09	11.81
1100	0.35	0.73	1.18	1.69	2.30	3.05	4.04	5.46	8.10	11.27
1150	0.35	0.74	1.18	1.69	2.30	3.06	4.05	5.48	8.13	10.78
1200	0.35	0.74	1.18	1.70	2.31	3.07	4.07	5.50	8.16	10.33
1250	0.35	0.74	1.19	1.71	2.33	3.09	4.09	5.54	8.21	9.92
1300	0.35	0.75	1.20	1.72	2.35	3.11	4.12	5.58	8.27	9.54
1350	0.36	0.76	1.21	1.74	2.37	3.14	4.16	5.63	8.35	9.18
1400	0.36	0.77	1.23	1.76	2.39	3.18	4.21	5.69	8.44	8.86
1450	0.37	0.78	1.24	1.78	2.42	3.22	4.26	5.77	8.55	8.55
1500	0.37	0.79	1.26	1.81	2.46	3.27	4.32	5.85	8.68	8.27
E										E
1800	0.35	0.75	1.20	1.72	2.34	3.11	4.12	5.57	8.26	6.89
1900	0.36	0.76	1.21	1.74	2.37	3.14	4.16	5.63	8.35	6.53
2000	0.36	0.77	1.23	1.77	2.41	3.20	4.23	5.73	8.50	6.20
2100	0.37	0.79	1.26	1.81	2.46	3.27	4.32	5.86	8.68	5.90
2200	0.38	0.81	1.29	1.86	2.53	3.35	4.44	6.01	8.91	5.64
2300	0.39	0.83	1.33	1.91	2.60	3.46	4.57	6.19	9.18	5.39
2400	0.41	0.86	1.38	1.98	2.69	3.58	4.73	6.41	9.50	5.17
2500	0.42	0.89	1.43	2.05	2.79	3.71	4.91	6.65	9.86	4.96
2600	0.44	0.93	1.49	2.14	2.91	3.86	5.11	6.92	10.26	4.77
2700	0.46	0.97	1.55	2.23	3.03	4.03	5.33	7.22	10.70	4.59
2800	0.48	1.01	1.62	2.33	3.17	4.21	5.57	7.54	11.18	4.43
2900	0.50	1.06	1.70	2.44	3.32	4.41	5.83	7.90	11.71	4.28
3000	0.52	1.11	1.78	2.56	3.48	4.62	6.12	8.29	12.28	4.13
3100	0.55	1.17	1.87	2.69	3.65	4.85	6.42	8.69	12.89	4.00
3200	0.58	1.23	1.96	2.82	3.84	5.10	6.74	9.13	13.54	3.87
3300	0.61	1.29	2.06	2.96	4.03	5.36	7.09	9.60	14.23	3.76
F										F
4000	0.48	1.02	1.63	2.33	3.18	4.22	5.58	7.56	11.21	3.10
5000	0.67	1.42	2.28	3.28	4.46	5.92	7.83	10.60	15.72	2.48
6000	0.96	2.03	3.26	4.68	6.37	8.45	11.18	15.14	22.45	2.07
7000	1.35	2.87	4.59	6.59	8.97	11.91	15.75	21.33	31.63	1.77
8000	1.86	3.94	6.32	9.07	12.34	16.39	21.68	29.35	43.53	1.55
9000	2.50	5.30	8.48	12.17	16.57	22.00	29.10	39.40	58.43	1.38
10000	3.27	6.94	11.12	15.96	21.73	28.85	38.17	51.68	76.63	1.24

TABLE 11

SB-392 FILM--EXPOSURE, I(photons/μm^2)

NET DENSITY, D
(SPECULAR-0.1>0.1 mA)

PHOTON ENERGY, E(eV)
WAVELENGTH, λ(A)

D

E(eV)	0.2	0.4	0.6	0.8	1.0	1.2	1.4	1.6	1.8	2.0	λ(A)
A											A
75	1.00 04	2.56 04	4.98 04	8.73 04	1.46 05	2.36 05	3.76 05	5.94 05	9.32 05	1.46 06	165.31
100	1.06 02	2.67 02	5.12 02	8.85 02	1.45 03	2.32 03	3.63 03	5.64 03	8.69 03	1.33 04	123.98
125	1.09 01	2.71 01	5.12 01	8.71 01	1.40 02	2.19 02	3.37 02	5.11 02	7.71 02	1.16 03	99.18
150	3.17 00	7.75 00	1.44 01	2.40 01	3.79 01	5.80 01	8.72 01	1.29 02	1.90 02	2.79 02	82.65
175	1.45 00	3.49 00	6.37 00	1.04 01	1.61 01	2.42 01	3.55 01	5.15 01	7.61 01	1.06 02	70.85
200	8.54-01	2.03 00	3.63 00	5.84 00	8.87 00	1.30 01	1.87 01	2.66 01	3.73 01	5.20 01	61.99
225	5.82-01	1.36 00	2.41 00	3.80 00	5.68 00	8.18 00	1.15 01	1.60 01	2.20 01	3.01 01	55.10
250	4.35-01	1.00 00	1.75 00	2.73 00	4.00 00	5.68 00	7.87 00	1.07 01	1.45 01	1.94 01	49.59
275	3.46-01	7.91-01	1.36 00	2.10 00	3.04 00	4.25 00	5.80 00	7.80 00	1.04 01	1.37 01	45.08
B											B
300	9.70 00	2.41 01	4.54 01	7.71 01	1.24 02	1.94 02	2.97 02	4.53 02	6.77 02	1.01 03	41.33
325	5.12 00	1.26 01	2.36 01	3.97 01	6.33 01	9.79 01	1.49 02	2.23 02	3.31 02	4.91 02	38.15
350	3.11 00	7.61 00	1.41 01	2.35 01	3.72 01	5.69 01	8.54 01	1.27 02	1.86 02	2.73 02	35.42
375	2.09 00	5.07 00	9.33 00	1.54 01	2.41 01	3.65 01	5.43 01	7.97 01	1.16 02	1.68 02	33.06
C											C
425	1.96 00	4.73 00	8.74 00	1.44 01	2.25 01	3.41 01	5.05 01	7.40 01	1.07 02	1.55 02	29.17
450	1.31 00	3.64 00	6.65 00	1.09 01	1.69 01	2.54 01	3.73 01	5.42 01	7.80 01	1.12 02	27.55
475	1.19 00	2.86 00	5.18 00	8.43 00	1.30 01	1.93 01	2.82 01	4.05 01	5.78 01	8.19 01	26.10
500	9.66-01	2.30 00	4.15 00	6.70 00	1.02 01	1.51 01	2.18 01	3.11 01	4.39 01	6.17 01	24.80
D											D
550	2.28 00	5.54 00	1.02 01	1.69 01	2.65 01	4.03 01	6.01 01	8.84 01	1.29 02	1.87 02	22.54
600	1.46 00	3.51 00	6.40 00	1.05 01	1.62 01	2.43 01	3.37 01	5.18 01	7.45 01	1.06 02	20.65
650	1.02 00	2.44 00	4.41 00	7.13 00	1.09 01	1.61 01	2.34 01	3.34 01	4.74 01	6.67 01	19.07
700	7.73-01	1.83 00	3.27 00	5.23 00	7.91 00	1.16 01	1.65 01	2.33 01	3.26 01	4.53 01	17.71
750	6.12-01	1.43 00	2.54 00	4.02 00	6.01 00	8.68 00	1.23 01	1.71 01	2.36 01	3.23 01	16.53
800	5.01-01	1.16 00	2.04 00	3.20 00	4.73 00	6.77 00	9.45 00	1.30 01	1.77 01	2.40 01	15.50
850	4.22-01	9.73-01	1.69 00	2.63 00	3.85 00	5.45 00	7.53 00	1.02 01	1.38 01	1.84 01	14.59
900	3.67-01	8.39-01	1.45 00	2.23 00	3.24 00	4.54 00	6.22 00	8.38 00	1.12 01	1.48 01	13.78
950	3.24-01	7.37-01	1.26 00	1.93 00	2.76 00	3.87 00	5.25 00	7.02 00	9.27 00	1.21 01	13.05
1000	2.92-01	6.59-01	1.12 00	1.70 00	2.43 00	3.36 00	4.52 00	5.99 00	7.85 00	1.02 01	12.40
1050	2.66-01	5.98-01	1.01 00	1.53 00	2.17 00	2.97 00	3.98 00	5.23 00	6.80 00	8.78 00	11.81
1100	2.46-01	5.50-01	9.23-01	1.39 00	1.96 00	2.67 00	3.55 00	4.64 00	5.00 00	7.70 00	11.27
1150	2.31-01	5.12-01	8.58-01	1.28 00	1.80 00	2.44 00	3.22 00	4.19 00	5.39 00	6.88 00	10.79
1200	2.18-01	4.83-01	8.04-01	1.20 00	1.67 00	2.25 00	2.97 00	3.84 00	4.92 00	6.25 00	10.33
1250	2.08-01	4.59-01	7.61-01	1.13 00	1.57 00	2.11 00	2.76 00	3.56 00	4.55 00	5.76 00	9.92
1300	2.00-01	4.39-01	7.26-01	1.07 00	1.49 00	1.99 00	2.60 00	3.34 00	4.25 00	5.37 00	9.54
1350	1.93-01	4.24-01	6.98-01	1.03 00	1.42 00	1.90 00	2.47 00	3.17 00	4.02 00	5.07 00	9.18
1400	1.88-01	4.12-01	6.77-01	9.92-01	1.37 00	1.82 00	2.37 00	3.03 00	3.84 00	4.84 00	8.86
1450	1.84-01	4.02-01	6.59-01	9.65-01	1.33 00	1.76 00	2.29 00	2.92 00	3.70 00	4.66 00	8.55
1500	1.82-01	3.95-01	6.46-01	9.44-01	1.30 00	1.72 00	2.23 00	2.84 00	3.59 00	4.52 00	8.27
E											E
1800	1.42-01	3.08-01	5.03-01	7.33-01	1.01 00	1.33 00	1.72 00	2.19 00	2.77 00	3.49 00	6.89
1900	1.40-01	3.03-01	4.94-01	7.18-01	9.84-01	1.30 00	1.68 00	2.14 00	2.70 00	3.40 00	6.53
2000	1.40-01	3.02-01	4.91-01	7.14-01	9.76-01	1.29 00	1.66 00	2.12 00	2.68 00	3.38 00	6.20
2100	1.40-01	3.02-01	4.90-01	7.11-01	9.72-01	1.28 00	1.65 00	2.11 00	2.67 00	3.37 00	5.90
2200	1.42-01	3.05-01	4.96-01	7.19-01	9.82-01	1.29 00	1.67 00	2.13 00	2.69 00	3.41 00	5.64
2300	1.44-01	3.11-01	5.04-01	7.31-01	9.98-01	1.32 00	1.70 00	2.16 00	2.74 00	3.48 00	5.39
2400	1.48-01	3.18-01	5.16-01	7.47-01	1.02 00	1.34 00	1.74 00	2.21 00	2.81 00	3.57 00	5.17
2500	1.52-01	3.27-01	5.30-01	7.67-01	1.05 00	1.38 00	1.78 00	2.28 00	2.89 00	3.69 00	4.96
2600	1.57-01	3.37-01	5.46-01	7.91-01	1.08 00	1.42 00	1.84 00	2.35 00	3.00 00	3.82 00	4.77
2700	1.62-01	3.49-01	5.65-01	8.18-01	1.12 00	1.47 00	1.91 00	2.44 00	3.11 00	3.98 00	4.59
2800	1.68-01	3.62-01	5.86-01	8.48-01	1.16 00	1.53 00	1.98 00	2.54 00	3.24 00	4.16 00	4.43
2900	1.75-01	3.76-01	6.09-01	8.82-01	1.20 00	1.59 00	2.06 00	2.65 00	3.39 00	4.36 00	4.28
3000	1.82-01	3.92-01	6.34-01	9.18-01	1.26 00	1.66 00	2.15 00	2.76 00	3.55 00	4.58 00	4.13
3100	1.90-01	4.08-01	6.62-01	9.58-01	1.31 00	1.73 00	2.25 00	2.89 00	3.72 00	4.81 00	4.00
3200	1.98-01	4.26-01	6.91-01	1.00 00	1.37 00	1.81 00	2.35 00	3.03 00	3.91 00	5.06 00	3.87
3300	2.07-01	4.46-01	7.22-01	1.05 00	1.43 00	1.90 00	2.47 00	3.18 00	4.10 00	5.34 00	3.76
F											F
4000	1.60-01	3.44-01	5.57-01	8.07-01	1.10 00	1.46 00	1.89 00	2.43 00	3.11 00	4.01 00	3.10
5000	2.20-01	4.74-01	7.69-01	1.12 00	1.53 00	2.03 00	2.65 00	3.43 00	4.45 00	5.83 00	2.48
6000	3.10-01	6.68-01	1.09 00	1.58 00	2.17 00	2.89 00	3.79 00	4.94 00	6.46 00	8.58 00	2.07
7000	4.32-01	9.32-01	1.52 00	2.21 00	3.04 00	4.06 00	5.34 00	7.00 00	9.22 00	1.24 01	1.77
8000	5.90-01	1.27 00	2.07 00	3.03 00	4.17 00	5.59 00	7.37 00	9.68 00	1.28 01	1.73 01	1.55
9000	7.88-01	1.70 00	2.77 00	4.05 00	5.59 00	7.49 00	9.90 00	1.30 01	1.73 01	2.34 01	1.38
10000	1.03 00	2.23 00	3.63 00	5.30 00	7.33 00	9.83 00	1.30 01	1.71 01	2.28 01	3.10 01	1.24

TABLE 12

2497 FILM--EXPOSURE, I(photons/μm²)

NET DENSITY, D
(SPECULAR-0.1-0.1 mA)

PHOTON ENERGY, E(eV)
WAVELENGTH, λ(A)

D

E(eV)	0.2	0.4	0.6	0.8	1.0	1.2	1.4	1.6	1.8	2.0	λ(A)
A											A
75	4.65 01	1.40 02	3.26 02	7.00 02	1.45 03	2.95 03	5.97 03	1.20 04	2.41 04	4.84 04	165.31
100	1.06 01	3.04 01	6.77 01	1.38 02	2.69 02	5.17 02	9.81 02	1.85 03	3.49 03	6.57 03	123.98
125	4.77 00	1.31 01	2.77 01	5.32 01	9.79 01	1.76 02	3.13 02	5.51 02	9.69 02	1.70 03	99.18
150	2.84 00	7.48 00	1.51 01	2.76 01	4.80 01	8.15 01	1.36 02	2.26 02	3.74 02	6.15 02	82.65
175	1.97 00	5.00 00	9.69 00	1.69 01	2.91 01	4.53 01	7.20 01	1.13 02	1.77 02	2.75 02	70.85
200	1.48 00	3.66 00	6.85 00	1.15 01	1.84 01	2.85 01	4.34 01	6.52 01	9.71 01	1.44 02	61.99
225	1.19 00	2.86 00	5.21 00	8.52 00	1.32 01	1.98 01	2.90 01	4.20 01	6.04 01	8.63 01	55.10
250	9.91-01	2.34 00	4.17 00	6.67 00	1.01 01	1.47 01	2.10 01	2.96 01	4.13 01	5.74 01	49.59
275	8.56-01	1.99 00	3.49 00	5.48 00	8.11 00	1.16 01	1.63 01	2.24 01	3.07 01	4.18 01	45.08
B											B
300	4.61 00	1.26 01	2.66 01	5.08 01	9.29 01	1.66 02	2.94 02	5.15 02	9.01 02	1.37 03	41.33
325	3.61 00	9.69 00	1.99 01	3.72 01	6.62 01	1.15 02	1.97 02	3.36 02	5.69 02	9.61 02	38.15
350	2.96 00	7.78 00	1.57 01	2.85 01	4.95 01	8.37 01	1.40 02	2.31 02	3.79 02	6.22 02	35.42
375	2.50 00	6.46 00	1.27 01	2.27 01	3.84 01	6.34 01	1.03 02	1.66 02	2.65 02	4.22 02	33.05
C											C
425	2.39 00	6.15 00	1.21 01	2.15 01	3.63 01	5.96 01	9.65 01	1.55 02	2.47 02	3.91 02	29.17
450	2.05 00	5.23 00	1.01 01	1.78 01	2.95 01	4.77 01	7.59 01	1.19 02	1.87 02	2.91 02	27.55
475	1.82 00	4.58 00	8.75 00	1.51 01	2.46 01	3.91 01	6.11 01	9.43 01	1.45 02	2.21 02	26.10
500	1.63 00	4.06 00	7.65 00	1.30 01	2.09 01	3.26 01	5.00 01	7.58 01	1.14 02	1.71 02	24.80
D											D
550	2.55 00	6.62 00	1.31 01	2.35 01	4.01 01	6.66 01	1.09 02	1.76 02	2.84 02	4.57 02	22.54
600	2.08 00	5.28 00	1.02 01	1.78 01	2.95 01	4.74 01	7.50 01	1.18 02	1.83 02	2.84 02	20.66
650	1.76 00	4.37 00	8.26 00	1.40 01	2.26 01	3.54 01	5.44 01	8.26 01	1.25 02	1.87 02	19.07
700	1.53 00	3.73 00	6.90 00	1.15 01	1.81 01	2.76 01	4.13 01	6.11 01	8.97 01	1.31 02	17.71
750	1.37 00	3.23 00	5.98 00	9.74 00	1.50 01	2.24 01	3.27 01	4.72 01	6.76 01	9.62 01	16.53
800	1.25 00	2.95 00	5.28 00	8.44 00	1.28 01	1.86 01	2.67 01	3.77 01	5.27 01	7.34 01	15.50
850	1.15 00	2.69 00	4.74 00	7.46 00	1.11 01	1.59 01	2.24 01	3.10 01	4.26 01	5.81 01	14.59
900	1.09 00	2.50 00	4.35 00	6.75 00	9.89 00	1.40 01	1.94 01	2.64 01	3.58 01	4.81 01	13.78
950	1.03 00	2.35 00	4.04 00	6.20 00	8.97 00	1.25 01	1.71 01	2.31 01	3.09 01	4.11 01	13.05
1000	9.93-01	2.23 00	3.80 00	5.77 00	8.27 00	1.14 01	1.55 01	2.06 01	2.73 01	3.60 01	12.40
1050	9.59-01	2.15 00	3.62 00	5.45 00	7.74 00	1.06 01	1.42 01	1.88 01	2.47 01	3.24 01	11.81
1100	9.36-01	2.08 00	3.48 00	5.21 00	7.35 00	1.00 01	1.33 01	2.75 01	2.29 01	2.98 01	11.27
1150	9.20-01	2.03 00	3.39 00	5.04 00	7.06 00	9.56 00	1.27 01	1.66 01	2.16 01	2.80 01	10.78
1200	9.10-01	2.00 00	3.32 00	4.91 00	6.86 00	9.25 00	1.22 01	1.59 01	2.06 01	2.67 01	10.33
1250	9.06-01	1.99 00	3.29 00	4.84 00	6.72 00	9.03 00	1.19 01	1.55 01	2.00 01	2.59 01	9.92
1300	9.06-01	1.98 00	3.26 00	4.79 00	6.64 00	8.90 00	1.17 01	1.52 01	1.96 01	2.54 01	9.54
1350	9.11-01	1.98 00	3.26 00	4.78 00	6.61 00	8.84 00	1.16 01	1.50 01	1.94 01	2.51 01	9.18
1400	9.19-01	2.00 00	3.27 00	4.79 00	6.62 00	8.83 00	1.16 01	1.50 01	1.93 01	2.50 01	8.86
1450	9.31-01	2.02 00	3.30 00	4.83 00	6.66 00	8.88 00	1.16 01	1.50 01	1.94 01	2.52 01	8.55
1500	9.46-01	2.05 00	3.35 00	4.89 00	6.73 00	8.97 00	1.17 01	1.52 01	1.96 01	2.54 01	8.27
E											E
1800	6.87-01	1.49 00	2.43 00	3.54 00	4.87 00	6.48 00	8.47 00	1.10 01	1.42 01	1.84 01	6.89
1900	7.03-01	1.52 00	2.48 00	3.61 00	4.96 00	6.61 00	8.63 00	1.12 01	1.44 01	1.88 01	6.53
2000	7.35-01	1.59 00	2.59 00	3.76 00	5.17 00	6.88 00	8.99 00	1.16 01	1.51 01	1.97 01	6.20
2100	7.69-01	1.66 00	2.70 00	3.93 00	5.40 00	7.18 00	9.38 00	1.22 01	1.58 01	2.07 01	5.90
2200	8.12-01	1.75 00	2.85 00	4.14 00	5.69 00	7.57 00	9.90 00	1.28 01	1.67 01	2.19 01	5.64
2300	8.60-01	1.85 00	3.01 00	4.39 00	6.02 00	8.02 00	1.05 01	1.36 01	1.77 01	2.33 01	5.39
2400	9.13-01	1.97 00	3.20 00	4.65 00	6.39 00	8.51 00	1.11 01	1.45 01	1.89 01	2.49 01	5.17
2500	9.70-01	2.09 00	3.40 00	4.95 00	6.80 00	9.05 00	1.19 01	1.54 01	2.01 01	2.66 01	4.96
2600	1.03 00	2.23 00	3.62 00	5.27 00	7.24 00	9.64 00	1.26 01	1.65 01	2.15 01	2.84 01	4.77
2700	1.10 00	2.37 00	3.86 00	5.61 00	7.71 00	1.03 01	1.35 01	1.76 01	2.30 01	3.05 01	4.59
2800	1.17 00	2.53 00	4.11 00	5.98 00	8.22 00	1.10 01	1.44 01	1.88 01	2.46 01	3.26 01	4.43
2900	1.25 00	2.69 00	4.38 00	6.38 00	8.77 00	1.17 01	1.54 01	2.00 01	2.63 01	3.49 01	4.28
3000	1.33 00	2.87 00	4.67 00	6.80 00	9.35 00	1.25 01	1.64 01	2.14 01	2.81 01	3.76 01	4.13
3100	1.42 00	3.06 00	4.98 00	7.25 00	9.97 00	1.33 01	1.75 01	2.28 01	3.00 01	4.00 01	4.00
3200	1.51 00	3.26 00	5.30 00	7.72 00	1.06 01	1.42 01	1.86 01	2.44 01	3.20 01	4.28 01	3.87
3300	1.61 00	3.47 00	5.64 00	8.22 00	1.13 01	1.51 01	1.99 01	2.60 01	3.42 01	4.57 01	3.76
F											F
4000	1.13 00	2.44 00	3.96 00	5.77 00	7.93 00	1.06 01	1.39 01	1.82 01	2.38 01	3.18 01	3.10
5000	1.78 00	3.83 00	6.24 00	9.09 00	1.25 01	1.68 01	2.21 01	2.89 01	3.81 01	5.12 01	2.48
6000	2.71 00	5.84 00	9.51 00	1.39 01	1.91 01	2.56 01	3.38 01	4.44 01	5.87 01	7.91 01	2.07
7000	3.96 00	8.54 00	1.39 01	2.03 01	2.80 01	3.75 01	4.95 01	6.51 01	8.63 01	1.17 02	1.77
8000	5.57 00	1.20 01	1.96 01	2.86 01	3.95 01	5.29 01	6.99 01	9.20 01	1.22 02	1.65 02	1.55
9000	7.58 00	1.64 01	2.67 01	3.90 01	5.38 01	7.21 01	9.53 01	1.26 02	1.67 02	2.26 02	1.38
10000	1.00 01	2.17 01	3.54 01	5.16 01	7.13 01	9.56 01	1.26 02	1.66 02	2.21 02	3.00 02	1.24

TABLE 13

2492 FILM--EXPOSURE, I(photons/μm²)

NET DENSITY, D
(SPECULAR-0.1<0.1 mA)

PHOTON ENERGY, E(eV)
WAVELENGTH, λ(A)

D

E(eV)	0.2	0.4	0.6	0.8	1.0	1.2	1.4	1.6	1.8	2.0	λ(A)
A											A
75	4.11 01	1.12 02	2.35 02	4.46 02	8.11 02	1.44 03	2.53 03	4.41 03	7.65 03	1.32 04	165.31
100	9.42 00	2.49 01	5.03 01	9.19 01	1.60 02	2.72 02	4.56 02	7.58 02	1.25 03	2.06 03	123.93
125	4.29 00	1.10 01	2.13 01	3.73 01	6.22 01	1.01 02	1.61 02	2.53 02	3.97 02	6.20 02	99.18
150	2.57 00	6.36 00	1.20 01	2.02 01	3.23 01	5.02 01	7.66 01	1.15 02	1.73 02	2.57 02	82.65
175	1.80 00	4.32 00	7.88 00	1.29 01	1.99 01	2.98 01	4.37 01	6.33 01	9.08 01	1.30 02	70.85
200	1.36 00	3.21 00	5.70 00	9.06 00	1.36 01	1.98 01	2.81 01	3.93 01	5.49 01	7.51 01	61.99
225	1.10 00	2.53 00	4.41 00	6.87 00	1.01 01	1.43 01	1.98 01	2.70 01	3.64 01	4.87 01	55.10
250	9.70-01	2.09 00	3.58 00	5.48 00	7.90 00	1.10 01	1.49 01	1.99 01	2.63 01	3.44 01	49.59
275	7.97-01	1.79 00	3.03 00	4.57 00	6.49 00	8.90 00	1.19 01	1.56 01	2.03 01	2.62 01	45.08
B											B
300	4.15 00	1.06 01	2.05 01	3.57 01	5.93 01	9.58 01	1.52 02	2.39 02	3.73 02	5.80 02	41.33
325	3.27 00	8.18 00	1.56 01	2.67 01	4.35 01	6.87 01	1.07 02	1.64 02	2.50 02	3.80 02	38.15
350	2.68 00	6.63 00	1.24 01	2.09 01	3.34 01	5.18 01	7.88 01	1.18 02	1.77 02	2.62 02	35.42
375	2.28 00	5.55 00	1.02 01	1.70 01	2.66 01	4.05 01	6.04 01	8.90 01	1.30 02	1.89 02	33.06
C											C
425	2.17 00	5.29 00	9.74 00	1.61 01	2.52 01	3.83 01	5.69 01	8.36 01	1.22 02	1.77 02	29.17
450	1.88 00	4.52 00	8.24 00	1.35 01	2.09 01	3.13 01	4.59 01	6.66 01	9.57 01	1.37 02	27.55
475	1.67 00	3.98 00	7.18 00	1.16 01	1.77 01	2.63 01	3.80 01	5.44 01	7.70 01	1.08 02	26.10
500	1.50 00	3.54 00	6.33 00	1.01 01	1.53 01	2.23 01	3.20 01	4.50 01	6.29 01	8.72 01	24.80
D											D
550	2.32 00	5.67 00	1.05 01	1.75 01	2.76 01	4.22 01	6.32 01	9.36 01	1.38 02	2.01 02	22.54
600	1.90 00	4.57 00	8.32 00	1.35 01	2.09 01	3.13 01	4.58 01	6.61 01	9.46 01	1.35 02	20.66
650	1.61 00	3.82 00	6.83 00	1.09 01	1.65 01	2.42 01	3.47 01	4.89 01	6.84 01	9.51 01	19.07
700	1.41 00	3.28 00	5.76 00	9.12 00	1.36 01	1.95 01	2.74 01	3.79 01	5.19 01	7.06 01	17.71
750	1.27 00	2.92 00	5.07 00	7.87 00	1.15 01	1.63 01	2.25 01	3.05 01	4.11 01	5.48 01	16.53
800	1.16 00	2.64 00	4.53 00	6.93 00	1.00 01	1.39 01	1.89 01	2.53 01	3.34 01	4.38 01	15.50
850	1.08 00	2.42 00	4.11 00	6.21 00	8.85 00	1.21 01	1.63 01	2.15 01	2.80 01	3.62 01	14.59
900	1.01 00	2.26 00	3.80 00	5.69 00	8.01 00	1.09 01	1.44 01	1.88 01	2.42 01	3.09 01	13.78
950	9.66-01	2.14 00	3.55 00	5.28 00	7.37 00	9.91 00	1.30 01	1.68 01	2.14 01	2.71 01	13.05
1000	9.27-01	2.04 00	3.36 00	4.95 00	6.86 00	9.15 00	1.19 01	1.53 01	1.93 01	2.42 01	12.40
1050	8.99-01	1.96 00	3.22 00	4.71 00	6.49 00	8.59 00	1.11 01	1.41 01	1.78 01	2.21 01	11.81
1100	8.79-01	1.91 00	3.11 00	4.53 00	6.20 00	8.17 00	1.05 01	1.33 01	1.66 01	2.06 01	11.27
1150	8.65-01	1.87 00	3.04 00	4.40 00	6.00 00	7.87 00	1.01 01	1.27 01	1.58 01	1.95 01	10.78
1200	8.57-01	1.85 00	2.99 00	4.31 00	5.85 00	7.65 00	9.76 00	1.22 01	1.52 01	1.87 01	10.33
1250	8.54-01	1.83 00	2.96 00	4.26 00	5.76 00	7.51 00	9.56 00	1.20 01	1.48 01	1.82 01	9.92
1300	8.55-01	1.83 00	2.95 00	4.23 00	5.71 00	7.43 00	9.43 00	1.18 01	1.45 01	1.79 01	9.54
1350	8.59-01	1.84 00	2.95 00	4.23 00	5.69 00	7.39 00	9.37 00	1.17 01	1.44 01	1.77 01	9.18
1400	8.67-01	1.85 00	2.97 00	4.25 00	5.71 00	7.40 00	9.37 00	1.17 01	1.44 01	1.76 01	8.86
1450	8.79-01	1.87 00	3.00 00	4.28 00	5.76 00	7.45 00	9.42 00	1.17 01	1.45 01	1.77 01	8.55
1500	8.94-01	1.90 00	3.04 00	4.34 00	5.83 00	7.54 00	9.53 00	1.18 01	1.46 01	1.79 01	8.27
E											E
1800	6.49-01	1.38 00	2.21 00	3.15 00	4.22 00	5.45 00	6.89 00	8.56 00	1.05 01	1.29 01	6.89
1900	6.64-01	1.41 00	2.25 00	3.21 00	4.30 00	5.56 00	7.02 00	8.72 00	1.07 01	1.32 01	6.53
2000	6.95-01	1.47 00	2.35 00	3.35 00	4.49 00	5.80 00	7.31 00	9.09 00	1.12 01	1.37 01	6.20
2100	7.27-01	1.54 00	2.46 00	3.50 00	4.69 00	6.05 00	7.63 00	9.48 00	1.17 01	1.43 01	5.90
2200	7.68-01	1.63 00	2.60 00	3.69 00	4.94 00	6.38 00	8.05 00	1.00 01	1.23 01	1.51 01	5.64
2300	8.13-01	1.72 00	2.75 00	3.91 00	5.23 00	6.75 00	8.52 00	1.06 01	1.31 01	1.60 01	5.39
2400	8.63-01	1.83 00	2.91 00	4.15 00	5.55 00	7.16 00	9.04 00	1.12 01	1.39 01	1.70 01	5.17
2500	9.18-01	1.94 00	3.10 00	4.41 00	5.90 00	7.62 00	9.61 00	1.20 01	1.48 01	1.81 01	4.95
2600	9.77-01	2.07 00	3.30 00	4.69 00	6.28 00	8.11 00	1.02 01	1.27 01	1.57 01	1.94 01	4.77
2700	1.04 00	2.20 00	3.51 00	5.00 00	6.69 00	8.64 00	1.09 01	1.36 01	1.68 01	2.07 01	4.59
2800	1.11 00	2.35 00	3.74 00	5.33 00	7.13 00	9.21 00	1.16 01	1.45 01	1.79 01	2.21 01	4.43
2900	1.18 00	2.50 00	3.99 00	5.68 00	7.60 00	9.82 00	1.24 01	1.55 01	1.91 01	2.36 01	4.28
3000	1.26 00	2.67 00	4.25 00	6.05 00	8.11 00	1.05 01	1.32 01	1.65 01	2.04 01	2.52 01	4.13
3100	1.34 00	2.84 00	4.53 00	6.45 00	8.64 00	1.12 01	1.41 01	1.76 01	2.18 01	2.69 01	4.00
3200	1.43 00	3.03 00	4.83 00	6.87 00	9.20 00	1.19 01	1.50 01	1.88 01	2.32 01	2.87 01	3.87
3300	1.52 00	3.22 00	5.14 00	7.31 00	9.80 00	1.27 01	1.60 01	2.00 01	2.47 01	3.05 01	3.76
F											F
4000	1.07 00	2.26 00	3.61 00	5.13 00	6.88 00	8.89 00	1.12 01	1.40 01	1.73 01	2.14 01	3.10
5000	1.68 00	3.56 00	5.68 00	8.09 00	1.08 01	1.40 01	1.78 01	2.22 01	2.75 01	3.40 01	2.48
6000	2.56 00	5.42 00	8.65 00	1.23 01	1.65 01	2.14 01	2.71 01	3.39 01	4.21 01	5.21 01	2.07
7000	3.74 00	7.93 00	1.27 01	1.80 01	2.42 01	3.13 01	3.97 01	4.97 01	6.17 01	7.65 01	1.77
8000	5.26 00	1.12 01	1.78 01	2.54 01	3.41 01	4.42 01	5.60 01	7.00 01	8.70 01	1.08 02	1.55
9000	7.17 00	1.52 01	2.43 01	3.46 01	4.65 01	6.02 01	7.63 01	9.55 01	1.19 02	1.47 02	1.38
10000	9.50 00	2.01 01	3.22 01	4.58 01	6.15 01	7.97 01	1.01 02	1.27 02	1.57 02	1.95 02	1.24

TABLE 14

2495 FILM--EXPOSURE, I(photons/μm²)

NET DENSITY, D
(SPECULAR-0.1-0.1 mA)

PHOTON ENERGY, E(eV)
WAVELENGTH, λ(A)

D

E(eV)	0.2	0.4	0.6	0.8	1.0	1.2	1.4	1.6	1.8	2.0	λ(A)
A											A
75	1.65 01	4.51 01	9.46 01	1.80 02	3.28 02	5.84 02	1.03 03	1.79 03	3.11 03	5.40 03	165.31
100	3.83 00	1.02 01	2.06 01	3.78 01	6.62 01	1.13 02	1.90 02	3.18 02	5.28 02	8.76 02	123.98
125	1.78 00	4.56 00	8.93 00	1.58 01	2.65 01	4.34 01	6.98 01	1.11 02	1.76 02	2.78 02	99.18
150	1.09 00	2.74 00	5.20 00	8.91 00	1.45 01	2.28 01	3.54 01	5.43 01	8.26 01	1.25 02	82.65
175	7.89-01	1.93 00	3.53 00	5.96 00	9.40 00	1.44 01	2.16 01	3.20 01	4.70 01	6.87 01	70.95
200	6.21-01	1.49 00	2.71 00	4.41 00	6.80 00	1.01 01	1.48 01	2.14 01	3.05 01	4.34 01	61.99
225	5.20-01	1.23 00	2.20 00	3.52 00	5.31 00	7.77 00	1.11 01	1.57 01	2.19 01	3.04 01	55.10
250	4.53-01	1.06 00	1.87 00	2.94 00	4.38 00	6.30 00	8.87 00	1.23 01	1.69 01	2.30 01	49.59
275	4.07-01	9.42-01	1.64 00	2.56 00	3.77 00	5.35 00	7.43 00	1.02 01	1.37 01	1.85 01	45.08
B											B
300	1.72 00	4.40 00	8.58 00	1.51 01	2.53 01	4.13 01	6.62 01	1.05 02	1.66 02	2.61 02	41.33
325	1.36 00	3.45 00	6.63 00	1.15 01	1.89 01	3.02 01	4.75 01	7.39 01	1.14 02	1.76 02	38.15
350	1.13 00	2.83 00	5.36 00	9.15 00	1.48 01	2.33 01	3.59 01	5.48 01	8.30 01	1.25 02	35.42
375	9.75-01	2.40 00	4.49 00	7.56 00	1.20 01	1.86 01	2.82 01	4.23 01	6.29 01	9.31 01	33.06
C											C
425	9.35-01	2.30 00	4.30 00	7.22 00	1.15 01	1.77 01	2.69 01	4.02 01	5.98 01	8.83 01	29.17
450	8.19-01	2.00 00	3.72 00	6.19 00	9.76 00	1.49 01	2.24 01	3.32 01	4.88 01	7.13 01	27.55
475	7.38-01	1.79 00	3.29 00	5.43 00	8.48 00	1.28 01	1.90 01	2.78 01	4.04 01	5.84 01	26.10
500	6.74-01	1.62 00	2.95 00	4.83 00	7.46 00	1.12 01	1.64 01	2.37 01	3.40 01	4.85 01	24.80
D											D
550	5.92-01	2.45 00	4.61 00	7.78 00	1.25 01	1.94 01	2.95 01	4.45 01	6.66 01	9.92 01	22.54
600	8.29-01	2.02 00	3.73 00	6.20 00	9.74 00	1.48 01	2.21 01	3.27 01	4.78 01	6.95 01	20.66
650	7.17-01	1.72 00	3.14 00	5.13 00	7.92 00	1.18 01	1.74 01	2.51 01	3.60 01	5.13 01	19.07
700	6.38-01	1.52 00	2.72 00	4.39 00	6.68 00	9.83 00	1.42 01	2.01 01	2.83 01	3.97 01	17.71
750	5.85-01	1.37 00	2.44 00	3.87 00	5.80 00	8.41 00	1.19 01	1.67 01	2.30 01	3.16 01	16.53
800	5.45-01	1.27 00	2.22 00	3.48 00	5.14 00	7.34 00	1.02 01	1.41 01	1.92 01	2.59 01	15.50
850	5.14-01	1.18 00	2.05 00	3.17 00	4.63 00	6.52 00	8.97 00	1.22 01	1.63 01	2.17 01	14.59
900	4.91-01	1.12 00	1.92 00	2.94 00	4.24 00	5.90 00	8.03 00	1.07 01	1.42 01	1.87 01	13.78
950	4.73-01	1.07 00	1.81 00	2.75 00	3.93 00	5.42 00	7.29 00	9.64 00	1.26 01	1.63 01	13.05
1000	4.59-01	1.03 00	1.73 00	2.60 00	3.68 00	5.02 00	6.69 00	8.76 00	1.13 01	1.45 01	12.40
1050	4.48-01	9.95-01	1.66 00	2.48 00	3.49 00	4.71 00	6.22 00	8.07 00	1.04 01	1.32 01	11.81
1100	4.40-01	9.71-01	1.61 00	2.39 00	3.33 00	4.47 00	5.85 00	7.53 00	9.58 00	1.21 01	11.27
1150	4.34-01	9.52-01	1.57 00	2.32 00	3.20 00	4.27 00	5.56 00	7.11 00	8.98 00	1.13 01	10.78
1200	4.30-01	9.39-01	1.54 00	2.26 00	3.11 00	4.12 00	5.33 00	6.78 00	8.52 00	1.06 01	10.33
1250	4.28-01	9.30-01	1.52 00	2.21 00	3.04 00	4.01 00	5.16 00	6.53 00	8.17 00	1.01 01	9.92
1300	4.27-01	9.24-01	1.51 00	2.18 00	2.98 00	3.92 00	5.03 00	6.34 00	7.90 00	9.77 00	9.54
1350	4.28-01	9.23-01	1.50 00	2.17 00	2.95 00	3.86 00	4.93 00	6.20 00	7.70 00	9.50 00	9.18
1400	4.30-01	9.24-01	1.50 00	2.16 00	2.92 00	3.82 00	4.87 00	6.11 00	7.57 00	9.32 00	8.86
1450	4.33-01	9.29-01	1.50 00	2.16 00	2.92 00	3.80 00	4.84 00	6.05 00	7.49 00	9.20 00	8.55
1500	4.37-01	9.37-01	1.51 00	2.17 00	2.93 00	3.80 00	4.83 00	6.03 00	7.45 00	9.15 00	8.27
E											E
1800	3.44-01	7.39-01	1.19 00	1.72 00	2.32 00	3.02 00	3.84 00	4.81 00	5.95 00	7.31 00	6.89
1900	3.49-01	7.47-01	1.20 00	1.72 00	2.33 00	3.03 00	3.84 00	4.79 00	5.92 00	7.26 00	6.53
2000	3.59-01	7.67-01	1.23 00	1.76 00	2.37 00	3.08 00	3.90 00	4.86 00	5.99 00	7.34 00	6.20
2100	3.70-01	7.88-01	1.26 00	1.80 00	2.43 00	3.14 00	3.97 00	4.94 00	6.09 00	7.46 00	5.90
2200	3.84-01	8.18-01	1.31 00	1.87 00	2.51 00	3.24 00	4.09 00	5.09 00	6.27 00	7.67 00	5.64
2300	4.01-01	8.52-01	1.36 00	1.94 00	2.60 00	3.36 00	4.24 00	5.28 00	6.49 00	7.95 00	5.39
2400	4.19-01	8.90-01	1.42 00	2.02 00	2.71 00	3.50 00	4.42 00	5.49 00	6.76 00	8.28 00	5.17
2500	4.40-01	9.33-01	1.49 00	2.12 00	2.84 00	3.66 00	4.62 00	5.74 00	7.07 00	8.65 00	4.96
2600	4.62-01	9.80-01	1.56 00	2.22 00	2.98 00	3.84 00	4.85 00	6.02 00	7.42 00	9.09 00	4.77
2700	4.87-01	1.03 00	1.64 00	2.34 00	3.13 00	4.04 00	5.10 00	6.33 00	7.80 00	9.56 00	4.59
2800	5.13-01	1.09 00	1.73 00	2.46 00	3.30 00	4.26 00	5.37 00	6.67 00	8.22 00	1.01 01	4.43
2900	5.41-01	1.15 00	1.83 00	2.60 00	3.48 00	4.49 00	5.66 00	7.04 00	8.67 00	1.06 01	4.28
3000	5.71-01	1.21 00	1.93 00	2.74 00	3.67 00	4.74 00	5.98 00	7.43 00	9.16 00	1.13 01	4.13
3100	6.04-01	1.28 00	2.04 00	2.90 00	3.88 00	5.01 00	6.32 00	7.86 00	9.69 00	1.19 01	4.00
3200	6.38-01	1.35 00	2.15 00	3.06 00	4.10 00	5.29 00	6.67 00	8.30 00	1.02 01	1.26 01	3.87
3300	6.74-01	1.43 00	2.27 00	3.23 00	4.33 00	5.59 00	7.06 00	8.78 00	1.08 01	1.33 01	3.76
F											F
4000	4.97-01	1.05 00	1.68 00	2.39 00	3.19 00	4.12 00	5.20 00	6.46 00	7.96 00	9.78 00	3.10
5000	7.37-01	1.56 00	2.49 00	3.54 00	4.74 00	6.12 00	7.73 00	9.63 00	1.19 01	1.47 01	2.48
6000	1.09 00	2.30 00	3.67 00	5.22 00	7.00 00	9.05 00	1.14 01	1.43 01	1.77 01	2.18 01	2.07
7000	1.56 00	3.30 00	5.27 00	7.50 00	1.01 01	1.30 01	1.65 01	2.06 01	2.55 01	3.15 01	1.77
8000	2.17 00	4.59 00	7.33 00	1.04 01	1.40 01	1.81 01	2.29 01	2.87 01	3.56 01	4.41 01	1.55
9000	2.93 00	6.21 00	9.91 00	1.41 01	1.89 01	2.45 01	3.11 01	3.88 01	4.82 01	5.98 01	1.38
10000	3.86 00	8.18 00	1.31 01	1.86 01	2.50 01	3.23 01	4.10 01	5.13 01	6.37 01	7.90 01	1.24

REFERENCES

[1]R. F. Benjamin, P. B. Lyons, and R. H. Day, "X-ray calibration of RAR 2490 film for application to laser plasma experiments," Appl. Opt. 16, 393-397 (1977).

[2]L. N. Koppel, "Sub-kilovolt x-ray calibration of photographic film," Advances in X-Ray Analysis (Plenum, New York, 1975), Vol. 18, pp. 146-153.

[3]L. N. Koppel, "X-ray calibration of film types SB-5 and RAR 2492 in the 1.5-8 keV region," ARACOR Document No. TR-112-08-02, March 1982.

[4]C. M. Dozier, D. B. Brown, L. S. Birks, P. B. Lyons, and R. F. Benjamin, "Sensitivity of x-ray film. II. Kodak NO-SCREEN film in the 1-100 keV region," J. Appl. Phys. 47, 3732-3739 (1976).

[5]B. L. Henke, H. T. Yamada, and T. J. Tanaka, Pulsed plasma source spectrometry in the 80-8000 eV x-ray region," Rev. Sci. Instrum. 54, 1311-1330 (1983).

[6]B. L. Henke and M. A. Tester, "Techniques of low-energy x-ray spectroscopy (0.1 to 2 keV region)," Advances in X-Ray Analysis (Plenum, New York, 1975), Vol. 18, pp. 76-106.

[7]B. L. Henke, P. Lee, T. J. Tanaka, R. L. Shimabukuro, and B. K. Fujikawa, "Low-energy x-ray interaction coefficients: photoabsorption, scattering, and reflection. E= 100-2000 eV Z=1-94," Atomic Data and Nuclear Data Tables 27, No. 1, 1-144 (1982).

[8]Linear zone plates kindly loaned to us by N. Ceglio's group, Lawrence Livermore National Laboratory.

[9]R. Ernst, Lawrence Livermore National Laboratory, private communication.

[10]B. H. Carroll, G. C. Higgins and T. H. James, Introduction to Photographic Theory, The Silver Halide Process (John Wiley and Sons, New York, 1980), pp. 19-27; C. E. Kenneth Mees and T. H. James (editors), The Theory of the Photographic Process, 3rd Ed. (Macmillan Co., New York, 1966); J. G. Streiffert, "Callier Q of various motion picture emulsions," J. Soc. Mot. Pict. Engrs. 49, 506-522 (1947); C. Tuttle, "The relation between diffuse and specular density," J. Opt. Soc. Am. 12, 559-565 (1926).

[11]J. P. Stoering and A. Toor, "X-ray calibration of Kodak NO SCREEN, Type-AA and Type-M in the 1-4.5 keV region," UCID 16775 (1975); D. B. Brown, J. W. Criss and L. S. Birks, "Sensitivity of x-ray films. I. A model for sensitivity in the 1-100 keV region," J. Appl. Phys. 47, 3722-3731 (1976).

[12]J. G. Streiffert, "Callier Q of various motion picture emulsions," J. Soc. Mot. Pict. Engrs. 49, 506-522 (1947).

[13]C. E. Kenneth Mees and T. H. James (editors), The Theory of the Photographic Process, 3rd Ed. (Macmillan Co., New York, 1966), pp. 190-191.

INVITED AND CONTRIBUTED RESEARCH PAPERS PRESENTED BY THE PRINCIPAL INVESTIGATOR 1983-1984

1983

- Some Recent Work in Low-Energy X-Ray Measurement and Theory
  - -Seminar at the Department of Physics, State University of New York at Stony Brook, May 1983
  - -Seminar at Brookhaven National Laboratory, Upton, New York, May 1983
  - -Seminar at Phillips Electronic Instruments, Inc., Mahwah, New Jersey, May 1983

- Seminar on Characterization of Multilayer Analyzers, Energy Conversion Devices, Inc., Troy, Michigan, June 1983

- A Two-Channel, Elliptical Analyzer Spectrograph for Absolute, Time-Resolving/Time-Integrating Spectrometry of ICF Plasmas in the 100-10,000 eV Region; 300-Channel, Large Aperture Picosecond X-Ray Streak Camera, 25th Annual Meeting of the Division of Plasma Physics, American Physical Society, November 7-11, 1983, Los Angeles

- Some Recent Work in Low-Energy X-Ray Physics and Technology, symposium on Electron- , X-ray- , and Ion-Spectroscopics and their Application to Surfaces, 38th Northwest Regional Meeting of the American Chemical Society, December 27-30, 1983, Honolulu, Hawaii.

1984

-Seminars on Low Energy X-Ray Physics and Technology

- At Lawrence Livermore National Laboratory, January 1984
- At Los Alamos National Laboratory, January 1984
- At Lawrence Berkeley Laboratory, January 1984
- At Sandia National Laboratory, January 1984
- X-Ray Physics and Technology in the U.S.A. Chinese Academy of Science. Beijing, People's Republic of China, June, 1984

- Absolute X-Ray Spectrographic Diagnostics for ICF Plasmas (100-10,000 eV Region); Time-Resolved X-Ray Line Emission Studies of Thermal Transport in Multiple Beam UV-Irradiated Targets, 26th Annual Meeting of the Division of Plasma Physics, American Physical Society, October 29 to November 2, 1984, Boston

RESEARCH PUBLICATIONS BY THE PRINCIPAL INVESTIGATOR
AND CO-WORKERS ON THIS RESEARCH PROGRAM

1979 - 1984

66. "Soft X-Ray Induced Secondary Electron Emission from Semiconductors and Insulators: Models and Measurements," Phys. Rev. B19, (1979) (w/ J. Liesegang and S. D. Smith), 3004-3021.

67. "Low Energy X-Ray Emission Spectra and Molecular Orbital Analysis of CH_4, CCl_4 and $CHCl_3$," J. Chem. Phys. 70, (1979) (w/ R. C. C. Perera), 5398-5406.

68. "The Characterization of Photocathodes for Application to Time-Resolved X-Ray Spectroscopy," Technical Progress Report, AFOSR 79-0027 and DOE DE-AS03-76SF00235, April 1979.

69. "Multilayer X-Ray Spectrometry in the 20-80 A Region: A Molecular Orbital Analysis of CO CO_2 in the Gas and Solid States," X-Ray Spectrometry 9, (1980) (w/ R. C. C. Perera), 81-89.

70. "X-Ray Spectroscopy in the 100-1000 eV Region," Nucl. Instrum. Methods 177, (1980), 161-171.

71. "Evaluation of High Efficiency CsI and CuI Photocathodes for Soft X-Ray Diagnostics," Appl. Opt. 19, (w/ E. B. Saloman and J. A. Pearlman), 749-753.

72. "The Characterization of X-Ray Photocathodes in the 0.1-10 keV Photon Energy Region," J. Appl. Phys. (March 1981) (w/ J. P. Knauer and K. Premaratne), 1509-1520.

73. "Low Energy X-Ray Interactions: Photoionization, Scattering, Specular and Bragg Reflection," AIP Conference Proceedings No. 75 on Low Energy X-Ray Diagnostics, Monterey, California (American Institute of Physics, New York, 1981), 146-155, D. T. Attwood and B. L. Henke, Editors.

74. "Low Energy X-Ray Spectroscopy with Crystals and Multilayers," AIP Conference Proceedings No. 75 on Low Energy X-Ray Diagnostics, Monterey, California (American Institute of Physics, New York, 1981), 85-100, D. T. Attwood and B. L. Henke, Editors.

75. "Appendix: The Atomic Scattering Factor, f + if, for 94 Elements and for the 100 to 2000 eV Photon Energy Region," AIP Conference Proceedings No. 75 on Low Energy X-Ray Diagnostics, Monterey, California (American Institute of Physics, New York, 1981) D. T. Attwood and B. L. Henke, Editors (w/ P. Lee, T. J. Tanaka, R. L. Shimabukuro and B. K. Fujikawa).

76. "X-Ray Diffraction in Multilayers," Opt. Commun. 37, Vol. 34, No. 3, 159-164 (1981), (P. Lee).

77. "Low-Energy X-Ray Interaction Coefficients: Photoabsorption, Scattering and Reflection," Atomic Data and Nuclear Data Tables 27, No. 1, (1982) (w/ P. Lee, T. J. Tanaka, R. L. Shimabukuro and B. K. Fujikawa), 1-143.

78. "The Stability of Cesium Iodide X-Ray Photocathodes," Nucl. Instrum. Methods 207, (1983) (w/ K. Premaratne and E. R. Dietz), 465-467.

79. "Pulsed Plasma Source Spectrometry in the 80-8000 eV X-Ray Region," Rev. Sci. Instrum. 54, (1983) (w/ H. T. Yamada and T. J. Tanaka), 1311-1330.

80. "Low-Energy X-Ray Response of Photographic Films: Part I. Mathematical Models," J. Opt. Soc. America (Dec. 1984) (w/ S. L. Kwock, J. Y. Uejio, H. T. Yamada and G. C. Young).

81. "Low-Energy X-Ray Response of Photographic Films: Part II. Experimental Characterization," J. Opt. Soc. America (Dec. 1984) (w/ F. G. Fujiwara, M. A. Tester, C. H. Dittmore and M. A. Palmer).

82. "Photon Counting Efficiency with High and Low Density CsI Photocathodes in the 100-10,000 eV Region," (w/ K. S. Tan and P. Y. Maeda), in preparation.

83. "X-Ray Diagnostics of Laser Plasmas with a Calibrated Elliptical Analyzer Spectrograph," Doctoral Thesis, University of Hawaii, Tina J. Tanaka, May 1983, 1-124.

84. "A Two-Channel, Elliptical Analyzer Spectrograph for Absolute Time-Resolving/Time-Integrating Spectrometry of Pulsed X-Ray Sources in the 100-10,000 eV Region," (w/ P. A. Jaanimagi), submitted to Rev. Sci. Instrum., Dec., 1984.

85. "Large Aperture Picosecond X-Ray Streak Camera," (w/ P. A. Jaanimagi), submitted to Rev. Sci. Instrum., Dec. 1984.

86. "Numerical Solution of Poisson's Equation," (w/ P.A. Jaanimagi), submitted to J. Comput. Physics, Nov. 1984.

In Preparation:

87. "A New, High Sensitivity, Low-Energy Spectrographic Facility."

88. "Multilayer Analyzers for Low-Energy X-Ray Spectroscopy (100-500 eV): Part I. Mathematical Models," (w/ H.T. Yamada).

89. "Multilayer Analyzers for Low-Energy X-Ray Spectroscopy (100-500 eV): Part II. Construction and Characterization," (w/ N. Balakrishnan and R. E. Tackaberry).

90. "Reflectivity Characteristics of Low-Energy X-Ray Mirror Monochromators," (w/ F. G. Fujiwara, R. E. Tackaberry and D. Kania).

END

FILMED

2-85

DTIC